IMPERIAL

Investigations of clathrate hydrate formation using advanced optical diagnostic techniques

Muhammad Afiq Bin Kamel

September 2025

Department of Chemical Engineering

Imperial College London

Submitted in part fulfilment of the requirements for the degree of
Doctor of Chemical Engineering of Imperial College London
and the Diploma of Imperial College London

Abstract

Clathrate hydrates are crystalline compounds that are formed when water is in contact with a hydrate former. It is found in the ocean layer and typically require high pressure and low temperature to form solids. The stability provided by the guest molecule allows hydrate to maintain in solid phase above the freezing point of water. This creates a technological challenge to attain flow assurance in oil and gas pipelines. Cyclopentane is a good analogue for natural gas due to the mild conditions required for its formation. The lack of studies at conditions below the freezing point of water limits the observation of its morphology variations compared to other types of hydrate former. The unexplored area of hydrate research able to provide information with high spatio-temporal resolutions offers an opportunity to enhance our understanding of the phenomenon.

Characterisation of freezing and hydrate formation was carried out to distinguish the two phenomena at temperatures below 273 K. The subcooling temperature for cyclopentane was successfully extended to 15 K revealed a morphological transformation of hydrate from polygonal to spherulitic crystals. Planar laser-induced fluorescence technique was developed for temperatures between 263 to 283 K. Based on spectral analyses, nile red in cyclopentane (1.74 %/K) and sulforhodamine B and fluorescein 27 in water (2.88 %/K) showed improvements in temperature sensitivity compared to other dyes used in previous studies. Spatio-temporally resolved information of temperatures below 270 K suggest there is significant heat released during hydrate formation to warrant an increase in temperature compared to experiments in the absence of hydrate. Analysis of flow data showed convection dominating the flow in the surrounding phase. Lower velocities in the drop observed in the hydrate case compared to non-hydrate indicate that hydrate film at the interface acts to confine the flow in the drop.

Declaration of Originality

I hereby certify that the material presented in this thesis is the result of my own original research. Where information has been derived from other sources, I confirm that this has been properly indicated and the source suitably referenced.

Copyright Statement

The copyright of this thesis rests with the author. Unless otherwise indicated, its contents are licensed under a Creative Commons Attribution-NonCommercial 4.0 International Licence (CC BY-NC).

Under this licence, you may copy and redistribute the material in any medium or format. You may also create and distribute modified versions of the work. This is on the condition that: you credit the author and do not use it, or any derivative works, for a commercial purpose.

When reusing or sharing this work, ensure you make the licence terms clear to others by naming the licence and linking to the licence text. Where a work has been adapted, you should indicate that the work has been changed and describe those changes.

Please seek permission from the copyright holder for uses of this work that are not included in this licence or permitted under UK Copyright Law.

Acknowledgements

I would like to express my sincere gratitude to my supervisor, Prof. Christos N. Markides for the guidance and support throughout my PhD. I am grateful for the opportunity to be part of the Clean Energy Processes (CEP) Laboratory and for allowing me to tinker in ACEX111. To Aleksei, you have been the greatest help inside and outside of the laboratory, teaching me the necessary experimental skills, helping with the processing of images and providing me with feedback and inputs. I am also greatly thankful to Konstantin, Dr. Surya Narayan and Dr. Victor Voulgaropoulos for their help and insights into laser-based experimental work. I would also like to acknowledge Majlis Amanah Rakyat for the financial support, which has made this work possible. To Luqman, Ali, Tarik, Aktar and Maribel, thank you for being part of this amazing journey.

Finally, and most importantly, I would like to express my deepest gratitude to Mak and Bapak, who have always supported and guided me in the most difficult of times. I am also extremely thankful to my lovely family, Kak Azu, Adek, Azizan, Izuan, Fatih and Rania for the unconditional love. Alhamdulillah.

Publications

The work that is the subject of this thesis and results from the experiments have appeared in:

- Kamel, M.A., Lobasov, A.S., Narayan, S., Pervunin, K. S., Markides, C. N. Hydrate growth over a sessile drop of water in cyclopentane. *Crystal Growth & Design*, 2023

- 21st International Symposium on the Application of Laser and Imaging Techniques to Fluid Mechanics, Lisbon, Portugal, July 2024. Evaluating the thickness of a cyclopentane hydrate film over a sessile water drop using PLIF and PIV. Kamel, M.A., Lobasov, A.S., Pervunin, K. S., Markides, C. N.

- 10th International Symposium on Turbulence, Heat and Mass Transfer, Rome, Italy, September 2023. Interfacial heat transfer during cyclopentane hydrate lateral growth over a sessile water drop. Kamel, M.A., Lobasov, A.S., Narayan, S., Pervunin, K. S., Markides, C. N.

- 17th International Heat Transfer Conference, Cape Town, South Africa, August 2023. Interfacial heat transfer during the lateral growth of hydrate film. Kamel, M.A., Lobasov, A.S., Narayan, S., Pervunin, K. S., Markides, C. N.

- 11th International Conference on Multiphase Flow, Kobe, Japan, April 2023. Dynamics of lateral hydrate growth and associated interfacial heat transfer processes: Backlight visualisation and temperature measurements.Kamel, M.A., Lobasov, A.S., Narayan, S., Pervunin, K. S., Markides, C. N.

- 1st European-American-Japanese Two-Phase Flow Group Meeting, Chamonix, France, October 2022. Experimental observation and temperature measurement during lateral growth of cyclopentane hydrate on a sessile droplet. Kamel, M.A., Lobasov, A.S., Narayan, S., Pervunin, K. S., Markides, C. N.

Nomenclature

Abbreviations

FWHM Full width half maximum

LIF Laser-induced fluorescence

PIV Particle image velocimetry

PLIF Planar laser-induced fluorescence

a_v	Volume expansion coefficient	1/K
$c_{p,w}$	Specific heat capacity of water	J/kg K
$c_{p,g}$	Specific heat capacity of hydrate former	J/kg K
C	Fitted parameter	-
C_m	Molar concentration of dye	mol/dm^3
d_p	Particle diameter	m
$E_{p,exp}$	Laser pulse energy	J
F	Fluorescence signal at wavelength	a.u.
Δh_h	Enthalpy of formation	J/kg
h	Heat transfer coefficient	W/m^2 K
I_o	Intensity of incident laser beam	W/m^2
I_{sat}	Saturation intensity	a.u.
I_{corr}	Corrected pixel intensity	a.u.
I_{corr}	Normalised corrected pixel intensity	a.u.
I_{flat}	Flat field pixel intensity	a.u.
I_{norm}	Normalised pixel intensity	a.u.
I_{raw}	Raw pixel intensity	a.u.
I_{sheet}	Laser sheet pixel intensity	a.u.
$I_{st,avg}$	Time-averaged pixel intensity	a.u.
$I_{s,avg}$	Spatially-averaged pixel intensity	a.u.
k	Proportionality constant	-
K_i	Constant (dependent on dye and optical path)	-
l	Fraction of hydrate film in hydrate former	m
l_{eff}	Effective heat transfer area per unit length	m
L	Optical path length	m
L_o	Characteristic length	m
m	Correction factor	-
n	Constant	-
r_c	Radius of curvature of hydrate front	m
R	Fluorescence ratio	a.u.
s	Sensitivity coefficient	%/K
St_k	Stokes number	-
t_{th}	Thermal relaxation time	s
t_{ind}	Induction time	s
t_r	Relaxation period	s
t_n	Nucleation period	s
t_o	Characteristic time	s
t_g	Growth period	s
ΔT	Subcooling temperature	K
T_f	Hydrate front temperature	K
T_b	Bulk temperature	K
T_{eq}	Hydrate equilibrium temperature	K
u_o	Liquid velocity	m/s
v_f	Growth rate/hydrate front velocity	m/s
V	Volume	m^3

α	Thermal diffusivity	m^2/s
β	Volumetric coefficient of thermal expansion	1/K
δ	Hydrate film thickness	m
ε_o	Molar extinction coefficient at the excitation wavelength	m^2/mol
λ	Wavelength	nm
λ_w	Thermal conductivity of water	W/m K
λ_g	Thermal conductivity of hydrate former	W/m K
μ	Dynamic viscosity	Pa s
ν_w	Kinematic viscosity of water	m^2/s
ν_g	Kinematic viscosity of hydrate former	m^2/s
ρ_h	Hydrate density	kg/m3
ρ_p	Particle density	kg/m3
ρ_w	Density of water	kg/m3
ρ_g	Density of hydrate former	kg/m3
Ω	Solid angle of collection	^{o}
η	Transmission efficiency of fluorescence to detector	-
σ	Thermodynamic driving force	K
σ_{reabs}	Reabsorption cross section	cm^2/molecule
Φ_l	Quantum yield	-

Contents

1 Introduction **1**

1.1 Motivation 1

1.2 Aims and objectives 2

1.3 Outline 4

2 Background **5**

2.1 Clathrate hydrate 5

2.2 Hydrate evolution and morphological transformation 7

2.3 Investigations of hydrate lateral growth 11

2.3.1 Overview of experimental hydrate studies 11

2.3.2 Hydrate induction 17

2.3.3 Modeling of hydrate lateral growth 19

2.4 Advanced optical diagnostic techniques 25

2.4.1 Planar laser-induced fluorescence thermometry 27

2.4.2 Particle image velocimetry 36

2.5 Summary 37

3 Experimental Methods **38**

3.1 Materials 38

3.2 Experimental facility 39

3.3 Hydrate induction procedure 42

3.4 Contact angle measurement 43

3.5 Backlight visualisation 44

3.6 Spectrometer 45

3.7 Planar laser-induced fluorescence (PLIF) thermometry 46

3.7.1 One-colour PLIF thermometry in cyclopentane 46

3.7.2 Two-colour PLIF thermometry in water drop 50

3.8 Particle image velocimetry (PIV) 54

4 Phenomenological characteristics of hydrates **58**

4.1 Ice and hydrate characterisations 59

4.2 Hydrate morphology 64

4.2.1 Hydrate nucleation and induction time 65

4.2.2 Hydrate morphology at varying subcooling temperature 70

4.3 Lateral growth rate of hydrate 77

4.4 Comparisons with hydrate growth rate predictions 82

4.4.1 Mori's hydrate growth model 82

4.4.2 Peng's hydrate growth model 85

4.4.3 Liu's modified hydrate growth model 89

4.5 Summary 94

5 Development of optical techniques for the study of hydrate formation 96

5.1 Fluorescent dye in cyclopentane 97

5.1.1 Concentration dependence of nile red in cyclopentane 100

5.1.2 Temperature dependence of nile red in cyclopentane 104

5.2 Fluorescent dye in water 105

5.2.1 Concentration dependence of sulforhodamine B and fluorescein 27 in water 105

5.2.2 Temperature dependence of sulforhodamine B and fluorescein 27 in water 109

5.3 Effect of additive on hydrate phenomenon 116

5.4 Challenges 118

5.5 Summary 123

6 Temperature and velocity measurements 125

6.1 Temperature and velocity fields 126

6.2 Velocity measurements 135

6.2.1 External and internal flows 135

6.2.2 Varying bulk liquid cyclopentane temperature 136

6.2.3 Velocity comparison between hydrate and non-hydrate cases 138

6.3 Temperature measurements 144

6.3.1 Validation of PLIF measurements 144

6.3.2 Temperature comparison between hydrate and non-hydrate cases 150

6.4 Summary 156

7 Conclusions and future outlooks **158**

7.1 Conclusions 158

7.2 Recommendations for future work 161

Bibliography **163**

Appendices **186**

A Fluorescence spectra of cyclopentane **187**

List of Tables

2.1 Characteristics and building blocks of hydrate crystal structures [1]. 6

2.2 Summary of experimental lateral hydrate growth rate studies for various hydrate formers. 14

2.3 Summary of the temperature sensitivities of fluorescent dyes. 31

2.4 Summary of the temperature sensitivities of fluorescent dye mixtures. 35

3.1 Selection of potential hydrate formers. 39

4.1 Experimental parameters for ice and hydrate characterisation experiments. . . . 60

4.2 Characterisation of cyclopentane hydrate growth mechanism based on crystal morphology. 81

4.3 Thermophysical properties of cyclopentane hydrate, water and liquid cyclopentane. The subscripts h, w and g represent hydrate, water and cyclopentane (guest former). 83

4.4 Values of parameters C and k at two extremes, where hydrate film is assumed to be either fully immersed in cyclopentane (Case 1) or water (Case 2). 86

5.1 Concentration of fluorescein 27 and sulforhodamine B in each dye mixture investigated. 108

5.2 Concentration of additive for optical measurements. 117

List of Figures

2.1 Schematic representation of the cavity formed by water molecules (black line) that encalthrate a molecule of hydrate former (red sphere). The example represents the smallest basic repeating unit of pentagonal dodecahedron (5^{12}). Adapted from Sloan Jr [1]. 6

2.2 Schematic of the evolution of hydrate from nucleation to complete hydrate conversion. Adapted from Taylor et al. [2]. 7

2.3 Summary of the variations in hydrate crystal morphology at a range of subcooling temperature, ΔT. All of the studies were performed in water except the ones noted with A: in sodium chloride solution and B: in seawater. CO_2: carbon dioxide; CH_4: methane; C_2H_6: ethane; C_3H_8: propane; cC_5: cyclopentane; m-cC_6: methylcyclohexane. Morphological information are sourced from: i. Ohmura et al. [3], ii. Oya et al. [4], iii. Tohidi et al. [5], iv. Uchida et al. [6], v. Ohmura et al. [7], vi. Jiang et al. [8], vii. Tanaka et al. [9], viii. Smelik and King [10], ix. Ueno et al. [11], x. Lee et al. [12], xi. Lee et al. [13], xii. Matsuura et al. [14], xiii. Karanjkar et al. [15], xiv. Mitarai et al. [16], xv. Kishimoto et al. [17], xvi. Sakemoto et al. [18], xvii. Cha et al. [19], xviii. Lim et al. [20], xix. Watanabe and Kato [21]. $^{+}$As expressed in the reference, possibly dendrite. 10

2.4 Hydrate induction time as a function of subcooling temperature for different hydrate formers: (i) natural gas (Mali et al. [22]), (ii) methane (Wang et al. [23]) and (iii) tetrahydrofuran (Liu et al. [24]). 19

2.5 General optical arrangement for temperature measurement using one-colour PLIF thermometry. Adapted from Chaze et al. [25]. 29

2.6 General optical arrangement for temperature measurement using two-colour PLIF thermometry. Adapted from Chaze et al. [25]. 34

3.1 Photograph of the hydrate cell from above showing the inner and outer compartments. 40

3.2 Photograph of O-ring adhered to the substrate (sapphire glass) with the purpose of ensuring the water drop is held at exactly the same position within the field of view of the camera. 41

3.3 Schematic drawing of the hydrate cell and arrangement of the visualisation system used for backlight imaging. TC stands for thermocouple. 44

3.4 Binarisation of raw image for the identification of drop interface and quantification of the peripheral length, S. The scale bar denotes 1 mm. 45

3.5 Example of raw images obtained from one-colour PLIF with top and side laser illuminations. The shadows are clearly seen at the periphery on both sides of the water drop when when laser is directed from above. 48

3.6 Time variations of spatially averaged fluorescence intensity, which is directly proportional to the pulse energy. 50

3.7 Dependence of the fluorescence intensity of nile red in cyclopentane on temperature for top (red) and side illuminations (blue). 51

3.8 Schematic drawing of the hydrate cell and optical arrangement of the two-colour PLIF system. Example of raw images obtained from the two cameras at specific spectral bands through a combination of optical filters are also shown. 52

3.9 Dependence of the fluorescence intensity of fluorescein 27 and sulforhodamine B in water on temperature. 53

3.10 Schematic illustration of the optical arrangement used in PIV measurements in cyclopentane with illumination directed from above the hydrate cell. 55

3.11 Schematic illustration of the optical arrangement used in PIV measurements in water drop with illumination directed from the bottom of the hydrate cell. . . . 56

3.12 Example of raw images obtained in particle image velocimetry (PIV) in (a) cyclopentane and (b) water. 57

4.1 Sequential images of a water drop supercooled in silicone oil at a temperature of 266 K at different stages of evolution: (a) original drop (b) ice layer covering the drop and (c) completely frozen drop with a conical tip. TC in the image denotes a thermocouple. 61

4.2 Sequential images of a water drop supercooled in cyclopentane at a temperature of 266 K at different stages of evolution: (a) hydrate growth at the drop interface (b) hydrate film covering the entire drop (c) internal freezing of the drop and (d) ice volume expansion. TC in the image denotes a thermocouple. 62

4.3 Comparison between the temporal variations of temperature inside a water drop undergoing freezing in silicone oil and a water drop subjected to both hydrate formation and freezing in cyclopentane. 64

4.4 Images of hydrate film appearing at the periphery of the drop. 67

4.5 Images of hydrate seeds appearing at the drop interface. 68

4.6 Average induction time of cyclopentane hydrate formation on sessile water drops over a range of subcooling temperatures. The confidence intervals quantify the stochastic nature of hydrate nucleation through the standard deviation of each data point. 69

4.7 Evolution of hydrate formation and growth at a subcooling temperature of 5.1 K. 70

4.8 A closer look on the morphology of hydrate film at a subcooling temperature of 5.1 K. (a) Hydrate crystals having distinctive striations. (b) Polygonal flat plate crystals with different geometries. 71

4.9 Schematic of preferential growth of crystal plates resulting in different crystal morphology. Adapted from Lee and Harris [26]. 71

4.10 Evolution of hydrate formation and growth at a subcooling temperature of 6.9 K. 72

4.11 Evolution of hydrate formation and growth at a subcooling temperature of 7.4 K. 73

4.12 A closer look on the morphology of hydrate film at a subcooling temperature of 7.4 K. (a) Floating spherulite crystals. (b) Hydrate crystals growing as dendrites with distinctive branching. 74

4.13 Evolution of hydrate formation and growth at a subcooling temperature of 11 K. 75

4.14 A closer look on the morphology of hydrate film at a subcooling temperature of 11 K. (a) Agglomeration of spherulites with rough texture. (b) Floating spherulite protruding into cyclopentane phase. 75

4.15 Evolution of hydrate formation and growth at a subcooling temperature of 15.2 K. 76

4.16 A closer look on the morphology of hydrate film at a subcooling temperature of 15.2 K. (a) Spherulites with smoother texture compared to the spherulites formed at a subcooling temperature of 15.2 K. (b) Agglomeration of spherulites with "tortoise shell" appearance. 76

4.17 Schematic of the position of a hydrate crystal with respect to the cyclopentane-water interface depending on its wettability. (a) Hydrophobic hydrate (b) Partially hydrophilic hydrate (c) Hydrophilic hydrate. Adapted from McClements [27]. . . 77

4.18 Comparison between average growth rate of cyclopentane hydrate as a function of subcooling temperature measured experimentally with those reported in the literature. 78

4.19 A schematic of morphological patterns at varying degree of subcooling starting from polyhedral crystals at low subcooling temperature and transitioning to dendrites followed by spherulites as the subcooling temperature increases. 82

4.20 Comparison between predicted values of the lateral growth rate of cyclopentane hydrate, v_{f} (using Mori's convective heat transfer model [28]) with experimentally measured data at varying subcooling temperature, ΔT. Each line corresponds to predicted values for constant hydrate film thickness, δ in the range of 140 to 600 microns. 84

4.21 Illustration of hydrate film relative to water and the hydrate former (adapted from Peng et al. [29]). If the hydrate film grows at a front velocity (i.e., growth rate) of v_{f} and viewing the hydrate film with a moving frame of reference fixed to the edge of the hydrate front, then water and hydrate former can be assumed to flow over the hydrate film at the same approach velocity. 86

4.22 Comparison between predicted values of the lateral growth rate of hydrate, v_{f} (using Peng's convective heat transfer model [29]) with experimentally measured data at varying subcooling temperature, ΔT. 87

4.23 Comparison between predicted values of the lateral growth rate of hydrate, v_{f} (using Peng's convective heat transfer model [29]) with experimentally measured data at varying subcooling temperature, ΔT. 88

4.24 A closer look of the geometry of hydrate front growing on the drop interface (in the boxed region. 89

4.25 Illustration of hydrate film relative to water and the hydrate former (adapted from Liu et al. [30]). The portion that is highlighted in red is the active area of the film that is involved in hydrate growth i.e., the hydrate front. 90

5.1 Photograph of a solution of Sulforhodamine B in ethanol and cyclopentane which was allowed to settle for 24 hours. 98

5.2 Absorption spectra of Sulforhodamine B dissolved in ethanol and cyclopentane at varying temperature. 99

5.3 Emission spectra of Sulforhodamine B dissolved in ethanol and cyclopentane at varying temperature 99

5.4 Photograph of a solution of nile red in cyclopentane which was allowed to settle for 24 hours. 100

5.5 Absorption spectra of nile red dissolved in cyclopentane at various concentrations (0.5, 1.2, 2, 5, 9 and 18 mg/L) at a temperature of 273 K and normalised to the maximum intensity of nile red absorption at a concentration of 18 mg/L. 101

5.6 Curve fitting for the integral of absorption intensity of nile red with concentration. Linear fit gives a coefficient of determination, $R^2 = 0.993$. 101

5.7 Emission spectra of nile red dissolved in cyclopentane at various concentrations (0.5, 1.2, 2, 5, 9 and 18 mg/L) at a temperature of 273 K and normalised to the maximum intensity of Nile Red emission at a concentration of 18 mg/L. 103

5.8 Curve fitting for the integral of emission intensity of nile red with concentration. Linear fit of the first four points gives a coefficient of determination, $R^2 = 0.9694$. 103

5.9 Example of the dependence of emission spectra of nile red dissolved in cyclopentane (1.2 mg/L) on temperature. 106

5.10 Absorption spectra of nile red dissolved in cyclopentane (1.2 mg/L) at varying temperature from 263 to 283 K. 106

5.11 LIF signal parameter, R as a function of temperature. The gradient of the fitted linear curve represents the temperature sensitivity, s for each concentration. The error bar indicates the uncertainty of the measurements. 107

5.12 Temperature sensitivity of the emission of nile red in cyclopentane (in %/K) at 0.5, 1.2 and 2 mg/L. 107

5.13 Normalised absorption spectra of fluorescein 27 and sulforhodamine B mixtures at varying concentration evaluated at a temperature of 273 K. The concentration of sulforhodamine B and fluorescein 17 in each mixture are as per Table 5.1. . . 109

5.14 Normalised emission spectra of fluorescein 27 and sulforhodamine B mixtures at varying concentration evaluated at a temperature of 273 K. The concentration of sulforhodamine B and fluorescein 17 in each mixture are as per Table 5.1. . . 110

5.15 Normalised emission spectra of Mixture 1 (fluorescein 27 (2.2 mg/L) and sulforhodamine B (1.1 mg/L)) at varying temperature from 263 to 283 K. 112

5.16 Normalised emission spectra of Mixture 2 (fluorescein 27 (9.1 mg/L) and sulforhodamine B (1.1 mg/L)) at varying temperature from 263 to 283 K. 113

5.17 Normalised emission spectra of Mixture 3 (fluorescein 27 (19.1 mg/L) and sulforhodamine B (1.1 mg/L)) at varying temperature from 263 to 283 K. 113

5.18 Normalised fluorescence intensity ratio as a function of temperature with curve fitting using second order polynomial for the three mixtures. 114

5.19 Sensitivity coefficient of the dye mixtures investigated between the temperature range of 263 to 283 K. The temperature sensitivities are obtained from the gradients of the linear fitted curves and are found to be 4.82, 3.42 and 2.26 %/K for Mixtures 1, 2 and 3, respectively. 115

5.20 Effect of additive on the contact angle between a water drop and liquid cyclopentane. 117

5.21 Effect of additive on the lateral growth rate of hydrate. 118

5.22 Laser power distribution for estimation of laser sheet thickness measured using a power meter as a razor blade moved along the traverse direction. 119

5.23 The gradient of the power measured. The laser sheet thickness is estimated based on half of the maximum gradient (FWHM). 120

5.24 An example of streaks in two-colour PLIF images after post-processing. 121

5.25 Spatial matching of laser sheet (top illumination) and camera focus plane using a razor blade to create a contrast in the image. The contrast line (boxed area) is used to fine tune the position of laser sheet and camera focus. 122

5.26 Spatial matching of laser sheet (side illumination) and camera focus plane using a razor blade to create a contrast in the image. The contrast line (boxed area) is used to fine tune the position of laser sheet and camera focus. 123

6.1 Instantaneous temperature fields from one-colour PLIF in liquid cyclopentane at a temperature of 266 K that surrounds a water drop (in the absence of hydrate formation) with a volume of 0.25 ml. The colour bar denotes temperature. The dashed line represents the stitching point of the two images obtained from top and side laser illumination and the shaded area represents the water drop and the shadowed region where temperature field was not extracted. 127

6.2 Instantaneous velocity fields from PIV in liquid cyclopentane at a temperature of 266 K that surrounds a water drop with a volume of 0.25 ml in the absence of hydrate formation. The colour bar denotes the flow speed. 129

6.3 Instantaneous temperature fields from two-colour PLIF of a water drop with a volume of 0.25 ml in the absence of hydrate formation at a bulk cyclopentane temperature of 266 K. The colour bar denotes temperature. 131

6.4 Instantaneous velocity fields from PIV of the internal flow in a water drop with a volume of 0.25 ml in the absence of hydrate formation at a temperature of 266 K. The colour bar denotes the flow speed. 132

6.5 Density of water as a function of temperature [31, 32]. Direction of internal flow when water at room temperature is deposited in cold liquid cyclopentane. 133

6.6 Instantaneous velocity fields from PIV of the internal flow in a water drop with a volume of 0.05 ml in the absence of hydrate formation at a temperature of 266 K. The colour bar denotes the flow speed. 133

6.7 Instantaneous temperature fields from two-colour PLIF of a water drop with a volume of 0.25 ml in the presence of hydrate formation at a bulk cyclopentane temperature of 266 K. The colour bar denotes temperature. 134

6.8 Vertical magnitude profiles along the centreline of the drop. (a) Internal flow (b) External flow. 136

6.9 Time evolution of horizontal velocity magnitude profiles crossing the vortices inside the water drop (0.25 ml) in the absence of hydrate formation at varying liquid cyclopentane temperature. 137

6.10 Geometry of flow speed profiles passing through the vortex/vortices (a) horizontal (b) vertical. 138

6.11 Time evolution of horizontal velocity magnitude profiles crossing the vortices inside the water drop (0.25 ml) for hydrate and non-hydrate cases at a liquid cyclopentane temperature of 270 K. 140

6.12 Time evolution of horizontal velocity magnitude profiles crossing the vortices inside the water drop (0.25 ml) for hydrate and non-hydrate cases at a liquid cyclopentane temperature of 266 K. 141

6.13 Time evolution of vertical velocity magnitude profiles crossing the vortex inside the water drop (0.05 ml) for hydrate and non-hydrate cases at a liquid cyclopentane temperature of 270 K. 142

6.14 Time evolution of vertical velocity magnitude profiles crossing the vortex inside the water drop (0.05 ml) for hydrate and non-hydrate cases at a liquid cyclopentane temperature of 266 K. 143

6.15 Example of two-colour PLIF image showing regions close to the drop interface where there is a loss of data as indicated by the dark band. 145

6.16 Temperature measurements obtained from PLIF thermometry at varying distance normal to the drop interface compared to thermocouple measurement after 240 seconds from the introduction of the water drop into liquid cyclopentane at 273.15 K in the absence of hydrate formation. The thermocouple measurement is shown in the figure only as a reference line and does not indicate temperature measurements at different points. 146

6.17 Comparisons between the variations of temperature measurements obtained from PLIF thermometry at 1 mm from the drop interface with the thermocouple measurements. 146

6.18 Temperature measurements obtained from one-colour PLIF thermometry at varying distance normal to the interface compared to the thermocouple readings at 240 and 300 seconds after the introduction of water drop in cold liquid cyclopentane. 147

6.19 Example of one-colour PLIF image of nile red in cyclopentane at $t = 300$ s at a bulk cyclopentane temperature of 273 K in the absence of hydrate formation. . . 148

6.20 Comparisons between the variations of temperature measurement obtained from one-colour PLIF thermometry at various distance normal to the interface. 150

6.21 Locations of the temperature evaluation near the drop interface are indicated by the grey squares in the images. 151

6.22 Evolution of temperature in water obtained using two-colour PLIF at varying liquid cyclopentane temperature: (a) 273 K, (b) 270 K and (c) 266 K, for a water drop with a volume of 0.25 ml. 152

6.23 Evolution of temperature in water obtained using two-colour PLIF at varying liquid cyclopentane temperature: (a) 273 K, (b) 270 K and (c) 266 K, for a water drop with a volume of 0.05 ml. 153

6.24 Evolution of temperature in cyclopentane obtained using one-colour PLIF at varying liquid cyclopentane temperature: (a) 273 K, (b) 270 K and (c) 266 K, for a water drop with a volume of 0.25 ml. 154

6.25 Evolution of temperature in cyclopentane obtained using one-colour PLIF at varying liquid cyclopentane temperature: (a) 273 K, (b) 270 K and (c) 266 K, for a water drop with a volume of 0.05 ml. 155

A.1 Fluorescence spectra of cyclopentane at an excitation wavelength of 355 nm. The peak is artifact from the instrument. 188

A.2 Fluorescence spectra of cyclopentane at an excitation wavelength of 527 nm. The peak is artifact from the instrument. 188

A.3 Fluorescence spectra of cyclopentane at an excitation wavelength of 532 nm. The peak is artifact from the instrument. 189

Chapter 1

Introduction

1.1 Motivation

Clathrate hydrates are naturally found deep in the ocean layers and in the permafrost regions. It is a major reserve of natural gas as large amount of hydrocarbon gases are trapped in cavities that are formed by hydrogen-bonded water molecules that encapsulate the gas molecules in a complex lattice. Formation of the crystalline solids or hydrates require high pressure and low temperature conditions, which is typical in such an environment. From the technological perspective, hydrate pose a challenge in flow assurance as it can also be formed in oil and gas pipelines. The extraction of natural gas require pressure up to hundreds of bar, while the temperature in subsea pipeline can fall within the thermodynamic condition where hydrate is stable, making pipelines susceptible to hydrate formation both during normal operation (i.e., in a flowing system) and during shutdowns (i.e., in a static condition), although less severe [33]. When hydrates agglomerate, they form plugs that restrict pipe flows, which not only cause production loss but also pose safety concerns. The cost to prevent such occurrence is estimated to be between 10 to 15 % of the production cost while the cost to remove plugs is in the order of several millions. The phenomenon of hydrate formation is therefore of prime importance in the field of flow assurance due to the risk of pipe plugging. As such, various efforts have been implemented to mitigate hydrate formation such as heat tracing of pipe walls [34],

injection of thermodynamic inhibitors [35], pipeline dehydration [36], on top of administrative control. However, these methods incur economic impact in the form of capital and operational costs. Moreover, processes tend to be operated within a safe operating envelope that includes a substantial safety margin, which means that there is opportunity cost associated to the potential from oil or gas that is not realised towards production. Hence, there is a drive towards understanding the mechanism of hydrate formation which will contribute towards providing optimal strategies to manage hydrates.

Hydrates also serve other important technological applications. For example, their selectivity for certain molecules make them useful in desalination [37, 38], gas separation [39, 40] and carbon capture and sequestration [41, 42], while their energy densities allow them to act as refrigerants [43, 44]. As hydrates are formed, the guest molecules become well-packed, that provide them with large storage capacities and is therefore suitable for energy storage and transportation [45, 46]. Predictive method is a useful tool to mitigate the risk of hydrate formation. However, to ensure a model is able to provide realistic results requires a good understanding of the complex phenomenon and measurement data to thoroughly validate the model. The literature is lacking in detailed spatio-temporally resolved information of temperature and flow during hydrate formation. Advanced optical diagnostic techniques are capable of capturing and extracting these information. It has been successfully utilised in other processes similar to hydrate formation e.g., freezing [47] and as such, extending its application to hydrate studies is a promising area of research.

1.2 Aims and objectives

Most studies on hydrate are focused on compounds commonly found in natural gas such as methane and carbon dioxide. However, these types of hydrate former require experiments to be conducted at high pressure conditions. Cyclopentane has been proposed to be an alternative hydrate former for laboratory studies due to the mild condition it requires to form hydrates at the expanse of a limited temperature range allowed in experiments. Most studies

on cyclopentane imposed such restriction for fear of ice contamination. Thus, experimental observations of cyclopentane hydrate below the freezing point of water remains limited. To perform hydrate experiments below the freezing point of water requires a study to distinguish the two phenomena. The present work also seeks to address the research gap in spatio-temporally resolved information on temperature and flow with the aim of advancing our understanding on hydrate formation and eventually facilitate relevant industrial operations. With planar laser-induced fluorescence (PLIF) thermometry and particle image velocimetry (PIV) techniques, the aim is to provide insights into the complex interaction between hydrodynamic and heat transfer phenomena during hydrate formation. Having these motivations in mind, the following objectives are set:

- Assess the possibility of extending the subcooling temperature range of cyclopentane hydrate by lowering the experimental condition to below the freezing point of water.
- Characterise freezing and hydrate formation through qualitative and quantitative means to distinguish the two phenomena and provide evidence for the lack of ice contamination at conditions below the freezing point of water.
- Conduct a series of visualisation experiments to determine the lateral growth rate of hydrate and assess the predictive methods in the literature against experimental results.
- Develop PLIF thermometry technique for the application in hydrate studies. Characterise the optical properties including the absorption and emission spectra of each fluorescent dye in water and cyclopentane and evaluate its temperature sensitivity and applicability for PLIF thermometry.
- Conduct experimental measurements using PLIF and PIV for a range of temperature and drop size at ambient pressure to capture the influence of hydrate formation on flow behaviour and temperature during hydrate formation.

1.3 Outline

The thesis is structured in seven chapters. Chapter 1 provides a brief introduction of the topic, motivation and objectives of the work. Chapter 2 presents a review of the literature on the study of clathrate hydrates and a review on fluorescent dyes and their application in liquid-liquid systems. The underlying theory are also discussed. Chapter 3 describes the experimental apparatus and methods employed in this work. Chapter 4 presents the phenomenological observations that includes the characterisation of freezing and hydrate formation. The experimental data are also compared with models available in the literature. Chapter 5 details the development of PLIF in hydrate studies that includes the characterisation of the optical properties of fluorescent dyes. Chapter 6 discusses the temperature and velocity measurements obtained using PLIF and PIV and highlights the ability of the techniques to capture differences between hydrate and non-hydrate cases. Lastly, Chapter 7 presents a summary of the main conclusions from this work and provide suggestions for future work.

Chapter 2

Background

2.1 Clathrate hydrate

Clathrate hydrates are crystalline inclusion compounds that are formed when water (host medium) is in contact with a hydrate former (guest medium). Under the right condition, the water molecules encapsulate the hydrate former forming a network of crystals cavities. The stability of the crystal lattice is provided by the molecules of the hydrate former that supports the structure of the cavities created by the host medium [48, 49], as schematically shown in Figure 2.1. Variations in the size of the guest molecules, give rise to various cage structures, according to the classification by Sloan Jr and Koh [50]. The most common structures are Structure I (sI), Structure II (sII) and Structure H (sH), which all share a common basic building block consisting of a small cavity made of pentagonally bonded water molecules having 12 faces called 5^{12} (pentagonal dodecahedra). Structure I (sI) is joined by a large 14–sided cavity with 12 pentagonal and 2 hexagonal faces ($5^{12}6^2$), while Structure II (sII) is linked by a large 16–sided cavity having 12 pentagonal and 4 hexagonal faces ($5^{12}6^4$). The crystal lattice formed by these structures are made up of a combination of small and large cavities as the basic repeating unit, $5^{12} + 5^{12}6^2$ for sI and $5^{12} + 5^{12}6^4$ for sII. Hydrates with Structure H are not commonly found in nature but are instead synthesised in the laboratory. It possesses a more complex combination of large 20–sided cavity with 12 pentagonal and 8 hexagonal faces ($5^{12}6^8$) and a medium 12–sided

cavity ($4^3 5^6 6^3$) along with a small 5^{12} cavity. The characteristic building blocks of hydrates are summarised in Table 2.1, which includes examples of hydrate formers for each structure. Further details on the classification of the hydrate structures can be found in Sloan Jr [1].

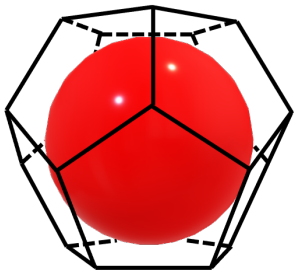


Figure 2.1: Schematic representation of the cavity formed by water molecules (black line) that encalthrate a molecule of hydrate former (red sphere). The example represents the smallest basic repeating unit of pentagonal dodecahedron (5^{12}). Adapted from Sloan Jr [1].

Table 2.1: Characteristics and building blocks of hydrate crystal structures [1].

Hydrate structure	sI		sII		sH		
Cage size	small	large	small	large	small	medium	large
Basic repeating unit	5^{12}	$5^{12}6^2$	5^{12}	$5^{12}6^4$	5^{12}	$4^3 5^6 6^3$	$5^{12}6^8$
Guest molecule size (nm)	0.4 - 0.6		0.6 - 0.7		0.8 - 0.9		
Hydrate former	methane, ethane, hydrogen sulfide, carbon dioxide		propane, cyclopentane, tetrahydrofuran, iso-butane		methane + neohexane, methane + isopentane, xenon + methylcyclohexane		

2.2 Hydrate evolution and morphological transformation

Lee et al. [51] interprets the evolution of hydrate in a gas-liquid environment as having three distinct stages. First it undergoes nucleation, where a cluster of molecules must form to a certain size spontaneously by overcoming an activation barrier to achieve a stable state [52]. The nuclei then grow along the water–hydrate former interface to form a thin layer of hydrate film in what is known as the hydrate lateral growth stage. Once the entire interface is covered with a layer of hydrate film, the hydrate growth then transitions to the thickening growth stage. Taylor et al. [2] proposed a similar model for hydrate formation in a liquid-liquid environment. A schematic of the growth stages are shown in Figure 2.2.

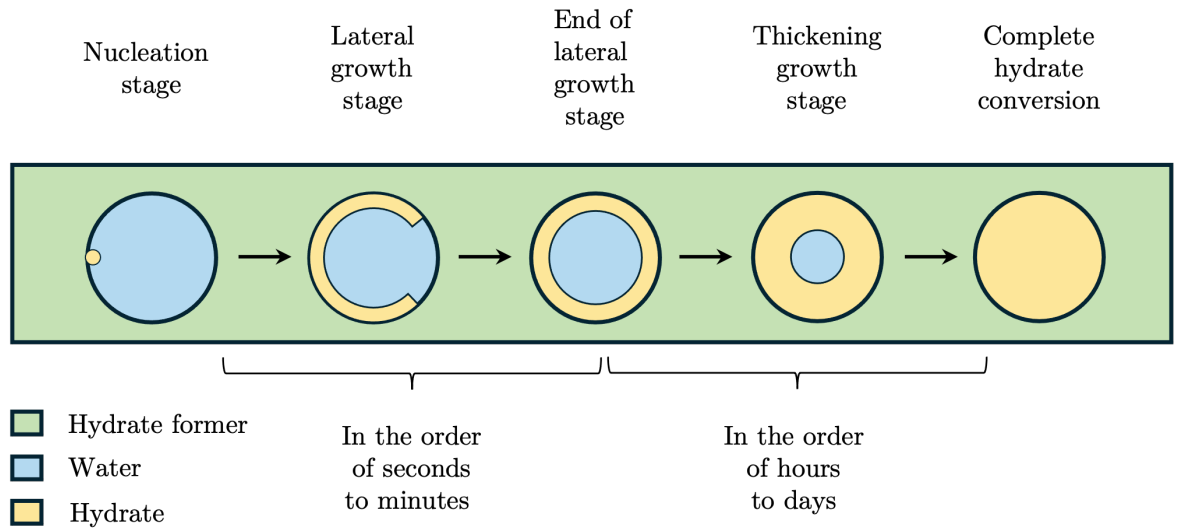


Figure 2.2: Schematic of the evolution of hydrate from nucleation to complete hydrate conversion. Adapted from Taylor et al. [2].

Observation of these growth stages through direct visualisation also provide mechanistic insights into its development process. Most visualisation work concentrate on the lateral growth stage, where the period of growth is in the order of seconds to minutes while the thickening stage is much longer, in the order of hours to days. At different conditions, hydrate undergo morphology transformations. Some of the early observations were reported by Uchida et al. [6] and co-workers. Ohmura et al. [3] observed a transition from polyhedral crystals to dendrites

for carbon dioxide hydrate with increasing thermodynamic driving force, which is often termed as the subcooling temperature or degree of subcooling, ΔT (Equation 2.1).

$$\Delta T = T_f - T_b \tag{2.1}$$

where T_{f} is the temperature at the hydrate front where hydrate is actively growing and T_{b} is the bulk temperature. Often times, the hydrate front temperature, T_{f} is assumed to be at the hydrate equilibrium temperature, T_{eq} [22, 53]. Similar observation was reported by Oya et al. [4] where the transition from polyhedral or polygonal to dendrites occurred when ΔT is approximately 2 K. In methane hydrate, the morphology transition was observed to occur at a higher degree of subcooling as compared to carbon dioxide hydrate. Formation of dendritic hydrate was observed at ΔT greater than 10.4 K [54, 7]. Martinez et al. [55] added on to the variation of hydrate morphology where methane hydrate was observed to transform from polyhedral crystals to spherulite with increasing ΔT. In general, hydrate exhibit polyhedral morphology at the lower end of the subcooling temperature and transition to dendrite and spherulite as the degree of subcooling increases. The transitional ΔT is dependent on the type of hydrate former.

Tetrahydrofuran has been used as alternative hydrate former in laboratory studies [56, 24] as it can form hydrates at ambient pressure. However, it is not a perfect analogue to natural gas as it is completely miscible in water, unlike methane and ethane. Cyclopentane is a hydrate former that is gaining more attention in the research community as it serves as a good analogue for natural gas hydrates in laboratory-scale research. It is stable at ambient pressure and therefore does not require high pressure equipment. However, its hydrate equilibrium temperature, at around 280 to 281 K [50, 18] limits the range of subcooling temperature in most studies to approximately 7 K to avoid competition between freezing and hydrate formation [57, 58]. Within the limited range of ΔT, Karanjkar et al. [15], Mitarai et al. [16], Kishimoto et al. [17] and Sakemoto et al. [18] could only observe polyhedral, polygonal or faceted crystals that are associated with low degree of subcooling. Limited number of research on cyclopentane hydrate reported morphology transformation to dendritic or spherulitic crystal (as shown in Figure 2.3)

and those that did, used a mixture of cyclopentane and other hydrate formers, for example a mixture of carbon dioxide, cyclopentane and hydrogen [20]. Thus the dendritic structure in the study could not solely be attributed to cylopentane. In addition, Lim et al. [20] managed to achieve a high subcooling temperature by conducting their experiment in a pressurised environment up to 60 bar. While there are other works on cyclopentane hydrate available in the literature that extended the range of subcooling temperature beyond 7 K, such as the works of Touil et al. [59] and Sun et al. [60] in sub-milimiter-sized capillary, neither of them characterised the morphology with subcooling temperature. The morphological transformations of different hydrate formers from various studies are summarised in Figure 2.3, which also highlights the gap in literature, particularly for cyclopentane hydrate. There is, therefore, an opportunity to explore the possibility of morphological transformation of cyclopentane hydrate at extended subcooling temperature range above 7 K.

Polyhedral, polygonal and faceted crystals are characterised by their smooth surface while dendritic and spherulitic crystals have feather-like and rough surface appearance. From the crystallographic perspective, Sunagawa [61] argues that dendritic growth occurs due to morphological instability along the growth front. Mullins and Sekerka [62] solved the problem of morphological instability theoretically by proposing a linear theory that demonstrates morphological destabilisation of spherical crystals can be attributed to thermal diffusion. Small perturbation occurring in a high supersaturation (or high degree of subcooling) environment creates non-uniform conditions at the growth front, resulting in preferential growth at certain locations. Crystal growth that is purely diffusion-limited would take a spherical form with no flat surface [61]. According to Li et al. [63], the morphological transformation occur in order to compensate for transport limitation that is experienced by the hydrate front. Thus, dendritic and spherulitic morphologies in hydrate act so as to increase the interfacial area available for heat and/or mass transfer as seen by the peaks and valleys that resulted in the rough appearance on these types of crystal habits.

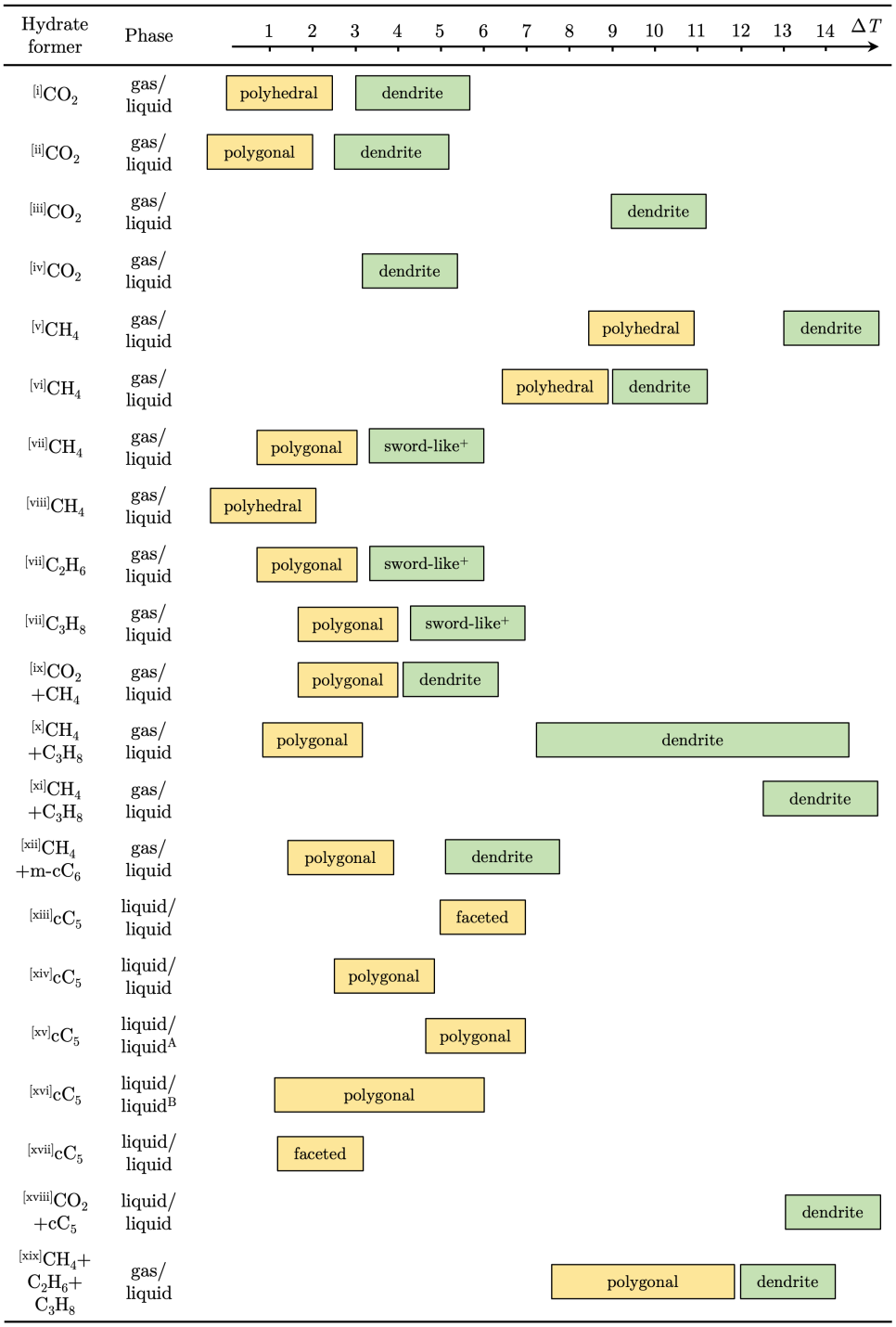


Figure 2.3: Summary of the variations in hydrate crystal morphology at a range of subcooling temperature, ΔT. All of the studies were performed in water except the ones noted with A: in sodium chloride solution and B: in seawater. CO_2: carbon dioxide; CH_4: methane; C_2H_6: ethane; C_3H_8: propane; cC_5: cyclopentane; m-cC_6: methylcyclohexane. Morphological information are sourced from: i. Ohmura et al. [3], ii. Oya et al. [4], iii. Tohidi et al. [5], iv. Uchida et al. [6], v. Ohmura et al. [7], vi. Jiang et al. [8], vii. Tanaka et al. [9], viii. Smelik and King [10], ix. Ueno et al. [11], x. Lee et al. [12], xi. Lee et al. [13], xii. Matsuura et al. [14], xiii. Karanjkar et al. [15], xiv. Mitarai et al. [16], xv. Kishimoto et al. [17], xvi. Sakemoto et al. [18], xvii. Cha et al. [19], xviii. Lim et al. [20], xix. Watanabe and Kato [21]. $^{+}$As expressed in the reference, possibly dendrite.

2.3 Investigations of hydrate lateral growth

2.3.1 Overview of experimental hydrate studies

A sizable number of experimental studies have been dedicated to the investigation of the lateral growth of hydrate. Table 2.2 summarised a selection of such studies for different types of hydrate former. Methane along with carbon dioxide are two of the most commonly studied hydrate formers since these two gases are the most abundant compounds in natural gas. As hydrates of these two gases are only stable at pressures above 29 [64] and 13.5 [65] bar for methane and carbon dioxide, respectively (corresponding to temperatures close to the freezing point of water), the experiments require high pressure apparatus that is able to withstand the extreme condition, not only for the hydrate cell walls but also the sight glass to allow direct visualisation of the phenomenon.

Tanaka et al. [9] utilised a stainless steel cell that is cooled with a brass cooling jacket and fitted with glass windows to study hydrate in a gas-liquid (water droplet) environment. A stage made of *Teflon* that holds a water droplet in place is located at the centre of the cell with a thermometer placed at the bottom of the stage to measure the droplet temperature. Freer et al. [66] constructed a high pressure visualisation cell using brass plates, fitted with sapphire windows for visualisation. The cell is encased in a *Textilite* insulating block to minimise heat gained from the environment. The brass plates are drilled with channels to allow circulation of coolant that provided cooling for the experiments. Insertion wells are also bored into the brass plate where a thermocouple is installed to provide bulk temperature readings.

In a gas (bubble)-liquid environment, Peng et al. [29] make use of a modified, commercially available pendant-drop apparatus that was originally designed for the study of interfacial tension of methane and water near hydrate formation conditions [67]. A Jefri pendant drop pump is used to introduce a bubble in the pressurised cell. Kitamura and Mori [68], on the other hand, constructed a cylindrical stainless-steel pressurised cell with two coaxial sections of different sizes dedicated for water and methane gas. The cell is fitted with a sapphire glass at the bottom of the cell for the purpose of visualisation. Cooling is achieved by placing the entire pressurised

cell in a transparent bath equipped with an immersion cooler. In some works [18, 69], a much simpler arrangement is used, for example, by immersing a test tube in a temperature controlled bath or via a cooling jacket to study cyclopentane hydrate.

Cyclopentane is a hydrate former that permits experiments to be conducted at ambient pressure. While this maybe convenient in terms of experimental handling with reduced safety risk and lower cost of construction, it is at the expense of experimental duration. As seen in Table 2.2, the growth rate of cyclopentane hydrate is reported to be about two orders of magnitude lower compared to that of methane and carbon dioxide hydrates. There is therefore, a motivation to extend ΔT range above 7 K, not only to observe a possible morphological transformation, as discussed in Section 2.2 but also to reduce the experimental duration of cyclopentane hydrate. Furthermore, increasing ΔT would also facilitate hydrate nucleation and reduce the induction time, which can take up to 24 hours [70].

Although most of the studies on cyclopentane hydrate mentioned the limitation on ΔT was to prevent ice contamination [71, 72], none of the work reported an attempt to characterise the phenomena of freezing and hydrate formation. The difficulty comes from the similarities between the physical appearances of ice and hydrate, which makes it challenging to distinguish between the two solids formed. However, there are other attributes that are unique to freezing, which can be exploited to characterise the phenomenon. For example, freezing is known to undergo recalescence, an event that occurs during the solidification of a subcooled liquid where there is a sudden temperature rise to the ice-water equilibrium temperature (or the freezing point of water) due to the release of latent heat. As the rate of freezing is relatively fast (in the order of 10^{-1} m/s at a ΔT of 15 K [73]), in addition to the latent heat of freezing being relatively larger compared to the latent heat of hydrate formation, there is a global temperature rise within the volume of water. Hence, a pointwise measurement using, for example, a thermocouple, is sufficient to record the increase in temperature during freezing and this has been widely reported in the literature [74, 75]. While heat is also released during the formation of hydrate, due to its solidification rate being relatively slower (in the order of 10^{-3} m/s at similar ΔT of 15 K [29]), the rise in temperature is likely to be observed locally. Thus, it is harder to use pointwise measurements to record the temperature increase during

the formation of hydrate unless multiple thermocouples are placed close to the interface, which could be intrusive to the hydrate phenomenon.

Generally, hydrate studies are performed in three types of interface. The hydrate former can either be in the form of: i. a bubble or droplet in water, ii. the surrounding phase that envelops a water droplet, iii. a planar interface with water. In majority of the studies, the formation of hydrate at the water-hydrate former interface is observed through direct visualisation using a combination of a camera and different types of zooming lenses or microscope through a sight glass. Since hydrate forms at the interface, only the portion that is in the direct optical path of the camera is visible. For the case of a planar interface, both portions of hydrate film in water and hydrate former are visible such as the work of Taylor et al. [2]. However, there is also a cause of concern as the sight glass that is in contact with water and hydrate former may have an influence on the hydrate growth. Beltrán and Servio [76] observed hydrate growth on a surface that goes beyond the water boundary at the interface resembling a halo. They refer to it as the 'bridge effect' where the propagation of hydrate on the surface of the wall or sight glass occurs as water is drawn out of the hydrate layer through capillary effect towards the glass. Therefore the lateral growth rate and film thickness of hydrate on a planar interface measured from the sight glass could potentially be apparent values rather than the actual hydrate growth and film thickness. Similar observation of the bridge effect was reported by Martinez et al. [55].

Measurement of hydrate growth rate on the interface of a droplet or bubble, on the other hand, would not be influenced by the bridge effect. However, it has its own limitation in that the portion of the hydrate film that is immersed in the droplet or bubble will not be visible and the measurement may not represent the total thickness of the hydrate film. Uchida et al. [77] utilised a Mach-Zehnder interferometer that observed changes in the refractive index due to a change in temperature at the hydrate front to locate and track the position of the hydrate front. This allowed the estimation of the growth rate and thickness of hydrate film.

Table 2.2: Summary of experimental lateral hydrate growth rate studies for various hydrate formers.

Hydrate former	Interface	Temperature range	ΔT	Growth rate (μm/s)	Visualisation	Reference
CH_4	Gas (bubble)/ liquid	273.4 - 289.4	2.5 - 14.5	(0.47 - 21.5) $\times 10^2$	Stereomicroscope + video camera	Peng et al. [29]
CH_4	Gas/liquid (droplet)	282.5 - 285.7	1.5 - 3.3	(0.66 - 49.9) $\times 10^2$	Microscope + CCD camera	Tanaka et al. [9]
CH_4	Gas/liquid	274.2 - 277.2	3.0 - 12.1	(0.22 - 6.90) $\times 10^2$	Microscope + CCD camera	Freer et al. [66]
CH_4	Gas (bubble)/ liquid	276.2	3.2 - 8.5	(3.3 - 3.88) $\times 10^2$	Stereomicroscope + caamera	Sun et al. [78]
CH_4	Gas/liquid	274.2	2.6 - 9.8	(0.24 - 5.45) $\times 10^2$	Microscope + video recorder	Kitamura and Mori [68]
CH_4	Gas/liquid	260 - 273	3.5 - 7.5	(0.42 - 2.85) $\times 10^2$	Microscope + CCD camera	Taylor et al. [2]
CO_2	Gas (bubble)/ liquid	273.4 - 279.4	1.6 - 8.5	(1.15 - 76.4) $\times 10^2$	Stereomicroscope + video camera	Peng et al. [29]
CO_2	Liquid (droplet)/ liquid	268.2 - 288.2	0.5 - 10.5	(0.769 - 18.7) $\times 10^3$	Microscope + camera + Mach-Zehnnder interferometer	Uchida et al. [77]

Hydrate former	Interface	Temperature range	ΔT	Growth rate (μm/s)	Visualisation	Reference
CO_2	Gas/ liquid (droplet)	280.4 - 281.5	0.6 - 1.7	(0.44 - 2.13) $\times 10^2$	Microscope + CCD camera	Ueno et al. [11]
C_2H_4	Gas (bubble)/ liquid	273.4 - 279.4	2.4 - 15.9	(0.56 - 40.2) $\times 10^2$	Stereomicroscope + video camera	Peng et al. [29]
C_2H_4	Gas/ liquid (droplet)	275.2 - 278	1.6 - 4.2	(0.34 - 14.3) $\times 10^2$	Microscope + CCD camera	Tanaka et al. [9]
C_3H_8	Gas/ liquid (droplet)	273.4 - 277.2	1.2 - 3.1	0.09 - 16.2	Microscope + CCD camera	Tanaka et al. [9]
cC_5	Liquid/liquid	274.6 - 278.8	1.4 - 5.6	0.05 - 2.76	Microscope + camera	Sakemoto et al. [18]
cC_5	Liquid/liquid	274.7 - 279.2	1.7 - 6.2	0.07 - 5.0	Microscope + camera	Stoner et al. [79]
cC_5	Liquid/liquid	274.2	6.2	3.5	Binocular magnifier + camera	Delroisse et al. [69]
cC_5	Liquid/liquid	275.9 - 279.5	1.4 - 5	0.04 - 1.3	Microscope + camera	Mitarai et al. [16]
cC_5	Liquid/liquid	274.2	6.5	2.2	Microscope	Morrissy et al. [80]
cC_5	Liquid/liquid	273 - 277.4	3 - 7.2	2.2 - 6.7	Video camera	de Baños et al. [81]

Hydrate former	Interface	Temperature range	ΔT	Growth rate (μm/s)	Visualisation	Reference
cC_5	Liquid/liquid	267.2 - 277.4	2.8 - 12.9	0.29 - 20.5	Microscope + camera	Touil et al. [59]
cC_5	Liquid/liquid	269.2 - 275.2	5 - 11	1.67 - 6.23	camera	Sun et al. [60]
CH_4 + $C_{10}H_{22}$	Gas/liquid/ liquid (droplet)	276 - 279.4	1.3 - 4.6	4.6 - 96.8	Microscope + CCD camera	Imasato et al. [82]
CH_4 + C_3H_8	Gas (bubble)/ liquid	273.4 - 279.4	7 - 16	6.5 - 51.5	Stereomicroscope + video camera	Peng et al. [29]

2.3.2 Hydrate induction

A liquid is said to be in metastable state when it is subjected to a condition below the freezing point, where it is expected to transition to a thermodynamically stable solid phase, but instead it remains in liquid form, which is outside of the stability region in its phase diagram. This is termed as a supercooled liquid. Water can remain in metastable state at temperatures as low as 234 to 236 K [83, 84]. Conversely, Roedder [85] observed the stretching of the metastability of ice made from frozen aqueous liquid inclusions in fluorite at temperatures above the melting point of ice (superheated ice). Natural gas hydrates, which are inclusion compounds made from water and hydrate formers, also exhibit metastability. The delay in the formation of hydrate, which is the period from when hydrate equilibrium temperature is reached to the moment upon which the first hydrate seeds are identified macroscopically is defined as the induction time, t_{ind}. According to Mullin [86], the induction time consists of i. a relaxation period (t_{r}) to achieve a quasi-steady state distribution of molecular clusters, ii. a nucleation period (t_{n}) in order to form a stable cluster and iii. a growth period (t_{g}) to allow the cluster to grow into a size that is large enough for it to be detectable. However, these different periods are indistinguishable and are lumped into the induction time as expressed in Equation 2.2.

$$t_{ind} = t_r + t_n + t_g \tag{2.2}$$

From the perspective of the oil and gas industry, it is desirable to prolongate the induction time so as to delay the formation of hydrate in oil and gas pipelines and thus hindering the onset of pipeline plugging. However, limitation in laboratory studies require experiments to be conducted within an acceptable time frame. Furthermore, hydrate nucleation are stochastic in nature, particularly at low thermodynamic driving force, which ultimately results in significant scatter in the hydrate induction time. This makes it challenging to achieve experimental repeatability for hydrate studies. However, studies have shown that the stochasticity of hydrate nucleation can be reduced by increasing the thermodynamic driving force [87], which in the crystallisation process, is typically regarded as the degree of supersaturation or subcooling.

Mali et al. [22] and Liu et al. [24] have shown that the induction time of hydrate reduces with increasing subcooling temperature. Figure 2.4 shows the influence of subcooling temperature on the hydrate induction time, normalised for different hydrate formers. As seen in Figure 2.4, there is a region in the subcooling temperature where the induction time increases sharply as the subcooling temperature reduces. Above this threshold, the induction time remains short and relatively constant. This serves as a motivation for further extending the range of subcooling temperature for cyclopentane hydrate beyond the limitation often imposed by the freezing point of water. Similarly, Natarajan et al. [87] increased the supersaturation by increasing the system pressure. Meanwhile Jensen et al. [88] reported that the induction time can also be affected by agitation and by shifting the supersaturation level through the addition of additives, which were also reported in several other studies [89, 90]. However, agitation and introduction of additives are not suitable methods of hydrate induction especially when the temperature is below the freezing point of water as they promote freezing, which would then compete and dominate over hydrate formation.

Additionally, the memory effect of water can further reduce the induction time. One of the first observations on the phenomenon was reported by Vysniauskas and Bishnoi [91], where hydrates form more readily when the water used to form hydrate has a history of ice or hydrate (i.e., thawed ice or dissociated hydrate). It was also shown that while the induction time was significantly reduced when the memory effect was utilised as a method of induction, the water history has no influence on the hydrate growth rate. Ho-Van et al. [92] utilised thawed hydrate crystal that was pre-prepared in a separate reactor, which was then transferred to the main reactor to study the mechanism of cyclopentane hydrate growth in brine. Conversely, Sakemoto et al. [18] took a different approach by placing a pre-prepared hydrate crystal into the test cell without thawing the crystal seed i.e. via contact nucleation. This approach, however, would be challenging when the experimental temperature is below the freezing point of water as it may cause a disturbance when the seed is in contact with water as it may promote freezing. Alternatively, Zylyftari et al. [93] employed thawed ice a precursor for hydrate formation where a temperature protocol was devised to convert water through a sequence from ice to thawed ice and eventually to hydrate.

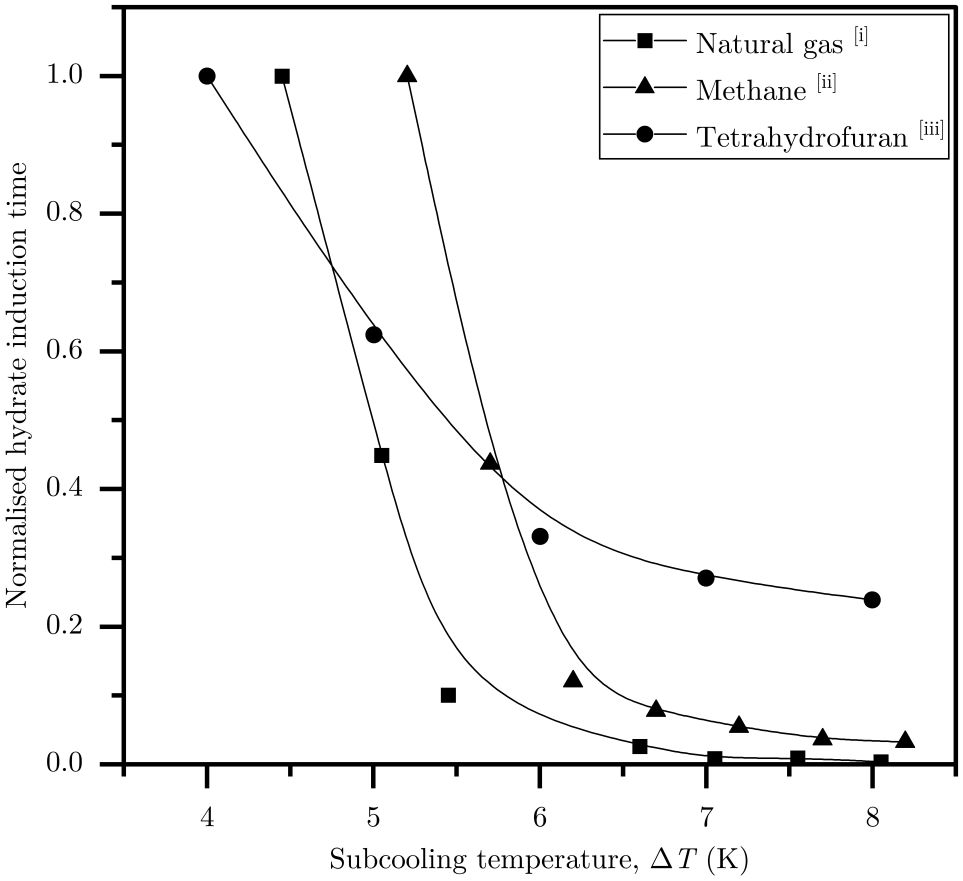


Figure 2.4: Hydrate induction time as a function of subcooling temperature for different hydrate formers: (i) natural gas (Mali et al. [22]), (ii) methane (Wang et al. [23]) and (iii) tetrahydrofuran (Liu et al. [24]).

2.3.3 Modeling of hydrate lateral growth

Many researchers have contributed to the effort to model the lateral growth of hydrate. The hydrate models published in the literature can be categorised into three main types based on the controlling mechanism: i. mass transfer, ii. intrinsic kinetics and iii. heat transfer. However, there is no standard model that could describe all of the observed hydrate growth behaviour. The different models are dependent on the experimental configurations (i.e. the type of reactor, the interface of water and the hydrate former). Moreover, the mechanisms could also differ based on the operating condition, in other words, on the supersaturation or subcooling temperature, which can be observed by the morphology of the hydrate film. According to Niu and Xu [94],

flat surfaces or facets of crystals forming various polygonal shapes are due to preferential crystal growth in certain directions in a kinetically-limited process. Changes to the morphologies of crystals may arise due to instabilities in the liquid-crystal interface caused by a rapid growth, which is limited by diffusion at the solidification front, resulting in dendritic morphologies [95]. In such growths, crystals tend to maximise its surface area through side-branching forming tree-like structures or dendrites, to allow heat to dissipate more quickly [96].

One of the first attempts to model the lateral growth of hydrate as a heat transfer-limiting process is by Uchida et al. [6]. They performed microscopic observations of carbon dioxide hydrate and observed dendritic growth at the water-carbon dioxide interface. In their experiments, they found that the lateral growth of carbon dioxide hydrate has a larger dependence on temperature compared to pressure, which led them to postulate that the rate-determining process is mainly heat diffusion from the solidification front. Their experimental data can be described by a linear equation as a function of the temperature difference between the hydrate equilibrium temperature and the bulk temperature, as shown in Equation 2.3,

$$v_f = C\Delta T \tag{2.3}$$

where C is a fitting parameter with a correlation coefficient of approximately 0.90. Additionally, they proposed a conductive heat balance at the hydrate front assuming quasi-steady, one-dimensional growth of a planar solid surface at the water-carbon dioxide interface. In such case, they approximated the temperature gradient at the hydrate front to be $(T_{\mathrm{f}}\text{-T})/r_{\mathrm{c}}$, where T_{f} is taken as the hydrate equilibrium temperature, as shown in Equation 2.4, which was used to estimate the thickness of hydrate film (where v_{f} is the lateral growth rate, ρ_{h} is the density of hydrate, ΔT is the subcooling and r_{c} is the radius of curvature of hydrate front which is assumed to be hemicircular in shape).

$$v_f \rho_h \Delta h_h = \frac{\lambda_w \Delta T}{r_c} \tag{2.4}$$

Mori [28], on the other hand, proposed an alternative convective heat transfer model, where the growth of hydrate is governed by the convective heat transfer that is induced in both water and hydrate former. The moving hydrate front is taken as the effective heat transfer area and is assumed to have a hemicircular shape, with each quadrant being in contact with water and the hydrate former. As hydrate film grows at a constant speed of v_{f}, taking a fixed frame of view at the moving hydrate front, water can be visualised as moving towards the hydrate front at velocity v_{f}. Heat balance at the hydrate front is expressed by Equation 2.5

$$v_f \delta \rho_h \Delta h_h = \frac{1}{4}\pi(\overline{h}_w + \overline{h}_g)\Delta T \tag{2.5}$$

where δ is the hydrate film thickness and is assumed to not be a function of ΔT. The average heat transfer coefficients, $\overline{h}$ (subscripts w and g represent water and hydrate former, respectively) were obtained from convective heat transfer correlation for creeping flow regime based on the work of Hilpert [97] as expressed in Equation 2.6.

$$\overline{Nu} = Re^{1/3} Pr^{1/3} \tag{2.6}$$

Using Equations 2.5 and 2.6, the lateral growth rate of hydrate can be correlated to ΔT by Equation 2.7,

$$v_f \delta = C \Delta T^{3/2} \tag{2.7}$$

where C is a coefficient that relies on the thermophysical properties of water, the solid hydrate and the hydrate former.

Comparing their model with the experimental data by Uchida et al. [6], they found that the lateral growth rate of carbon dioxide hydrate is better correlated to $\Delta T^{3/2}$ as compared to the linear relation proposed by Uchida et al. [6]. However the same model does not agree well with the experimental data of carbon dioxide hydrate by Hirai et al. [98] potentially due to the

assumption of constant hydrate film thickness with respect to subcooling temperature. It has been shown through interferometric measurements that the film thickness of R-134a hydrate is inversely proportional to the subcooling temperature, ΔT [99]. Furthermore, the assumption in the model whereby the hydrate film is considered to be immersed in water and the hydrate former phase in equal proportion is rather arbitrary.

Building on from the model proposed by Mori [28], Peng et al. [29] suggested an alternative model with further improvements by taking the hydrate film thickness, δ to be inversely proportional to the subcooling temperature, ΔT (Equation 2.8).

$$\delta = \frac{k}{\Delta T} \tag{2.8}$$

where k is a proportionality constant. Additionally, the fraction of hydrate film that is immersed in the hydrate former phase is taken as a variable, l, that is dependent on the composition of the hydrate former instead of taking a fixed arbitrary value. Similar to Mori [28], the hydrate front is assumed to be hemicircular in shape, in which the curvature, r_{c} is approximated to be $\delta/2$. Taking these assumptions as well as Equation 2.8 into consideration, the lateral growth rate of hydrate can expressed as Equation 2.9

$$v_f = \psi \Delta T^{5/2} \tag{2.9}$$

$$\psi = \frac{C}{k} \tag{2.10}$$

where ψ is defined by Equation 2.10 and C is a coefficient that is dependent on the thermophysical properties of solid hydrate, water and the hydrate former. The contribution of water and hydrate former to the lateral growth rate in the heat transfer model through the immersion of the hydrate film in each of the phase is embedded in the formulation of the parameter C, as expressed by Equation 2.11. The model showed good agreement with experimental data of lateral growth rate with respect to ΔT and the estimation of the hydrate film thickness is

qualitatively consistent with the experimental observation.

$$C = \left[\frac{A}{2\rho_{\mathrm{h}}\Delta h_{\mathrm{h}}} \left(\frac{\lambda_{\mathrm{w}}}{\nu_w^{1/3}} Pr_{\mathrm{w}}^{1/3} \left(\pi - \cos^{-1}\left(1 - \frac{2l}{\delta}\right)\right) + \frac{\lambda_{\mathrm{g}}}{\nu_{\mathrm{g}}^{1/3}} Pr_{\mathrm{g}}^{1/3} \cos^{-1}\left(1 - \frac{2l}{\delta}\right)\right)\right]^{3/2} \tag{2.11}$$

While Mori [28] and Peng et al. [29]'s heat transfer models are based on forced convection, Liu et al. [30] argues that in a quiescent environment, the hypothesis of forced convection is questionable. They instead proposed that the mechanism of heat transfer is more likely to be via natural convection. A buoyancy effect in the surrounding fluid immediately ahead of the hydrate front is naturally caused by the difference in temperature between the bulk fluid and hydrate front as heat of formation is released. As hydrates are known to be good thermal insulators [6], the heat released at the hydrate front is removed through natural convection to fluids that is in contact with the newly-formed hydrate film i.e. water and hydrate former. The heat balance at the hydrate front can be expressed as Equation 2.12,

$$v_f \delta \rho_h \Delta h_h = (h_g l_{h-g} + h_w l_{h-w}) \Delta T \tag{2.12}$$

where l is the effective heat transfer area per unit length of the newly-formed hydrate (subscripts w, g and h refer to water, hydrate (guest) former and hydrate, respectively; h-w and h-g represent water and hydrate former that are in contact with the solid hydrate, respectively).

Liu et al. [30] took a different approach in terms of the geometry of the hydrate front compared to the hemicircular front taken by Uchida et al. [6], Mori [28] and Peng et al. [29] by assuming that it consists of two parts: a flat horizontal plate that is in contact with gaseous methane (hydrate former) and an incomplete horizontal circular cylinder that is in contact with water. Using Nusselt correlations for natural convection [100, 101, 102, 103] and taking the geometries in methane and water into account, the correlations in Equations 2.13 and 2.14 were used to derive the relation between growth rate and subcooling temperature, ΔT (Equation 2.15).

$$Nu_g = \alpha(Gr_g Pr_g)^{0.2} \tag{2.13}$$

$$Nu_w = 0.5\alpha(Gr_w Pr_w)^{0.25} \tag{2.14}$$

$$v_f = \frac{C_1 \alpha a_{v,w}^{0.25} \Delta T^{1.25}}{\delta^{0.25}} + \frac{C_2 \alpha a_{v,g}^{0.2} \Delta T^{1.2}}{\delta^{0.4}} \tag{2.15}$$

C_1 and C_2 are coefficients that are dependent on the thermophysical properties of water, the hydrate former and hydrate, a_v is the volume expansion coefficient for each phase and α is a correction factor for the heat transfer coefficients since $Gr \ll 1$. In this model, they have also assumed that the hydrate film thickness is inversely proportional to the subcolling temperature, ΔT, similar to the approach taken by Peng et al. [29] (Equation 2.8). Using α and k that were obtained from regression analysis, the model agrees well with experimental data. They also reported a lower average error for the estimation of hydrate film thickness compared to other heat transfer models [29, 66, 104].

While most of the works that attempted to model the lateral growth of hydrate reported good agreement with experimental results, they are still limited to one or more fitted parameters. These parameters, which are obtained empirically, tend to depend on the conditions of the experiments, experimental apparatus' geometry, as well as the time and spatial scales of the experiments. Moreover, these models only reflect the average growth of hydrates, whereas the nucleation and growth occur and release heat locally, which requires continuous tracking. Therefore, obtaining field information would be a step forward in advancing the knowledge on hydrate growth in laboratories, and thus promoting investigations of fundamental nature.

2.4 Advanced optical diagnostic techniques

Hydrate formation is in itself a complex phenomenon. It involves heat and mass transfer, reaction kinetics, as well as interactions between fluid mechanics and thermodynamics. Hydrate nucleation and growth can occur at any point along the hydrate former-water interface and as such any temperature change as a result of the release of heat of hydrate formation is likely to be observed locally. Therefore, it would be useful to perform spatio-temporally resolved measurements to capture the dynamics of hydrate formation and to obtain as much information as possible to describe the phenomenon. Earlier efforts relied on relatively simple measurements, for example, using thermocouples to extract temperature information (as briefly mentioned earlier in Section 2.3) during hydrate formation. Most of the studies outlined in Table 2.2 employed one or two thermocouples placed at a distance from the interface to measure the bulk temperature in each phase. Since hydrate formation is an interfacial phenomenon, placing an array of thermocouple close to the water-hydrate former interface to track changes in temperature would potentially have an effect on hydrate nucleation [105] and also on the fluid dynamics of the process.

Advanced optical diagnostic techniques such as planar laser-induced fluorescence (PLIF) and particle image velocimetry (PIV) are promising techniques to obtain whole-field temperature and velocity information, as well as hydrate growth rates, which would be useful in moving towards hydrate prediction using first principle modeling that combines the effect of both heat and mass transfer. Laser-induced fluorescence (LIF) is an optical technique that relies on the absorption and emission of a substance after being excited with a light source. The emission of fluorescence is a result of the return of a photon to the ground state after excitation because it is unstable in the excited state. During the relaxation period, some energy is lost which result in a Stokes shift of the emission wavelength, thus making the emission slightly red-shifted.

The fluorescent species are typically organic dyes such as rhodamines, cyanines, fluoresceins and coumarins. Some of the dyes are influenced by the condition of the surrounding fluid, which therefore allows them to be used as proxies to determine the local properties of the fluid. Recording of the fluorescence emission would then allow visualisation of flow and phase

distribution and measurements of parameters of interest to be made through proper calibration. The imaging technique can be used to perform quantitative measurements such as species concentration, temperature and pH as well as qualitative analysis such as interfacial tracking of multiphase flows. The technique is inherently non-intrusive and will not potentially affect the nucleation and dynamics of hydrate formation. PIV, on the other hand, is an optical method that provides flow visualisation and also measures instantaneous velocity of a fluid flow. The measurement is obtained by seeding the fluid with tracer particles that are sufficiently small such that they follow the fluid motion closely. A light source can be used to illuminate the particles for better visibility. Successive images of the particles can be processed to calculate the velocity of the fluid.

There have been very few attempts to apply advanced optical techniques for the study of clathrate hydrate. Brown and Ni [106] utilised LIF to measure phase distribution of water with the aid of a fluorescent dye that is soluble in water but insoluble in the hydrate-former phase (liquid cyclopentane). The measurement allowed them to track the evolution of hydrate growth by capturing sequential images of the region of interest (ROI), which give information on the advancing solid-liquid interface or hydrate front. In their case, the measured hydrate growth rate is in the thickening growth stage, which has also been measured with other techniques such as magnetic resonance imaging (MRI) [107] and laser interferometry [99]. Measurements of the lateral growth stage of hydrate using the same technique is more challenging because of the thickness of hydrate film, in the order of microns, which requires optical devices with high spatial resolution. Hence most of the previous studies in the literature rely on direct visualisation, which gives an average lateral growth rate rather than instantaneous growth rate. Hirai et al. [108] successfully measured pH distribution to study the effect of hydrate film on the dynamics of liquid carbon dioxide as part of strategy for deep sea carbon dioxide disposal. Using PIV, Sabase and Nagashima [109] studied the expansion of the hydrate crystal agglomerate to elucidate the mechanism of hydrate thickening. The distinct shapes on the rough surface morphology of the hydrate agglomerate are used as reference points to replace tracer particles to track the expansion of the hydrate agglomerate.

2.4.1 Planar laser-induced fluorescence thermometry

Temperature measurement is a crucial parameter in the study of hydrates. In some works, it is defined as the driving force for hydrate formation. Most modelling works assume that the hydrate front is at the three-phase hydrate equilibrium temperature. However, it is challenging to measure the hydrate front temperature due to the moving interface. In addition, the presence of thermocouple at the interface may affect the dynamics of the flow and the nucleation kinetics. This thus makes PLIF thermometry a good prospect for temperature measurements in hydrate studies as it is a non-intrusive technique. Although, to the best of the author's knowledge, PLIF thermometry has not been applied for the study of clathrate hydrates, it has been used to study freezing, a phenomenon involving phase change from liquid to solid that is similar to hydrate formation. Stiti et al. [47] performed temperature measurements of supercooled droplets using two-colour PLIF thermometry to a temperature as low as 256 K. In their study, they further extended the technique to three-colour/two-dye to obtain the ice fraction during freezing. Conversely, Volkov and Strizhak [110] captured the temperature recording of a suspended water droplet during ice melting using both one-colour and two-colour PLIF thermometry. The two different techniques showed an average difference of 0.25 K.

Temperature measurements can be performed with LIF by taking advantage of the temperature dependence of the fluorescent dyes. This arises due to variations in absorption cross section at the excitation wavelength and/or quantum efficiency with temperature, allowing the measurement of fluorescent intensity to represent the temperature field. According to Chaze et al. [25], the fluorescence signal, F_λ emitted at wavelength λ in a volume V can be expressed as

$$F_\lambda = \eta \frac{\Omega}{4\pi} \varepsilon_o \phi_\lambda \frac{I_o}{1 + \frac{I_o}{I_{sat}}} C_m V \tag{2.16}$$

where I_o is the intensity of the incident laser beam, C_m is the molar concentration of the dye molecules, η is the transmission efficiency of the fluorescence light to the detector, Ω is the solid angle of collection, ε_o is the molar extinction coefficient at the excitation wavelength of the laser beam, Φ_λ is the fluorescence quantum yield and I_sat is the saturation intensity of the

dye. The expression can be rewritten as a ratio at temperature T and an arbitrary reference temperature T_{o} as shown in Equation 2.17 with $g_{\mathrm{o},\lambda}(\mathrm{T})$ defined as the ratio of the quantum yields (Equation 2.18).

$$\frac{F_\lambda(T)}{F_\lambda(T_o)} = g_{o,\lambda}(T)\frac{1+\frac{I_o}{I_{sat}(T_o)}}{1+g_{o,\lambda}(T)\frac{I_o}{I_{sat}(T_o)}}\frac{\varepsilon(T)}{\varepsilon(T_o)} \tag{2.17}$$

$$g_{o,\lambda}(T) = \frac{\Phi_\lambda(T)}{\Phi_\lambda(T_o)} \tag{2.18}$$

Two of the parameters in Equation 2.17 are temperature dependent (the quantum yield, Φ_λ embedded in $g_{\mathrm{o},\lambda}$ and the absorption cross section, ε,) which thus contribute to the temperature sensitivity. The sensitivity of the dye to temperature can be quantified by introducing the sensitivity coefficient, s that represents the change in fluorescence intensity to a change in temperature (Equation 2.19). Assuming that s is independent of temperature, Equation 2.19 can be written as Equation 2.20.

$$s = \frac{1}{F}\frac{dF}{dT} \tag{2.19}$$

$$s = \frac{ln\frac{F(T)}{F(T_o)}}{T-T_o} \tag{2.20}$$

Temperature measurements based on laser-induced fluoresence signal was first developed using a single dye at a single spectral band [111, 112] (one-colour PLIF). The selection of proper fluorescent dye for PLIF thermometry is an important step to obtain good temperature measurements. Sutton et al. [113] describes the selection criteria of the fluorescent dye as folows:

- The dye must be soluble in the fluid of interest.
- The dye must exhibit sufficient temperature dependence over a suitable temperature range.
- The absorption and emission of the dye must be spectrally separable.

- The reabsorption of the emitted fluorescence signal must be minimal.

Numerous studies have applied one-colour PLIF thermometry in water, mostly involving heating above room temperature, and some involving cooling below room temperature, as summarised in Table 2.3. Comparing the temperature sensitivities of different fluorescent dyes, it is seen that some dyes such as rhodamine B and sulforhodamine B are more sensitive at relatively low temperature as indicated by the negative sensitivity coefficients, while some others like fluorescein disodium and fluorescein 27 are sensitive at higher temperature as reflected by the positive sensitivity coefficients. In contrast, hydrophobic fluorescent dyes that are soluble in non-polar or organic fluids like hydrocarbon compounds that can become hydrate-formers are scarce. Pyrromethene 597-8C9 is a potential candidate that has been used for PLIF thermometry in diesel [114] and kerosene [115]. However, utilising pyrromethene 597-8C9 in hydrate studies can be cost prohibitive. Another potential candidate is nile red that has been used for temperature determination in non-polar heat transfer fluids [116].

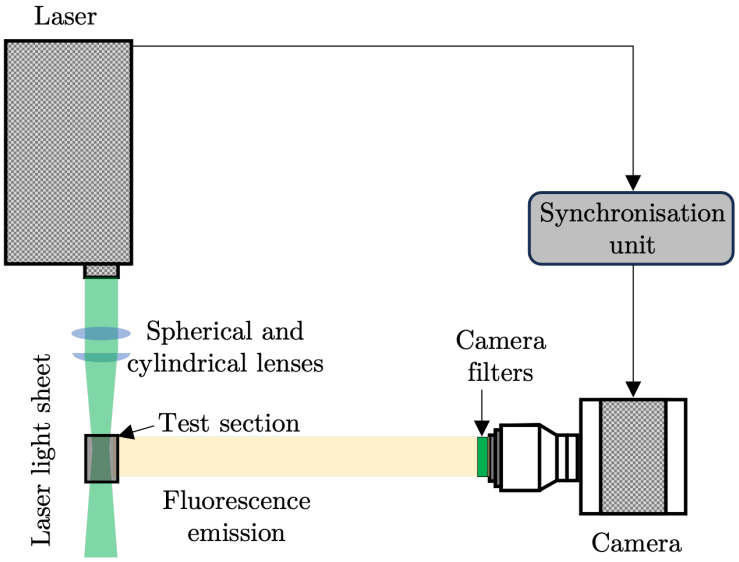


Figure 2.5: General optical arrangement for temperature measurement using one-colour PLIF thermometry. Adapted from Chaze et al. [25].

The optical arrangement for one-colour PLIF only requires one camera to capture the fluorescent emisison of the dye upon laser excitation and therefore is relatively easy to apply. A general

optical layout of one-colour PLIF thermometry is as shown in Figure 2.5. However, the technique is susceptible to measurement error if the experimental condition is not strictly controlled. Such an error may be a result of variations in pulse-to-pulse laser light intensity, changes in dye concentration and temperature gradient. Changes in temperature can also cause changes in density which subsequently result in variations of refractive index. This results in a shadowgraph effect (thermal lens), in which there exist local variations in fluorescence intensity that introduce error in temperature measurement [117]. In addition, curved interfaces such as that found in wavy flows, droplets and bubbles can cause reflections at the interface [118] which result in changes in signal intensity captured by the camera which does not exclusively originate from temperature variations. A ratiometric approach can overcome or minimise these issues. A reference that is independent of temperature is used to obtain a fluorescence ratio with the temperature sensitive dye.

The fluorescence signal, F_{i} collected at spectral bands 1 and 2 in a measuring volume V at temperature T can be written as Equations 2.21 and 2.22, where K_{i} is a constant that depends on the dye and optical path, C_{i} is the fluorescent dye concentration and I_{o} is the intensity of the incident laser beam.

$$F_1 = K_1 C_1 V I_o e^{s_1 T} \tag{2.21}$$

$$F_2 = K_2 C_2 V I_o e^{s_2 T} \tag{2.22}$$

Taking a ratio between the two spectral bands at temperature T gives an expression as per Equation 2.23 and a normalised ratio can be obtained by normalising Equation 2.23 with a reference ratio at a known temperature T_{o} to obtain Equation 2.24. The overall temperature sensitivity, s of the fluorescent dye mixture can be obtained using Equation 2.25.

$$R_{12} = \frac{F_1}{F_2} = \frac{K_1 C_1}{K_2 C_2} e^{(s_1 - s_2)T} \tag{2.23}$$

Table 2.3: Summary of the temperature sensitivities of fluorescent dyes.

Fluorescent dye	Medium	Excitation (nm)	Sensitivity coefficient (%/K)	Temperature range (K)	Reference
Rhodamine B	Water	488	-2	289 to 313	Kim et al. [119]
Rhodamine B	Water	488	-2.3	288 to 313	Hishida and Sakakibara [120]
Rhodamine B	Water	532	-1.5 to -2	273 to 323	Volkov and Strizhak [110]
Rhodamine B	Water	532	-1.59	293 to 353	Sutton et al. [113]
Rhodamine B	Water + ethylene glycol	532	+0.15	273 to 343	Liu and Lu [121]
Rhodamine B	Water	532	-2.38	300 to 353	Chaze et al. [25]
Rhodamine B	Water	532	-0.8	294 to 333	Rochlitz and Scholz [122]
Rhodamine B	Water	532	-0.8	293 to 353	Bruchhausen et al. [123]
Rhodamine 110	Water	488	+0.13	289 to 313	Kim et al. [119]
Rhodamine 110	Water	532	+0.9	294 to 333	Rochlitz and Scholz [122]
Rhodamine 6G	Water	532	-0.07	300 to 353	Chaze et al. [25]
Rhodamine 640	Water	532	+0.05	300 to 353	Chaze et al. [25]
Sulforhodamine B	Water	532	-2.43	300 to 353	Chaze et al. [25]
Sulforhodamine B	Water	532	-1.58	293 to 353	Sutton et al. [113]
Sulforhodamine B	Water	514	-1.55	293 to 333	Coppeta and Rogers [124]
Sulforhodamine 640	Water	532	-0.06	399 to 353	Chaze et al. [25]
Fluorescein disodium	Water	488	-0.3	298 to 318	Walker [125]
Fluorescein disodium	Water	488	-0.16	293 to 333	Coppeta and Rogers [124]
Fluorescein disodium	Water	514	+2.43	293 to 333	Coppeta and Rogers [124]
Fluorescein 27	Water	532	+3.5	293 to 353	Sutton et al. [113]
Fluorescein 27	Water	532	+1.88	300 to 353	Chaze et al. [25]
Pyrromethene 597-8C9	Diesel	532	+0.5	298 to 388	Wolff et al. [114]
Pyrromethene 597-8C9	Kerosene	532	-1.3	243 to 323	Doublet et al. [115]

$$\frac{R_{12}}{R_{12,o}} = e^{(s_1-s_2)(T-T_o)} \tag{2.24}$$

$$s = s_1 - s_2 = \frac{ln(\frac{R_{12}}{R_{12,o}})}{(T-T_o)} \tag{2.25}$$

There are two ways to achieve the ratiometric approach. The first approach is the two-colour/one-dye technique that was first introduced by Lavieille et al. [126] to overcome the need to maintain a constant ratio of dyes during experiments as the temperature sensitivity depends on the dye concentrations in the mixture. Certain dyes have temperature sensitivity that vary with wavelength. The technique exploits this characteristic by obtaining fluorescence intensity ratio at two spectral bands with considerably different temperature sensitivity. In selecting the appropriate spectral bands, one may encounter a band with low energy. In such a case, a photomultiplier could be useful to amplify the fluorescence signal. Another issue that may arise is self-absorption at the spectral band which may be different at the two spectral bands. This effect is more apparent for large droplets with large optical paths, leading to errors in temperature measurements. To overcome the issue of re-absorption in large optical paths, Lavieille et al. [127] proposed a method based on three spectral bands that allows the quantification of the re-absorption of fluorescence signal. The technique requires strict criteria for the selection of the spectral bands to accomodate temperature and absorption sensitivities. Introducing additional spectral band also translates to increasing complexity of optical setup.

In performing two-colour/one-dye technique, Bruchhausen et al. [123] took the approach of performing temperature calibration curves for different optical paths to evaluate the effect of reabsorption. Such an approach requires extensive experimental effort especially when there is a big influence of reabsorption and varying optical paths such as the case of measurements of droplet evaporation or in sprays where there are significant volume changes. While the technique overcomes the issue of variation in local laser intensity and changes in volume under the condition that reabsorption is not an influencing factor, it has a lower temperature sensitivity compared to the one-colour/one-dye technique. This is because the temperature

sensitivity is limited by the two spectral bands selected whereas the entire range of temperature sensitivity can be used for one-colour PLIF.

The second alternative to the ratiometric approach utilise two dyes that emit at two different wavelengths, also known as the two-colour/two-dye technique. The two spectral bands selected should ideally correspond to the peak emission of each dye with good spectral separation to minimise spectral conflict. The dyes should also have different sensitivities to temperature. Table 2.4 shows the overall temperature sensitivities of different fluorescent dye combinations. When the technique was first developed by Sakakibara and Adrian [128], the dyes were selected such that one is sensitive to temperature and the other has little to no sensitivity to temperature. Sutton et al. [113] proposed using dyes with opposing temperature sensitivities, which, theoretically, will increase the overall sensitivity (as shown in Equation 2.25). They reported a significant increase in temperature sensitivity, up to 7% at 323 K. In a later study, Shafii et al. [129] took the same approach for dyes dissolved in ammonium chloride solution and reported similar improvement in temperature sensitivity compared to the original work by Sakakibara and Adrian [128]. A disadvantage of the two-colour/two-dye approach is the possibility of interference occurring between the two dyes resulting in spectral conflict. The error in measurement can be minimised by maintaining low dye concentrations. Another issue with the technique is that the resulting temperature sensitivity is dependent on the dye concentrations in the mixture [128]. However, this is only an issue when measurement involves large volume changes such as combustion or evaporative sprays.

When performing this technique, an issue may arise when the excitation is at a higher wavelength compared to the peak emission of one of the dyes. Sutton et al. [113] dealt with it by proper selection of filters to separate the emission of the two dyes and thus capturing the two peak emissions, including the anti-stokes portion of one of the dyes, in addition to using a notch filter to block the light source interference. The same approach was used by Aguiar et al. [130] to study boiling. The two-colour PLIF technique requires an additional camera to capture the two spectral bands which are directed to each camera with the aid of a beam splitter at 45° incident angle. The fluorescence emission in each spectral band are separated using a combination of interference and notch filters. In the ratiometric approach, the images captured by the two

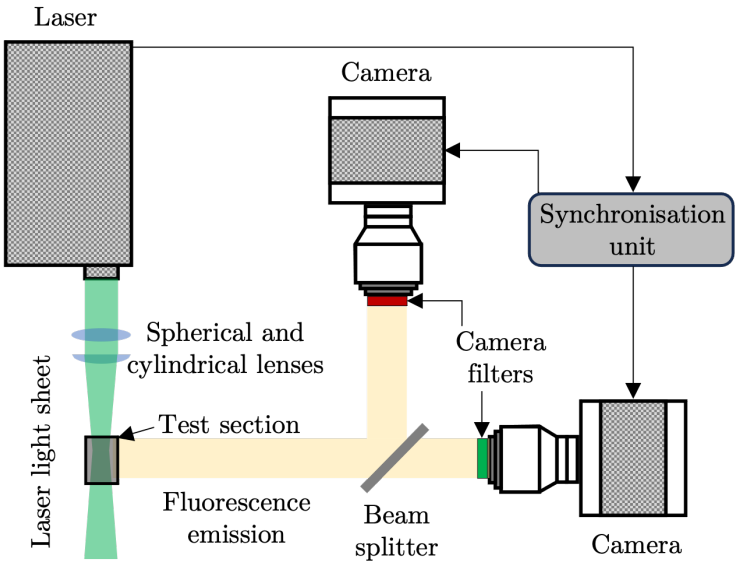


Figure 2.6: General optical arrangement for temperature measurement using two-colour PLIF thermometry. Adapted from Chaze et al. [25].

cameras have to be corresponded pixel-by pixel. Therefore the optical arrangements require proper adjustment and tuning. Additional fine tuning can be performed with the help of a calibration target and further spatial correction can be performed in post-image processing to compensate for camera misalignment [120]. A typical optical layout of two-colour PLIF thermometry is shown in Figure 2.6.

Table 2.4: Summary of the temperature sensitivities of fluorescent dye mixtures.

Fluorescent dye	Medium	Excitation (nm)	Sensitivity coefficient (%/K)	Temperature range (K)	Reference
Sulforhodamine B + Fluorescein 27	Water	532	+7	303 to 343	Sutton et al. [113]
Sulforhodamine B + Fluorescein	Ammonium chloride solution	514.5	-4	277 to 293	Shafii et al. [129]
Sulforhodamine B + Rhodamine 110	Water	532	-2.56	256 to 278	Stiti et al. [47]
Sulforhodamine 101 + Fluorescein	Water	527	+1	358 to 373	Aguiar et al. [130]
Sulforhodamine 640 + Fluorescein	Water	532	+3	293 to 338	Chaze et al. [25]
Rhodamine B + Rhodamine 110	Water	488	-1.6 to -1.7	288 to 313	Sakakibara and Adrian [128]
Rhodamine B + Fluorescein 27	Water	532	+6.5	303 to 343	Sutton et al. [113]
Rhodamine B + Fluorescein 27	Water	532	+4	293 to 353	Tan et al. [131]

2.4.2 Particle image velocimetry

Several studies have employed PIV to capture the internal flow in water droplets during freezing. Karlsson et al. [132] performed PIV inside a sessile water droplet that is placed on cold plate aiming to investigate the influence of natural convection and/or Marangoni convection on the internal flow within the droplet. The PIV measurement was performed using fluorescent tracers (Rhodamine B-coated polystyrene particles, density: 1050 kg/m^3, diameter: 3.16 μ). The laser used to illuminate the fluorescent particle was directed from the bottom of the water droplet to get a two-dimensional slice along the centreline of the droplet. Following on from the work of Karlsson et al. [132], Fagerström and Ljung [133] studied the impact of freezing on the internal flow of a water droplet by comparing the flow direction and internal velocity between freezing and non-freezing water droplets using the same fluorescent particles for PIV measurements. However, the laser sheet in their study was directed from the side. In both studies, the water droplets were exposed to air. Taking a different approach, Voulgaropoulos et al. [134] performed PIV measurements inside a sessile water droplet that is surrounded by oil in sub-zero temperatures in a free convection arrangement to study the freezing dynamics and flow-field characteristics. They utilised Rodhamine 6G-coated PMMA particles (density: 1190 kg/m^3, diameter: 10 μm) and performed the PIV measurement by exciting the fluorescent particles from the bottom of the droplet. Fluorescent tracer particles were used instead of reflective tracers to minimise reflection effect from the water-oil and ice-water interface.

2.5 Summary

A thorough review of the literature on hydrate studies was performed and gaps in research were identified. Firstly, there is an opportunity to explore the possibility of morphological transformation of cyclopentane hydrate at extended subcooling temperature range. Crystal morphology provides a qualitative way to characterise the mechanism of crystal growth. While morphological transformation of hydrate has been reported for carbon dioxide, methane and mixtures of hydrocarbon compounds, cyclopentane hydrate morphology is limited to polygonal crystals. The morphology of cyclopentane hydrate at ΔT greater than 7 K remains unexplored as the attention was drawn to ΔT of less than 7 K to avoid the risk of ice interference.

Secondly, numerous experimental studies exist on hydrates with most studies utilising visualisation techniques to measure growth rate and to obtain qualitative observation of hydrate film. A small number of studies have utilised advanced optical diagnostic techniques in hydrates to measure growth rate and pH using PLIF as well as visualising the expansion of hydrate agglomerate using PIV. It is evident that there is potential for the advancement of PLIF and PIV techniques for hydrate studies, which are able to provide whole-field quantitative information of temperature and flow. These information would not only give insights into the phenomena of hydrate formation but would also provide experimental data that can be used for model validation for future works on hydrate prediction.

Chapter 3

Experimental Methods

This chapter contains the description of all the materials, experimental apparatuses and techniques used to study hydrate. Firstly, the experimental facility, consisting of a hydrate cell and its constituent parts, are described in detail, along with the experimental protocol used to produce hydrates. Secondly, the methods used for the characterisation of fluorescent dyes and additives in liquid cyclopentane are presented. This is followed by the experimental techniques applied and methods used to analyse the collected data.

3.1 Materials

Hydrate formation tend to favour high pressure and relatively low temperature conditions. For example, methane hydrates, being the most abundant form of hydrate in nature, is stable at a pressure of 27 bar and temperature of 274.15 K. However, performing laboratory experiments with highly flammable fluids at high pressure poses safety concerns and extra safety precaution have to be taken. In a pioneering work to develop optical techniques for hydrate application involving Class 4 laser, an alternative test fluid to natural gas hydrate formers with reduced safety risk was considered. There are very few hydrate formers that are able to form hydrates at atmospheric pressure. The options considered are as listed in Table 3.1. The final selection of hydrate former is based on the properties of the fluid, particularly its boiling point in order

Table 3.1: Selection of potential hydrate formers.

Hydrate former	Boiling point (K)	Hazard
Cyclopentane	323	Flammable
Cyclopropane	240	Highly flammable & asphyxiant
Isobutane	261	Highly flammable
Dichloromethane	312	Eye irritant

to maintain the hydrate former in liquid phase at ambient condition, as well as hazards related to fluid handling. Cyclopentane is a promising choice that has been used in a number of hydrate studies [135, 136, 79]. Cyclopentane hydrate is stable at atmospheric pressure below an equilibrium temperature of 280.7 K [50, 18]. It therefore makes it a good option as a hydrate former to study the evolution of hydrate in a laboratory-scale research, as the risk of operating flammable compounds at high pressure is reduced, thus making the experiment safer and easier, without the need for high-pressure equipment.

The liquid cyclopentane was purchased from Merck KGaA (reagent grade, purity $\geq$ 98%). Other fluids used in the experiments are monoethylene glycol (Aqua 1200E) purchased from Aqua Cooling, silicone oil purchased from Dow Corning (viscosity 28 mPa s, density 980 kg/m^3 and ultra-pure deionised water with electrical conductivity of 10 μS obtained from Elga Centra R200 water purification system.

3.2 Experimental facility

The experiments were conducted using a modified cell, originally designed for boiling studies and later adapted for hydrate research. The cell is constructed from stainless steel with 6-mm thick walls and consists of two sections. The inner compartment (Figure 3.1, measuring 60 $\times$ 60 $\times$ 80 mm, serves as the main test section and holds 120 ml of test fluid (liquid cyclopentane or silicone oil). Visual access into the test section is provided through four 20-mm diameter, 3-mm thick round quartz glass windows installed on each side of the cell. Additionally, the bottom of the cell features a 20 $\times$ 20 mm square sapphire-glass window of 1

mm in thickness, allowing optical access from below. The top of the cell is sealed with a 6-mm thick stainless steel plate, which separates the outer compartment from the inner section. It is equipped with a 50 × 20 mm rectangular opening at the centre of the plate to allow optical access from above.

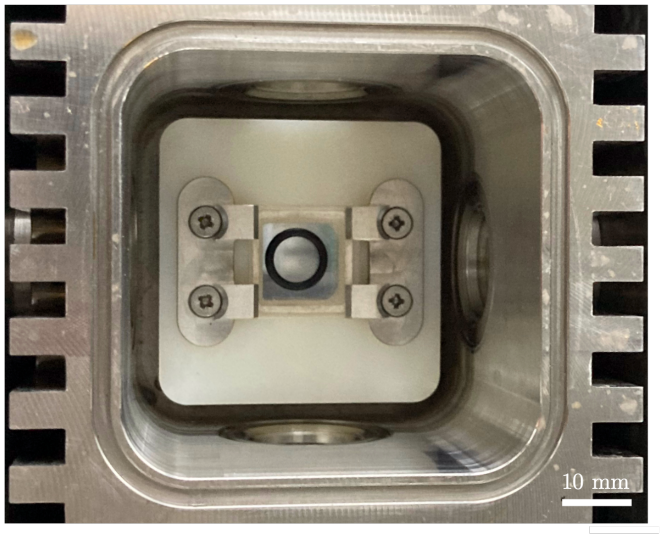


Figure 3.1: Photograph of the hydrate cell from above showing the inner and outer compartments.

The outer section of the cell is designed for coolant circulation, featuring corrugated walls to enhance heat transfer area. It is connected to an external cooler (Stuart SRC5, power: 450 W, pumping rate: 9 litre/minute, bath capacity: 3 litres) for final heat removal. A mixture of monoethylene glycol and water in a 1:1 volume ratio is used as the cooling fluid. To minimise heat gain from the environment, the tubing is covered with insulation. Similarly, the hydrate cell is also insulated and encased by a transparent acrylic casing to prevent condensation of atmospheric moisture and icing on the cell's outer surface, as temperature within the cell can drop below 273.15 K during experiments. Condensation is further avoided by using silica gel beads to dry the air in the window chambers (the space between each quartz-glass window and the casing). A low-velocity stream of dry air also created an air blanket around the external surface of the acrylic casing, preventing optical distortion caused by moisture condensation in the optical path.

To establish a sessile water drop on the pedestal inside the cell, deionsed water was introduced into the test fluid using a Braintree Scientific BS-800 syringe pump together with a 60 ml

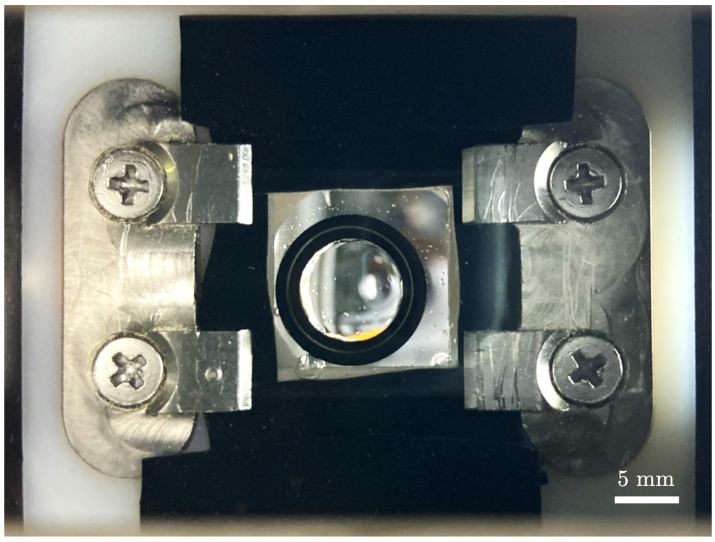


Figure 3.2: Photograph of O-ring adhered to the substrate (sapphire glass) with the purpose of ensuring the water drop is held at exactly the same position within the field of view of the camera.

syringe. A standard rubber O-ring (diameter = 8 and 11 mm, rim width = 1.5 mm) was adhered to the sapphire glass (test substrate) at the bottom of the cell with adhesive glue (the main component is polyvinyl acetate) as shown in Figure 3.2. The purpose of the O-ring is to hold the drop in place exactly in the same position within the field of view of the camera.

Fluid temperatures in the surrounding and drop phase were measured using mineral insulated T-type thermocouples. The diameter of the thermocouples is 0.5 mm, which is sufficiently fine to give rapid and accurate temperature measurements. The two thermocouples are placed on either side of the inner compartment to measure temperature of the surrounding phase. Meanwhile, the temperature in the drop phase was measured using a thermocouple that was inserted beneath one side of the O-ring. The signals from the thermocouples were logged and processed with a data acquisition (DAQ) system through a LabView interface. The sampling of data was performed at a rate of 1 Hz. All the thermocouples were calibrated to an accuracy of $\pm$ 0.15 K in a bath against a digital thermometer certified with UKAS calibration.

3.3 Hydrate induction procedure

When water is cooled below the normal freezing point of 273.15 K, it can remain in liquid phase down to a temperature of 235 K [137, 138]. In this condition, it is called as supercooled water, where water is thermodynamically less stable than ice and remains in a metastable liquid state. Any disturbance to the metastable state would initiate the crystallisation of water to ice. However, if left undisturbed, freezing can occur in a stochastic manner [139].

Similar to the case of freezing, nucleation of hydrate can be delayed. The time taken from when the hydrate equilibrium temperature is reached to the moment when the first hydrate seeds are identified macroscopically is defined as the induction time, t_{ind}. As there is a large variation in the time taken for hydrates to nucleate at the same thermodynamic driving force [50], in the order of seconds to hours [140, 141], it is imperative that an induction protocol is developed where experiments can be replicated and performed in a laboratory environment within an acceptable time limit. According to Li et al. [142], introducing a warm water droplet onto a cold environment to create thermal disturbance is an effective way to reduce the induction time of tetra-*n*-butylammonium bromide (TBAB) as compared to gradually reducing the temperature of water drop and the environment. However, through the cyclopentane hydrate experiments, it was found that there were instances when hydrate formation did not occur even after 30 minutes.

To this end, we exploited the memory effect of water, similar to the approach used by Peixinho et al. [57], in addition to the method proposed by Li et al. [142] to improve experimental repeatability. Cyclopentane was first cooled to 265.7 K followed by the introduction of water drop (at ambient temperature) using a syringe pump onto the pedestal inside the hydrate cell. Freezing was then initiated by dropping an ice chip onto the newly generated drop. Once the water drop turned to ice, the temperature in the cuvette was gradually raised to 281.15 K to melt the ice. Between the temperatures of 273.15 and 280.9 K, water is in the hydrate stability zone and formed hydrate readily as a result of the memory effect of water. Above 280.9 K, hydrate began to decompose. The water drop was then removed manually using a syringe and the test section was then cooled to the desired experimental temperature.

In practice, the drop was not removed completely as some residual micro-droplets were left on the substrate and/or the O-ring surface, which acted as hydrate precursors for another drop of the same volume introduced later for the experiment. The removal of the drop was different from the approach taken by Peixinho et al. [57] who used the same drop for their experiments. The removal step was necessary particularly for PLIF and PIV measurements where additives (fluorescent dyes and tracer particles) were present in water, which required uniform concentrations of the additives in the drop to provide good measurement quality that is representative to the parameters of interest. Moreover, the introduction of a warm drop in cold cyclopentane creates a disturbance in the system that aids in hydrate nucleation and further assisting hydrate induction.

3.4 Contact angle measurement

Contact angle measurements were performed using KRUSS Drop Shape Analyser at ambient temperature. The instrument features a camera, manufactured by IDS Imaging, equipped with a microscopic lens and a high-power monochromatic LED that emits blue light at 470 nm to provide backlighting for the sessile drop, creating a high-contrast image. The camera captures the brightness difference between the region occupied by the droplet and the illuminated background, producing a greyscale image.

The measurements were carried out by injecting a droplet of water using a syringe pump into a glass cuvette filled with liquid cyclopentane, ensuring the droplet was completely immersed. The captured images were processed by an in-built KRUSS ADVANCE software (V.1.12), which fitted the contour of the droplet to a get a tangent between the detected edge and the baseline. Additives were introduced either in the water or the cyclopentane to evaluate their effects on the contact angle between the two phases. The contact angle measurements with additives were compared to a reference case where no additives were present.

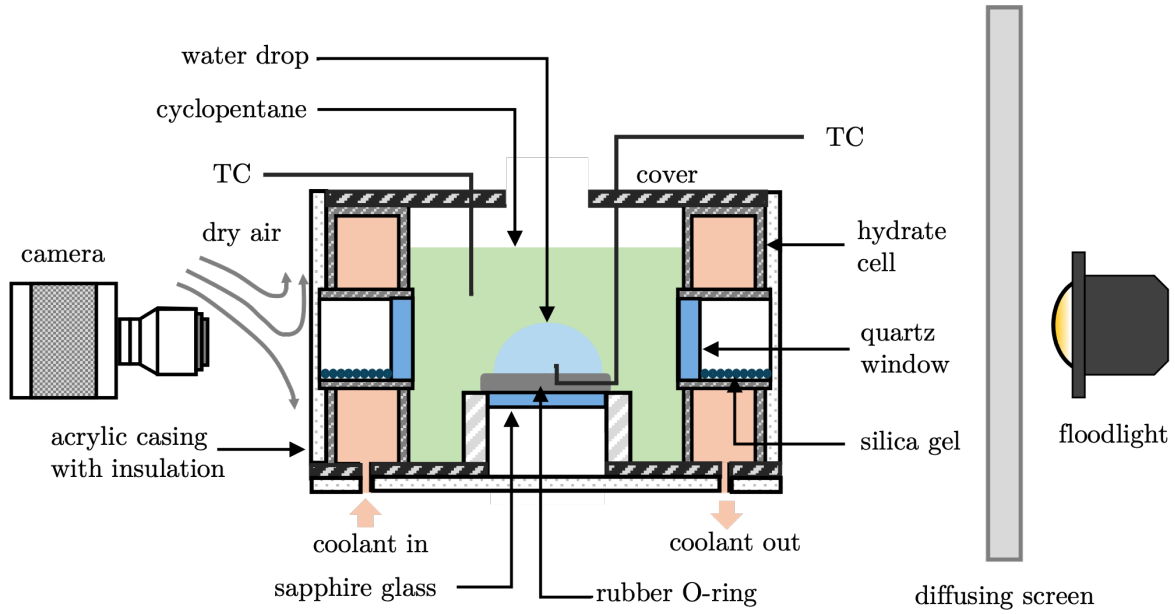


Figure 3.3: Schematic drawing of the hydrate cell and arrangement of the visualisation system used for backlight imaging. TC stands for thermocouple.

3.5 Backlight visualisation

Hydrate formation occurs at the water-cyclopentane interface. As the hydrate grows laterally along the drop interface, its thickness alters the contour of the cyclopentane-hydrate boundary compared to the original water-cyclopentane interface. The resulting hydrate film covering the drop has a semi-opaque appearance, and the contrast between the surrounding cyclopentane phase and the water drop enables visual tracking of hydrate growth via backlighting. Recordings were captured using an Olympus i-Speed 3 camera with a resolution of 1280 × 1024 pixels, equipped with a Sigma 105 mm lens at a frame rate of 1 Hz, with a continuous backlighting provided by a 100 W LED floodlight (colour temperature: 6500 K). To ensure uniform illumination, a 3-mm thick acrylic sheet was used as light diffusing screen between the light source and the hydrate cell. A schematic of the visualisation system used for macroscopic observations and optical measurements of hydrate growth rate and hydrate film thickness is shown in Figure 3.3.

Quantification of the average growth rate of hydrates were obtained by analysing image sequence of hydrate films forming and growing on the drop interface. Raw images were binarised using the Otsu method [143] which computes an optimal threshold value based on the global property of an intensity histogram. The drop was distinguished from the background based on the threshold

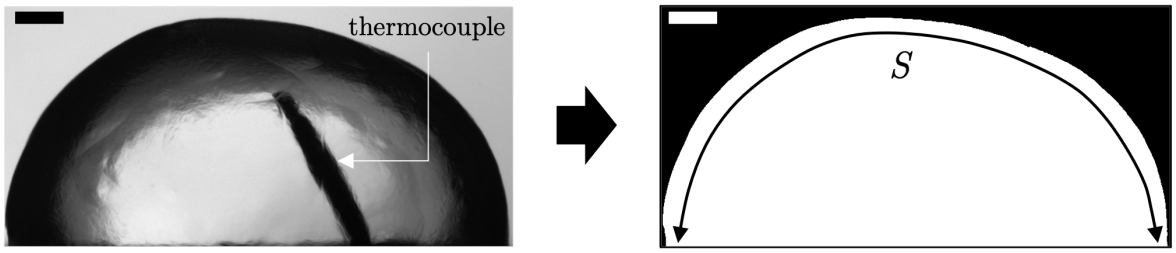


Figure 3.4: Binarisation of raw image for the identification of drop interface and quantification of the peripheral length, S. The scale bar denotes 1 mm.

value, thus providing an outline of the drop interface, as shown in Figure 3.4. The peripheral length of the drop, S, was then evaluated by summing up distances between each adjoining pixels along the outline of the drop interface in the binarised image. The image processing based on the steps mentioned were performed using the *imbinarize* (image binarisation) and *regionprops* (length measurement) functions in MATLAB. The hydrate film growth rate can then be calculated using Equation 3.1

$$v = \frac{S}{2t_{\mathrm{f}}} \tag{3.1}$$

where t_{f} is the time elapsed from when a hydrate seed was first observed macroscopically (taken as starting point, $t = 0$) to the moment whereupon the drop interface was completely covered by a hydrate film. Since the hydrate film grew simultaneously from either sides of the drop in the two-dimensional image, as shown in Figure B, t_{f} corresponds to the period required for hydrates to cover half the drop interface i.e. from the O-ring to the apex. Therefore, the coefficient of two stands in the denominator of Equation 3.1.

3.6 Spectrometer

Fluorescence and absorbance measurements were conducted using a Horiba Duetta UV-VIS spectrometer equipped with a four-position Peltier cuvette sample tray (wavelength range: 250 to 1000 nm, working temperature: 233 to 378 K). The temperature of the sample tray was

controlled by circulating propylene glycol pumped through a thermostatic bath and temperature monitoring was fulfilled by an internal resistance temperature detectors (RTDs). The emission and absorption intensities were measured using a Hellma quartz cuvettes (optical path length: 10 mm, total volume: 4 mL), at temperatures ranging from 263 to 283 K with a temperature step of 2 K. Since the temperatures examined could drop below the freezing point of water, stirring was not used to prevent the sample from freezing. Hence the equilibration time was set at 1 minute to allow enough time for the temperature to stabilise in the small sample cuvette.

Data acquisition was carried out using Horiba EzSpec software. First, the background signal was measured by recording the absorption and emission signal from an empty cuvette. Then the absorption measurements of the fluorescent dyed solutions were performed between the wavelength range of 400 to 700 nm with a spectral width of 1 nm. For the emission measurement, the excitation wavelength was set at 532 nm, consistent with the Nd:YAG lasers used in PLIF and PIV measurements. The slit size was fixed at 5 nm for both excitation and emission. To prevent signal saturation, typically observed at high concentrations of fluorescent dye, the integration time was set at 0.05 s. Six solutions of nile red in cyclopentane were prepared at various concentrations (0.5, 1.2, 2, 5, 9 and 18 mg/L) to assess the linearity of concentration dependent absorption. For the case of fluorescent dyes in water, three mixtures of fluorescein 27 and sulforhodamine B were prepared at different concentrations ratios. The concentration of sulforhodamine B in all three mixtures were kept constant at 1.1 mg/L. Since fluorescein-27 has a low absorption cross-section at 532 nm, its concentration was varied (2.2, 9.1 and 19.1 mg/L) to determine the optimum ratio for good temperature sensitivity.

3.7 Planar laser-induced fluorescence (PLIF) thermometry

3.7.1 One-colour PLIF thermometry in cyclopentane

Instantaneous temperature distributions in cyclopentane during nucleation and growth of hydrate were obtained using a one-colour PLIF technique. A non-polar, temperature-sensitive fluorescent

dye, nile red was dissolved in liquid cyclopentane with a concentration of 1.2 mg/L. The dye is hydrophobic, which is an important property to ensure that there is no transfer of fluorescent dye into water when the cyclopentane and water are in contact with each other. Liquid cyclopentane has a density of 751 kg/m^3. Hence in a hydrate experiment, it acts as the surrounding phase that envelops a water drop. Upon introduction of a water drop into cyclopentane, the drop would sink and rest on the substrate in the hydrate cell. As such, the one-colour PLIF thermometry measurement is performed by directing the laser sheet from the top of the hydrate cell so that the laser sheet has direct optical access to the phase of interest (cyclopentane). However, due to the curvature of the drop, the incident light casts shadows at the periphery of the drop as shown in Figure 3.5. Since hydrate grows from the base of the drop, as discussed in Chapter 4, ideally the temperature measurement in cyclopentane should cover at least one half of the drop from the base to the apex and the phenomenon can be assumed to be symmetrical. As such, there is a loss of useful information in the shadowed region along the base of the drop. Due to the size limitation of the opening in the top cover of the hydrate cell, which allowed laser to pass through, it was not possible to adjust the laser head to an angle that would illuminate one side of the drop fully. To overcome this limitation, a second laser is directed from the side of the hydrate cell to illuminate the drop from the base to a position close to the apex (Figure 3.5).

Two Litron Nd:YAG lasers (wavelength: 532 nm, maximum pulse energy: 50 mJ at 100 Hz and 200 mJ at 15 Hz) equipped with LaVision and Dantec Dynamics sheet optics (divergence angles: 4° and 13.8°) were employed to generate two thin laser sheets. To obtain the images, the lasers are operated in double pulse mode whereby the first pulse is sent to the laser head positioned at the top of the hydrate cell and the second pulse to the laser head directed from the side. The pulses are set with a short time delay of 55.31 μs to obtain quasi-simultaneous image capturing. The approach allows fluorescence information from one side of the shadowed region (from the base) to be recovered thereby allowing about 80% of the temperature close to the drop interface to be measured as opposed to about 60% when the drop is illuminated only from the top. A drawback in this approach is that the total instantaneous raw images captured is double in size, requiring large storage capacity. A LaVision Imager MX 2M-160

CMOS camera was used to capture fluorescence signals induced by each laser separately at a frame rate of 2 Hz. The camera was fitted with a Sigma 105 mm f/2.8 EX DG Macro lens, with a 550-nm long-pass filter (Miswest Optical Systems). The resulting image pixel resolution is 26 μm/pixel.

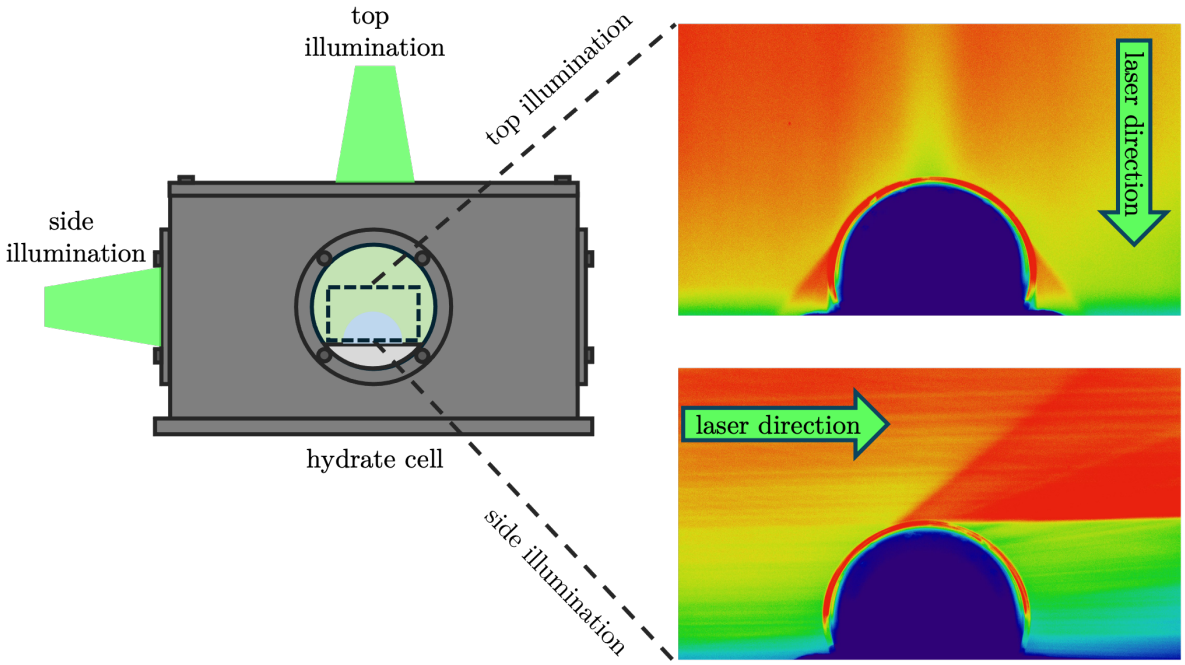


Figure 3.5: Example of raw images obtained from one-colour PLIF with top and side laser illuminations. The shadows are clearly seen at the periphery on both sides of the water drop when when laser is directed from above.

The images captured which contains PLIF signal are processed separately using the same image processing routine, which was built in-house using Python. The processing routine includes steps to correct for systematic errors consisting of: (i) background subtraction (ii) laser sheet and absorption correction (iii) pulse-to-pulse laser energy correction. The steps are as follows:

1. Each image contains dark current which exist due to thermal energy within the camera sensor which gives signal readout even when no photons are incident on the camera. Additionally, scattered light from the surrounding could also contribute to the background noise. The correction is performed by filling the test section with cyclopentane without any fluorophore. Laser sheet at the same configuration and setting as the actual experimental run is shone at the same plane and images are recorded to capture the background noise.

The noise is quantified by taking an average of a set of 200 images, which accounts to a maximum intensity of 40 counts. The background image, which has the same region of interrogation (ROI) as the actual experimental run, is then subtracted from each instantaneous PLIF image with intensity recorded in the range of 800 to 1800 counts. This translates to a signal-to-noise of ∼20:1 (at a minimum), which is an acceptable signal strength for high quality image data, according to Herold and Ghandhi [144].

2. Each laser has spatial non-uniformity in intensity profile across the laser sheet. Moreover, as the laser sheet travels through the optical path, the beam is attenuated due to absorption effect. Prior to each experimental run, the hydrate cell is filled with doped cyclopentane and the temperature is brought to the desired operating temperature. When the temperature is stable, the lasers are switched on and at least 50 images are recorded. The images are then averaged to obtain the sheet image. Each instantaneous raw image from the experimental runs are normalised by the sheet image based on Equation 3.2 where I is the pixel intensity at each pixel (x,y) and $\bar{I}$ is the average intensity.

$$I_{corr}(x,y) = \frac{I_{raw}(x,y)}{I_{sheet}(x,y)}.\overline{I_{sheet}} \tag{3.2}$$

3. A drawback of one-colour PLIF technique is that it is susceptible to variation in pulse-to-pulse laser energy, which introduces error into the measurement. To overcome this challenge, spatial averaging of the fluorescence signal of each instantaneous image are taken, $I_{\mathrm{s,avg}}$. The time variation of the spatially-averaged fluorescence intensity, $I_{\mathrm{s,avg}}$ (Figure 3.6) is directly proportional to the laser pulse energy, $E_{\mathrm{p,exp}}$ and its deviation from the time-averaged intensity, $I_{\mathrm{st,avg}}$ is used for image correction based Equation 3.3.

$$I_{corr,norm}(x,y) = I_{norm}(x,y).\frac{I_{st,avg}}{I_{s,avg}} \tag{3.3}$$

where $I_{\mathrm{corr,norm}}$ is the corrected normalised intensity and $E_{\mathrm{p,ref}}$ is the reference laser pulse energy.

Temperature calibration of nile red dissolved in cyclopentane for one-colour PLIF images was

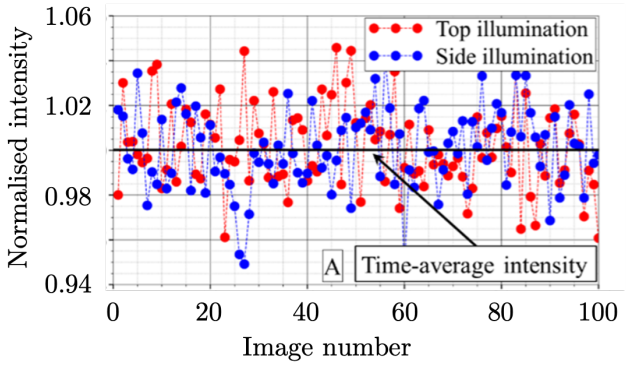


Figure 3.6: Time variations of spatially averaged fluorescence intensity, which is directly proportional to the pulse energy.

performed by placing a 0.5 mm T-type thermocouple in the hydrate cell, close to the ROI but not in the direct path of the laser sheet to minimise the effect of reflection, which may introduce error to the PLIF measurement. The temperature of liquid cyclopentane in the hydrate cell was gradually reduced at five intervals from 265 to 293 K. Recording of LIF images was started only when the bulk temperature in cyclopentane was stable for at least five minutes. At each temperature step, 200 images were recorded to obtain one data point for the temperature calibration. The images were then averaged and processed using the same procedure as previously described. Figure 3.7 shows the temperature calibration curves obtained from the experiment. The temperature sensitivity of nile red in cyclopentane from the experiment is between 1.66 to 1.81 %/K. The fluorescence signal captured in the form of image counts are then converted to temperature using the temperature calibration curve. Finally, the two images obtained from top and side illuminations were stitched to produce an image of temperature field.

3.7.2 Two-colour PLIF thermometry in water drop

In separate experiments, sulforhodamine B (Exciton) and fluorescein 27 (Sigma Aldrich), at concentrations of 1.1 mg/L and 9.1 mg/L respectively, were dissolved in water to employ the two-colour PLIF temperature measurements. The experiments were performed with a double-pulsed Litron ND:YAG laser (wavelength: 532 nm, maximum pulse energy: 200 mJ at 15 Hz) directed from the bottom of the hydrate cell. Image recordings were taken using two

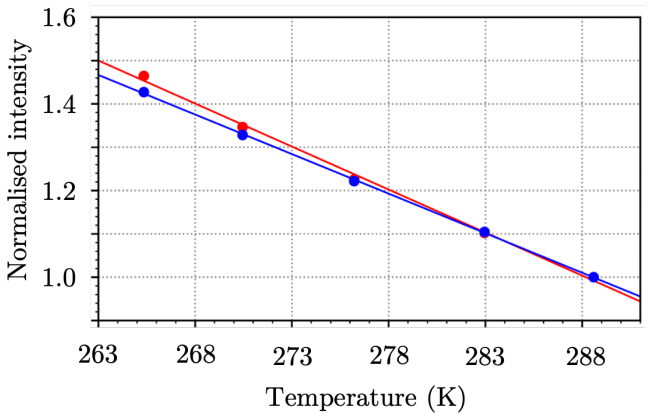


Figure 3.7: Dependence of the fluorescence intensity of nile red in cyclopentane on temperature for top (red) and side illuminations (blue).

sCMOS cameras operated in single frame mode, arranged in a configuration as shown in Figure 3.8. The fluorescence emission was sent to both cameras with the aid of a pellicle beam splitter (reflectance: 45% transmittance: 55%). A combination of 540 nm short-pass (band 1), 570 nm long-pass (band 2) and 532 nm notch filters were used to separate the fluoresence emission for each fluorophore and to block the laser beam. Since the signal collected from band 1 was weaker compared to the signal from band 2, it was therefore necessary to increase the gain of the camera. The gain was set at 10 for both cameras to increase their sensitivities to capture light. A neutral density filter was fitted on camera 2 to reduce its brightness to avoid over-saturating the camera.

To obtain pixel correspondence between the images captured by the two cameras. Identical lenses (Sigma 105 mm f/2.8 EX DG macro lens) were mounted onto the cameras. The cameras were aligned with the help of a LaVision microcalibration target with dots of known distances printed on a transparent glass plate placed inside the hydrate through the opening of the top cover. The target was mounted onto a microstage to aid in its positioning to the centre of the rubber O-ring. The focus of the camera was then adjusted to focus on the target using the printed dots as reference. The spatial calibration was performed following the steps outlined by Sakakibara and Adrian [128]. First, the location of each dot in the images captured by the cameras were identified to obtain the coordinate of each dot. Then a third order polynomial function was fitted to obtain the correspondence between each point. All the images captured

during the experiments were then spatially calibrated using the same polynomial function.

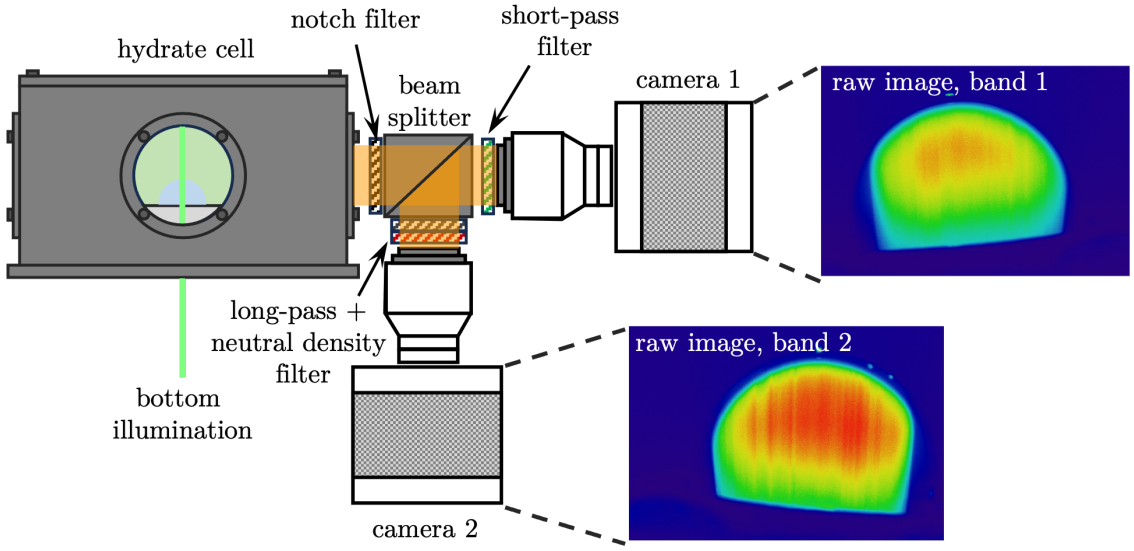


Figure 3.8: Schematic drawing of the hydrate cell and optical arrangement of the two-colour PLIF system. Example of raw images obtained from the two cameras at specific spectral bands through a combination of optical filters are also shown.

The images captured are processed using a routine that corrects for systematic error consisting of (i) background subtraction (ii) flat field correction. The steps are as follows:

1. A similar approach for background subtraction as described in Section 3.7.1 was taken where the magnitude of the background signal was determined by averaging a set of two hundred images taken in the absence of fluorescent dye in water. A maximum background intensity of 10 counts was subtracted from each instantaneous PLIF image where the intensities recorded were in the range of 1100 to 1200 and 800 to 1050 counts, for band 1 and band 2, respectively. This translates to a signal-to-noise ratio of ∼80:1.

2. The cameras used in image recording may show uneven response due to local variations in the optical transmission, for example vignette effect that causes the image to be brighter at the centre [145, 146]. This effect can be corrected with the flat-field correction process. Recording of flat-field images for each band was started only when the bulk temperatures in the water drop and cyclopentane were equal and stable for at least 5 minutes. These images with intensity, $I_{\text{flat}}(x,y)$ were then averaged to obtain the averaged flat-field

intensity, $\overline{I_{flat}}$. Each instantaneous image with intensity $I(x,y)$ were then corrected using Equation 3.4.

$$I_{corr}(x,y) = \frac{I(x,y)}{I_{flat}(x,y)}.\overline{I_{flat}} \tag{3.4}$$

The temperature calibration of fluorescein 27 and sulforhodamine B was performed by placing a thermocouple through the rubber O-ring at the base of the water drop. The temperature of water was reduced at 5 intervals from 266 to 289 K. Recording was started only when the temperature in the water drop was stable for at least 5 minutes. At each temperature step, 200 images were recorded. The images were then averaged and processed using the same procedure outlined earlier. A ratio between the intensities obtained from cameras 1 and 2 at each temperature step was then calculated to plot the dependence of the mixture of fluorescent dyes with temperature, as shown in Figure 3.9. The resultant sensitivity coefficient obtained from the experiment for Fluorescein 27 and Sulforhodamine B is 2.88 %/K. Similarly, ratio of intensities from instantaneous images recorded from experimental runs were taken and finally converted to temperature using the temperature calibration curve.

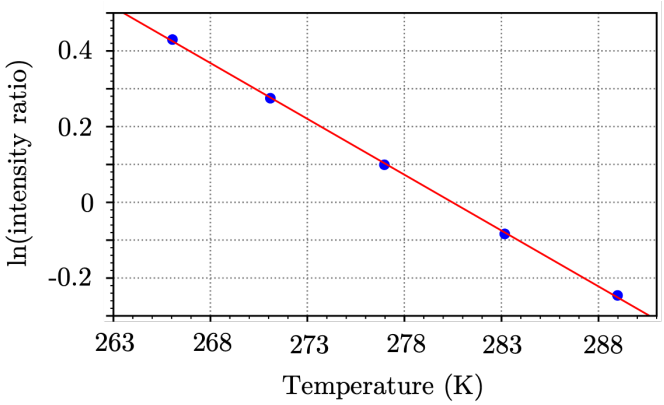


Figure 3.9: Dependence of the fluorescence intensity of fluorescein 27 and sulforhodamine B in water on temperature.

3.8 Particle image velocimetry (PIV)

Particle image velocimetry (PIV) is a measurement technique that can measure the velocity distribution across a planar area of a flow field. This is can be achieved by seeding the fluid with tracer particles. In order for the particles to follow the streamlines of the flow, they have to be neutrally buoyant i.e., the density of the particles have to be comparable to the suspension liquid such that they remain in suspension throughout the duration of the experiment. Tracking of the particles is attained by illuminating the flow of field of interest with a laser sheet. The size of the particles should be large enough such that sufficient amount light is scattered (or fluoresce in the case of fluorescent particles) by the particles that can be captured by a camera. At the same time, the particles should not be too large to a point that they can influence the results of the experiments.

$$St_k = \frac{t_o u_o}{L_o} \tag{3.5}$$

$$t_o = \frac{\rho_p d_p^2}{18\mu_l} \tag{3.6}$$

$$St_k = \frac{\rho_p d_p^2}{18\mu_l}\frac{u_l}{L_o} \tag{3.7}$$

A way to measure the fidelity of the tracer particles is by calculating the Stokes number, $\mathrm{St_k}$, given by Equation 3.5. It is defined as the ratio of the characteristic time of a particle (particle relaxation time), t_o to the characteristic time of the flow ($u_\mathrm{o}/L_\mathrm{o}$, where u_o is the liquid velocity and L_o is the characteristic length). In Stokes flow, the Reynolds number is less than 1 and the particle relaxation time, t_o is a function of the particle density, ρ_p, the particle diameter, d_p and the dynamic viscosity of suspension liquid, μ_l and can be expressed as Equation 3.6. According to Tropea et al. [147], any flow tracing errors by the particles are less than 1% if the St_k is less than 0.1.

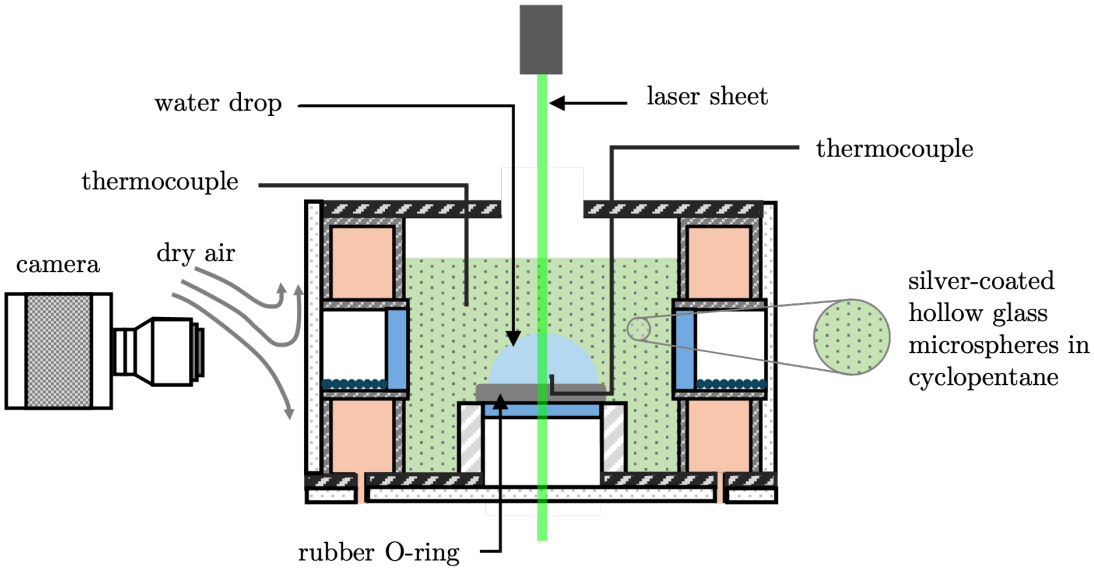


Figure 3.10: Schematic illustration of the optical arrangement used in PIV measurements in cyclopentane with illumination directed from above the hydrate cell.

PIV measurements in liquid cyclopentane was performed by employing 32 μm diameter silver-coated hollow glass microspheres sourced from Microsphere Technology Ltd with a relative density of 0.98 to the suspension liquid. The water drop was seeded with 7.6 μm fluorescent polystyrene particles (PS FluoRed) sourced from microparticles GmbH. The particles have a relative density of 1.05. Evaluating the Stokes number of both particles using an alternative expression (Equation 3.7) give values in the order of 10^{-6}, which meet the condition set out by Tropea et al. [147]. Prior to each experimental run, the suspension was sonicated in a bath sonicator (model: TH-30A Vevor®, capacity: 6.5 L, frequency 40 kHz, power: 180 W) for at least 10 minutes to separate individual tracer particles, thus minimising aggregation, and to obtain uniform distribution of particles in the liquid suspension. Two sets of experiments were performed, where in one case, hydrate formation occurs at the drop interface through hydrate induction, as detailed out in Section 3.3 while in another case, no hydrate formation was involved. The measurements were performed over a temperature range to 265.65 to 273.15 K.

The PIV measurements in cyclopentane and water were performed in separate experiments. The flow was illuminated by a laser sheet generated by a Litron Nd:YAG laser that emits at 532 nm (maximum pulse energy 50 mJ), which was directed from above for the case of cyclopentane (Figure 3.10) and from the bottom of the hydrate cell in the case of water drop

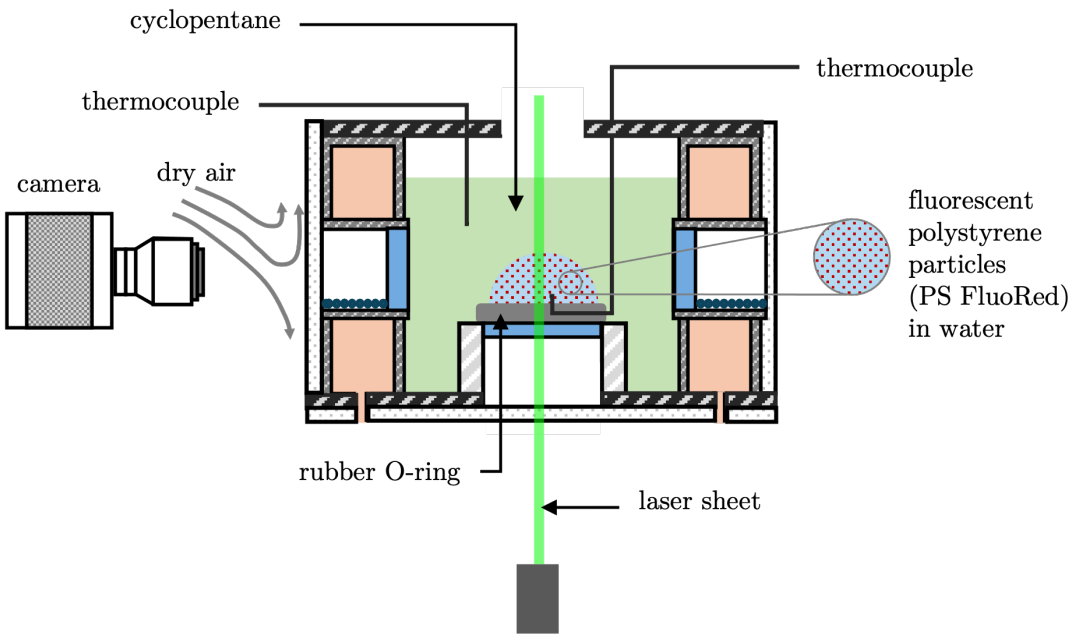
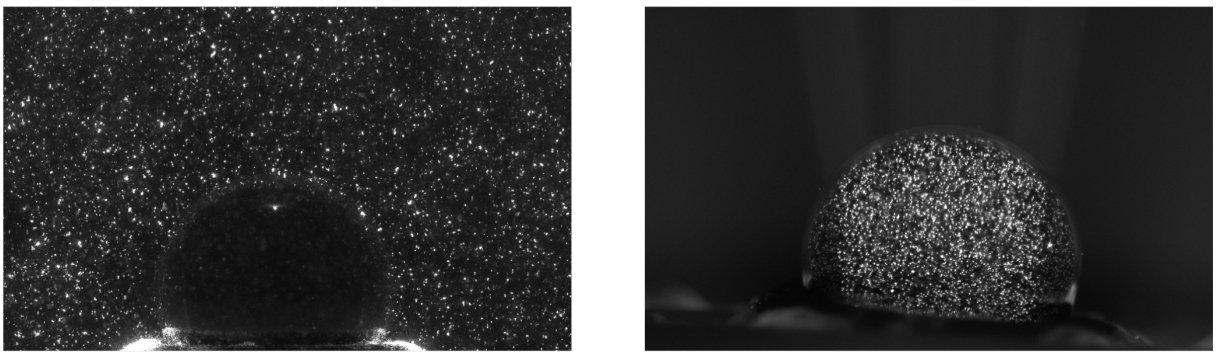


Figure 3.11: Schematic illustration of the optical arrangement used in PIV measurements in water drop with illumination directed from the bottom of the hydrate cell.

(Figure 3.11). Mie scattering or fluorescence of laser irradiation that strikes the particle were captured in double frame mode with a time delay of 12857.42 μs between the pulses using LaVision Imager MX 2M-160 sCMOS camera fitted with a Sigma 105 mm f/2.8 EX DG Macro lens. The camera was placed perpendicular to the laser sheet. Images were recorded at a frame rate of 2 Hz for a duration of at least 500 seconds for each experimental run. The frame repetition rate was selected to minimise the amount of energy absorbed by the substrate such that the heating effect by the laser can be neglected. Sample images of the particles in cyclopentane and water are shown in Figure 3.12. The images were spatially calibrated using a LaVision microcalibration target that was placed in the plane of the laser sheet to correct for optical distortion and facilitated scaling of the images.

The image processing was undertaken using LaVision's *DaVis* 10.2 software package along with custom Python code for post-processing. First, the images were preprocessed by applying geometric mask to remove areas outside of the region of interest. Then the 'subtract sliding background' in *DaVis* was implemented with a filter length of 4 pixels to enhance the intensity difference between the particles and the liquid to aid particle identification for the next step of processing. PIV vectors were calculated using the 'time resolved sliding sum of correlation



(a) Cyclopentane (b) Water

Figure 3.12: Example of raw images obtained in particle image velocimetry (PIV) in (a) cyclopentane and (b) water.

procedure' with multipass approach, whereby the interrogation window was decreased from 256 × 256 pixels to 64 × 64 pixels (cyclopentane) and 64 × 64 to 32 × 32 (water). The interrogation windows in the multipass approach has an overlap of 50% to produce vector fields with high stability and accuracy by ensuring that the same particles were correlated based on information from many image pairs. As the position of the drop interface changed with respect to temperature, the drop interface was determined by averaging 20 images at different time periods. Due to the movement of particles in successive images captured by the camera, the averaged image produced motion-blur effect of the particles and thus provides an outline of the drop interface. The averaged images were then used as reference to apply dynamic mask using Python on the vector fields to ensure that the velocity field near the interface was adequately captured. The spatial resolutions of the raw image of particles and velocity vectors are 6.5 μm/pixel and 160 μm/vector, respectively.

Chapter 4

Phenomenological characteristics of hydrates

In nature, clathrate hydrates are formed when hydrate formers such as hydrocarbon molecules (e.g. methane, ethane, propane) and small gaseous molecules (e.g. carbon dioxide, hydrogen sulfide, nitrogen, hydrogen) are in contact with water at temperatures below the hydrate equilibrium temperature. Due to the complexity of the phenomena, most laboratory studies on hydrate formation were performed using common hydrate formers such as methane, ethane and carbon dioxide. Hydrates of these compounds require relatively high pressure, which not only pose safety risks (for example, operating flammable gases at high pressure) but also incur high cost. Hydrate of compounds that are stable at ambient pressure are rare. One such example is cyclopentane that has a hydrate equilibrium temperature between 280 to 281 K [50, 148, 18]. Most cyclopentane hydrate studies were performed within a limited temperature range whereby the temperature in the experiments were kept above the freezing point of water of 273 K [135, 93, 71] to avoid potential competition between ice and hydrate formation. This puts a constrain on cyclopentane as a good analogue for the study of hydrate as natural gas hydrates experience subcooling that is one order of magnitude higher [149]. The characteristic appearance of hydrate based on its shape and size i.e., its morphology, has been observed to change with subcooling temperature [18, 9]. However, such a change in morphology has not

been reported for cyclopentane hydrate. Therefore, the potential of extending the subcooling temperature of cyclopentane hydrate to temperatures below the melting point of water is explored.

In what follows, Section 4.1 describes the differences between freezing and hydrate formation below the freezing point of water. This includes qualitative analysis of images obtained through shadowgraph imaging and quantitative results of temperature from thermocouple measurement taken inside the water drop. In Section 4.2, the transformation of hydrate film morphology with respect to subcooling temperature are presented, which further strengthens the motivation to perform hydrate studies at temperatures below the melting point of water. The lateral growth rates of hydrates are then discussed in Section 4.3 followed by comparisons between experimental data with hydrate growth models from the literature.

4.1 Ice and hydrate characterisations

Experiments were carried out using the experimental facility based on the procedure described in Chapter 3. The two phenomena were characterised by observing the appearance or morphology of the solid formed, the change in temperature of the water drop during the phase change process and the rate of solid formation. To this end, shadowgraph imaging was employed and two sets of experiments were performed. In one case, silicone oil was used as the surrounding phase where hydrate formation was suppressed. As such, the water drop that was deposited into the silicone could only undergo freezing. For the second case, silicone oil was replaced with cyclopentane where both hydrate and freezing phenomena could potentially occur. While water can remain in supercooled state down to a temperature of 235.15 K [150, 151, 152, 153] for pure water and in extremely controlled condition through homogeneous nucleation, often times freezing occurs through heterogeneous nucleation at temperatures above 250 K [154]. In addition, ice nucleation rate increases with decreasing temperature [155] thus increasing the probability of freezing. Therefore the experiments were conducted at a moderate temperature of 266 K to investigate the likelihood of hydrate forming before ice nucleation. As there maybe

temperature non-uniformity across the hydrate cell, since cooling was only provided from the side walls, for simplicity, the bulk temperature was taken at the centre of the cell using a thermocouple placed through the side of the O-ring (prior to introduction of the water drop). The temperature was chosen such that it is low enough to initiate hydrate nucleation and allow enough time for hydrate to grow but warm enough that ice will not nucleate and dominate over hydrate formation. To further facilitate hydrate formation, a temperature protocol as described in Section 3.3 was followed. The experimental conditions are as presented in Table 4.1.

Table 4.1: Experimental parameters for ice and hydrate characterisation experiments.

Pressure, p	1	atm
Bulk temperature, T_B	266	K
Drop volume, V	0.25	ml

Image recordings of the phase change processes were recorded at a frame rate of 1 frame per second and the sequence of events are shown in Figures 4.1 and 4.2 for water drop in silicone oil and cyclopentane, respectively. In Figure 4.1, freezing qualitatively underwent two distinct stages where a sudden change in opacity of the water drop was observed followed by a gradual change in the shape of the drop to form a sharp pointy tip and further darkening of the drop silhouette. The change in opacity between Figures 4.1(a) and (b) were captured in successive images which indicated that the first stage of freezing was a rapid process compared to the second stage. This observation is consistent with the observation of drop freezing reported by Dash et al. [156] and Schremb and Tropea [73]. In addition, the final shape of the frozen drop with a conical tip as shown in Figure 4.1(c) is characteristic of a freezing water drop as widely reported in literature [157, 158, 159, 160]. The freezing process of supercooled water can therefore be described as having two successive stages [161, 73]:

1. A rapid (initial) step that results in a partial phase transition from liquid to solid where either a thin layer of ice is formed at the interface or the formation of an ice-water mixture (mushy state) [162].

2. A slower (subsequent) step where the remaining liquid in the core of the drop turns to

solid i.e. solidification of the inner volume of the drop.

According to Petrenko and Whitworth [163], the change in opacity during the first stage of freezing is due to the release of dissolved air ahead of the freezing front. Since the freezing rate of the first stage is high, some microbubbles could get trapped in the ice film, causing light to scatter as it transmits through the drop [164]. Additionally, it could also be argued that during the first stage of freezing, the drop is in mushy state whereby the presence of ice particles causes light to scatter and therefore result in the opacity change.

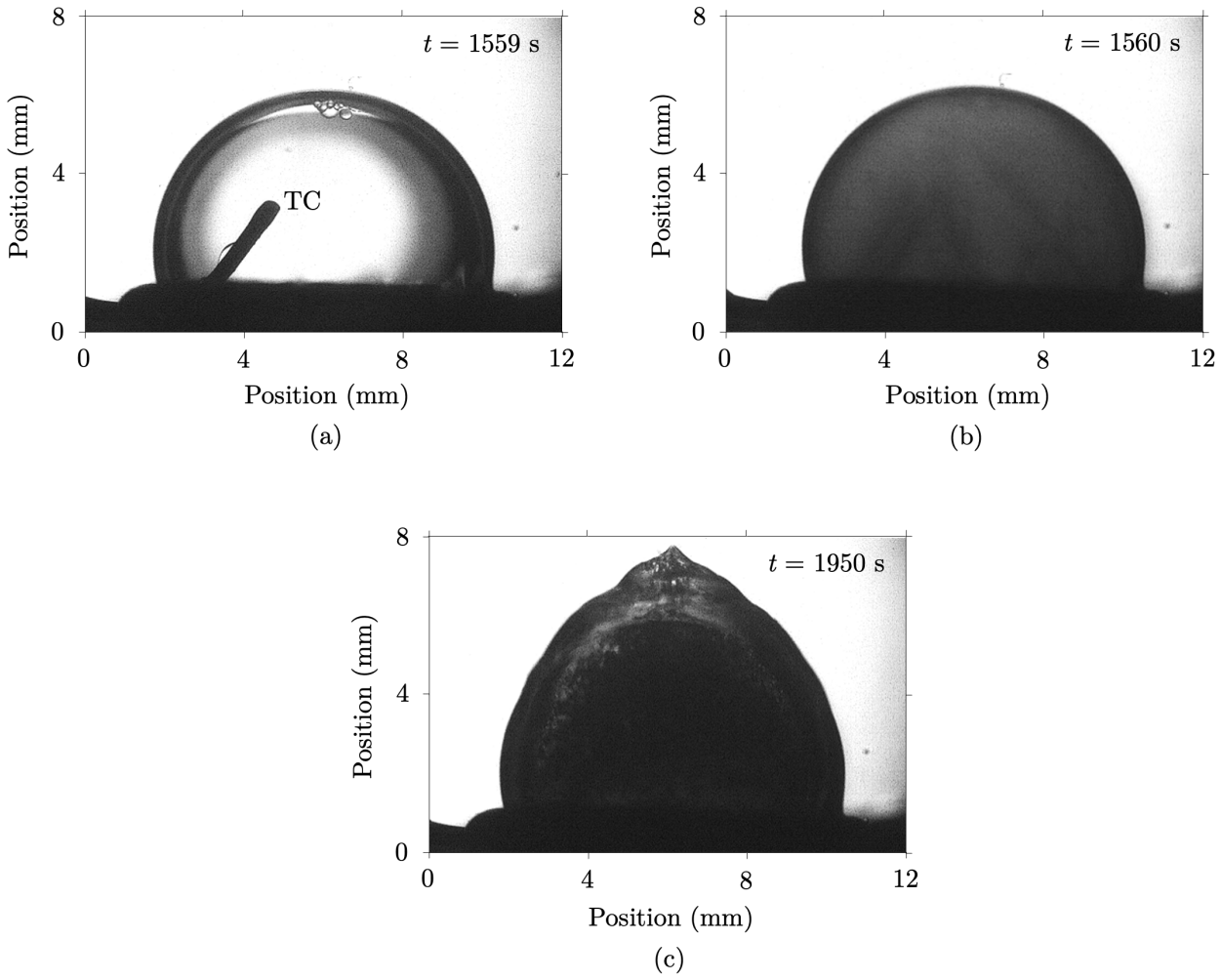


Figure 4.1: Sequential images of a water drop supercooled in silicone oil at a temperature of 266 K at different stages of evolution: (a) original drop (b) ice layer covering the drop and (c) completely frozen drop with a conical tip. TC in the image denotes a thermocouple.

In contrast, the drop in Figure 4.2 is more translucent and appears to be macroscopically rougher with visible dents on the solid film that formed at the interface (Figures 4.2 (a) and

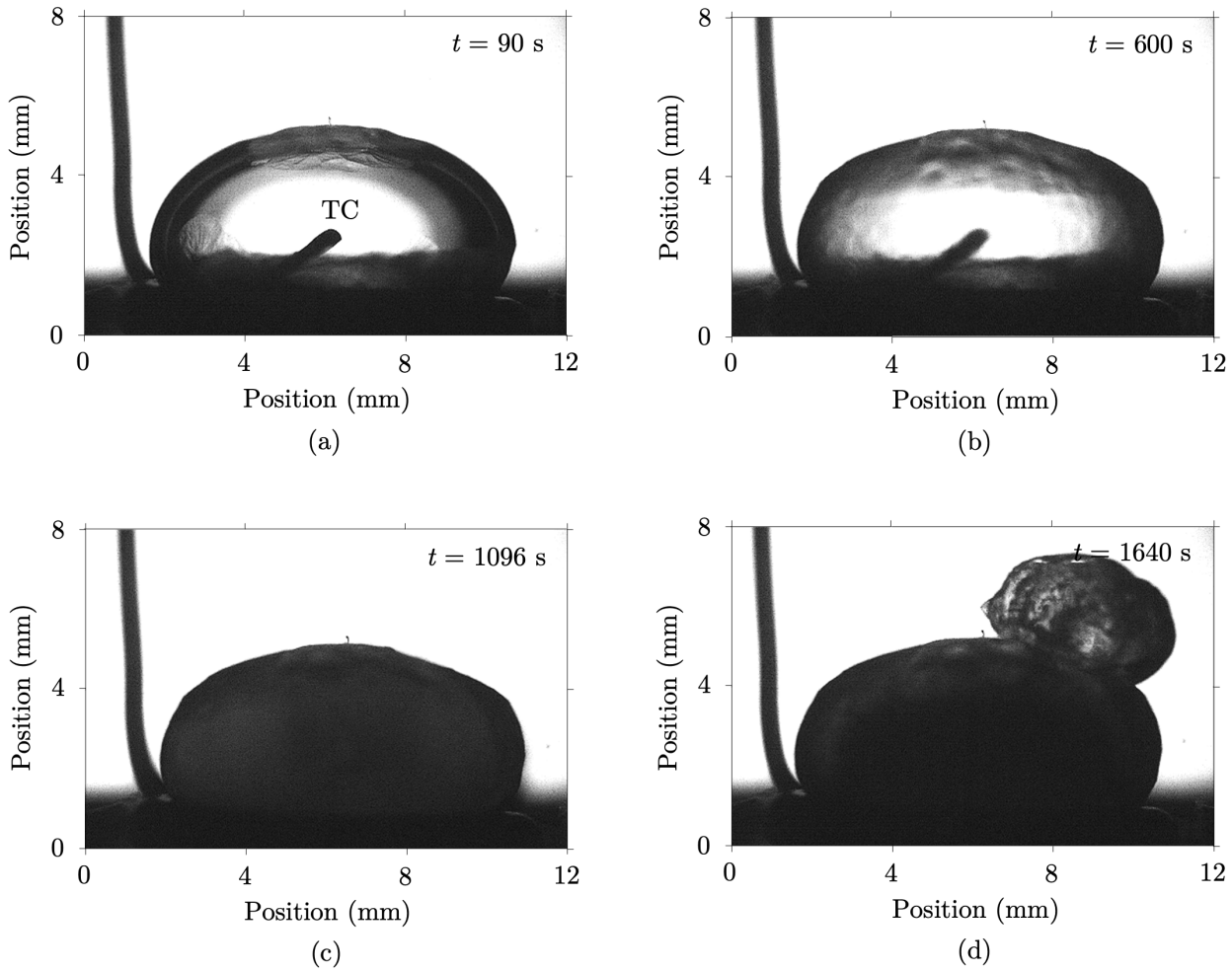


Figure 4.2: Sequential images of a water drop supercooled in cyclopentane at a temperature of 266 K at different stages of evolution: (a) hydrate growth at the drop interface (b) hydrate film covering the entire drop (c) internal freezing of the drop and (d) ice volume expansion. TC in the image denotes a thermocouple.

(b)). The growth of the film is also observed to be significantly slower compared to the drop freezing in silicone oil despite having similar bulk surrounding temperature and drop size. This points to the possibility that the translucent film that formed on the interface in Figure 4.2(b) is cyclopentane hydrate. The slower phase change process of the drop in Figure 4.2 (liquid cyclopentane) compared to the drop in Figure 4.1 (silicone oil) meant that dissolved air in water could potentially escape without being trapped in the hydrate film thus permitting light to transmit with less scatter through the film. This gives the hydrate film a clearer appearance as compared to the ice film observed in the freezing experiment. In Figure 4.2 (c), the drop shows a sudden change in opacity similar to the observation made in Figure 4.1, which could possibly be attributed to the nucleation of ice in the drop that initiated freezing. The relatively

higher rate for both stages of freezing compared to the growth rate of hydrate also means that freezing dominates the phase change process in the drop, turning the remaining liquid in the drop to ice. As freezing occurs, the drop experienced volume expansion. However, the presence of a rigid hydrate film at the drop interface prevents the remaining water in the drop to freeze and form the characteristic singular tip at the drop apex as observed in Figure 4.1(c). As pressure builds up in the drop during freezing, the weakest spot on the the hydrate film fractured, forcing residual water to flow out of the drop and freeze with an irregular shape.

In order to further substantiate the qualitative observations on the differences between the two phenomena, evolution of temperature inside the drops during the phase change processes, measured using a thermocouple, are plotted as shown in Figure 4.3. In the case of water drop in silicone oil, the temperature in the drop is initially seen to decrease to the bulk silicone oil temperature. When ice nucleates, the temperature inside the drop rises to 273.15 K. The sharp rise in temperature, known as recalescence, is a consequence of rapid formation kinetics of ice in supercooled liquid which is accompanied by a sudden release of latent heat. This is evident in Figure 4.3 at $t = 1560$ seconds. Thereafter, the drop undergoes the second stage of freezing at a relatively slower rate as the rate is controlled by heat transfer and the temperature is seen to maintain at the freezing equilibrium temperature for a period of time. Subsequently the drop cools to the bulk silicone oil temperature. This trend fits the distinctive characteristic of the temperature evolution during freezing of a supercooled water drop as has been previously described by Hindmarsh et al. [75] and Tavakoli et al. [74].

Conversely, an increase in temperature during the nucleation and evolution of cyclopentane hydrates could not be detected through the thermocouple measurements unlike the freezing experiment. This could potentially be due to the comparatively slower growth rate of hydrate crystals. Additionally, an increase in temperature as a result of heat of formation may potentially be more localised to regions closer to the drop interface.

The temperature profile of water drop in cyclopentane revealed that there is a temperature spike to 273.15 K at $t = 1100$ seconds, that was long after the complete coverage of the drop interface by a hydrate film which ended approximately 300 seconds after water drop was deposited into

cyclopentane. This is consistent with the qualitative observation whereby the darkening of the drop silhouette in Figure 4.2(c) can be confirmed to be caused by freezing. This also serves as quantitative evidence of the lack of ice contamination during the first stage of hydrate growth (the period between $300 < t < 1100$ seconds). Therefore, it is possible to perform hydrate experiments below the melting point of water without having ice contamination. Thus, the range of subcooling temperature of cyclopentane can be further extended and explored to study the lateral growth of cyclopentane hydrates at temperatures below the melting point of water of 273.15 K through a proper temperature protocol and appropriate data filtration based on the characterisation described in this section to distinguish between the two phenomena.

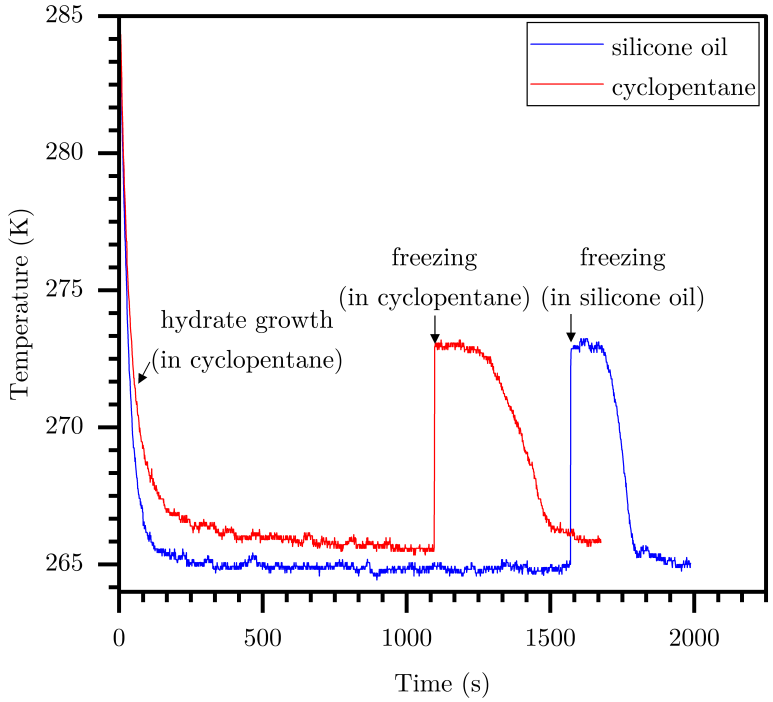


Figure 4.3: Comparison between the temporal variations of temperature inside a water drop undergoing freezing in silicone oil and a water drop subjected to both hydrate formation and freezing in cyclopentane.

4.2 Hydrate morphology

Variations in the morphology of cyclopentane hydrate crystals have been reported in the literature [93, 165, 166, 69] for temperatures above 273.15 K. Here, the morphology of cyclopentane hydrates at bulk cyclopentane temperatures, T_b, between 265 K to 276 K are presented. The

schematic and experimental protocol are as described in Chapter 3. A LaVision sCMOS camera fitted with a Sigma 105 mm f/2.8 EX macro lens was employed to record the cyclopentane hydrate crystallisation. Images of cyclopentane hydrate forming on the drop interface were taken macroscopically for classification and comparison. Five different T_b (275.75 K, 273.95 K, 273.45 K, 269.85 K and 265.65 K) corresponding to subcooling temperatures, ΔT, of 5.1 K, 6.9 K, 7.4 K, 11 K and 15.2 K were considered.

4.2.1 Hydrate nucleation and induction time

It was observed that hydrate film appeared to grow at the periphery of the drop (Figure 4.4) where there is a three-phase contact point between water-cyclopentane-rubber O-ring. The imperfections on the O-ring may have aided in the nucleation of hydrate. According to Bai et al. [167], the influence of solid surfaces on hydrate formation may be due to the rearrangement of the local structure of water close to the liquid-solid interface that provides alternative pathways to the formation of hydrate. While this may not be surprising as surface roughness is known to promote nucleation [168], it has also been observed that in some cases, hydrate seed can also appear at any location on the drop interface as evident in Figure 4.5 particularly at subcooling, ΔT below 6.9 K. It is also interesting to note that some of the hydrate seeds have specific geometrical patterns for example, a pentagonal (Figure 4.5(a) and a triangular crystal (Figure 4.5(b)). No such observation was seen at subcooling temperature, ΔT above 6.9 K. As the nucleation seeds increased in size, they slid down along the interface towards the rubber O-ring by gravity.

Once settled, the seeds grew laterally along the interface in the direction towards the drop apex acting as the centre of hydrate crystal growth. This suggests that when ΔT is below 6.9 K, there are two different mechanisms of cyclopentane hydrate nucleation that can trigger hydrate growth: 1. Surface nucleation induced by surface imperfection and 2. Nucleation at a random location on the interface possibly due to contact at the drop interface with hydrate nucleating particle such as impurities present in either cyclopentane or water phase, similar to contact freezing experienced by water drop when in contact with atmospheric aerosol [169]. On the

other hand, there is only one mechanism (surface nucleation) observed for cyclopentane hydrate nucleation at $\Delta T > 6.9$ K.

Figure 4.6 shows the dependence of the average hydrate induction time, $\langle t_{\mathrm{i}} \rangle$, calculated based on at least four repeated runs, on ΔT. There are two distinct regions in Figure 4.6 with the separation point at $\Delta T = 7$ K. At lower subcooling temperatures ($\Delta T < 7$ K), hydrate nucleation is more stochastic with a wider scatter in induction time (min: 372 s and max: 5179 s at $\Delta T = 5$ K). A 95% confidence interval was calculated based on five repeated measurements using t-value of the student distribution. The confidence intervals quantify the stochastic nature of hydrate nucleation through the standard deviation of each data point. The stochasticity is substantially suppressed for $\Delta T > 7$ K (min: 9 s and max: 21 s at $\Delta T = 15$ K) and the dependence of hydrate induction time on ΔT is significantly reduced. The sudden change in dependence of induction time is not unique to cyclopentane hydrate but was also reported in the literature for methane [170, 23], tetrahydrofuran [24] and natural gas hydrates [22]. Comparing the results of the induction time in Figure 4.6 and the qualitative observation, the large variation in induction time at $\Delta T < 7$ K can be explained by the different nucleation mechanism that triggers hydrate growth. Contact nucleation is less predictable because it depends on both the driving force for nucleation. i.e. the subcooling temperature and on the possibility of collision between the drop and the hydrate nucleating particle. When $\Delta T > 7$ K, the driving force for nucleation is sufficiently high to trigger surface nucleation which significantly suppressed the stochasticity of cyclopentane hydrate nucleation. This further strengthens the motivation to perform experiments at extended subcooling above 7 K to ensure better experimental repeatability for cyclopentane hydrate.

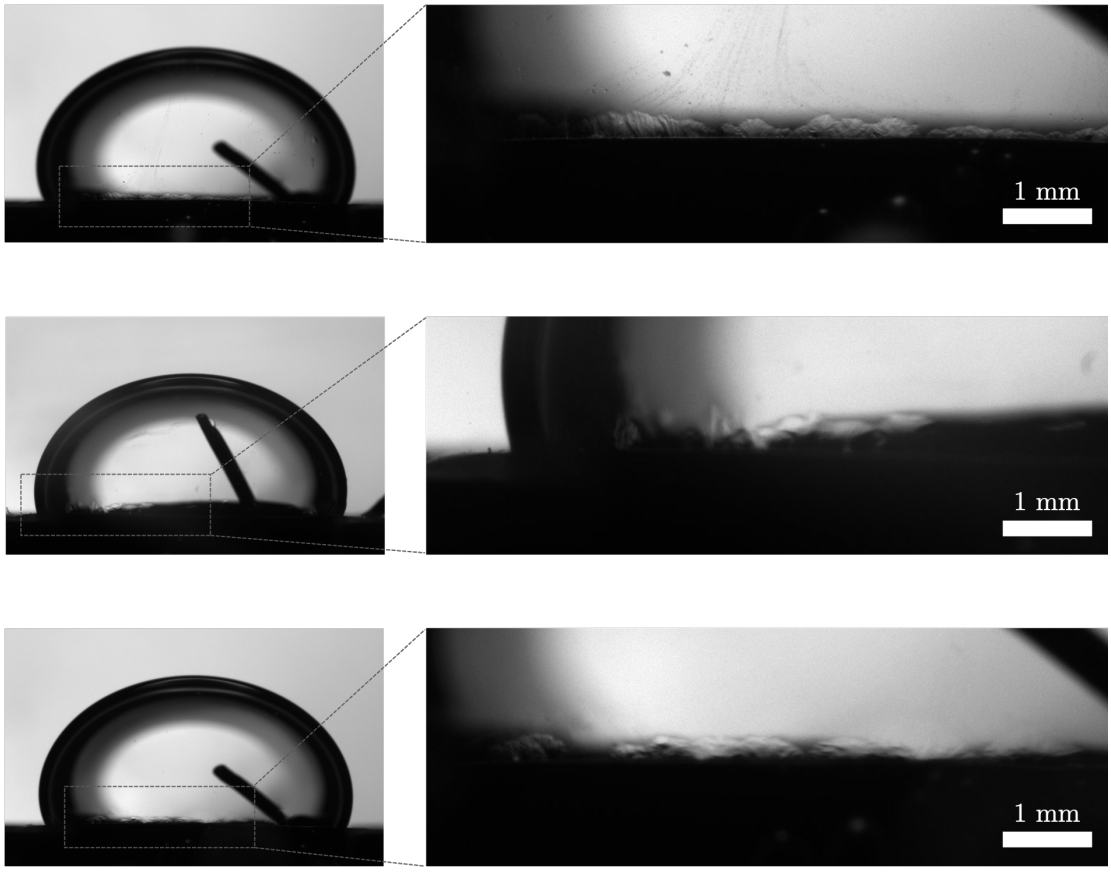


Figure 4.4: Images of hydrate film appearing at the periphery of the drop.

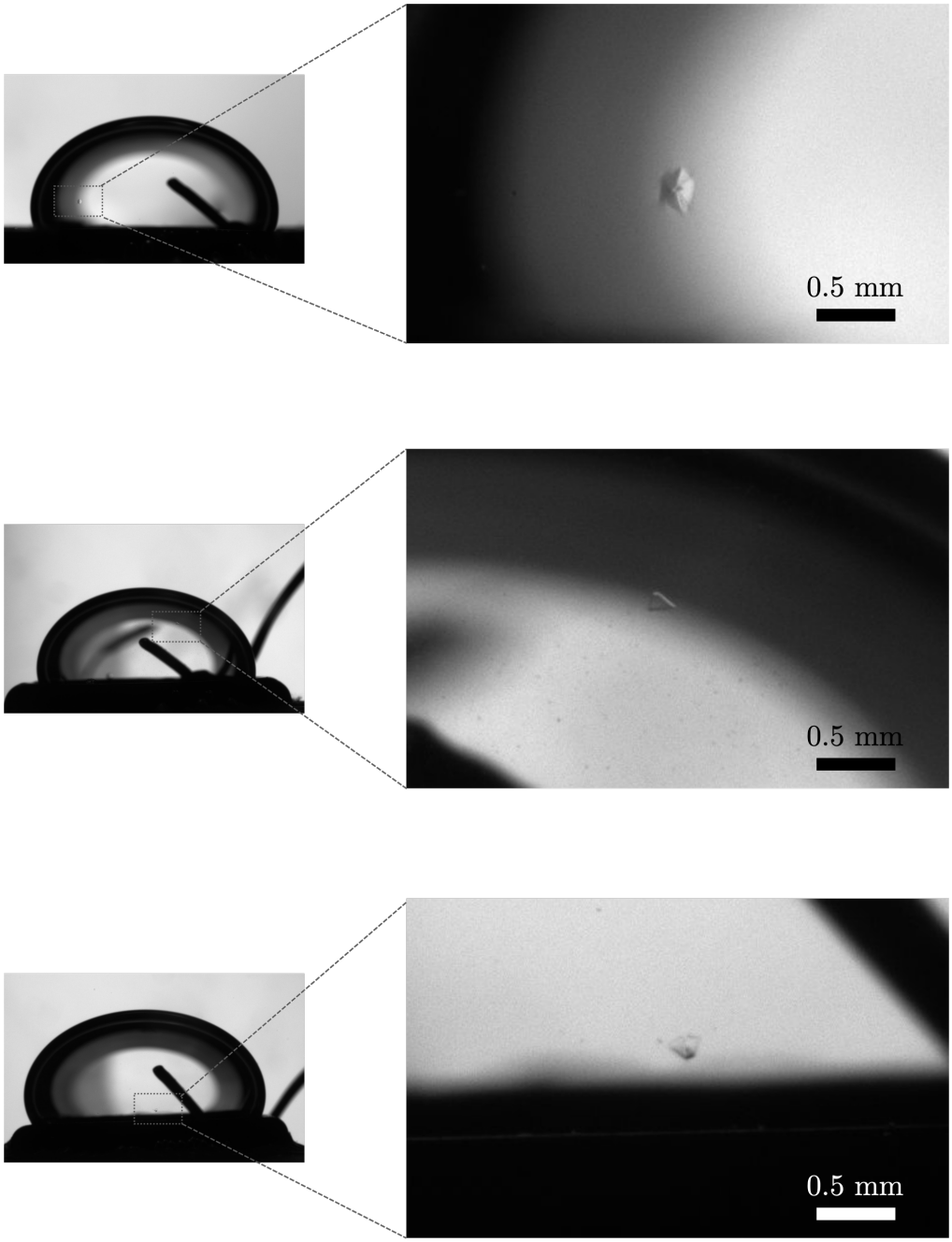


Figure 4.5: Images of hydrate seeds appearing at the drop interface.

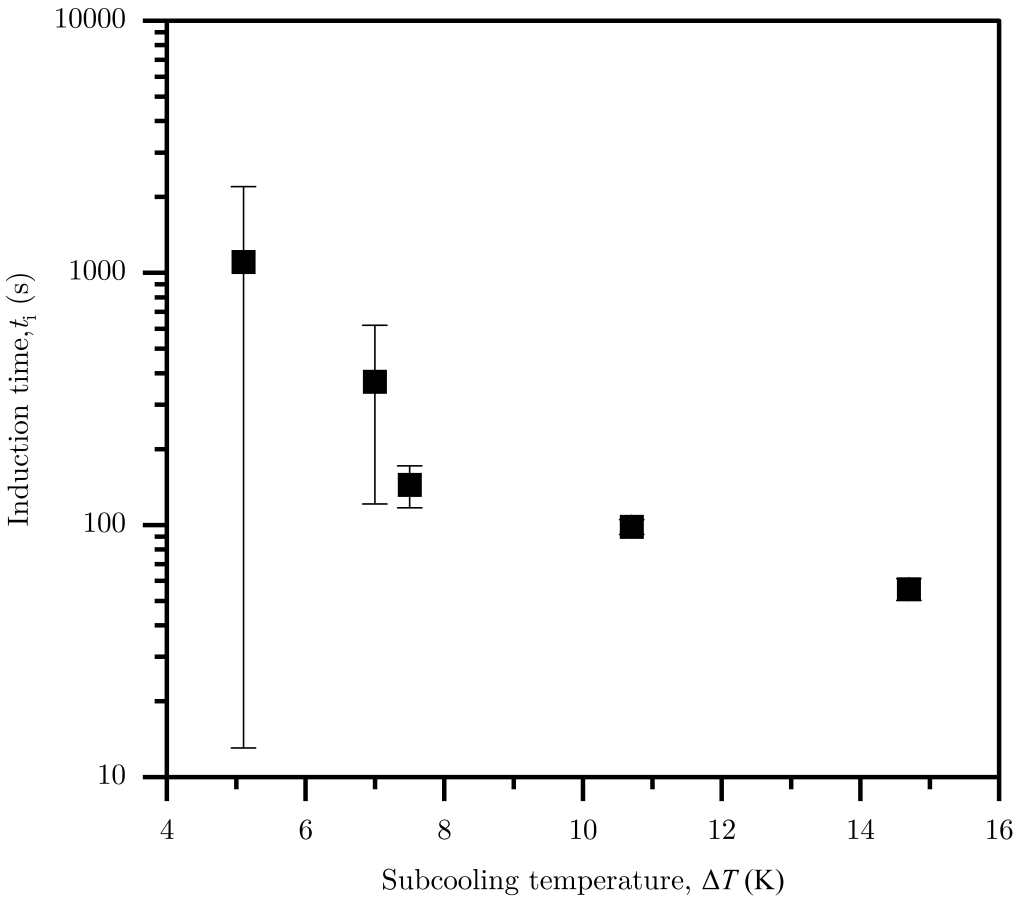


Figure 4.6: Average induction time of cyclopentane hydrate formation on sessile water drops over a range of subcooling temperatures. The confidence intervals quantify the stochastic nature of hydrate nucleation through the standard deviation of each data point.

4.2.2 Hydrate morphology at varying subcooling temperature

The morphology and dynamics of the growth of hydrate film was observed to differ with a change in the subcooling temperature. The observations in the experiments are presented in the order of the system subcooling.

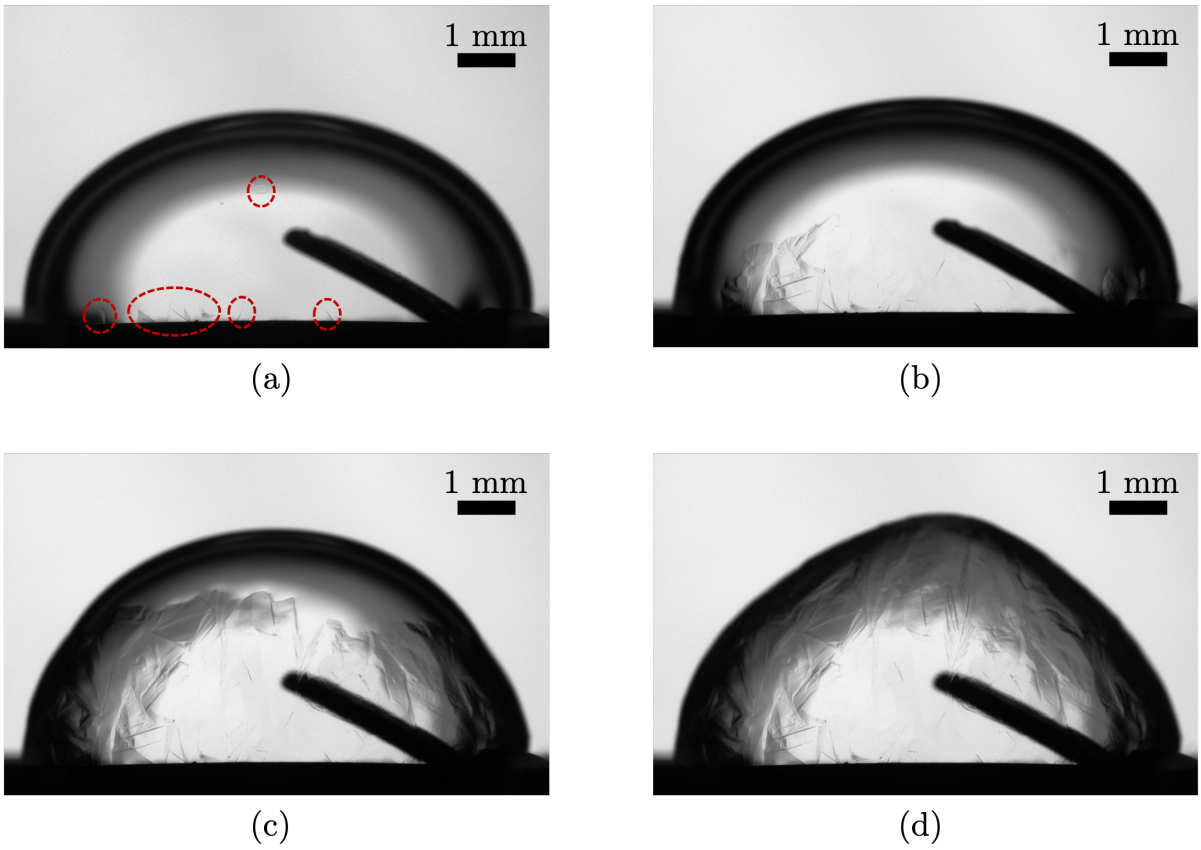


Figure 4.7: Evolution of hydrate formation and growth at a subcooling temperature of 5.1 K.

Figure 4.7 shows a typical evolution of hydrate formation and growth observed at $\Delta T = 5.1$ K. Hydrate seeds were seen to appear at multiple points dispersed at the circumference and immediately above the rubber O-ring (as indicated in red circles in Figure 4.7(a)). The seeds then acted as centers of hydrate crystal growth, which grew outwards with polygonal structures. Over time, the polygonal hydrate crystals evolved into highly striated plates and the imbrication of these plates contributed to the final stepped appearance as shown in Figure 4.8(a). In Figure 4.8(b), different polygonal flat plat crystals were sighted (e.g. hexagonal, triangle) floating at the interface, which then impinged with the primary hydrate front forming a surface mosaic. The growth of the crystal seeds into plates indicate that there is preferential

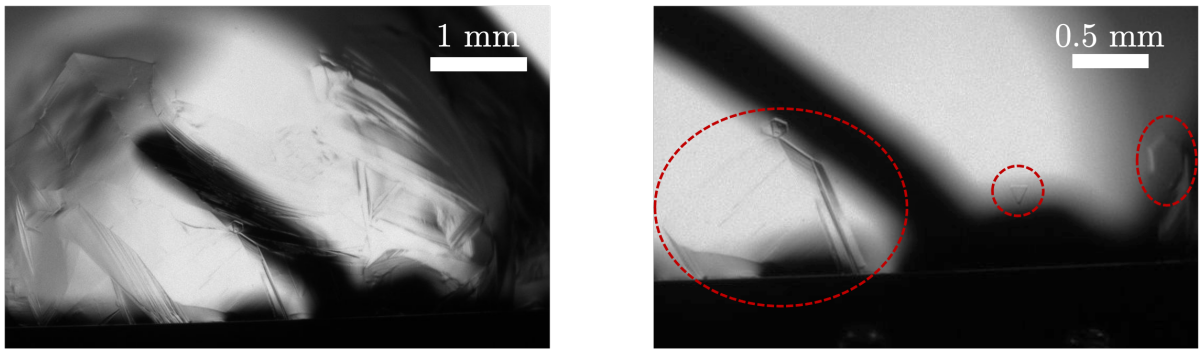


Figure 4.8: A closer look on the morphology of hydrate film at a subcooling temperature of 5.1 K. (a) Hydrate crystals having distinctive striations. (b) Polygonal flat plate crystals with different geometries.

growth of the hydrate crystal in the direction parallel to the hexagonal axis (i.e. faster lateral growth) compared to the side that is perpendicular to the axis (slower longitudinal growth) as summarised in Figure 4.9. As a result, a film layer of hydrate crystal is created at the interface. It is also evident in Figures 4.7(c) and (d) that the assembly of hydrate crystals of different geometrical patterns at random created a hydrate front that is not uniform.

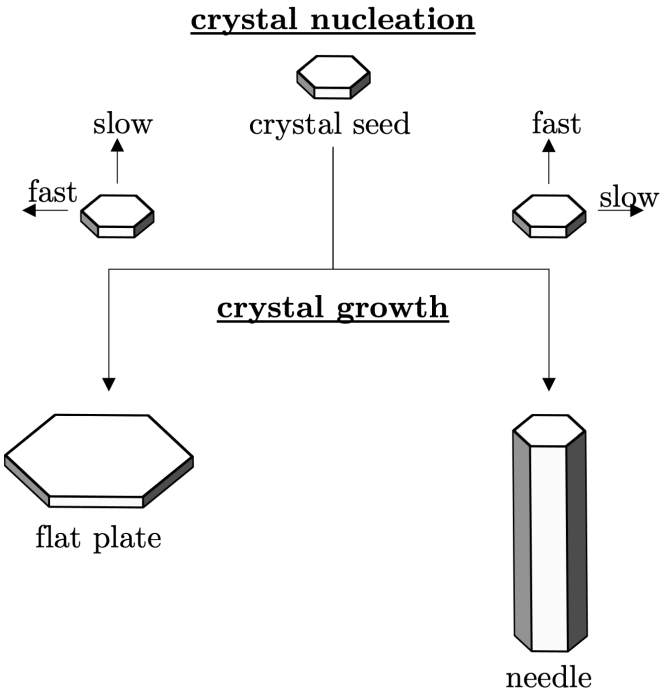


Figure 4.9: Schematic of preferential growth of crystal plates resulting in different crystal morphology. Adapted from Lee and Harris [26].

As ΔT was progressively increased to 6.9 K, the centres of hydrate crystal growth took the form

of dendrites instead of polyhedral structures to form semi-circular arc-shaped fronts 4.10(a). Multiple hydrate crystals growing at different points then coalesced and grew as a single primary hydrate front, as illustrated in 4.10(b). The branching of the dendritic structures created wrinkles on the drop interface along the direction of front propagation, giving the hydrate film a macroscopically rough appearance 4.10(d). The transition from polyhedral to dendritic crystals as a function of ΔT was also reported by Sakemoto et al. [18] and Maruyama and Ohmura [171] for cyclopentane hydrates (Type sII) with the transition occurring at ΔT of 5.8 and 5 K respectively. Similar morphological transition were also observed for other hydrate formers of different hydrate structural types e.g. sI [54] and sH [14].

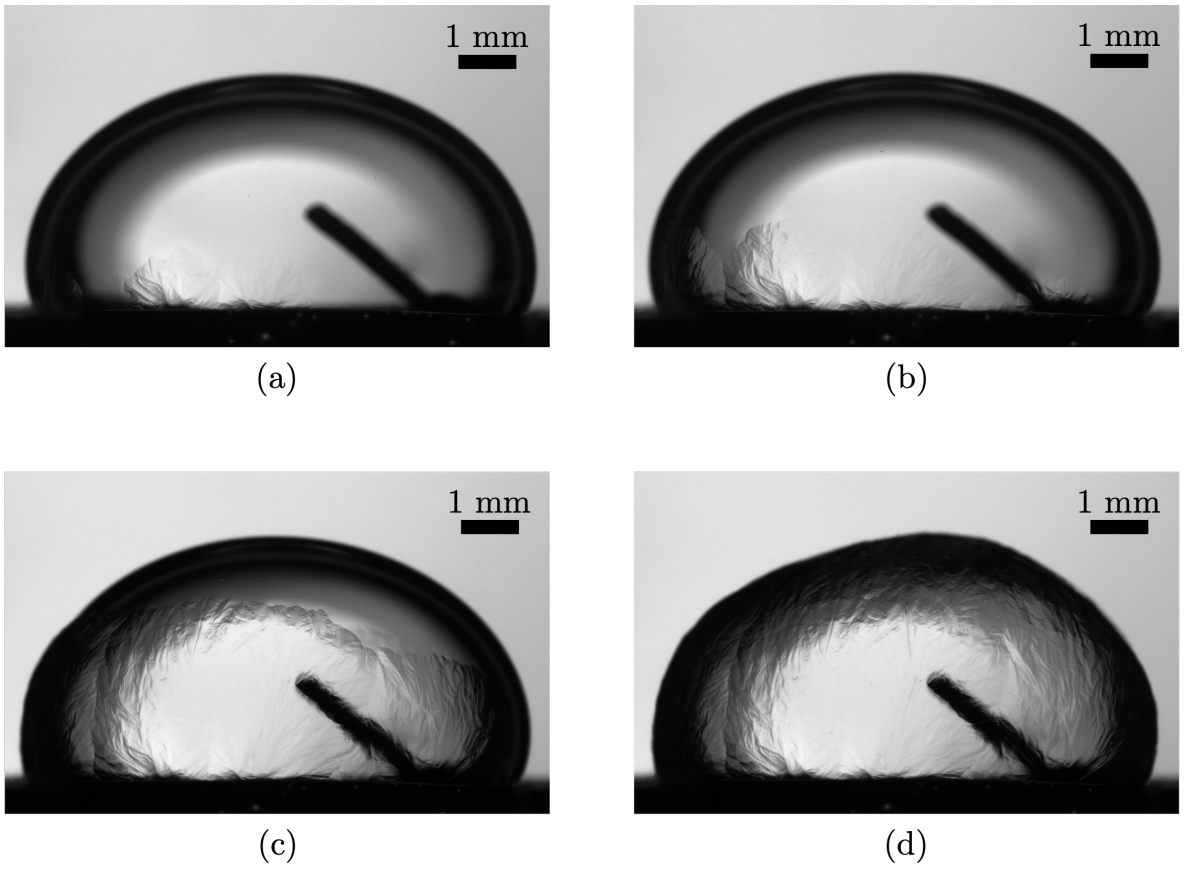


Figure 4.10: Evolution of hydrate formation and growth at a subcooling temperature of 6.9 K.

When ΔT was further increased to 7.4 K, the hydrate film maintained its dendritic morphology with more dendrites forming at the periphery of the drop as shown in Figures 4.11(a) and (b). In addition, floating three-dimensional circular crystals or spherulites were also observed (Figure 4.12(a), that potentially originated from secondary nucleation sites at random locations on the drop interface. Similar spherulite sighting was also reported by Martínez de Baños et al.

[172] for cyclopentane hydrates in the presence of a water-soluble fluorescent dye at $\Delta T \approx$ 7.7 K. Simultaneous growth of hydrates in the form of dendrites with clearly visible branches or fractal as evident in Figure 4.12(b) and spherulites (Figure 4.12(a)) indicates that another morphological transition could possibly occur if ΔT was increased even further.

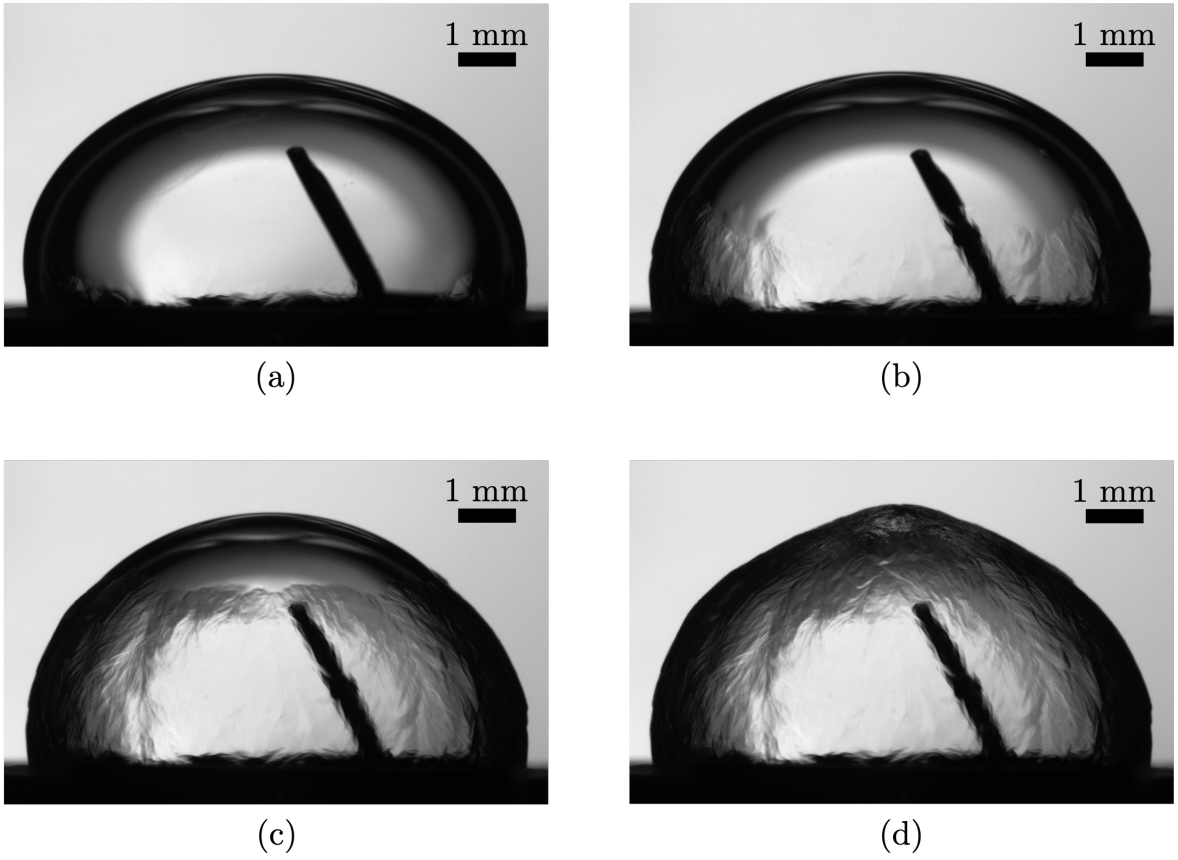


Figure 4.11: Evolution of hydrate formation and growth at a subcooling temperature of 7.4 K.

Increasing the ΔT to 11 and 15.2 K confirmed the morphological transition to purely spherulitic structures (Figures 4.13 and 4.15). Hydrate growth started at the periphery of the drop at both subcooling temperatures with the hydrate film appearing more textured, and therefore more visible at ΔT of 11 K (Figure 4.13(a)) compared to ΔT of 15.2 K (Figure 4.15(a)). Then spherulites started to appear at random locations on the drop interface. The delayed appearance of spherulites after the growth of a ring of hydrate film at the drop periphery suggests that the birth of spherulites is due to secondary nucleation. The rise in the subcooling temperature subsequently augmented the rate of crystal nucleation with a greater number of individual spherulites appearing at the drop interface (Figure 4.15(b)). An increase in ΔT from 11 to 15.2 K also saw the spherulites becoming larger in size but with a relatively smoother texture

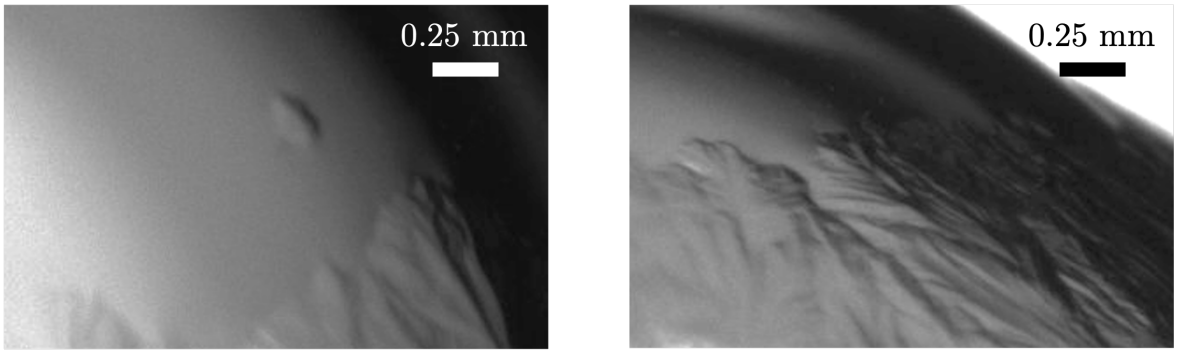


Figure 4.12: A closer look on the morphology of hydrate film at a subcooling temperature of 7.4 K. (a) Floating spherulite crystals. (b) Hydrate crystals growing as dendrites with distinctive branching.

as shown in Figure 4.16(a) compared to Figure 4.14(a). The spherulites, as individual floating crystals, maintained their positions at the cyclopentane-water interface, which is expected since cyclopentane hydrate density of 965 kg/m^3 falls between the density of liquid cyclopentane and water [173]. Overtime, the spherulites settled around the bottom of the drop periphery. Agglomeration of the individual spherulites formed polycrystals with distinct grain boundaries. This resulted in a "tortoise shell" appearance (Figures 4.13(d), 4.14(a), 4.15(d) and 4.16(b) on the drop interface. To the best of our knowledge, this research is the first to report on the purely spherulitic crystal growth morphology of cyclopentane hydrates at temperatures below the freezing point of water of 273 K.

Figure 4.14(b) demonstrated that the hydrate film appeared to protrude mostly into the cyclopentane phase. This is an indication that its wettability, qualitatively defined here as the fraction at which the film is immersed in water as schematically shown in Figure 4.17, is low. This observation contradicts with the assumption often made in hydrate modelling studies [66, 174, 30] where hydrate film are regarded as hydrophilic or completely wetted in water (Figure 4.17 (c)). While such an observation has previously been reported by Hirata and Mori [56] based on tetrahydrofuran hydrates, it should be noted that tetrahydrofuran, as a hydrate former, is miscible in water and therefore produced a hydrophilic hydrate film. As such, the wettability of a hydrate film may vary depending on the type of hydrate former, which is an important consideration in modelling studies. This phenomenon is similar to observations made

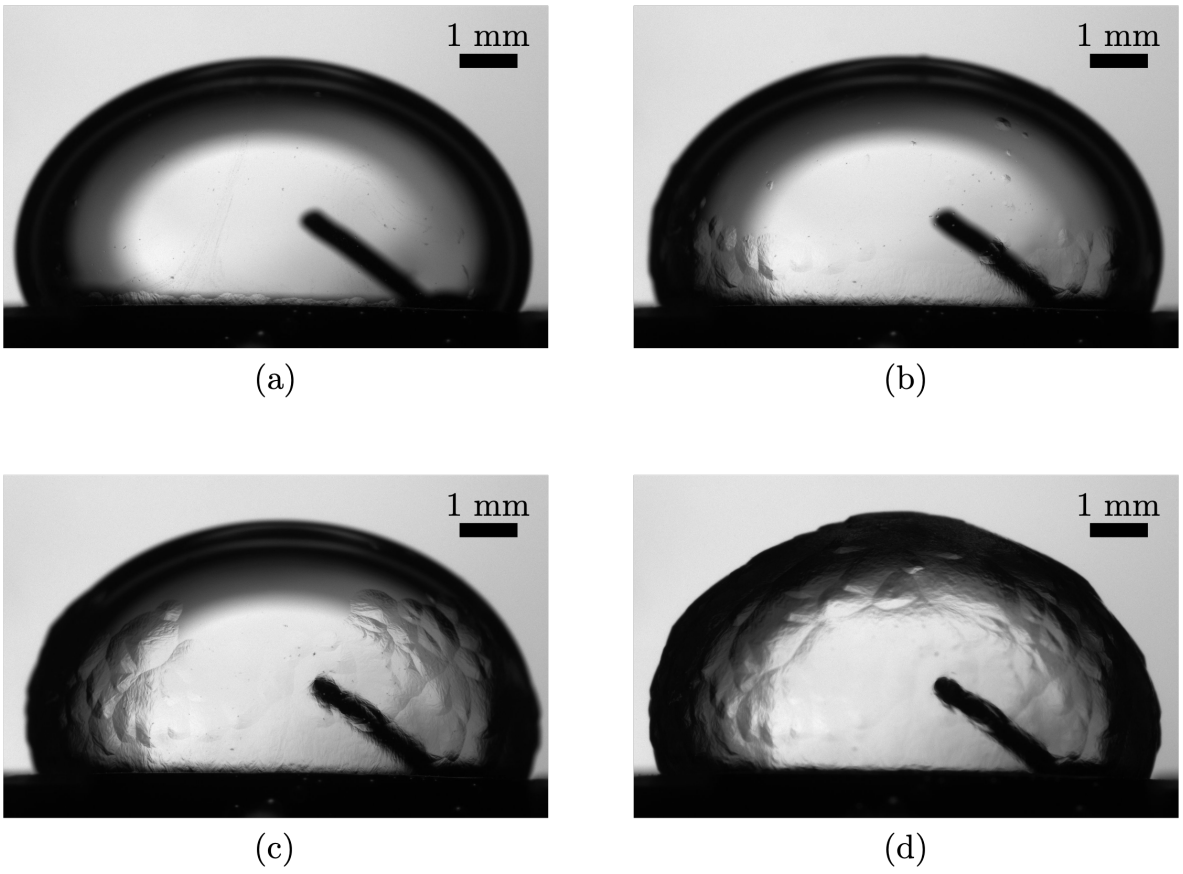


Figure 4.13: Evolution of hydrate formation and growth at a subcooling temperature of 11 K.

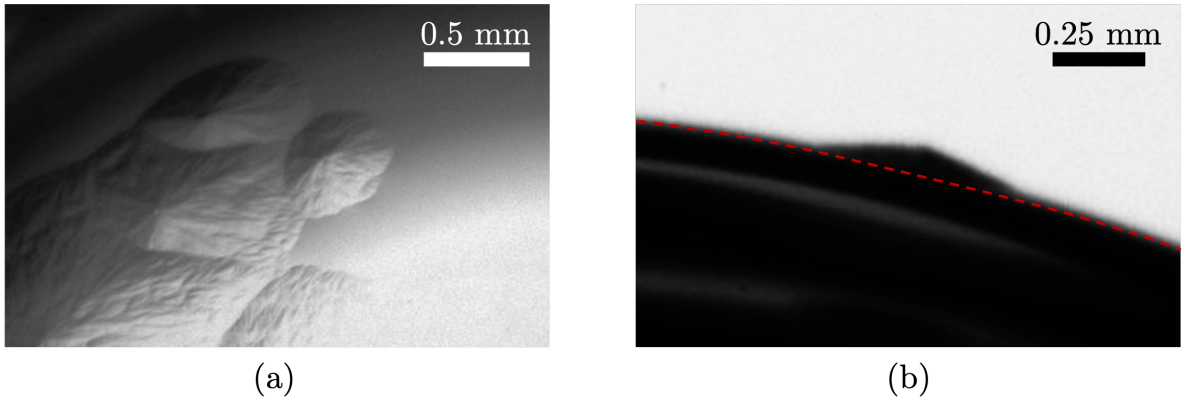


Figure 4.14: A closer look on the morphology of hydrate film at a subcooling temperature of 11 K. (a) Agglomeration of spherulites with rough texture. (b) Floating spherulite protruding into cyclopentane phase.

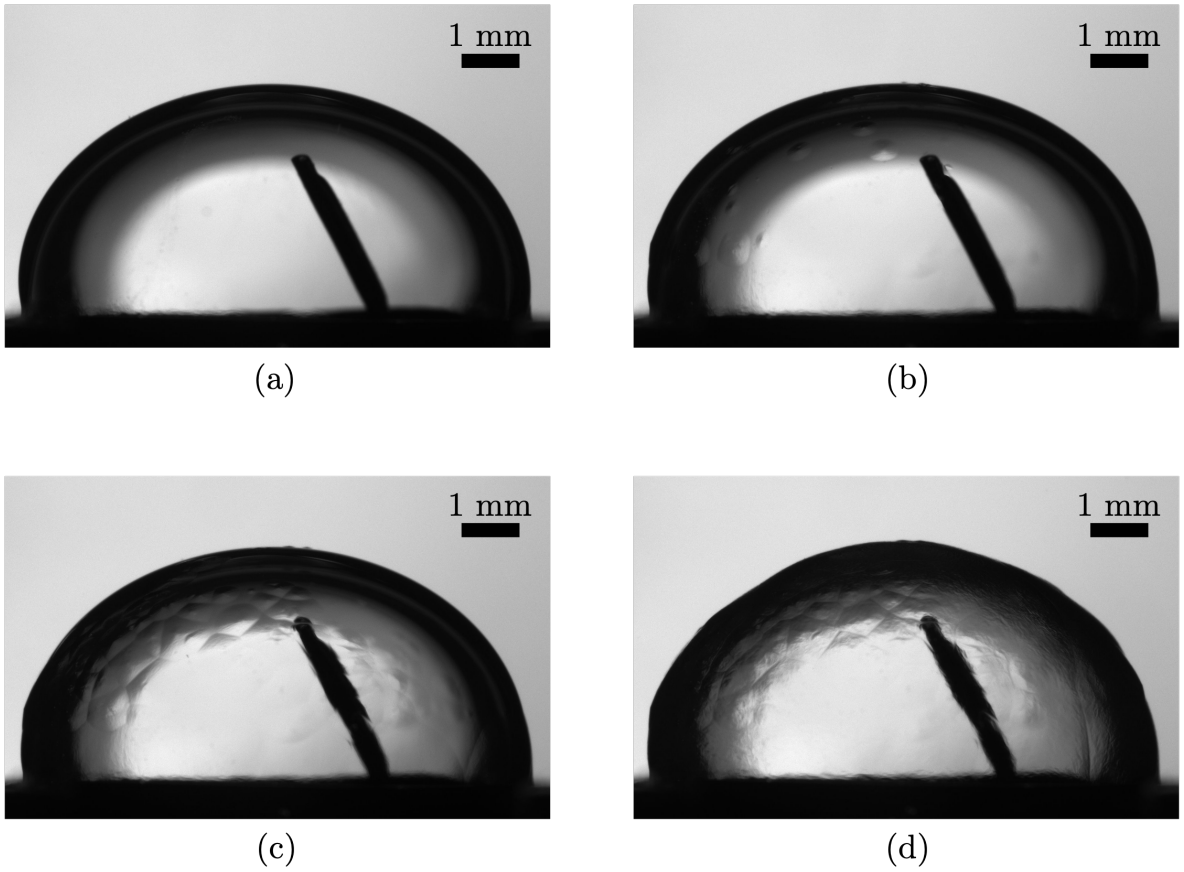


Figure 4.15: Evolution of hydrate formation and growth at a subcooling temperature of 15.2 K.

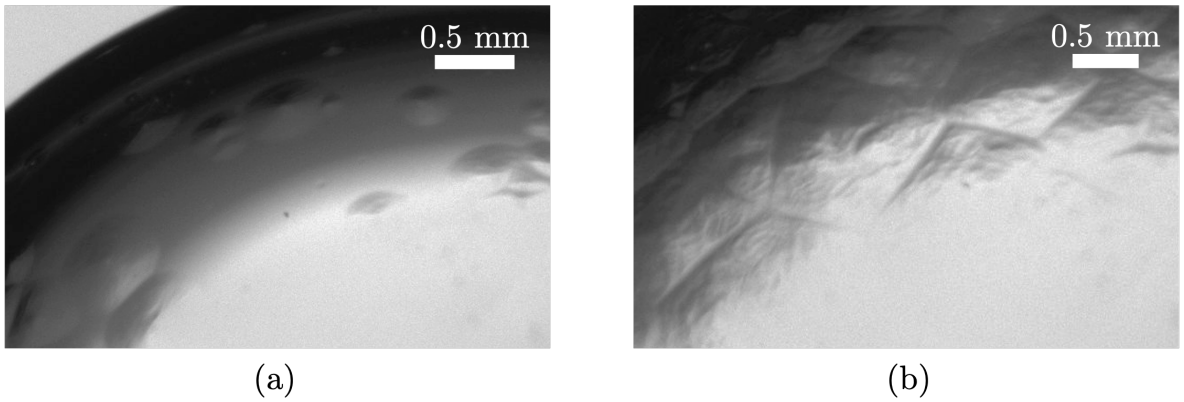


Figure 4.16: A closer look on the morphology of hydrate film at a subcooling temperature of 15.2 K. (a) Spherulites with smoother texture compared to the spherulites formed at a subcooling temperature of 15.2 K. (b) Agglomeration of spherulites with "tortoise shell" appearance.

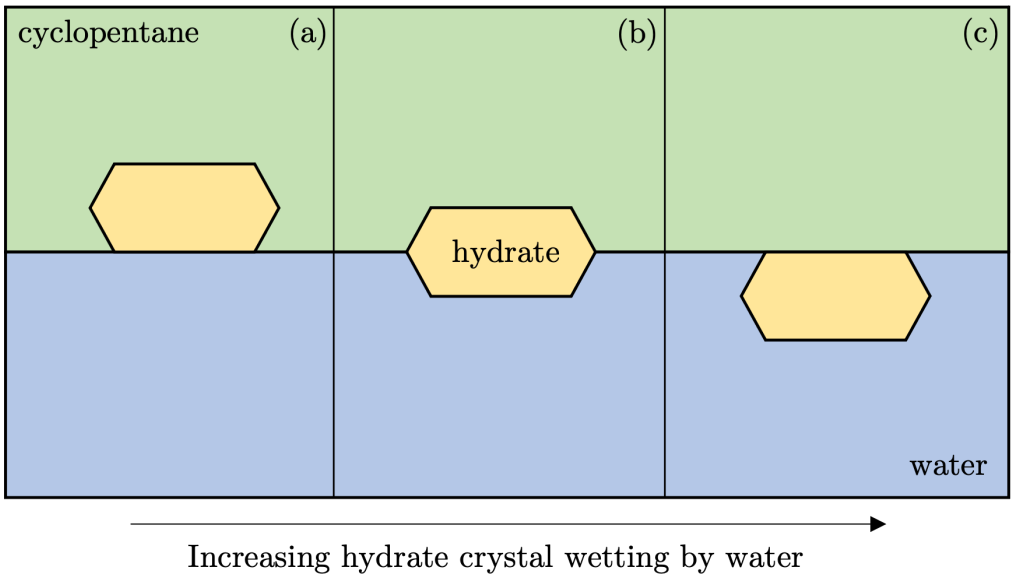


Figure 4.17: Schematic of the position of a hydrate crystal with respect to the cyclopentane-water interface depending on its wettability. (a) Hydrophobic hydrate (b) Partially hydrophilic hydrate (c) Hydrophilic hydrate. Adapted from McClements [27].

by Boode and Walstra [175] and Ergun et al. [176] of fat crystals forming at water-oil interfaces. In addition, the subcooling temperature could also influence the water wettability of hydrate film as shown by Stoner et al. [79] where it was reported that the affinity of cyclopentane hydrate towards water or its hydrophilicity decrease with an increase in subcooling temperature. This is consistent with our observation at subcooling temperature above 11 K whereby the hydrate film is not completely hydrophilic as shown by the protrusion of hydrate film into the cyclopentane phase, which can be represented by either Figure 4.17 (a) or (b). Such an observation provides insight into the dominant phase (water or the hydrate former) where transport phenomena occur in order to sustain the growth of hydrate.

4.3 Lateral growth rate of hydrate

The average lateral growth rate of the cyclopentane hydrate film, v_f, was estimated using the procedure outlined in Section 3.5. Figure 4.18 shows the variation of average lateral growth of hydrate, v_f at varying subcooling temperature, ΔT. At ΔT greater than 7 K, v_f is a linear function of ΔT. This trend, although not the values themselves, is consistent with the results

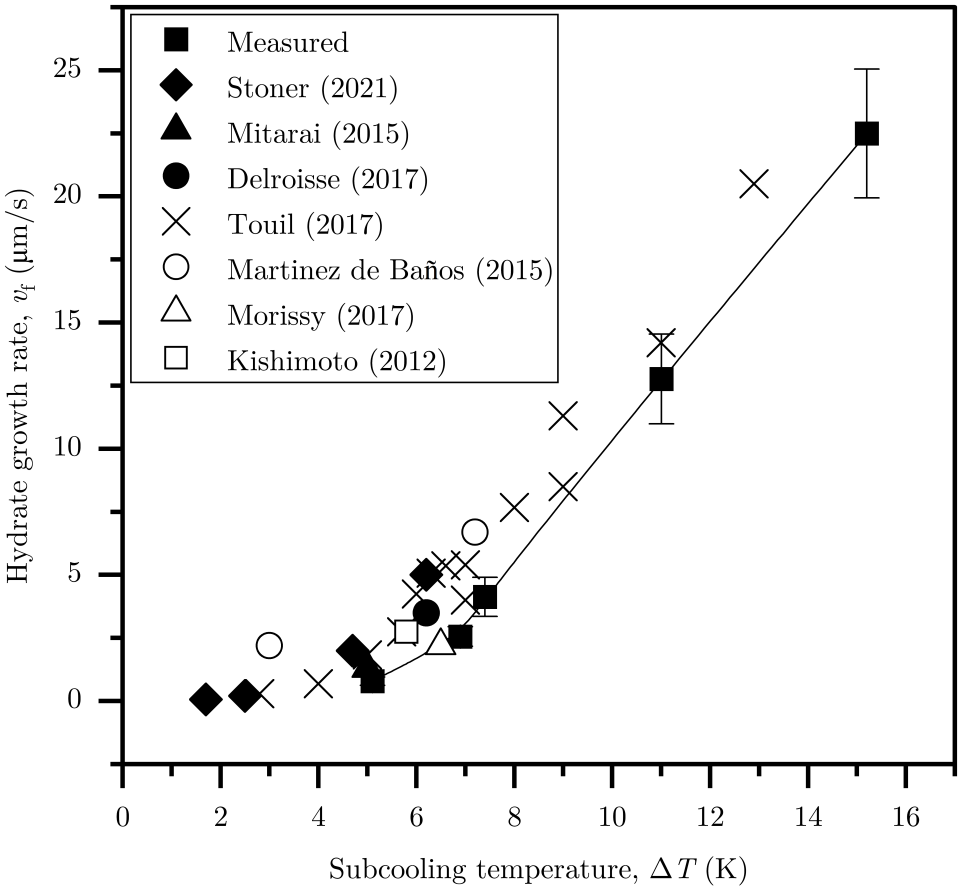


Figure 4.18: Comparison between average growth rate of cyclopentane hydrate as a function of subcooling temperature measured experimentally with those reported in the literature.

reported by Touil et al. [59]. The discrepancies between the two studies and the present research can be attributed to different system arrangements. In their case, the experiments were performed in capillaries where the growth rate could be influenced by the tube walls and interfacial tension, which Beltrán and Servio [76] described as the "bridge effect". The phenomenon was first hypothesised by Servio and Englezos [177] who observed hydrate growth beyond the original water boundary i.e. hydrate growth ahead of the advancing water front on a foreign surface or substrate. This may have also affected the position of the inflection point present in Figure 4.18, where there was a change in the dependence of the growth rate on ΔT. The data points from Touil et al. [59] showed that the inflection point is at $\Delta T \approx 5$ K compared to $\Delta T \approx 7$ K in the experiments in this research. The presence of a rubber O-ring, which was adhered to the glass substrate as described in Section 3.2, prevented the spreading of the hydrate "bridge" on the glass substrate.

The morphological transformations observed in the figures presented in Section 4.2.2 suggests that the change in hydrate appearance is associated to the hydrate growth dynamics and may have given rise to the inflection point at $\Delta T \approx 7$ K. From the crystallographic perspective, the presence of the inflection point in Figure 4.18 may have been caused by a switch in the crystal growth mechanism, such as that described by the Burton-Cabrera-Frank (BCF) theory [178]. According to the theoretical consideration given by Sunagawa [61], the growth rate of a crystal, v_{f} following BCF is given by

$$v_f = K\sigma^n \tag{4.1}$$

where K is a proportionality constant, n is a positive number and σ is a driving force. The degree of departure from a thermodynamic equilibrium state corresponds to the driving force for crystal growth. The departure may arise either by lowering the temperature or increasing the concentration.

Crystal growth mechanisms can be classified into three main groups: spiral, two-dimensional nucleation and adhesive type [61]. In addition, Sunagawa [61] described the relation in Equation 4.1 as having two bending points which are related to the change in growth mechanisms. Spiral growth mechanism occur at a low driving force and does not require the molecules to overcome an energy barrier i.e., the driving force possessed by the molecules, σ, is below a certain threshold value, σ'. The crystals grow in a self-perpetuating manner and is initiated at a dislocation. As the crystal develop layer-by-layer forming spiral steps, it creates atomically smooth crystal interface. The relation between growth rate and the driving force is described by Equation 4.1 with $n = 2$. In contrast, when the system is in a high thermodynamic driving force such that it exceeds the threshold value corresponding to the second bending point, σ", crystals can grow in any crystallographic direction because it has enough energy to overcome all energy barriers, thus forming macroscopically round-shaped crystals [179]. In this case, $n = 1$, which gives rise to a linear dependence of growth rate with respect to driving force. Between the first and second threshold, σ' and σ", the crystal growth undergo two-dimensional nucleation growth mechanism, which is the transitional stage between the spiral and adhesive-type growth,

for which the value of n falls between 1 and 2.

Relating the observation on hydrate formation to the general crystal growth mechanism as theorised by Sunagawa [61], as described above, the driving force for the case of hydrate can be regarded as the degree of subcooling i.e. $\sigma \leftrightarrow \Delta T$. The linear trend observed in Figure 4.18 suggests that when $\Delta T > \Delta T$" ≈ 7 K, cyclopentane hydrate undergoes an adhesive-type growth. In this temperature range, hydrate growth can be characterised by dendritic and spherulitic crystal development. As the hydrate interface becomes atomically rougher due to the active adhesive-type growth mechanism, its morphological stability is reduced. This creates heterogeneities on the interface of the supercooled water drop which thus stimulates secondary nucleation. According to Gránásy et al. [180], randomisation of local crystallographic orientation occurred due to the birth crystal nucleation at the growth front which gives rise to dendritic and spherulitic crystals.

While the focus of this research is for T_{B}, below 273 K (i.e., $\Delta T > 7$ K), it is worth discussing about the one data point obtained in this research that is above 273 K. Based on the morphological characterisation proposed by Sunagawa [61], the striations on the hydrate film observed in Figure 4.8 are characteristic of hopper (i.e. layered polyhedral) face crystals, which suggests that the two-dimensional nucleation growth mechanism prevails in the hydrate development at $\Delta T = 5.1$ K. Hence, when $\Delta T < \Delta T$" ≈ 7 K, the hydrate evolution is governed by either the spiral or two-dimensional nucleation growth mechanism. This is consistent with data reported by Stoner et al. [79] and Touil et al. [59] (Figure 4.18) for $\Delta T < 7$ K where the growth rate obeys a power law relation (with $n > 1$) with respect to the subcooling temperature. The transition between the spiral and two-dimensional nucleation growth mechanisms that occurs at ΔT' is however, beyond the scope of this research. The characteristics of the growth mechanisms of cyclopentane hydrates are summarised in Table 4.2.

At low degrees of subcooling, the hydrate growth occurs relatively slowly, allowing the hydrate crystals to develop in an orderly manner, resulting in faceted, polyhedral structures. According to Nanev [181], the stability of the polyhedral crystal shapes is attributed to the minimal

Table 4.2: Characterisation of cyclopentane hydrate growth mechanism based on crystal morphology.

Bulk temperature, T_B (K)	Subcooling temperature, ΔT (K)	n	Crystal morphology	Crystal growth mechanism
> 273.15	< 7	> 1	polygonal	spiral or two-dimensional nucleation
< 273.15	> 7	1	dendritic and spherulitic	adhesive

diffusion effect at low degrees of subcooling, where the local environment near the hydrate front remains relatively uniform. As the degree of subcooling increases, the thermodynamic driving force is greater leading to faster growth rate. Instabilities begin to develop at the hydrate front due to more pronounced diffusion effects, such as localised decrease in the concentration of water or cyclopentane and localised increase in temperature gradient. This non-uniformity at the hydrate front promotes preferential growth in certain regions, causing branching that eventually leads to dendritic structures.

Dendritic crystal growth is also widely recognised as being governed by diffusion-limited processes, where the attachment of molecules from the supercooled environment occurs rapidly and without significant kinetic barriers [182]. Consequently, the morphological transition to dendritic growth at ΔT above 7 K indicates that cyclopentane hydrate growth has entered the diffusive regime. As ΔT increases further, the growth rate accelerates even more and the high thermodynamic driving force leads to an increase in the nucleation rate, as demonstrated in Figures 4.13 and 4.15. The resulting morphological pattern of cyclopentane hydrate is illustrated in the pattern map in Figure 4.19.

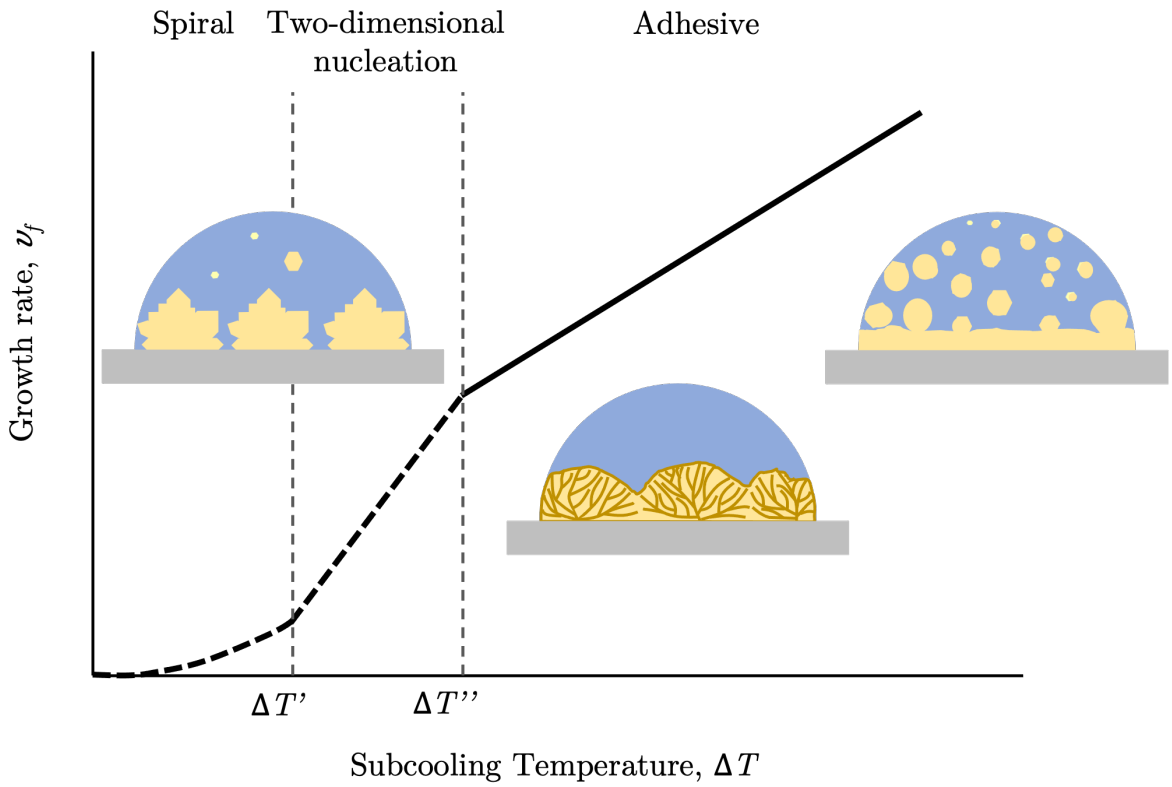


Figure 4.19: A schematic of morphological patterns at varying degree of subcooling starting from polyhedral crystals at low subcooling temperature and transitioning to dendrites followed by spherulites as the subcooling temperature increases.

4.4 Comparisons with hydrate growth rate predictions

In this section, the results of hydrate lateral growth rate obtained from visualisation experiments are compared to hydrate growth models available in literature. A modified model based on the work of Liu et al. [30], taking into account of the differences in phases of fluids involved, is also presented.

4.4.1 Mori's hydrate growth model

A convective heat transfer model proposed by Mori [28] for carbon dioxide hydrate in a liquid-liquid environment can be written in the following form:

$$v_{\mathrm{f}}\delta = C\Delta T^{3/2} \tag{4.2}$$

Table 4.3: Thermophysical properties of cyclopentane hydrate, water and liquid cyclopentane. The subscripts h, w and g represent hydrate, water and cyclopentane (guest former).

Property	Range	Unit	Reference
ρ_{h}	965	kg/m^3	[183]
Δh_{h}	269000	J/kg	[173]
λ_{w}	0.534 - 0.552	W/m K	[184]
λ_{g}	0.154 - 0.158	W/m K	[21]
ν_{w}	(1.47 - 2.38) $\times$ 10^{-6}	m^2/s	[185]
ν_{g}	(7.21 - 7.98) $\times$ 10^{-7}	m^2/s	[186]
κ_{w}	(1.26 - 1.32) $\times$ 10^{-7}	m^2/s	[187]
κ_{g}	(1.18 - 1.22) $\times$ 10^{-7}	m^2/s	[188]
ρ_{w}	998.8 - 1000	kg/m^3	[31]
ρ_{g}	762.5 - 772.2	kg/m^3	[186]
$c_{\mathrm{p,w}}$	4205 - 4252	J/kg K	[189]
$c_{\mathrm{p,g}}$	1670 - 1712	J/kg K	[190]
β_{w}	-(1.5 - 22.8) $\times$ 10^{-5}	1/K	[191]
β_{g}	(1.2 - 1.24) $\times$ 10^{-3}	1/K	[192]

$$C = \left[\frac{\pi A}{4 \rho_{\mathrm{h}} \Delta h_{\mathrm{h}}} \left(\frac{\lambda_{\mathrm{w}}}{\kappa_{\mathrm{w}}^{1/3}} + \frac{\lambda_{\mathrm{g}}}{\kappa_{\mathrm{g}}^{1/2}} \right) \right]^{3/2} \tag{4.3}$$

where v_{f} is the hydrate growth rate, δ is the hydrate film thickness and ΔT is the temperature difference between the bulk and the hydrate front (i.e. $\Delta T = T_{\mathrm{f}} - T_{\mathrm{b}} = T_{\mathrm{eq}} - T_{\mathrm{b}}$). C is a parameter that depends on the thermophysical properties of water, the hydrate former (cyclopentane) and hydrate. A is a constant in the Nusselt correlation taken as 1/3, as determined by Mori [28] based on forced convective heat transfer around a cylinder to represent a hemicircular hydrate film front. Taking the same geometrical assumption and mode of heat transfer, the value of A is retained as 1/3. ρ_{h} is the density of cyclopentane hydrate, Δh_{h} is the heat of hydrate formation, λ is the thermal conductivity and κ is the thermal diffusivity. The subscripts h, w and g represent hydrate, water and the hydrate former, respectively. The thermophysical properties of cyclopentane hydrate, water and cyclopentane are summarised in Table 4.3.

In this model, the hydrate film thickness is assumed to be constant. Taylor et al. [2] reported the film thickness of cyclopentane hydrate to be between 15 to 40 μm for subcooling temperatures, ΔT between 4 to 10 K while Brown and Koh [71] reported an average value of 36.9 μm when $\Delta T = 6.7$ K. Figure 4.20 compares the predicted hydrate growth rate from model proposed by Mori [28] with the average hydrate growth rate measured experimentally, as presented earlier in Section 4.3. The solid curves in Figure 4.20 illustrate the relationship between hydrate growth and subcooling temperature, using arbitrary hydrate film thickness, δ ranging from 40 to 140 microns. While Mori's model [28] provided a good prediction for carbon dioxide hydrate using data from Uchida et al. [6], none of the curves in Figure 4.20 show a strong correlation with the measured growth rates for cyclopentane hydrate. The data points also show that the measured hydrate growth rates align with the predicted values at different δ values. This suggests that the film thickness of cyclopentane hydrate varies with subcooling temperature, ΔT such that the thickness increases as the subcooling temperature decreases.

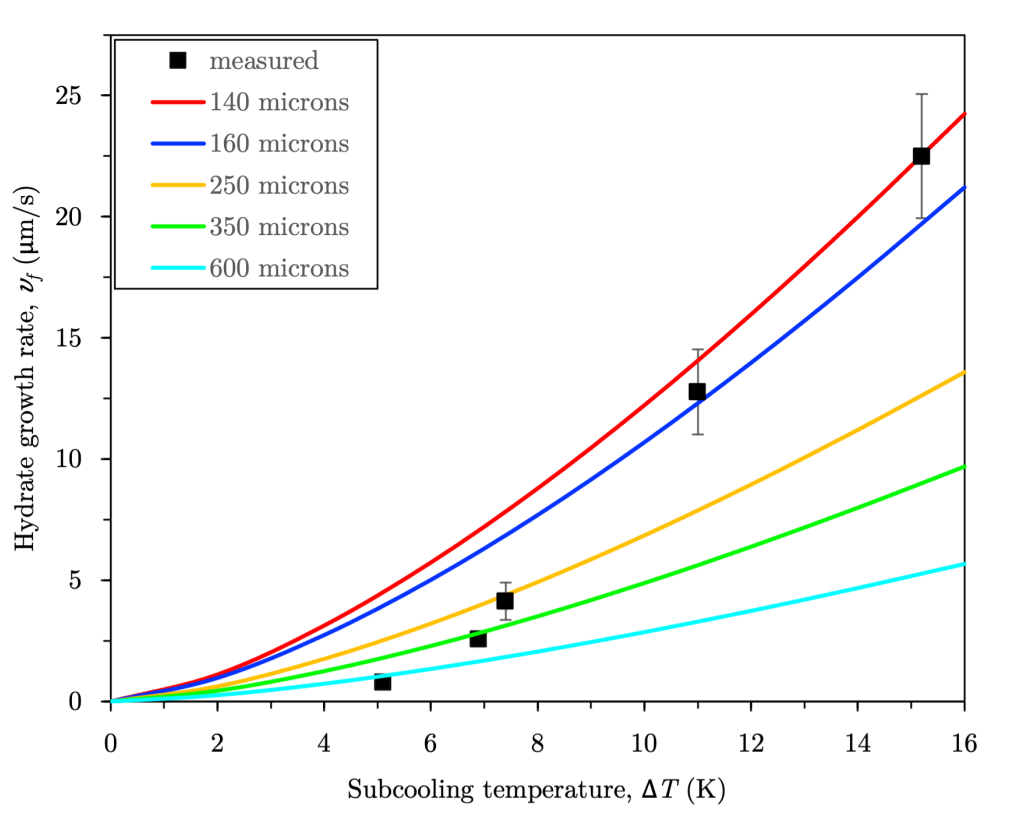


Figure 4.20: Comparison between predicted values of the lateral growth rate of cyclopentane hydrate, v_{f} (using Mori's convective heat transfer model [28]) with experimentally measured data at varying subcooling temperature, ΔT. Each line corresponds to predicted values for constant hydrate film thickness, δ in the range of 140 to 600 microns.

4.4.2 Peng's hydrate growth model

Peng et al. [29] then extended the model to account for variation in hydrate film thickness by assuming that the hydrate film thickness,δ is inversely proportional to the subcooling temperature, ΔT (Equation 4.4). Equation 4.2 can then be written as Equation 4.5.

$$\delta = k/\Delta T \tag{4.4}$$

$$v_f = \psi \Delta T^{5/2} \tag{4.5}$$

$$\psi = C/k \tag{4.6}$$

where k is the proportionality constant and C is modified to take into account of the position of hydrate film in relation to its position in water and hydrate former (cyclopentane), as expressed in Equation 4.7. The portion of hydrate film that is immersed in the hydrate former denoted as l is illustrated in Figure 4.21.

$$C = \left[\frac{A}{2\rho_{\mathrm{h}} \Delta h_{\mathrm{h}}} \left(\frac{\lambda_{\mathrm{w}}}{\nu_w^{1/3}} Pr_{\mathrm{w}}^{1/3} \left(\pi - \cos^{-1}\left(1 - \frac{2l}{\delta}\right)\right) + \frac{\lambda_{\mathrm{g}}}{\nu_{\mathrm{g}}^{1/3}} Pr_{\mathrm{g}}^{1/3} \cos^{-1}\left(1 - \frac{2l}{\delta}\right)\right)\right]^{3/2} \tag{4.7}$$

The value of ψ in Equation 4.5 was determined by regressing the experimental data using the least squares method, yielding a value of 2.59×10^{-8} with a correlation coefficient R^2 of 0.9617. This value of ψ is then inserted into Equation 4.5 to obtain the predicted values of hydrate growth rate, v_{f} as a function of subcooling temperature,ΔT. Figure 4.22 shows good agreement between the calculated values and experimental data. Since the exact position of the hydrate film at the cyclopentane-water interface is unknown, the film thickness is estimated by assuming two cases: Case 1, where the film is fully immersed in cyclopentane ($l = \delta$), and Case 2, where

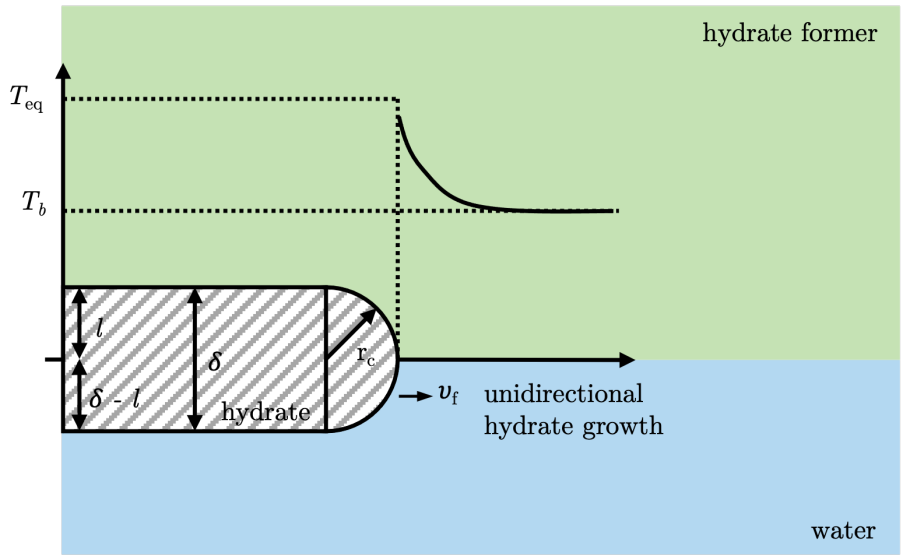


Figure 4.21: Illustration of hydrate film relative to water and the hydrate former (adapted from Peng et al. [29]). If the hydrate film grows at a front velocity (i.e., growth rate) of v_f and viewing the hydrate film with a moving frame of reference fixed to the edge of the hydrate front, then water and hydrate former can be assumed to flow over the hydrate film at the same approach velocity.

Table 4.4: Values of parameters C and k at two extremes, where hydrate film is assumed to be either fully immersed in cyclopentane (Case 1) or water (Case 2).

	Case 1: $l = \delta$	Case 2: $l = 0$
C	1.59×10^{-11}	1.02×10^{-10}
k	6.15×10^{-4}	3.95×10^{-3}

it is fully immersed in water ($l = 0$). These estimations provide the minimum and maximum possible film thickness. A hydrate film that is partially immersed would have a thickness falling within the range determined by Case 1 and Case 2. Using the fit value of ψ, the parameters C and k are calculated from Equations 4.6 and 4.7, as shown in Table 4.4 for both cases. With the values of k known, the hydrate film thickness, δ can then be determined using Equation 4.4 at varying subcooling temperatures, ΔT.

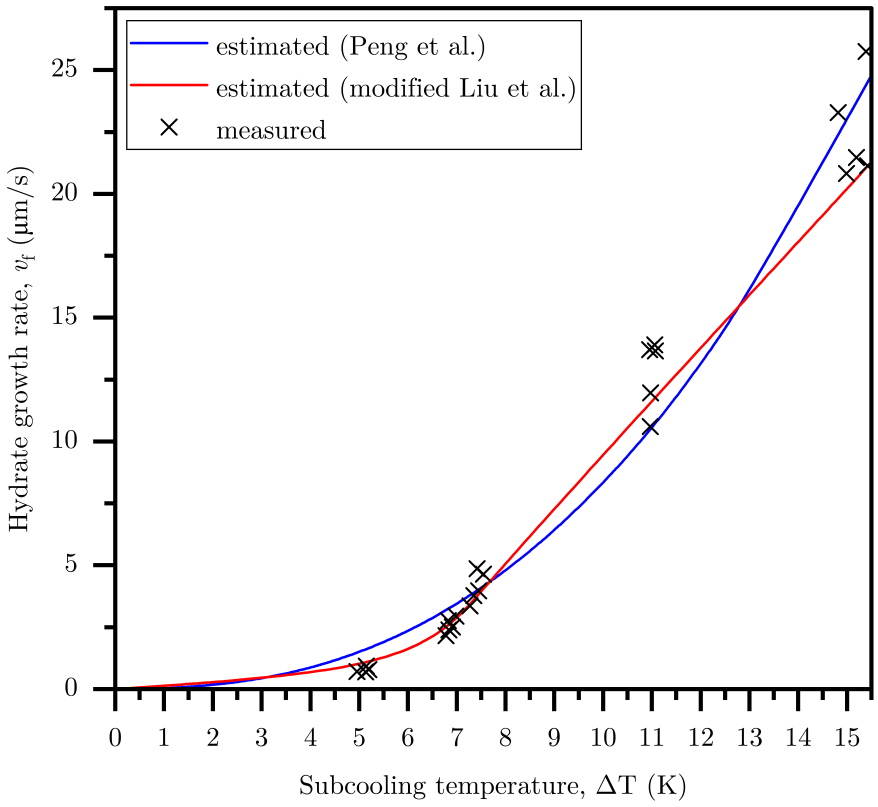


Figure 4.22: Comparison between predicted values of the lateral growth rate of hydrate, v_f (using Peng's convective heat transfer model [29]) with experimentally measured data at varying subcooling temperature, ΔT.

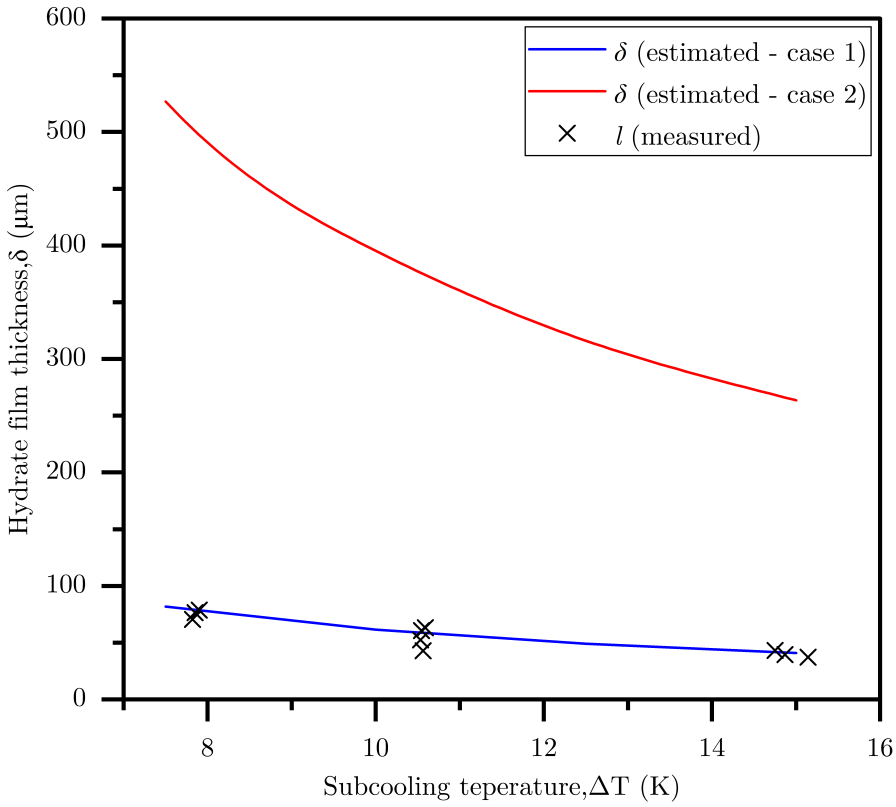


Figure 4.23: Comparison between predicted values of the lateral growth rate of hydrate, v_f (using Peng's convective heat transfer model [29]) with experimentally measured data at varying subcooling temperature, ΔT.

Hydrate film thickness

In the hypothetically scenario where the hydrate film is fully immersed in water (Case 2), the predicted thickness ranges from 260 to 530 microns for a subcooling temperature between 7.5 to 15 K, as depicted in Figure 4.23. Conversely, when the film is fully immersed in cyclopentane (Case 1) the thickness is estimated to be an order of magnitude thinner, between 40 to 80 microns for the same subcooling range. Notably, the thickness values for Case 1 align more closely with those reported by Taylor et al. [2] and Brown and Koh [71]. Additionally, direct visualisation images were used to measure the hydrate film thickness in cyclopentane, l_{meas}. Figure 4.24 provide a sample image of hydrate film growing at the drop interface where the thickness is estimated by measuring the distance between the contours of the drop and the hydrate film. The measurements of l_{meas} were found to be in strong agreement with the hydrate film thickness calculated in Case 1, suggesting that the hydrate film observed in Figure 4.24 is fully immersed in cyclopentane, i.e., $\delta = l_{meas} = l$. Despite a good agreement between

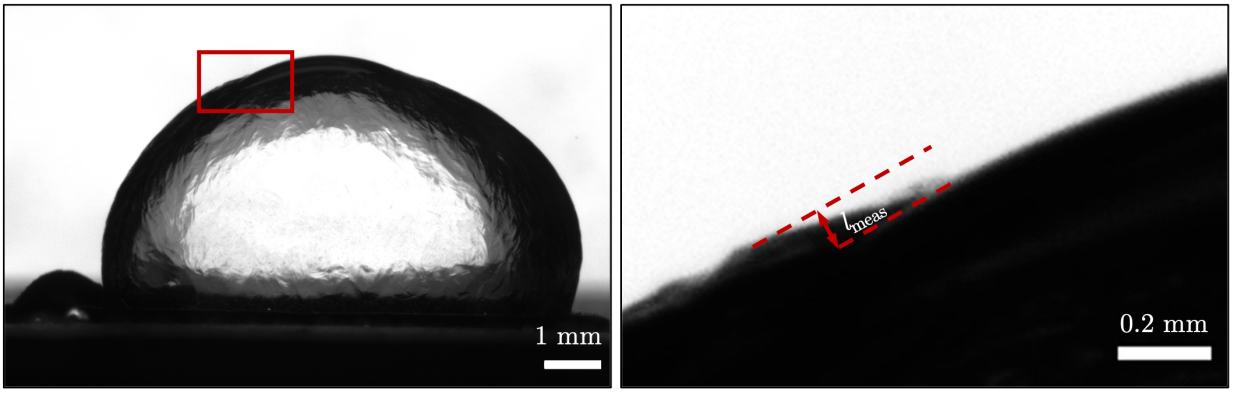


Figure 4.24: A closer look of the geometry of hydrate front growing on the drop interface (in the boxed region.

the hydrate growth model proposed by Peng [29] with experimental measurements, there are a few concerns on the basis upon which the model was derived. Firstly, the geometry of the hydrate front as macroscopically observed in Figure 4.24 is considerably different from the hemispherical assumption (Figure 4.21) made by by Peng et al. [29]. As the hydrate film is fully immersed in cyclopentane, the consequence of the hemispherical assumption in the model is that it neglects the heat transfer into the water drop, which may potentially be significant. Secondly, the model was derived on the basis of forced convective heat transfer [28, 29], which may not be appropriately applied to a hydrate growth model where the change in temperature at the hydrate front, which is often assumed to be at the equilibrium temperature [2, 66, 29, 28], is likely to experience natural convection instead.

4.4.3 Liu's modified hydrate growth model

Liu et al. [30] addressed these two concerns by proposing a hydrate model for gas-liquid interface. In what follows, the model is modified for the application of hydrate growing at a liquid-liquid interface, which will then be compared with the results from the cyclopentane hydrate experiments. In the case of cyclopentane acting as the hydrate former, the hydrate film is completely immersed in the hydrate former phase (Figure 4.24), which differ from the approach taken by Liu et al. [30] for methane gas hydrate. The hydrate front that is in contact with cyclopentane has a curved surface whereas the portion of the hydrate front that is in contact with water is planar, as illustrated in Figure 4.25. While hydrate may grow as

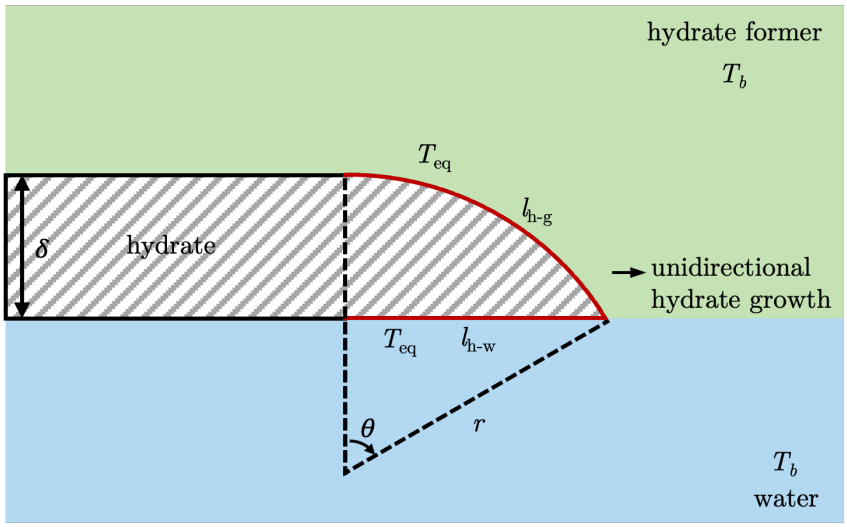


Figure 4.25: Illustration of hydrate film relative to water and the hydrate former (adapted from Liu et al. [30]). The portion that is highlighted in red is the active area of the film that is involved in hydrate growth i.e., the hydrate front.

flat crystal facets microscopically, on the macroscopic level, they appear as curved interface as evident in Li et al. [63] and Li et al. [193] and taken by Liu et al. [30] as a basis of hydrate front geometry. The curved hydrate front has also been observed macroscopically in this study as shown in Figure 4.14. The hydrate film is assumed to grow unidirectionally with a non-porous structure having a constant thickness. The heat balance at the hydrate front is expressed as follows

$$v_{\mathrm{f}}\delta\rho_{\mathrm{h}}\Delta h_{\mathrm{h}} = (h_{\mathrm{g}}l_{h-g} + h_{\mathrm{w}}l_{h-w})\Delta T \tag{4.8}$$

$$l_{\mathrm{h-g}} = \delta\cos^{-1}\left(1 - \frac{r}{\delta}\right) \tag{4.9}$$

$$l_{\mathrm{h-w}} = (2r\delta - \delta^2)^{0.5} \tag{4.10}$$

where v_{f} is the hydrate growth rate, δ is the hydrate film thickness, ρ_{h} is the hydrate density, Δh is the heat of hydrate formation, h is the heat transfer coefficient (subscripts g and w represent hydrate (or guest) former and water, respectively), l is the area per unit length

of the hydrate front that is in contact with the respective phases (subscripts h-g and h-w represent the hydrate-guest and hydrate-water interfaces, as expressed in Equations 4.9 and 4.10 respectively). The parameter r in Figure 4.25 is the radius of curvature of the hydrate front having the same order of magnitude as the film thickness, δ. Here, the radius of curvature is assumed to be equal to the film thickness, i.e., $r = \delta$. The hydrate front is assumed to be held at the hydrate equilibrium temperature and therefore, the degree of subcooling, ΔT can be calculated as $\Delta T = T_{\mathrm{eq}}\text{-}T_{\mathrm{b}}$. For simplicity, the bulk temperature, T_{b} of both the hydrate former and water are assumed to be at the same temperature.

$$Nu = A(Ra)^B \tag{4.11}$$

$$Nu = hL/\lambda \tag{4.12}$$

$$Ra = GrPr = \frac{g\beta\Delta TL^3}{\nu\alpha} \tag{4.13}$$

The temperature gradient formed as a result of hydrate formation cause a change in the density near the hydrate front. This gives rise to a density gradient that cause a buoyancy effect where heat is transferred locally by natural convection. The general form of Nusselt correlation can be written in the form expressed in Equation 4.11, where h is the heat transfer coefficient, λ is the thermal conductivity, g is the gravitational acceleration, β is the volumetric coefficient of thermal expansion, ν is the kinematic viscosity and α is the thermal diffusivity. The parameter L is the characteristic length and A and B are the coefficients of correlation.

The geometric characteristic of the heat transfer area are treated in two parts: 1. An incomplete horizontal circular cylinder in an infinite space to represent the curved surface that is in contact with the hydrate former (liquid cyclopentane); 2. A horizontal square plate in water to represent the planar surface that is in contact with water. Birkebak and Abdulkadir [194] performed experiments for natural convection from the under side of a square heated flat plate in water,

which is analogous to the interface of hydrate front with water, and obtained values of 0.516 and 0.2 for A and B, respectively for laminar flow. The value of B is consistent with that reported by Lewandowski et al. [101] for horizontal, rectangular, isothermal plates.

On the other hand, the values of A and B for a curved surface are taken as 0.5 and 0.25, respectively based on correlations developed by Saville and Churchill [102] and Dennis et al. [103], similar to the approach taken by Liu et al. [30]. It should be noted that these correlations are applicable to large Grashof numbers. For the case of hydrate, the thickness of the hydrate film tend to be in the order of microns, which makes the Grashof number to be small and indicates that the heat transfer at the hydrate front could be a combination of conduction and convection process. As such, a correction factor, m is introduced for the heat transfer coefficient and the proposed correlations are given as Equations 4.14 and 4.15 for cyclopentane and water.

The growth rate of hydrate can be expressed as Equation 4.16 by substituting Equations 4.14 and 4.15 into 4.8. The hydrate film thickness, δ is taken as a variable that is inversely proportional to the subcooling temperature, ΔT, i.e., $\delta = \mathrm{k}/\Delta T$, where k is a proportionality constant. The parameters C_1 (Equation 4.17) and C_2 (Equation 4.18) depend on the thermophysical properties of the fluids involved in the heat transfer as well as the newly formed hydrate (where the subscripts g,w and h represent cyclopentane, water and hydrate) (Table 4.3).

The values of k and m are regressed from the experimental results, where k is 6.63 $\times$ 10^{-4} (with a correlation coefficient R^2 of 0.9407) while the correction factor, m increases with increasing subcooling temperature from 0.02 to 0.08 (for $5 \leq \Delta T \leq 15$). The change in m is due to changes in the contribution towards convective heat transfer, which by the looks of it, is very small and therefore does not affect the mechanism of heat transfer that is dominated by conduction given how small the Rayleigh numbers are for the range of conditions investigated for cyclopentane hydrate. The difference between the mechanism of heat transfer investigated by Liu et al. [30] who reported a combination of conduction and convection for methane hydrate in a gas-liquid environment, is likely due the significantly higher growth rate of methane hydrate (one to two orders of magnitude larger compared to cyclopentane hydrate). As such, more heat of formation is released during the growth of methane hydrate which may have induced natural convection

locally near the hydrate front.

$$Nu_g = 0.5m(Gr_g Pr_g)^{0.25} \tag{4.14}$$

$$Nu_w = 0.5m(Gr_w Pr_w)^{0.2} \tag{4.15}$$

$$v_f = \frac{C_1 m}{\delta^{0.25}}\Delta T^{1.25} + \frac{C_2 m}{\delta^{0.4}}\Delta T^{1.2} \tag{4.16}$$

$$C_1 = \frac{\pi \lambda_g^{0.75} \rho_g^{0.5} c_{p,g}^{0.25} \beta_g^{0.25} g^{0.25}}{2^{2.25} \mu_g^{0.25} \rho_h \Delta h_h} \tag{4.17}$$

$$C_2 = \frac{\lambda_w^{0.8} \rho_w^{0.4} c_{p,w}^{0.2} \beta_w^{0.2} g^{0.2}}{2^{0.6} \mu_w^{0.2} \rho_h \Delta h_h} \tag{4.18}$$

Comparisons between the predictions of hydrate lateral growth rate using the model developed by Peng et al. [29], a model modified from Liu et al. [30] and the experimental measurements are shown in Figure 4.22. While predictions from both models fit well with the measurement data, they are both semi-empirical models and are therefore, only applicable to the range of conditions investigated. Some parameters in the model provide physical insights of the phenomena, for example the parameters C_1 and C_2 that depends on the thermophysical properties of the fluids, show the dominant phase for heat transfer. However, the presence of the fitted parameter provide vagueness in the understanding of the phenomenon of hydrate formation. In addition, from the modified model of Liu et al. [30], the growth of cyclopentane hydrate is shown to be dominated by conduction, which is not explicit in the model proposed by Peng et al. [29]. Moreover, hydrate formation can potentially occur while the drop is cooling down, which was an essential step for hydrate induction process to reduce experimental duration. This transient process is not captured in both models that assume steady state condition. A more rigorous solution such as a numerical model, which is out of the scope of this study, would be able

to capture the dynamics of the simultaneous processes of cool down and hydrate formation. The temperature and velocity fields obtained using techniques such as planar laser induced fluorescence (PLIF) thermometry and particle image velocimetry (PIV) would be useful to collect temperature and velocity information for model validation.

4.5 Summary

In this chapter, a phenomenological study of hydrate through direct visualisation experiments is presented. Previous studies of cyclopentane hydrate are limited to temperatures above the freezing point of water to avoid ice contamination. In this work, the temperature range was extended to as low as 266 K. The phenomena of freezing and hydrate formation were characterised by performing experiments on a water drop at similar conditions but in different medium, whereby freezing was performed in silicone oil to suppress hydrate formation while hydrate formation was performed in cyclopentane. Distinguishing features between the two phenomena were observed based on the appearance of solids formed (e.g, changes in the drop shape, opacity and rate of solid formation) and temperature measurements in the drop. Both the qualitative and quantitative analyses showed enough evidence to suggest that it is possible to perform cyclopentane hydrate experiments at temperatures below 273 K without ice contamination.

In previous studies, cyclopentane hydrate has only been reported to posses polygonal or faceted morphology [16, 17, 18]. When the range of subcooling temperature was further extended up to 15 K, it was observed that the morphology of cyclopentane hydrate underwent several transitions, from polygonal to dendrites and subsequently to spherulites. This observation is similar to reports on crystal morphology of other hydrate formers e.g., methane [7, 195] and carbon dioxide [5] and therefore showed that cyclopentane is a good analogue of natural gas for the study of clathrate hydrates. From the crystallographic perspective, it was postulated that hydrate film growth can be governed by different mechanisms, whole roles change with subcooling temperature.

Since dendritic crystals are formed through diffusion limited processes [182], we postulated that the lateral growth rate of hydrate is limited by heat transfer. The lateral growth rates obtained from the visualisation experiments were compared with models that are available in literature. Modification of Liu et al.'s [30] model for the growth of hydrate on a liquid-liquid interface was also presented. Predictions from Peng et al.'s [29] and modified Liu et al.'s [30] models showed good agreement with the experimental result. However, both models relied on fitted parameters and therefore were not able to provide a clear understanding of the phenomenon. Moreover, the models are based on steady-state assumption, and therefore are not able to capture the dynamics of drop cool down and hydrate formation that occur in the hydrate experiments. Spatio-temporally resolved measurements of temperature and velocity would be useful to provide insights into the interaction of hydrodynamics and heat transfer processes during hydrate formation.

Chapter 5

Development of optical techniques for the study of hydrate formation

In this chapter, the development of planar laser-induced fluorescence (PLIF) and particle image velocimetry (PIV) for a new application in the study of clathrate hydrate is presented. In principal, PLIF requires a species that is able to emit light upon excitation. Typically, this is achieved through the addition of fluorescent dye, for example, one that is temperature-sensitive such as rhodamine B [113, 25], rhodamine 110 [122] and fluorescein disodium [196, 124]. All of these examples are fluorescent dyes that are soluble in water. Fluorophore that is soluble in organic solvent, on the other hand, is scarce. As such, an attempt was made to confirm if cyclopentane itself is a fluorophore since cyclohexane, its closest cyclic alkane has been shown to emit fluorescence [197]. In collaboration with King Fahd University of Petroleum and Minerals, the emission of liquid cyclopentane was measured using a Horiba spectrofluorometer (Fluorolog ®-3 HR320) with a useful wavelength range from 190 to 860 nm. Other than artifact peaks from the instruments, there was no observable fluorescence emission from cyclopentane (Appendix A). This also confirms a 1970's work by Hirayama et al. [198].

The development of PLIF thermometry in liquid cyclopentane in this work which has not previously been studied is described in Section 5.1. Measurements of absorption and emission of fluorescent dye in cyclopentane and water are presented in Sections 5.1 and 5.2, respectively.

This results include variations in the spectra of the fluorophore with temperature between 263 to 283 K to obtain the temperature sensitivities of the fluorophores. Temperature sensitivities of fluorophore for PLIF application within this temperature range is also an under-explored area of research. The effect of the additives on the fluid and the phenomena of hydrate formation is presented in Section 5.3. Lastly, the limitation of the optical techniques used in this work is described in Section 5.4.

5.1 Fluorescent dye in cyclopentane

Cyclopentane is a colourless liquid and is a non-polar solvent. Due to the limited number of fluorescent dyes that can be dissolved in non-polar liquid, the first attempt was to take advantage of the properties of ethanol so that polar fluorescent dyes, which are more commercially available, can be used in liquid cyclopentane. Ethanol is a universal solvent. It has a polar end due to its hydroxyl (OH) group which can dissolve polar fluorescent dyes. The alkyl side on the other end is non-polar and is miscible in cyclopentane. The mixture was prepared by first dissolving sulforhodamine B in ethanol and the solution was then added into cyclopentane. A homogeneous mixture of sulforhodamine B in ethanol and cyclopentane was produced as shown in Figure 5.1 and no precipitation was observed after 24 hours.

The absorption and emission spectra of the mixture was then obtained using a spectrometer as shown in Figures 5.2 and 5.3 respectively. The fluorescent dye in the mixture is observed to absorb light throughout the range of wavelength investigated (400 to 700 nm). Between 400 to 600 nm, the absorption spectra at different temperatures almost overlap. The dye also appears to still absorb light between 600 to 700 nm albeit at a lower magnitude. This can cause an issue with reabsorption due to spectral conflict between the absorption and emission spectra. As shown in Figure 5.3, the emission of sulforhodamine B in ethanol and cyclopentane is temperature sensitive between the wavelength of 540 to 600 nm whereby fluorescence emission increases with increasing temperature. Above 610 nm, the dye appears to be insensitive to temperature. This is an indication that the fluorophore could potentially

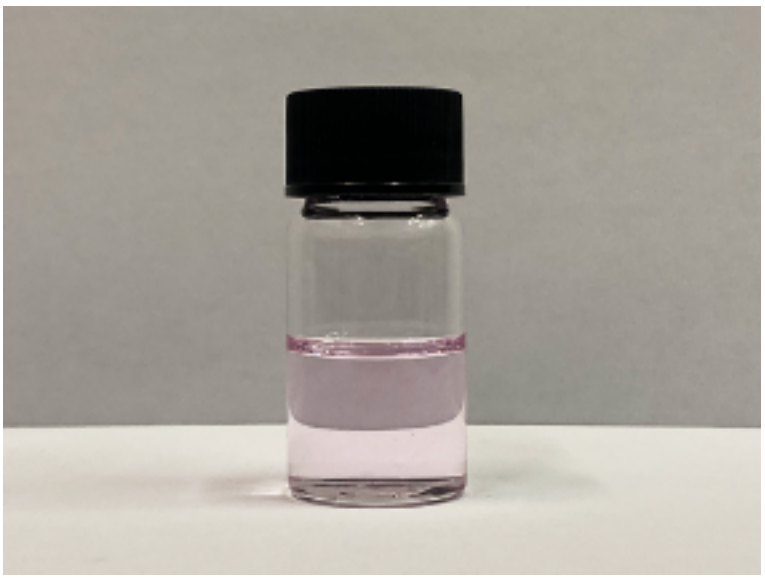


Figure 5.1: Photograph of a solution of Sulforhodamine B in ethanol and cyclopentane which was allowed to settle for 24 hours.

be used in two-colour/one-dye PLIF thermometry by proper spectral separation using optical filters. However since there is a spectral conflict, the absorption and emission spectra should be analysed in more detail. According to Chaze et al. [25], if the absorption coefficient of the absorbing dye is not a function of temperature, then the spectral conflict can be corrected through normalisation of the fluorescence ratio between two spectral bands by a reference taken at the same optical path length. For example, the fluorescence intensity ratio can be obtained by taking the first band between 540 to 600 nm and the second band between 620 to 700 nm. However as evident in Figure 5.2, absorption above 600 nm is dependent on temperature and therefore cannot be corrected. Since the absorption decreases with increasing temperature, which is the opposite to the dependence of fluorescence emission observed below 600 nm, it explains why the emission spectra collapses above 600 nm, which could be interpreted as temperature independence of the emission.

Additionally, as the hydrate experiment required the introduction of a water drop into liquid cyclopentane, a test was performed to check for dye migration. It was observed that there was a transfer of fluorescent dye into the water drop, potentially carried by ethanol, which is miscible in water. This is a critical issue for temperature measurement using the PLIF method as the concentration of fluorescent dye in cyclopentane is no longer constant. As a result, the fluorescence intensity in cyclopentane is a function of both temperature and concentration,

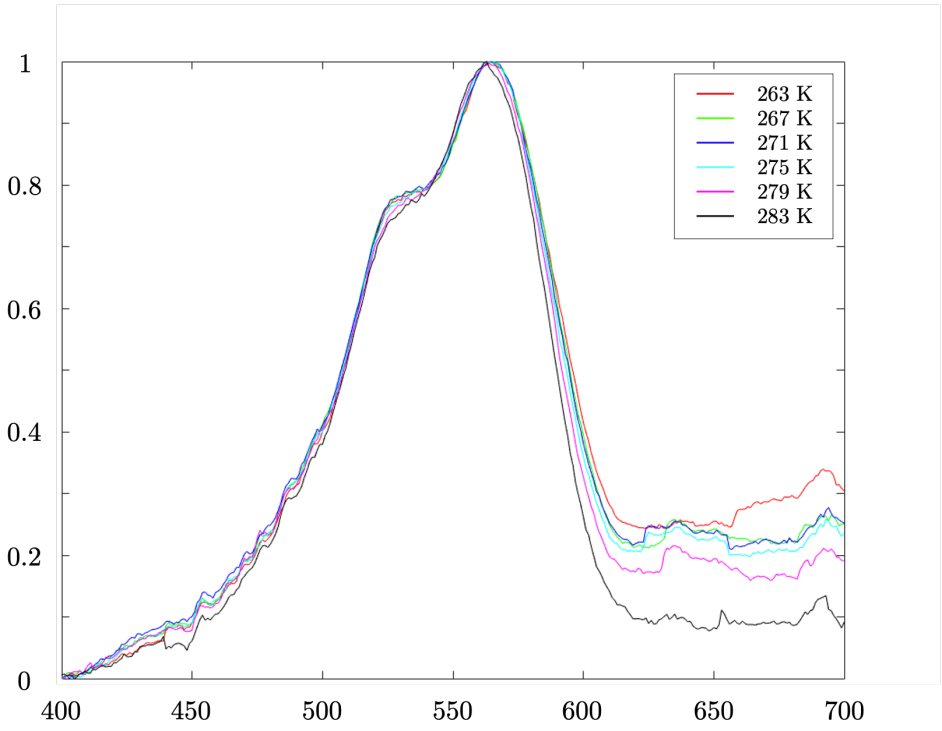


Figure 5.2: Absorption spectra of Sulforhodamine B dissolved in ethanol and cyclopentane at varying temperature.

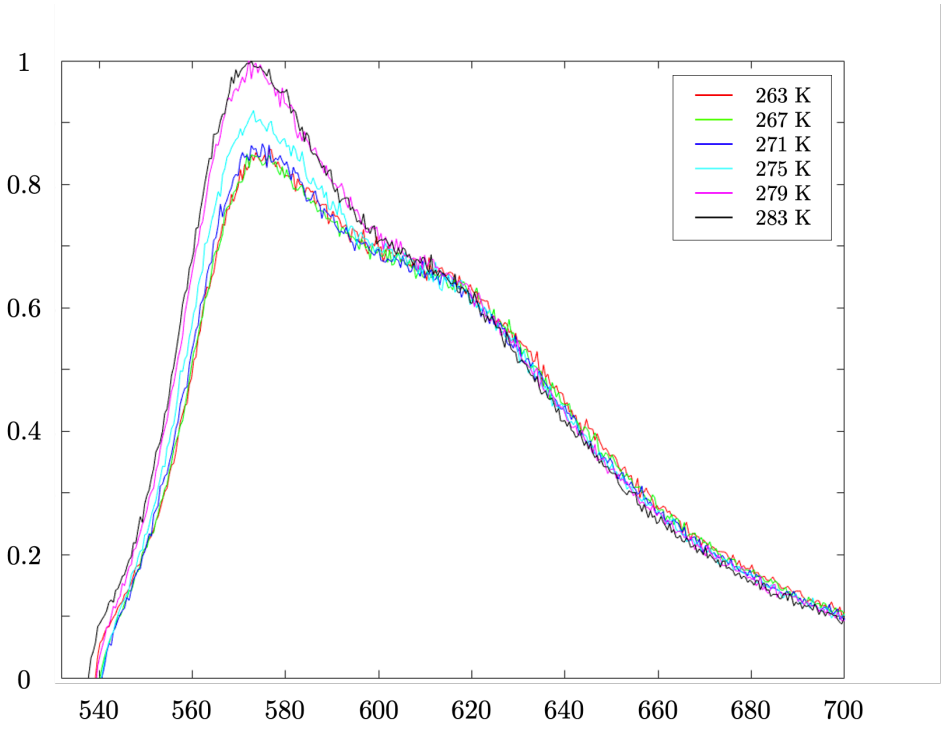


Figure 5.3: Emission spectra of Sulforhodamine B dissolved in ethanol and cyclopentane at varying temperature

.

which makes the interpretation of the effect of temperature on emission intensity more complex.

Alternatively, the fluorophore nile red is commonly applied in the field of biology as a tracer for lipid [199] and organic solvents [200]. Recently, Koegl et al. [201] utilised nile red for PLIF thermometry in fuel blend composed of n-decane and butanol. It appears to dissolve in cylopentane without any precipitation observed after 24 hours (Figure 5.4). In what follows, a characterisation of the absorption and emission of nile red in liquid cyclopentane is presented in order to develop a PLIF thermometry technique for the study of cyclopentane hydrate.



Figure 5.4: Photograph of a solution of nile red in cyclopentane which was allowed to settle for 24 hours.

5.1.1 Concentration dependence of nile red in cyclopentane

The absorption spectra of nile red in liquid cyclopentane at various concentrations (0.5, 1.2, 2, 5, 9 and 18 mg/L) are shown in Figure 5.5. The absorption signals were measured at a temperature of 273 K. The results obtained are then normalised against a reference, taken as the maximum absorption intensity of Nile Red in cyclopentane at a concentration of 18 mg/L. The absorption signal shows that the fluorophore absorbs light between 400 to 550 nm with two distinct peaks at 491 and 518 nm, where the two peaks are almost equivalent in intensity. The absorption intensity increases linearly with increasing concentration. This is represented by the integral of absorption intensities throughout the wavelength investigated for different

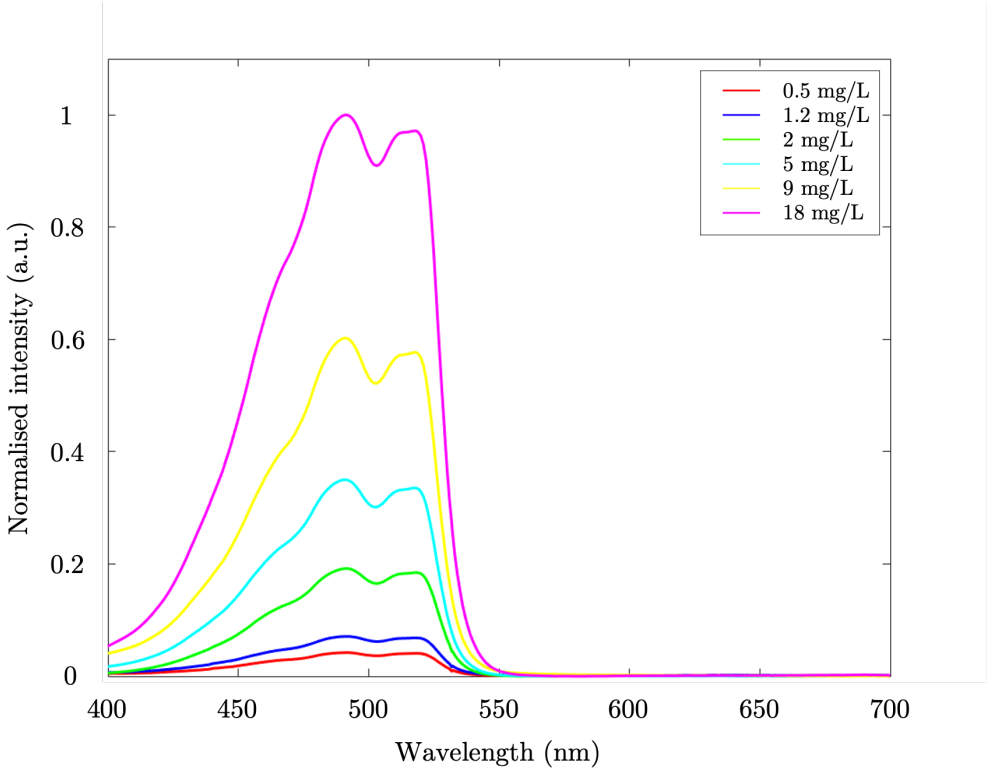


Figure 5.5: Absorption spectra of nile red dissolved in cyclopentane at various concentrations (0.5, 1.2, 2, 5, 9 and 18 mg/L) at a temperature of 273 K and normalised to the maximum intensity of nile red absorption at a concentration of 18 mg/L.

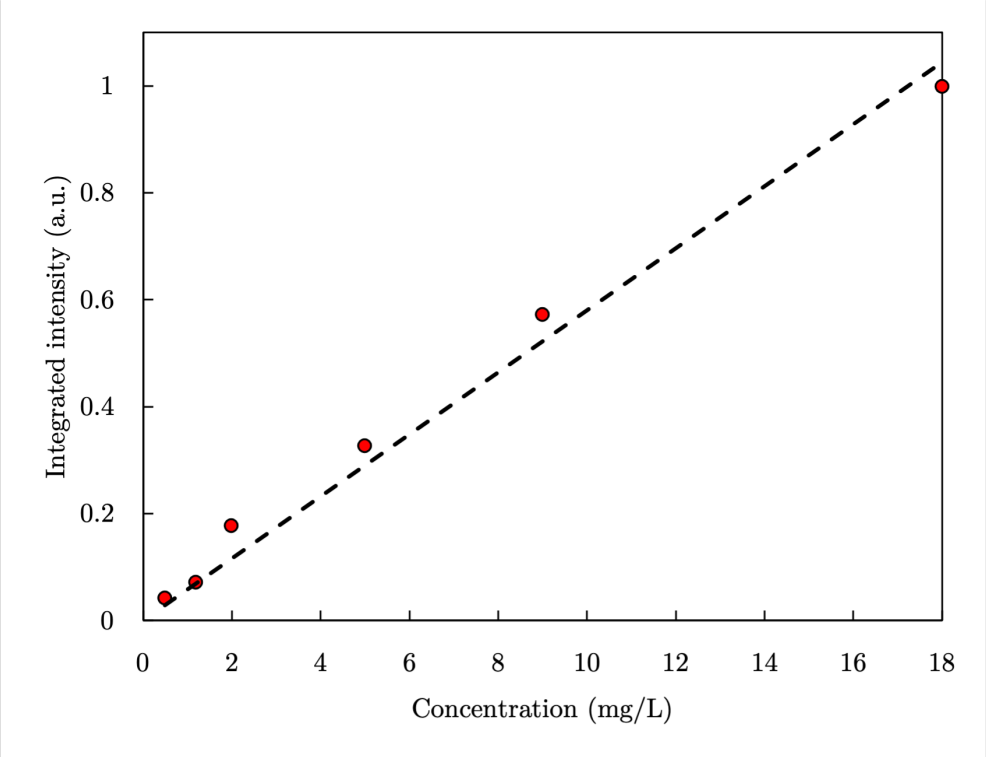


Figure 5.6: Curve fitting for the integral of absorption intensity of nile red with concentration. Linear fit gives a coefficient of determination, $R^2 = 0.993$.

concentrations, as shown in Figure 5.6. The coefficient of determination, R^2 for the linear curve fitting as displayed in Figure 5.6 gives a value of 0.993, which confirms the linearity of the concentration-dependent absorption of all the concentration investigated.

Figure 5.7 shows the emission spectra of nile red in cyclopentane at different concentrations of 0.5, 1.2, 2, 5, 9 and 18 mg/L. The sample was excited at a wavelength of 532 nm and at a temperature of 273 K. Similarly, the results are normalised to the maximum emission intensity at a concentration of 18 mg/L. At all the concentrations investigated, the fluorophore emits between 500 to 700 nm. Comparing Figures 5.5 and 5.7, there is a small overlap at the tail end of the absorption spectra with the emission spectra (between 500 to 540 nm). Based on the Beer-Lambert Law, the amount of light absorbed after travelling through an optical path length, L in a medium containing fluorescent dye will result in a reduction of the fluorescence intensity depending on the reabsorption cross-section, $\sigma_{\text{reabs}}(\lambda)$ and the number of non-excited (ground state) dye molecules per cm^3, $N_{\text{dye}}(L)$ can be written in the following relation:

$$I(\lambda, L) = I_{\text{o}} exp\left[-\int_0^L \sigma_{\text{reabs}}(\lambda) N_{\text{dye}}(L')dL'\right] \tag{5.1}$$

where I_{o} is the initial intensity prior to reabsorption occuring i.e. at $L = 0$.

The number of non-excited dye molecules per cm^3 can also be expressed as the concentration of dye. Therefore, the effect of reabsorption can be minimised by maintaining a low concentration of dye. Figure 5.8 shows the dependence of fluorescence emission to dye concentration, which is represented by the integral of emission intensities throughout the wavelength investigated. It appears that the dependence of emission intensity on the dye concentration is linear up to a concentration of 5 mg/L. A linear curve-fitting for the first four points gives a coefficient of determination, $R^2 = 0.996$. As the concentration is increased beyond 5 mg/L, the dependence of fluorescence emission on dye concentration deviate away from linearity. This is an indication that there is significant absorption of emitted fluorescence along the optical path, which leads to the decrease in fluorescence intensity for concentration higher than 5 mg/L. Henceforth, only the results of nile red at concentrations of 0.5, 1.2 and 2 mg/L will be discussed.

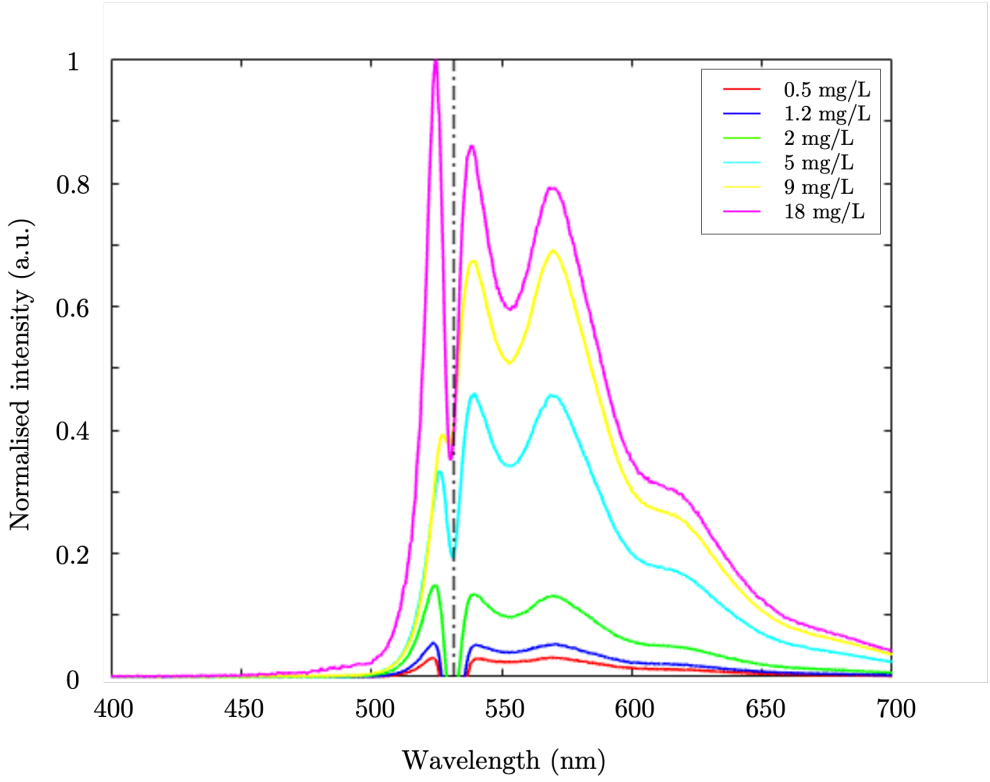


Figure 5.7: Emission spectra of nile red dissolved in cyclopentane at various concentrations (0.5, 1.2, 2, 5, 9 and 18 mg/L) at a temperature of 273 K and normalised to the maximum intensity of Nile Red emission at a concentration of 18 mg/L.

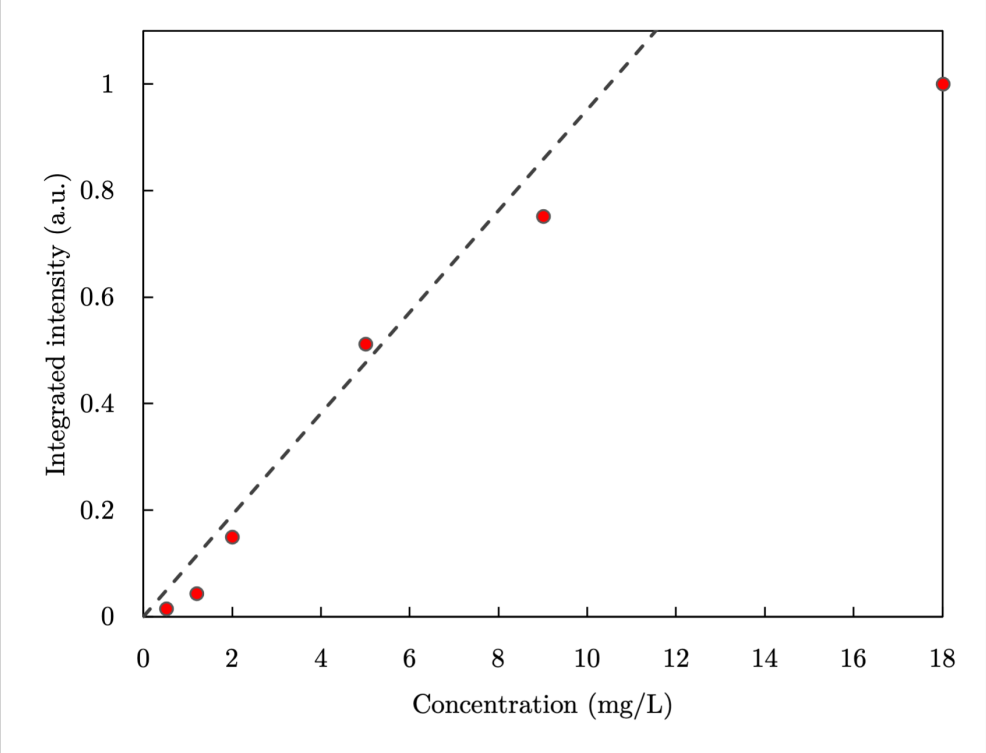


Figure 5.8: Curve fitting for the integral of emission intensity of nile red with concentration. Linear fit of the first four points gives a coefficient of determination, $R^2 = 0.9694$.

5.1.2 Temperature dependence of nile red in cyclopentane

Nile red in liquid cyclopentane displays a gradual increase in emission intensity with decreasing temperature in the investigated temperature range between 263 to 283 K. The spectra for different concentration of nile red (0.5, 1.2 and 2 mg/L) have the same trend and shape where emission is detected between 532 to 700 nm. The only difference observed between the spectra of different concentration is on the intensity of emission. An example of the spectra (1.2 mg/L) is shown in Figure 5.9. The dependence of fluorescence emission on temperature may originate from the variation in quantum yield and absorption cross section with temperature. Since excitation at 532 nm is at the tail-end of the absorption spectrum, only the region between 540 to 570 nm is of interest. From Figure 5.10, it is observed that the absorption cross section between 540 to 700 nm is almost independent of temperature. Therefore the sensitivity of nile red in cyclopentane as shown in Figure 5.9 is due to changes in quantum yield as a function of temperature. According to Chaze et al. [25], the temperature sensitivity of a fluorophore can be quantified through the relative change in the fluorescence intensity, F through the introduction of a sensitivity coefficient, s (Equation 2.19). Assuming that s is not dependent on temperature, Equation 2.19 can then be integrated to obtain Equation 2.20 where T_{o} is an arbitrary temperature. The temperature sensitivity can be estimated through the gradient of the plot of $ln\left(\frac{F(T)}{F(T_o}\right)$ as shown in Figure 5.11. Fitting a linear line onto the experimental measurements for concentration of 1.2 mg/L ($R^2 = 0.991$) evaluated at a wavelength of 570 nm reveals that the temperature sensitivity is ~ 2.63 %/K.

Temperature sensitivity of fluorophore can also be wavelength-dependent. The sensitivity coefficient, s was calculated for each wavelength between 540 to 700 nm using Equation 2.20 by taking $T_{\mathrm{o}} = 283$ K and $T = 263$ K. Figure 5.12 shows the variation in temperature sensitivity with wavelength from 540 to 700 nm. As planar laser induced fluorescence thermometry is typically applied by taking fluorescence signals from a range of wavelength or spectral band by the use of optical filters, the temperature sensitivity of nile red in cyclopentane for planar laser induced fluorescence can be estimated as the mean sensitivity in the spectral band.

Ideally, a two-colour PLIF thermometry approach is preferred for the measurement of temperature

in cyclopentane due its advantage over a one-colour PLIF approach. Limitation in the availability of non-polar fluorophore has rendered it difficult to apply the two-colour/two-dye technique. Therefore, an assessment is made to check the potential of using nile red in a two-colour/one-dye technique. The approach, first introduced by Lavieille et al. [126] exploits the wavelength-dependent temperature sensitivity whereby fluorescence ratio is taken at two spectral bands with strong sensitivity difference. However, this is not observed in Figure 5.12, where variation in temperature sensitivity over the spectrum fluctuates around the average sensitivity of about 2.53%/K instead of having a distinct and stable difference. Hence, nile red is unsuitable for two-colour PLIF thermometry in cyclopentane, unless a suitable second dye is found, which can be explored in future work. As such, the fluorophore is applied in this study using the one-colour PLIF.

5.2 Fluorescent dye in water

PLIF thermometry in water or aqueous solution [113, 129, 128, 196] is well researched compared to cyclopentane. There are different dye combinations available with reportedly high temperature sensitivity. Sutton et al. [113] reported a sensitivity as high as 7 %/K for sulforhodamine B and fluorescein 27 for a temperature range between 293 to 343 K. For cold application, Volkov and Strizhak [110] obtained a temperature sensitivity of 1.5 to 2 %/K using Rhodamine B (273 to 283 K) while Stiti et al. [47] achieved a sensitivity of 2.56 %/K for a dye mixture of sulforhodamine B and rhodamine 110 (256 to 278 K). In this study, the application of the promising combination of sulforhodamine B and fluorescein 27 from the work of Sutton et al. [113] is extended for a temperature range between 263 to 283 K.

5.2.1 Concentration dependence of sulforhodamine B and fluorescein 27 in water

As discussed earlier in Section 5.1.1, reabsorption is a known issue in two-colour PLIF thermometry. If more than one fluorescent dye is used, the possibility of overlap between the absorption and emission spectra is increased. This effect can be minimised by using low dye concentration.

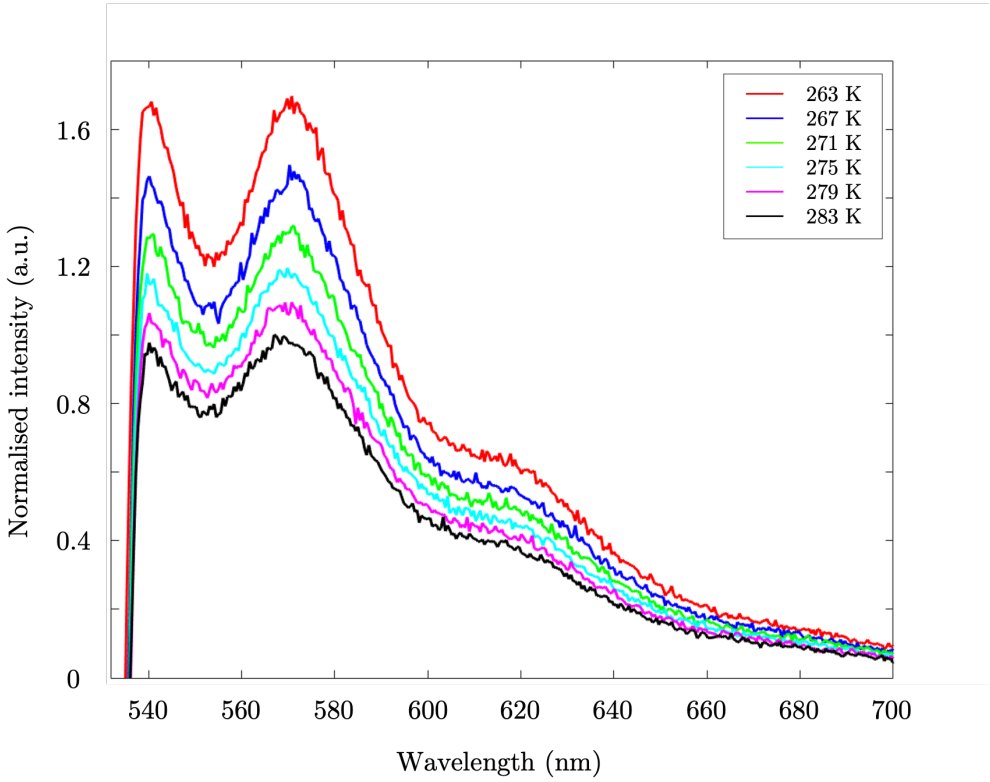


Figure 5.9: Example of the dependence of emission spectra of nile red dissolved in cyclopentane (1.2 mg/L) on temperature.

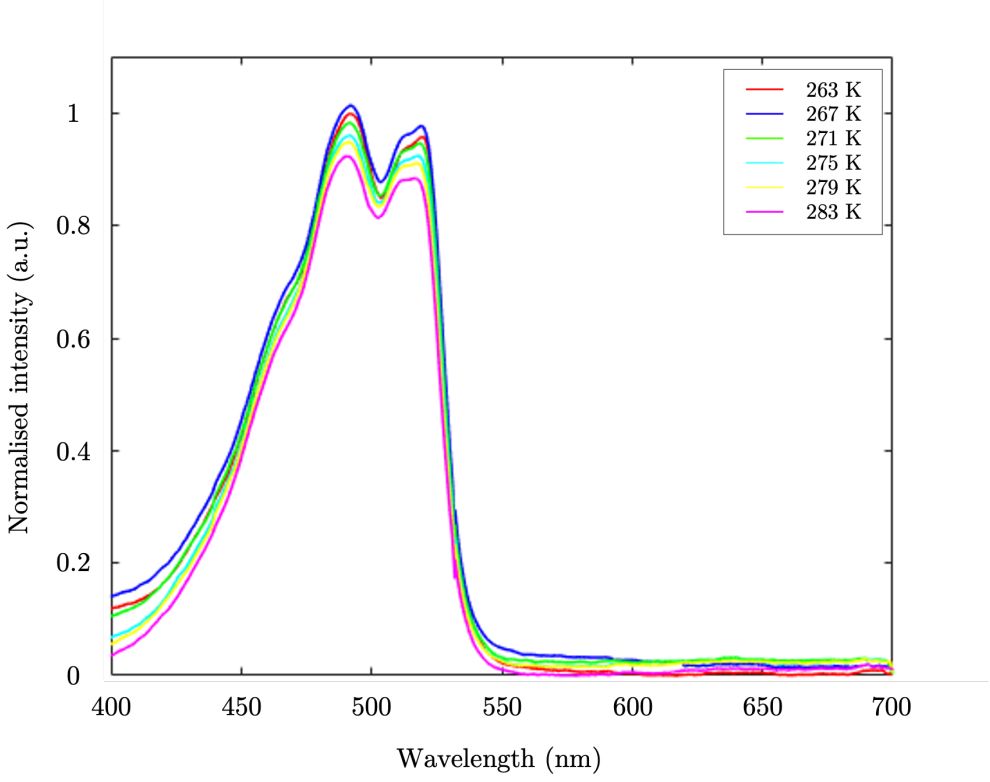


Figure 5.10: Absorption spectra of nile red dissolved in cyclopentane (1.2 mg/L) at varying temperature from 263 to 283 K.

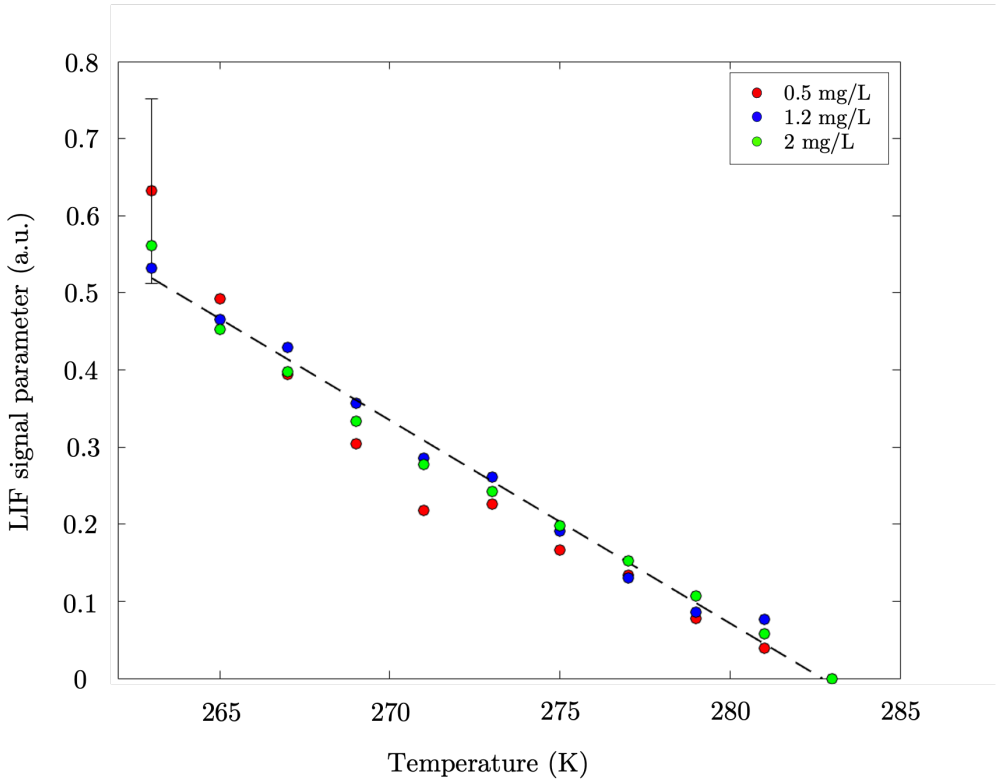


Figure 5.11: LIF signal parameter, R as a function of temperature. The gradient of the fitted linear curve represents the temperature sensitivity, s for each concentration. The error bar indicates the uncertainty of the measurements.

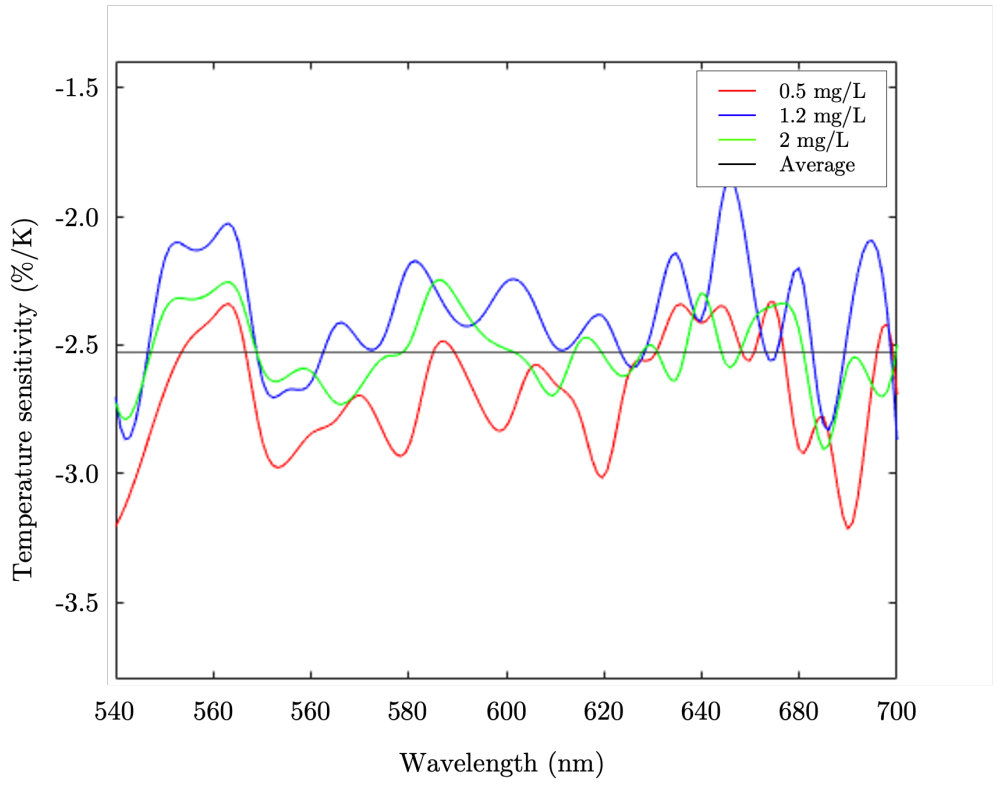


Figure 5.12: Temperature sensitivity of the emission of nile red in cyclopentane (in %/K) at 0.5, 1.2 and 2 mg/L.

Chaze et al. [25] suggested that the concentration of dye should be in the order of 10^{-6} mol/L. An exception is made for fluorescein 27 whereby its concentration can be increased up to 10^{-4} mol/L due to the small absorption cross section at 532 nm. The higher concentration needed for fluorescein 27 is necessary in order to obtain sufficient fluorescent signal from the fluorophore. On this basis, the concentration of sulforhodamine B in the dye mixture is kept at 1.1 mg/L (1.9×10^{-6} mol/L) while varying the concentration of fluorescein 27 at 2.2, 9.1 and 19.1 mg/L (5.5×10^{-6}, 4×10^{-6} and 4.7×10^{-6} mol/L respectively) to optimise the concentration of the dye mixture. A summary of the concentration of the dye mixtures is as listed in Table 5.1.

Table 5.1: Concentration of fluorescein 27 and sulforhodamine B in each dye mixture investigated.

Mixture	fluorescein 27 (mg/L)	sulforhodamine B (mg/L)
1	2.2	1.1
2	9.1	1.1
3	19.1	1.1

Figure 5.13 shows the absorption spectra for different mixture concentrations normalised to the maximum absorption intensity for each mixture. There is no shift in the peak observed for all three solutions. The first peak at 502 nm is from the contribution of fluorescein 27 while the second peak at 566 nm is from the absorption of sulforhodamine B. However, with increasing concentration of fluorescein 27, the ratio between the peaks become larger which suggests that the absorption of fluorescein 27 becomes more dominant. Consequently, the emission of fluorescein 27 (first peak at 540 nm) turns stronger with increasing concentration ratio between the two fluorescent dyes as shown in Figure 5.14 (evaluated at 273 K).

The emission spectra shows two distinct peaks at 540 and around 580 nm. For Mixture 1, the first peak (fluorescein 27) is much lower compared to the second peak (sulforhodamine B). This can be an issue for two-colour PLIF and will be discussed further in Section 5.2.2. It is also important to note that the second peak of the emission spectra for the mixture with the highest concentration of fluorescein 27 (Mixture 3) is slightly blue-shifted to 579 nm as compared to the other two dye solutions where the peak is at 581 nm. This is attributed to the reabsorption

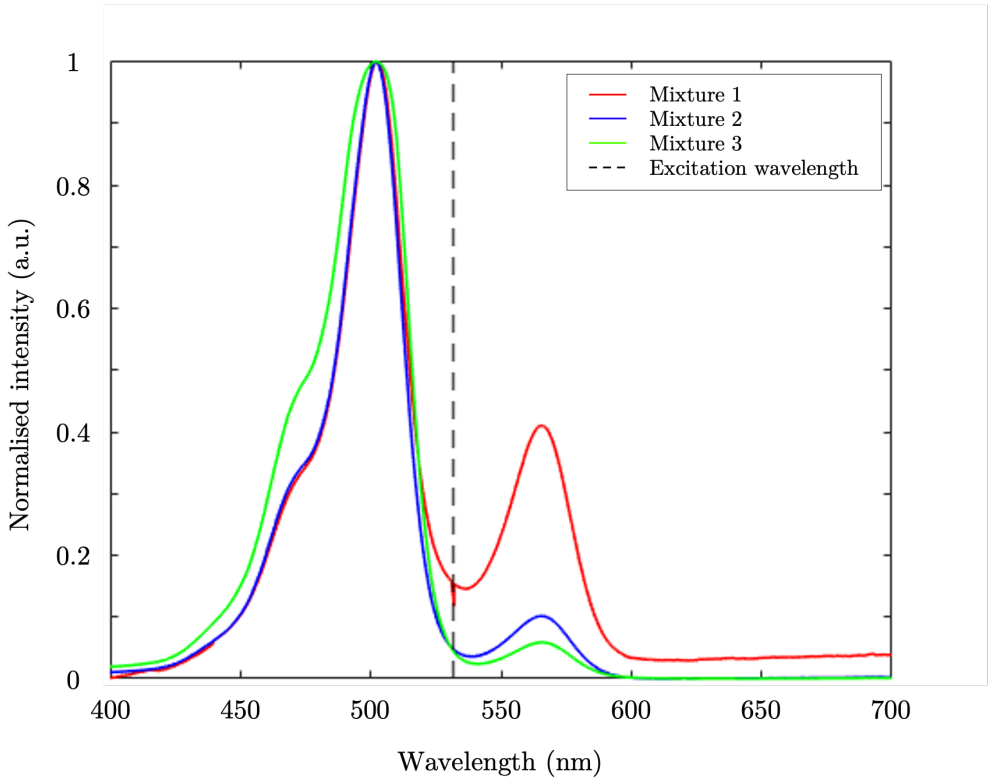


Figure 5.13: Normalised absorption spectra of fluorescein 27 and sulforhodamine B mixtures at varying concentration evaluated at a temperature of 273 K. The concentration of sulforhodamine B and fluorescein 17 in each mixture are as per Table 5.1.

of the emission of fluorescein 27 at wavelengths greater than the excitation wavelength (532 nm) by its own self along the optical path. Thus the second peak (for the Mixture 3) is not purely the emission of sulforhodamine B but also consist of the contribution from fluorescein 27 which causes the peak to move towards shorter wavelength.

5.2.2 Temperature dependence of sulforhodamine B and fluorescein 27 in water

The temperature-dependent emission spectra of sulforhodamine B and fluorescein 27 mixtures are shown in Figure 5.15 (Mixture 1), Figure 5.16 (Mixture 2) and Figure 5.17 (Mixture 3) for temperatures between 263 to 283 K. As mentioned in Section 5.2.1, there are two distinct peaks at 540 and around 580 nm that are attributed of the two dyes used in the mixture. An increase in temperature leads to an increase in emission intensity of the first peak at 540 nm i.e. positive dependence of fluorescence intensity on temperature ($dI/dT > 0$). This appears to be

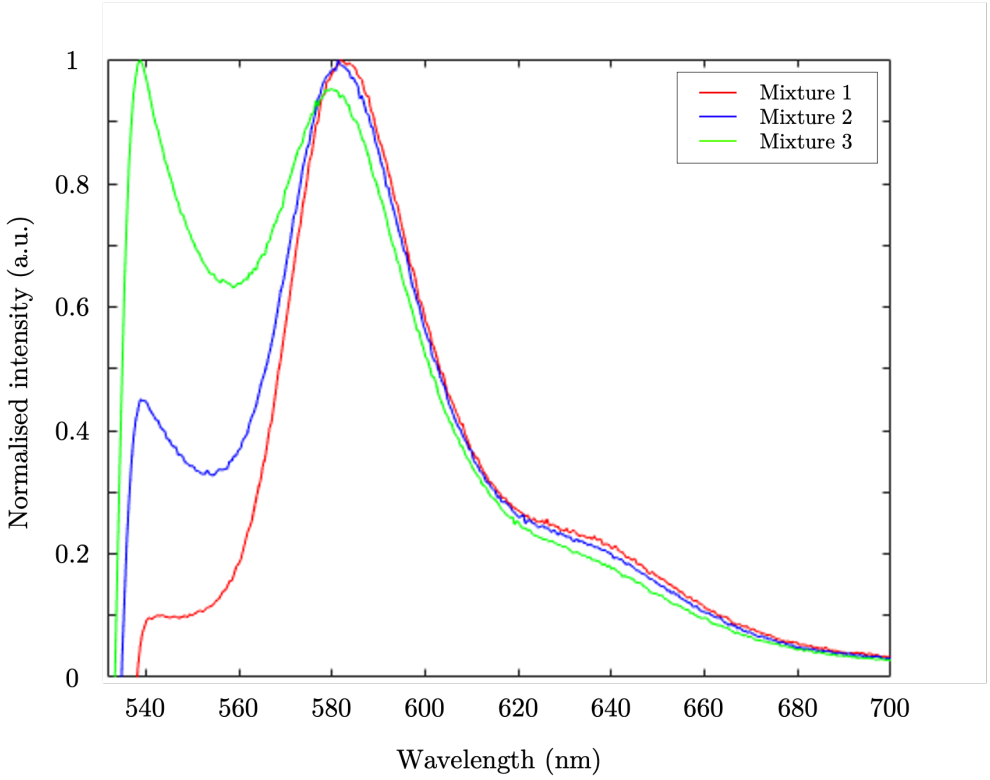


Figure 5.14: Normalised emission spectra of fluorescein 27 and sulforhodamine B mixtures at varying concentration evaluated at a temperature of 273 K. The concentration of sulforhodamine B and fluorescein 17 in each mixture are as per Table 5.1.

a characteristic of fluorescein 27 regardless if it is applied for low temperature measurements (in this case from 263 to 283 K), or for warmer temperature in the range of 290 to 350 K as in the case of Sutton et al. [113] and Estrada-Pérez et al. [202]. On the other hand, sulforhodamine B (the second peak at around 580 nm) has the opposite dependence on temperature where its emission intensity decreases with increasing temperature i.e. $(dI/dT < 0)$). This observation is consistent with the study by Stiti et al. [47] at similar temperature range (256 to 278 K) and also at warmer temperature between 288 to 350 K [113, 129].

The dominance of the fluorescence emission of sulforhodamine B over fluorescein 27 as clearly seen in Figure 5.15 is unfavourable because the large difference in fluorescence intensity between the two dyes could potentially cause difficulties in the actual optical setup. For example, in balancing the laser power for excitation such that the emission from the dominant dye will not saturate the camera sensor and at the same time, the fluorescence intensity from the weaker dye has good signal-to-noise ratio. Since the dependence of the fluorescence intensity of two dyes on temperature are in the opposite direction, it is also unfavourable for the signal of fluorescein 27 to dominate over sulforhodamine B as it is likely to reduce the temperature sensitivity of the mixture (Figure 5.17). The emission spectra of Mixture 2 (Figure 5.16) shows a better spread with respect to temperature.

The application of two-colour PLIF thermometry is based on the change in fluorescence intensity ratio of the two fluorophore with temperature. This is realised by isolating fluorescence signal at appropriate spectral bands using optical filters. The fluorescence signal from the two spectral bands are then used to obtain the fluorescence ratio, R_{12}

$$R_{12} = \frac{F_1}{F_2} \tag{5.2}$$

where subscripts 1 and 2 indicate spectral band 1 and band 2. The sensitivity coefficient,s for two-colour PLIF thermometry can then be expressed by normalising T_{12} to a reference fluorescence ratio, $T_{12\mathrm{o}}$ at a known temperature T_{o}

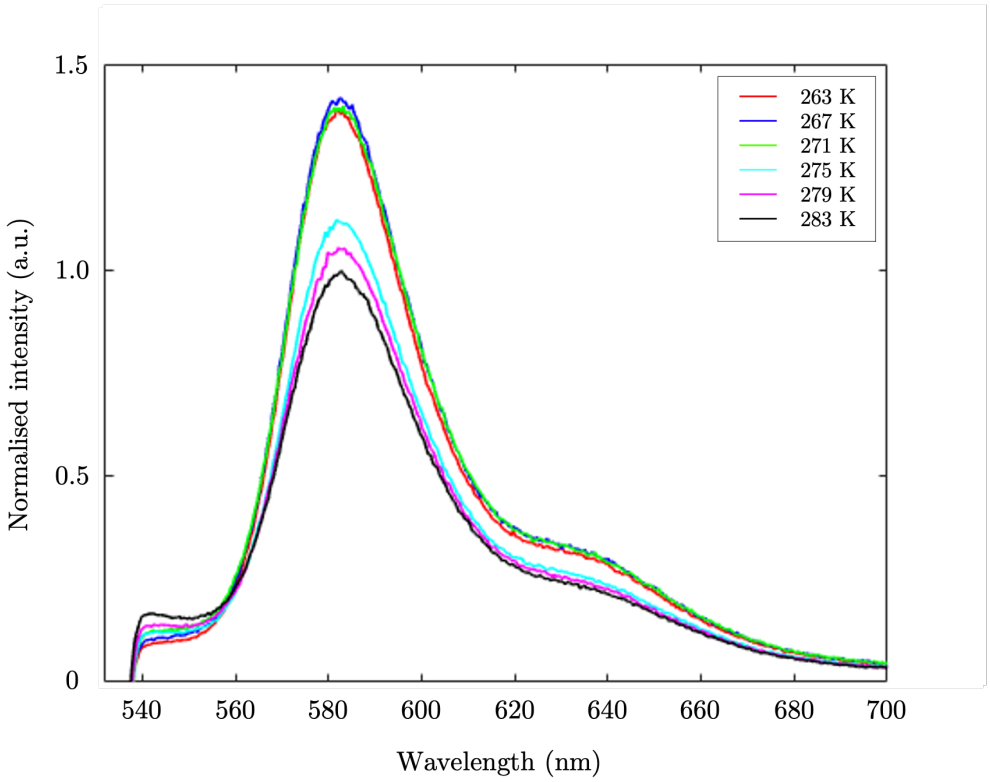


Figure 5.15: Normalised emission spectra of Mixture 1 (fluorescein 27 (2.2 mg/L) and sulforhodamine B (1.1 mg/L)) at varying temperature from 263 to 283 K.

$$s = \frac{ln\left(\frac{R_{12}}{R_{12o}}\right)}{T - T_o} \tag{5.3}$$

Separation of the spectral bands also depend on the commercial availability of optical filters. Thus, estimation of temperature sensitivity based on emission spectra is evaluated based on the useful range of the optical filter. For the case of fluorescein 27 and sulforhodamine B mixture, the spectral bands are selected based on a combination of a shortpass filter (Edmund Optics, cut-on wavelength 540 nm) and a notch filter (Thorlabs, centre wavelength 533 nm) for band 1 and a longpass filter (Midwest Optical Systems, cut-on wavelength 550 nm) for band 2. The fluorescence signal obtained from the spectrometer is then integrated between 535 to 540 nm for band 1 and 550 to 700 nm for band 2 in accordance with the optical filters. The intensities I_1 and I_2 at each temperature point are used to calculate the fluorescence ratio, R_{12} (Equation 5.2). Normalisation of the fluorescence ratio for each temperature point between 263 to 283 K is performed by taking a reference temperature at 283 K.

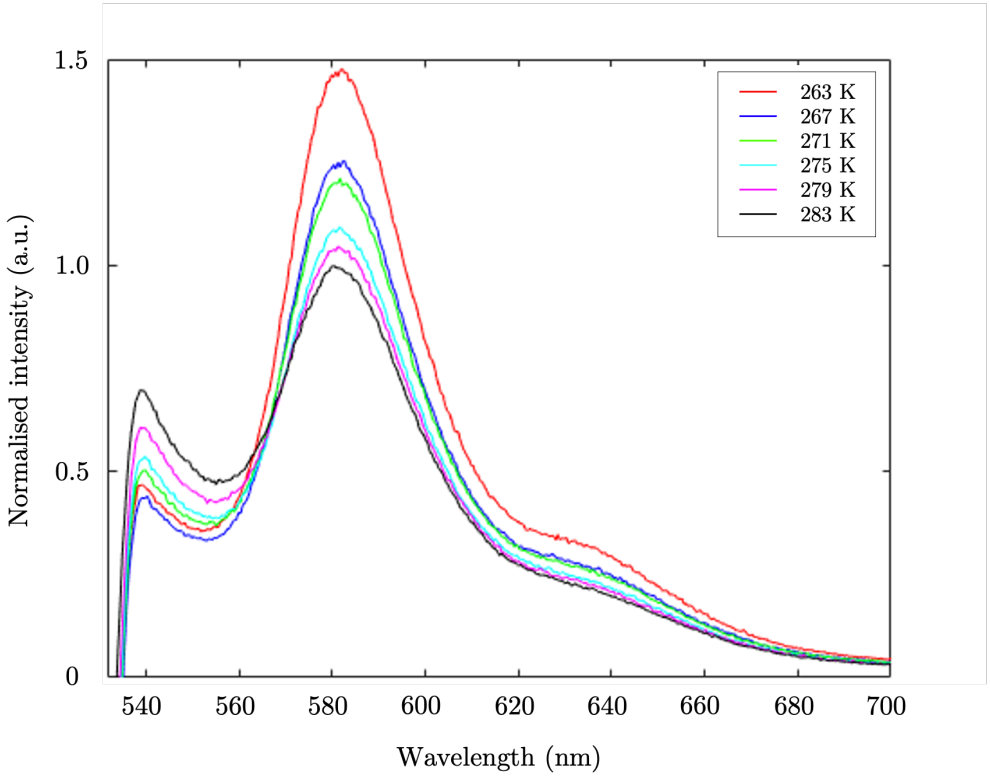


Figure 5.16: Normalised emission spectra of Mixture 2 (fluorescein 27 (9.1 mg/L) and sulforhodamine B (1.1 mg/L)) at varying temperature from 263 to 283 K.

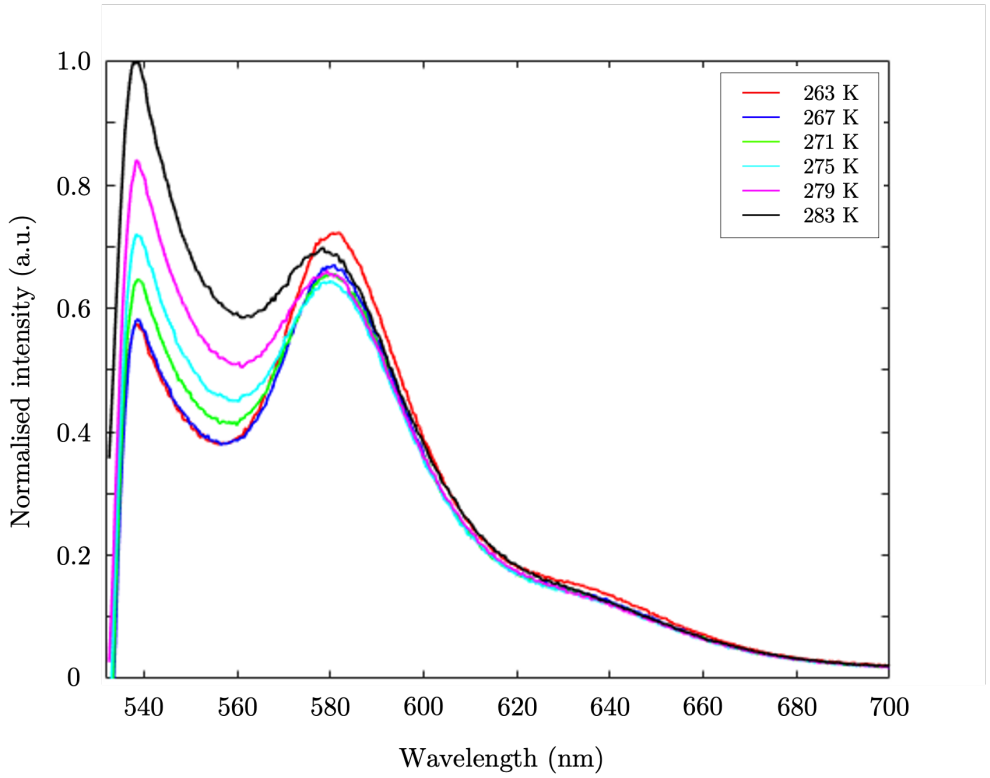


Figure 5.17: Normalised emission spectra of Mixture 3 (fluorescein 27 (19.1 mg/L) and sulforhodamine B (1.1 mg/L)) at varying temperature from 263 to 283 K.

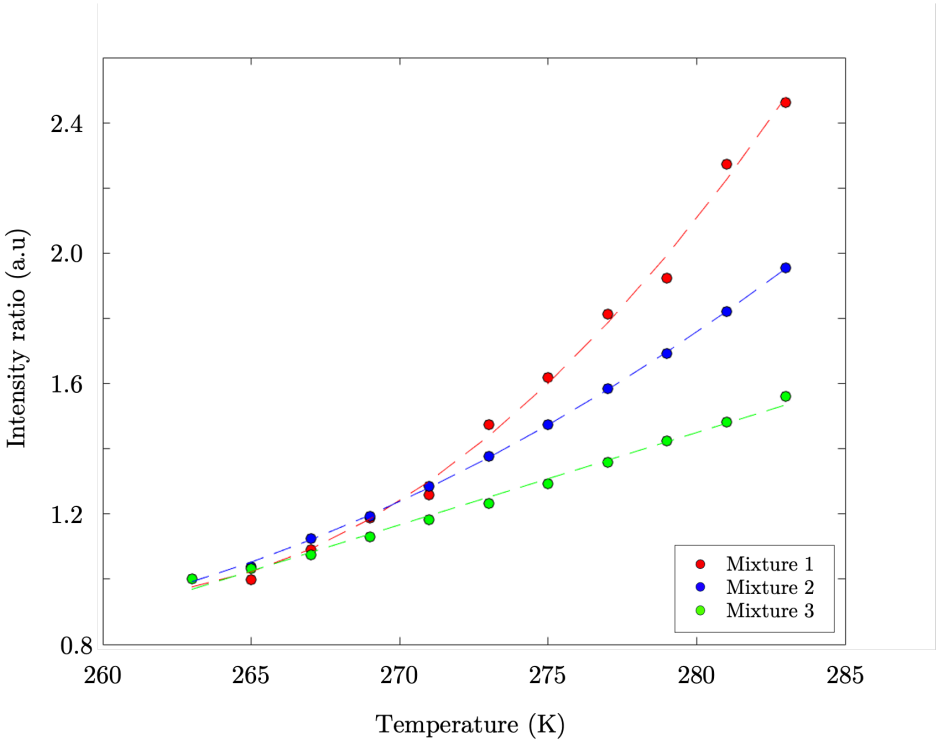


Figure 5.18: Normalised fluorescence intensity ratio as a function of temperature with curve fitting using second order polynomial for the three mixtures.

It is observed that the dependence of the fluorescence ratio on temperature is not linear, as shown in Figure 5.18. The experimental measurements were fitted with second-order polynomial curves in which the coefficient of determination, R^2 are 0.9952, 0.9997 and 0.9995 for Mixture 1, 2 and 3 respectively. Evaluating the temperature sensitivity using Equation 5.3 reveals that the temperature sensitivity increases with decreasing concentration of Fluorescein 27 (Figure 5.19). The average sensitivities of the dye mixtures are 4.82 (Mixture 1), 3.42 (Mixture 2) and 2.26 %/K (Mixture 3), which further confirms the postulate made earlier on fluorescein 27 signal dominating over sulforhodamine B with increasing concentration of fluorescein 27. The fluorescein 27 and sulforhodamine B mixture shows improved temperature sensitivity, particularly for Mixture 1 and 2 in this study, compared to the mixture of rhodamine 110 and sulforhodmaine B (2.56 %/K) as reported by Stiti et al. [47] at similar temperature range (256 to 278 K). The most suitable concentration of dye mixture for two-colour PLIF in hydrate experiment among the three solutions investigated is 9.1 mg/L fluorescein 27 and 1.1 mg/L sulforhodamine B (Mixture 2).

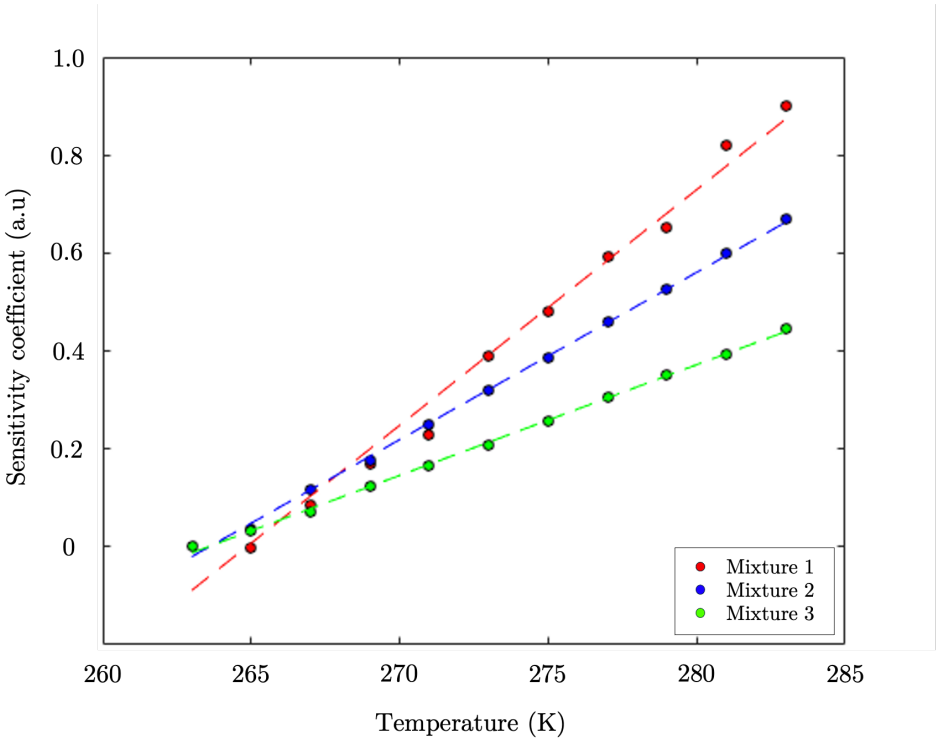


Figure 5.19: Sensitivity coefficient of the dye mixtures investigated between the temperature range of 263 to 283 K. The temperature sensitivities are obtained from the gradients of the linear fitted curves and are found to be 4.82, 3.42 and 2.26 %/K for Mixtures 1, 2 and 3, respectively.

5.3 Effect of additive on hydrate phenomenon

The optical techniques used in this study, PLIF and PIV, require the addition of fluorescent dyes and tracer particles. Other than factors such as temperature sensitivity and signal-to-noise ratio to determine a suitable concentration for optical measurements as discussed in Sections 5.1 and 5.2, the concentration of the fluorophore should also not influence the phenomenon investigated. The same applies to the particles used in PIV. Since hydrate formation is an interfacial phenomenon, the effect of additive is investigated by measuring the contact angle of the solutions used in the optical measurements as listed in Table 5.2. Six different samples were tested and the results were compared against a control (Sample 1) which was deionised water and liquid cyclopentane without any additive. The details of the measurements are as described in Section 3.4. The results are averaged over at least five measurements and the uncertainty is taken as one standard deviation.

Figure 5.20 shows that measurements of contact angle with the addition of fluorescent dyes and tracer particles. The contact angle of all the samples fall within the measurement uncertainty of the control as represented by the dashed lines. To further confirm that the additives for optical measurements are not intrusive to the hydrate phenomenon, the lateral growth of hydrate were measured using backlight imaging. The lateral growth rates were measured by doping both water and cyclopentane to show the maximum effect of the additives. The results are shown in Figure 5.21 where it is revealed that additives at the concentration listed in Table 5.2 have minimal influence on the hydrate growth. Therefore, the optical measurements are non-intrusive for hydrate experiments and are expected to be good representations of the hydrate phenomenon.

Table 5.2: Concentration of additive for optical measurements.

Sample	Phase with additive	Optical technique	Additive	Concentration
1	-	-	No additive	-
2	Cyclopentane	PLIF	Nile red	1.2 mg/L
3	Water	PLIF	Fluorescein 27 + Sulforhodamine B	9.1 mg/L + 1.1 mg/L
4	Cyclopentane	PIV	Conductosphere	400 ppm
5	Water	PIV	PS Fluored	80 ppm
6	Water	PIV	PS Fluored	40 ppm

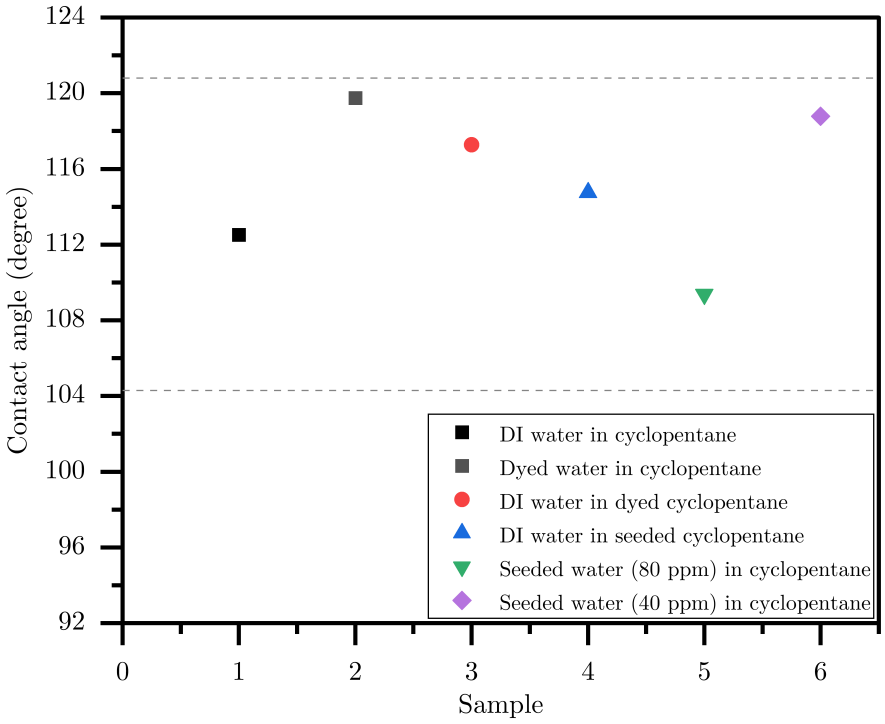


Figure 5.20: Effect of additive on the contact angle between a water drop and liquid cyclopentane.

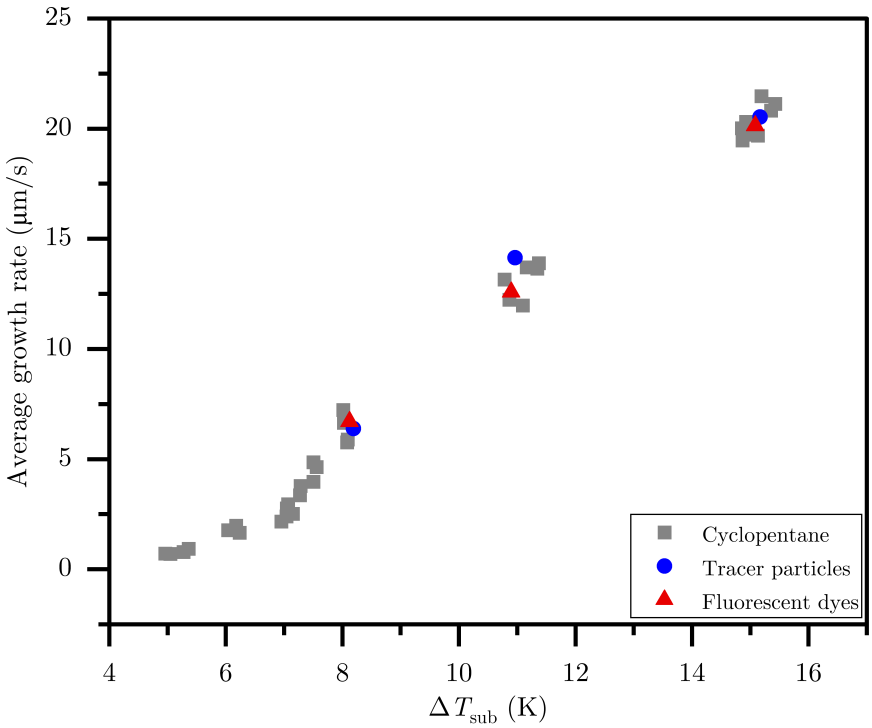


Figure 5.21: Effect of additive on the lateral growth rate of hydrate.

5.4 Challenges

While performing the measurements of two-colour PLIF thermometry in the drop, it was discovered that there is a small band of about 0.4 mm in thickness close to the drop interface where fluorescence signal is much lower. The data in the darker band is irretrievable even by taking ratiometric approach. The loss of information is due to the curvature of the drop and the thickness of the laser sheet. At the interface, the curvature of the drop causes the thickness of the plane of liquid that is excited by the laser sheet to reduce. Thus the contribution of fluorescence close to the interface that is captured by the camera sensor is lower compared to the area in the plane where the thickness of liquid excited is the same as the thickness of the laser sheet.

The measurement of laser sheet thickness was conducted using a sharp razor blade on a microstage. Initially the blade was positioned to completely block the laser from reaching a power meter (Gentec-EO Miro Altitude) placed in the same axis as the laser head. The blade was then gradually moved along the traverse direction, perpendicular to the laser sheet, which

resulted in a gradual increase in power recorded by the power meter up until a point when it reached a maximum. The point with a maximum power value corresponds to the position where the blade was no longer blocking the laser sheet. The distribution of laser power along the distance travelled by the blade is shown in Figure 5.22. The thickness of the laser sheet was estimated by taking the gradient of the laser power and taking the full width half maximum (FWHM) of the laser distribution (Figure 5.23). The laser sheet thickness is estimated to be 0.4 mm. In future work, the dark band could potentially be minimised by further reducing the thickness of the laser sheet, for example by modifying the laser beam through the addition of a cylindrical lens.

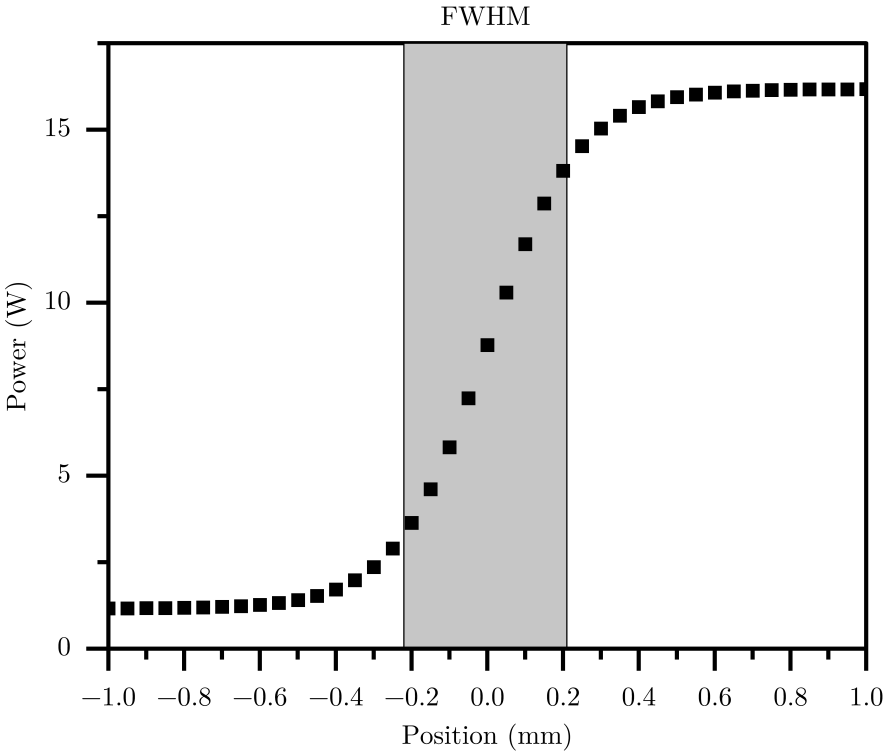


Figure 5.22: Laser power distribution for estimation of laser sheet thickness measured using a power meter as a razor blade moved along the traverse direction.

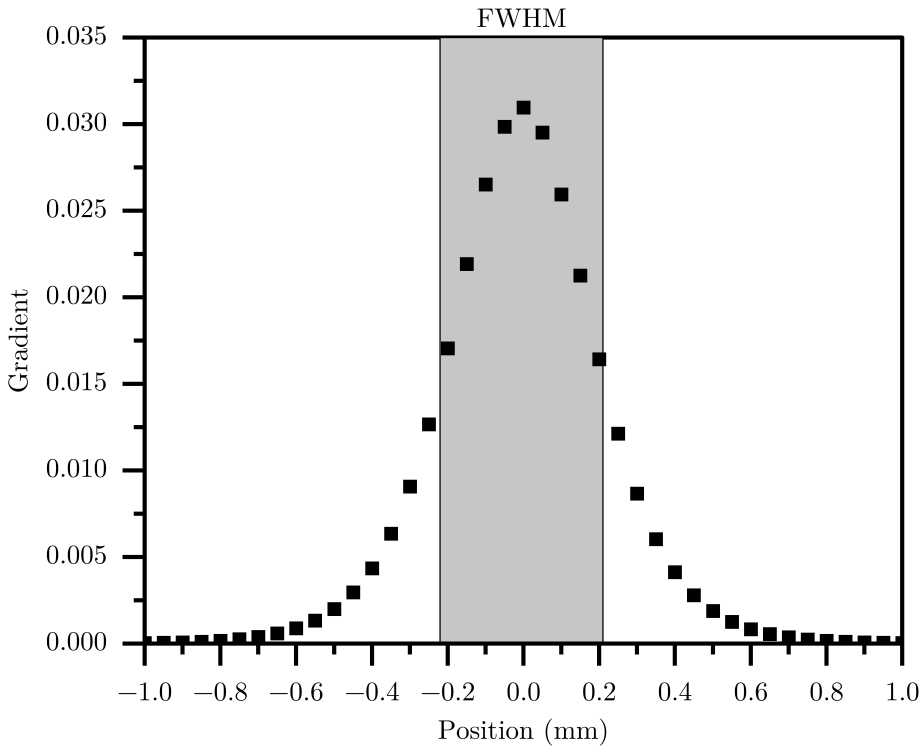


Figure 5.23: The gradient of the power measured. The laser sheet thickness is estimated based on half of the maximum gradient (FWHM).

A major issue encountered in the two-colour PLIF thermometry measurement is the presence of streaks in the images of some of the experimental runs as shown in Figure 5.24. The streaks could not be removed by simply taking a ratio of the fluorescence signals. These areas are excluded from temperature analysis. There are several possibilities that may have produced these streaks, for example, condensation at the bottom acrylic cover of the hydrate cell or glass substrate and dust settling on the laser head. The obstructions in the optical path causes the incident light to have different intensity in these regions which consequently changes the fluorescence ratio and is different from the temperature calibration curve. While several steps have been taken to minimise these occurrences, for example, by ensuring the space between the glass substrate and acrylic cover is dry by filling the space will silica gel and directing dry air to to the acrylic cover to minimise condensation, the streaks in some experimental run could not be removed completely. When analysing the temperature fields, the streaks appearing due to limitations in the experimental arrangement is excluded from consideration. For future work, the experiments should be performed in a dry enclosure.

Another possibility for the streaks appearing is the presence of microdroplets on the substrate. These microdroplets are remnants of thawed iced which was removed from the substrate prior to every hydrate experiments. The procedure of having thawed ice and having it removed was necessary as a method of hydrate induction [203, 204]. This requires further improvement in the experimental protocol possibly through a different method of hydrate induction, which is beyond the scope of this study.

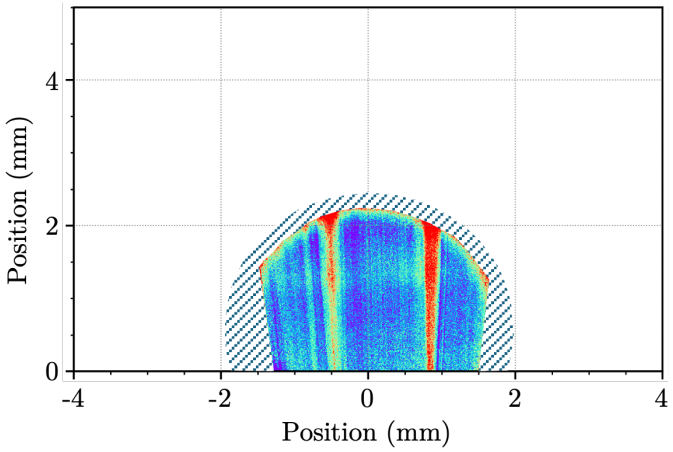


Figure 5.24: An example of streaks in two-colour PLIF images after post-processing.

As discussed in Section 3.7, each measurement technique comes with its own limitations, which has its own uncertainties. For one-colour PLIF thermometry, these limitations comes in the form of camera noise, background interference, absorption effect, pulsation in laser intensity and temperature calibration. Steps to minimise these errors have been applied through correction procedures as previously described. However, residual error may still exist. In addition, since the images were taken from two sides (top and side illumination), uncertainty could also arise from misalignment of the laser sheets with respect to each other as well as to the camera focus plane. Factors that could cause the mismatch in spatial overlapping are, for example, human error and vibrations of equipment and/or optical components. These sort of errors cannot be directly quantified and are therefore minimised as much as possible.

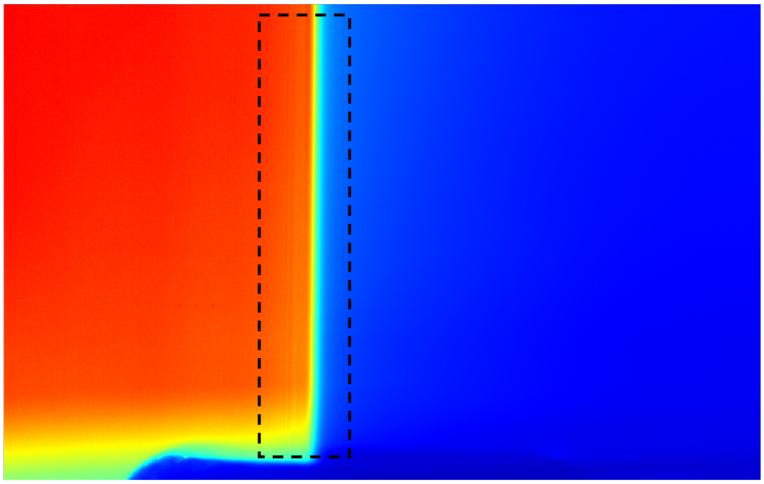


Figure 5.25: Spatial matching of laser sheet (top illumination) and camera focus plane using a razor blade to create a contrast in the image. The contrast line (boxed area) is used to fine tune the position of laser sheet and camera focus.

Spatial matching of the laser sheets and camera focus plane were achieved by placing a razor blade to purposely obstruct a portion of the laser sheet thereby only exciting a portion of liquid in the ROI. This created a contrast in the image as shown in Figures 5.25 and 5.26, which aided the tuning of the position of the laser sheets and the camera focus such that the images produced by the camera (using double frame mode) are focused on the same plane. This is verified by the clear contrast observed in the boxed area in Figures 5.25 and 5.26 showing distinct orange, yellow and green lines. A spatial mismatch between the laser sheets and camera focus plane would have resulted in blurry images where these lines would not have been clearly defined. Quantification of error for two-colour PLIF thermometry is more complex as it involves a plethora of factors that could affect measurement uncertainties e.g., the type of fluorescent dye, spectral mixing, concentration of dye mixtures, optical misalignments, thickness of laser sheet, in addition to the factors mentioned in the one-colour PLIF technique. Nonetheless, special care was taken to minimise measurement error in instantaneous temperature measurement, which is estimated to be ± 1 K. This is comparable to the measurement uncertainties reported by Stiti et al. [47] at similar temperature range. Other works reported uncertainty values in the range of ± 0.8 to 1.5 K [129, 128].

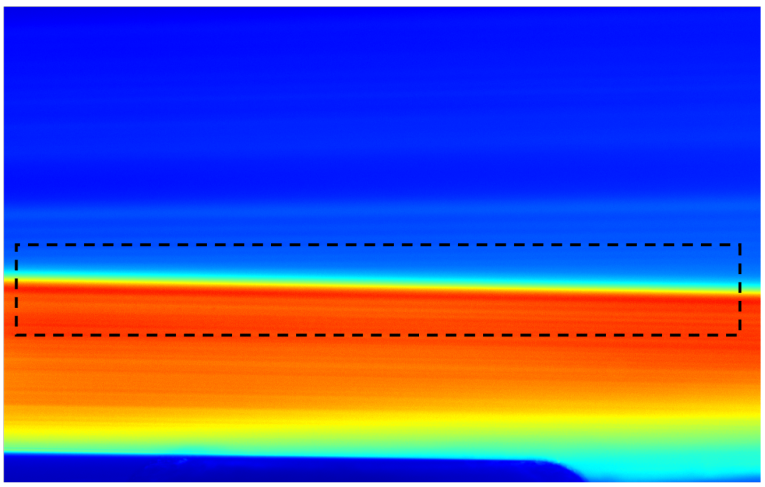


Figure 5.26: Spatial matching of laser sheet (side illumination) and camera focus plane using a razor blade to create a contrast in the image. The contrast line (boxed area) is used to fine tune the position of laser sheet and camera focus.

5.5 Summary

To the best of our knowledge, planar laser-induced fluorescence (PLIF) thermometry have not been employed in the study of clathrate hydrate. In this chapter, we presented the development of two-colour and one-colour PLIF techniques for temperature measurements in water and cyclopentane, which is the selected hydrate former. While PLIF thermometry in water has been widely researched, the use of the technique in cyclopentane or any other organic solvent is rather limited. Consequently, the selection for the appropriate temperature-sensitive dye that is soluble in cyclopentane is challenging. Since cyclohexane, the closest cyclic alkane to cyclopentane fluoresces [197], we first investigated the self-fluorescence of cyclopentane in collaboration with King Fahd University of Petroleum and Minerals. However, there was no observable emission of cyclopentane at excitations in the range of 355 to 532 nm. Our attempt to test the self-fluorescence of cyclopentane also confirms a 1970's work by Hirayama et al. [198]. An attempt was also made to utilise sulforhodamine B, a commonly available hydrophilic fluorescent dye, by first dissolving it in ethanol before adding the solution into cyclopentane. Characterisation of the mixture of sulforhodamine B, ethanol and cyclopentane was performed

using a spectrometer to obtain its absorption and emission spectra. However, the presence of significant spectral conflict between the absorption and emission spectra has rendered the mixture of sulforhodamine B, ethanol and cyclopentane unsuitable for PLIF thermometry. Moreover, the dye from the mixture was observed to transfer into water when the two liquid phases came into contact.

Subsequently, we investigated the suitability of nile red as a temperature-sensitive fluorescent dye in cyclopentane. By performing characterisation of nile red in cyclopentane with a spectrometer will prove the usability of the dye for temperature measurements using PLIF. This will also create an avenue for future experimental work with PLIF involving organic liquids. Analysis of the absorption and emission spectra of nile red in cyclopentane showed promising results with an average temperature sensitivity of 2.53 %/K, which is higher than what has been reported for other fluorophores in organic liquids such as pyrromethene 597-8C9 in kerosene [115] (0.5 %/K) and in diesel [114] (1.3 %/K). However, analysis of the spectra also showed that nile red in cyclopentane is unsuitable for two-colour/one-dye PLIF technique as there was no distinct change in temperature sensitivity observed for a range of wavelength between 540 to 700 nm. In spite of that, its potential for two-colour/two-dye PLIF thermometry is still open through the use of a second dye and can be explored in future work. Hence, application of PLIF thermometry for the study hydrate with cyclopentane as the hydrate former proceeded with the one-colour PLIF approach.

Previous two-colour PLIF thermometry studies showed that a mixture of sulforhodamine B and fluorescein 27 had the highest sensitivity at 7 %/K [113] for temperature in the range of 303 to 343 K. We further extended this temperature range to temperatures between 263 to 283 K. Characterisation of the dye mixture was performed at varying concentrations and the optimum concentration was found to be 9.1 mg/L of fluorescein 27 and 1.1 mg/L of sulforhodamine B, taking into consideration of not just the temperature sensitivity but also the linearity of the intensity ratios of the two dyes with temperature. The temperature sensitivity at the optimum concentration was found to be 3.42 %/K, which is an improvement from the mixture of rhodamine 110 and sulforhodamine B used by Stiti et al. [47] (2.56 %/K) at similar temperature range (256 to 278 K).

Chapter 6

Temperature and velocity measurements

In this chapter, results obtained by applying the laser based measurement techniques described in Chapter 3 with further details explained in Chapter 5 are presented and discussed. Hydrate is known to have a long induction time [205, 206], in addition to having stochastic nucleation process, as previously mentioned in Section 4.2. Therefore, an induction protocol was required to reduce the experimental time and computational requirement during data collection. This was achieved by introducing water drop at room temperature into cold cyclopentane to induce a thermal disturbance. According to Li et al. [142], the high temperature gradient reduces the Gibbs free energy required for nucleation and thus reduces the induction time, as compared to the case when the drop is cooled gradually with the surrounding phase. While Li et al. [142] reported that this method is effective in reducing the induction time for tetra-n-butylammonium bromide (TBAB), it was found in the cyclopentane hydrate experiments that there were instances when hydrate formation did not occur even after 30 minutes, based on visual confirmation from direct imaging. Therefore, induction using the memory effect of water was also utilised [91] by using thawed iced to provide template for hydrates and thus improves the repeatability of experiments.

Due to the drop cooling involved in the induction protocol, it is not possible to isolate the phenomenon of hydrate formation independently. The significant temperature difference between the water drop and the surrounding cyclopentane at the onset of cooling triggers natural

convection in both liquid phases. Consequently, the experiments were conducted by comparing two scenarios: in the presence and in the absence of hydrate formation. The experiments in the absence of hydrate were performed by omitting the memory effect of water to lengthen the induction time and thus the water drop was only subjected to cooling by the surrounding phase within the duration of the experiment. The experiments were carried out for three different water drop sizes with volumes of 0.05, 0.25 and 0.7 ml.

The aim of this chapter is to present the results obtained from, Particle Image Velocimetry (PIV), one-colour and two-colour Planar Laser-induced Fluorescence (PLIF) that have been developed for hydrate application, as discussed in Chapter 5. The limitations of the measurements techniques and the conjectures made due to the current limitations are also discussed.

6.1 Temperature and velocity fields

Figures 6.1 and 6.2 show example of temperature and velocity fields in the surrounding cyclopentane phase. Since the water droplet was introduced at room temperature into the cold liquid cyclopentane, for reasons explained earlier with respect to hydrate induction, there exist regions of warm and cold temperature that induces natural convection due to variations in liquid density with temperature. Comparing the thermal and velocity maps, the presence of a warm zone directly above the drop apex is due to a stagnation point where there is a confluence of flow, as shown by the flow visualisation pattern, from each side of the drop. Therefore, the density of liquid of cyclopentane is at a minimum in this region, which pushes the liquid cyclopentane upwards as a result of buoyancy effect. As the water drop is placed right at the centre of the pedestal inside the hydrate cell, the flow surrounding the drop shows a symmetrical flow pattern. Qualitatively, the velocity is seen to decrease over time as the temperature of the water drop equilibrates with the bulk temperature of the surrounding phase. The maximum time required for the drop to stabilise to the equilibrium temperature after a sudden temperature change can be estimated using the thermal relaxation time, t_{th}. Mathematically, it can be estimated using Equation 6.1.

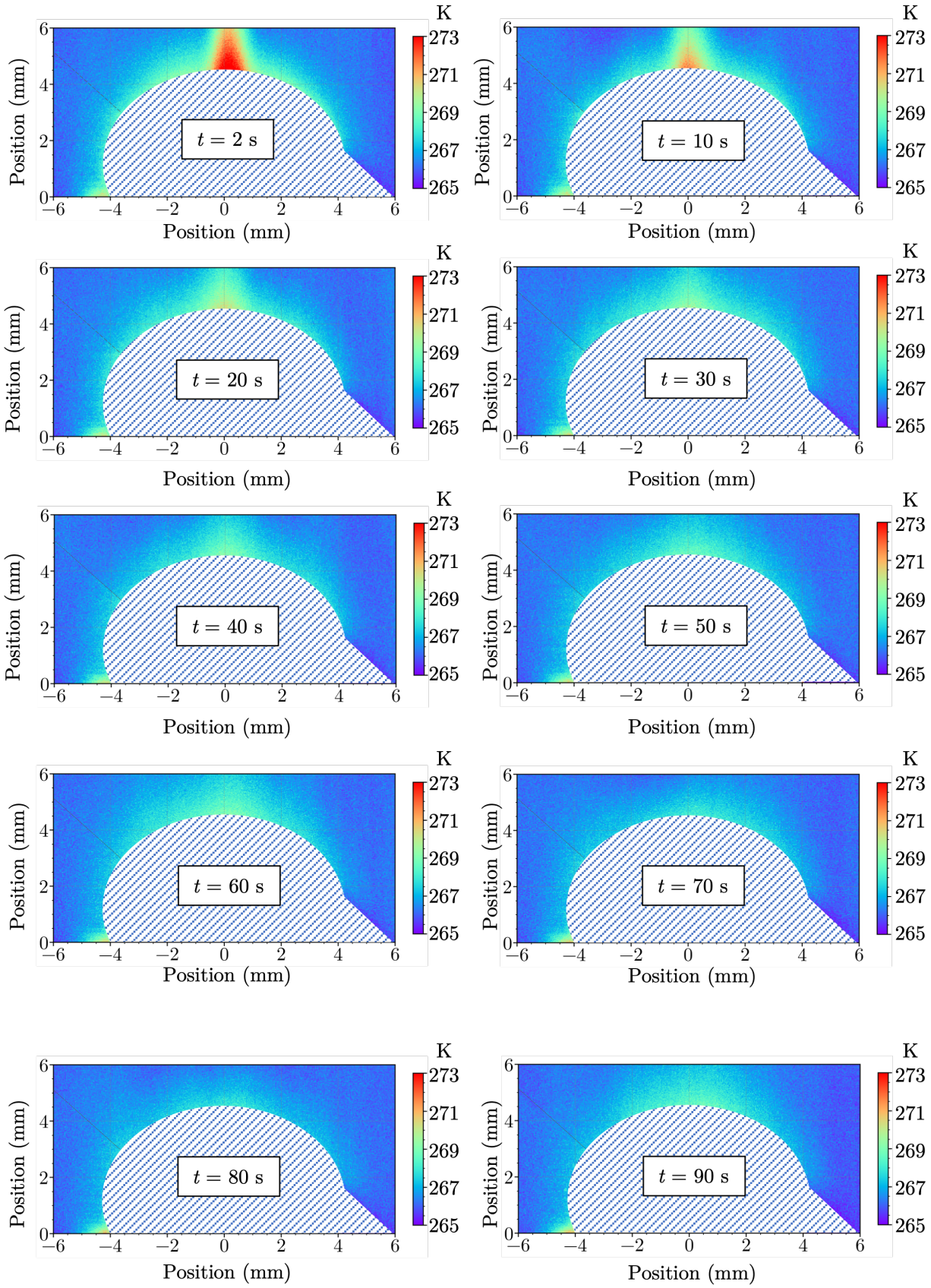


Figure 6.1: Instantaneous temperature fields from one-colour PLIF in liquid cyclopentane at a temperature of 266 K that surrounds a water drop (in the absence of hydrate formation) with a volume of 0.25 ml. The colour bar denotes temperature. The dashed line represents the stitching point of the two images obtained from top and side laser illumination and the shaded area represents the water drop and the shadowed region where temperature field was not extracted.

$$t_{\mathrm{th}} = h^2/\alpha_{\mathrm{w}} \tag{6.1}$$

where h is the height of the drop and α_{w} is the thermal diffusivity of water. The thermal relaxation time for the water drops are approximately 50, 90 and 200 seconds for volumes of 0.05, 0.25 and 0.7 ml, respectively. After this period has elapsed, the water drop is expected to equilibrate to the bulk temperature. As a result, the effect of convection is much weaker, which is evident in Figure 6.2 for a drop of volume 0.25 ml. The temperature fields shown in Figure 6.3 for a 0.25 ml water drop (in the absence of hydrate) show that the temperature is almost uniform at $t = 60$ and 70 seconds. Since hydrate formation, which is an exothermic process, and drop cooling have competing effects, ideally a shorter relaxation time is preferred in order to minimise the effect of convection. Hence, it would be more challenging to observe the effect of hydrate formation for the large drop (volume 0.7 ml) that has a longer thermal relaxation time. Therefore, analysis of the temperature and velocity measurements are focused on water drops with volumes of 0.05 and 0.25 ml.

The temperature inside the water drop and its internal flow for a water drop with a volume of 0.25 ml are shown in Figures 6.3 and 6.4 at a bulk cyclopentane temperature of 266 K. Initially, water is observed to flow downwards along the centreline forming two vortices. After ten seconds, the direction of the internal flow undergoes a reversal. This is due to the special property of water, namely its density that has a maximum at 277 K. When a water drop at room temperature is introduced in cold liquid cyclopentane, the core of the drop is warmer than the edges or the region that is in contact with the interface. If the temperature at the core is greater than 277 K, the liquid in the core that is less dense will rise at the centreline. As the core temperature cools to 277 K, the liquid at the core then becomes denser than the edges and will sink which then causes a change in the direction of the internal flow. This is shown schematically in Figure 6.5. The same flow pattern is observed when the drop volume

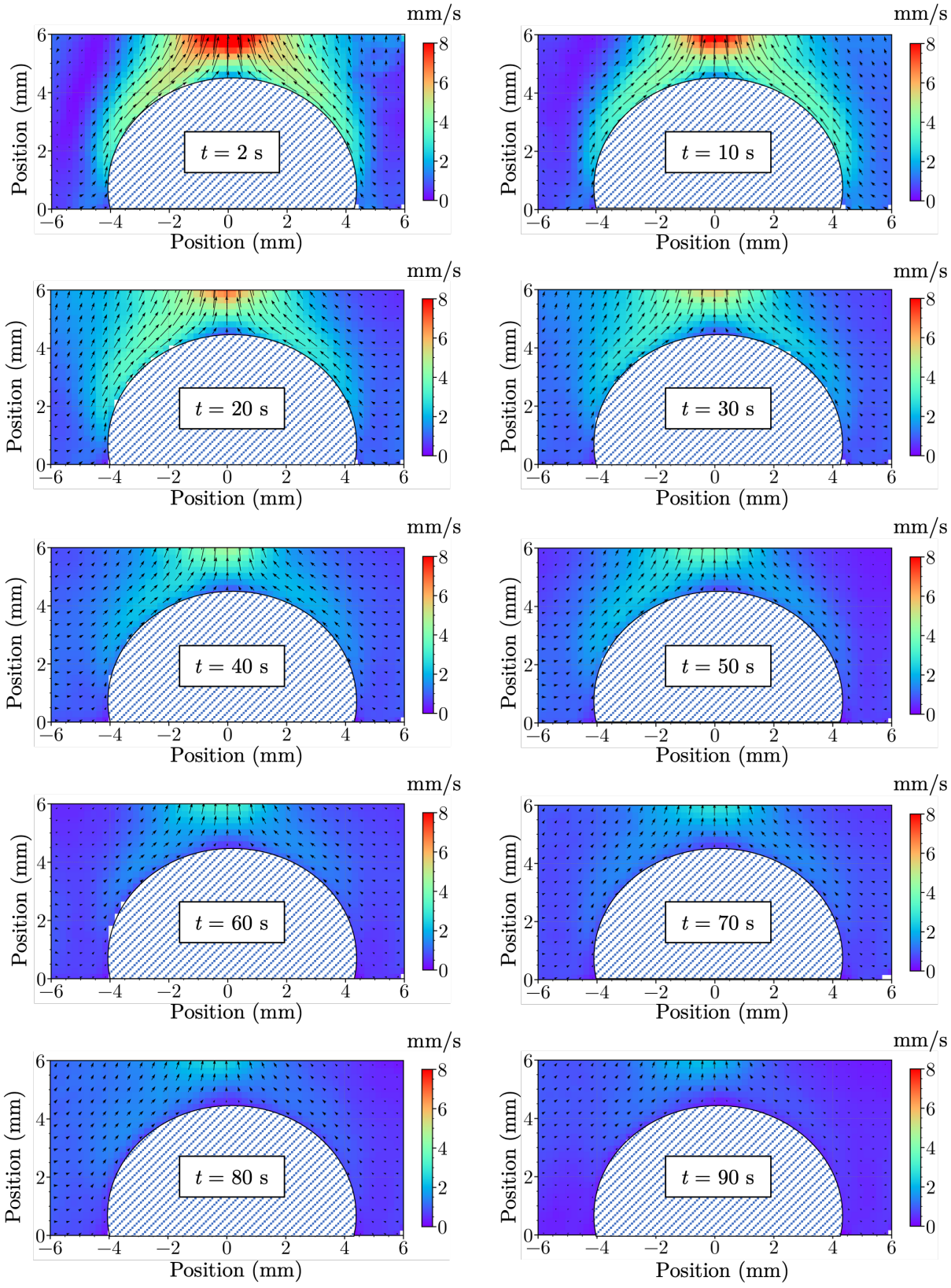


Figure 6.2: Instantaneous velocity fields from PIV in liquid cyclopentane at a temperature of 266 K that surrounds a water drop with a volume of 0.25 ml in the absence of hydrate formation. The colour bar denotes the flow speed.

is increased to 0.7 ml. However, the internal flow pattern is notably different when the drop volume is decreased to 0.05 ml. As evident in Figure 6.6, water in the drop moves in a circular motion with a single vortex at the centre despite being subjected to a symmetrical external flow around the drop. Reversal of flow that is observed in Figure 6.4 for 0.25 ml drop is also not seen for the case of the smaller drop (volume = 0.05 ml). The shape of the drop, being a spherical cap where the height of the drop is greater than its radius, as well as the limitation in size that constrains the flow may have contributed to the circular flow pattern with a single vortex instead of the double vortices seen in the larger drops.

A limitation in the application of the PLIF thermometry technique in droplets is the presence a region close to the interface where it is not possible to extract temperature information. This is shown by the shaded region in Figure 6.3. The same observation was reported by Volkov and Strizhak [207]. Additionally, the presence of the O-ring on the glass substrate to fix the ROI in the field of view of the camera have also casted shadows on the sides of the drop. Validation of the temperature measurement is discussed further in Section 6.3.

Figure 6.7 presents a sequence of thermal mapping in the water drop, under the condition where hydrate formation is present. The whole-field temperature images illustrate how hydrate solidification differs from the recalescence observed during freezing. During freezing, the temperature spike of supercooled water to its freezing point occurs throughout the entire volume of the drop, making it easily detectable by a point source measurement, such as a thermocouple [74]. In contrast, during hydrate formation, no such temperature spike is detected in the drop qualitatively, based on the thermal map. Any temperature rise may occur locally at the growing hydrate front. Further analysis of temperature is discussed Section 6.3.2.

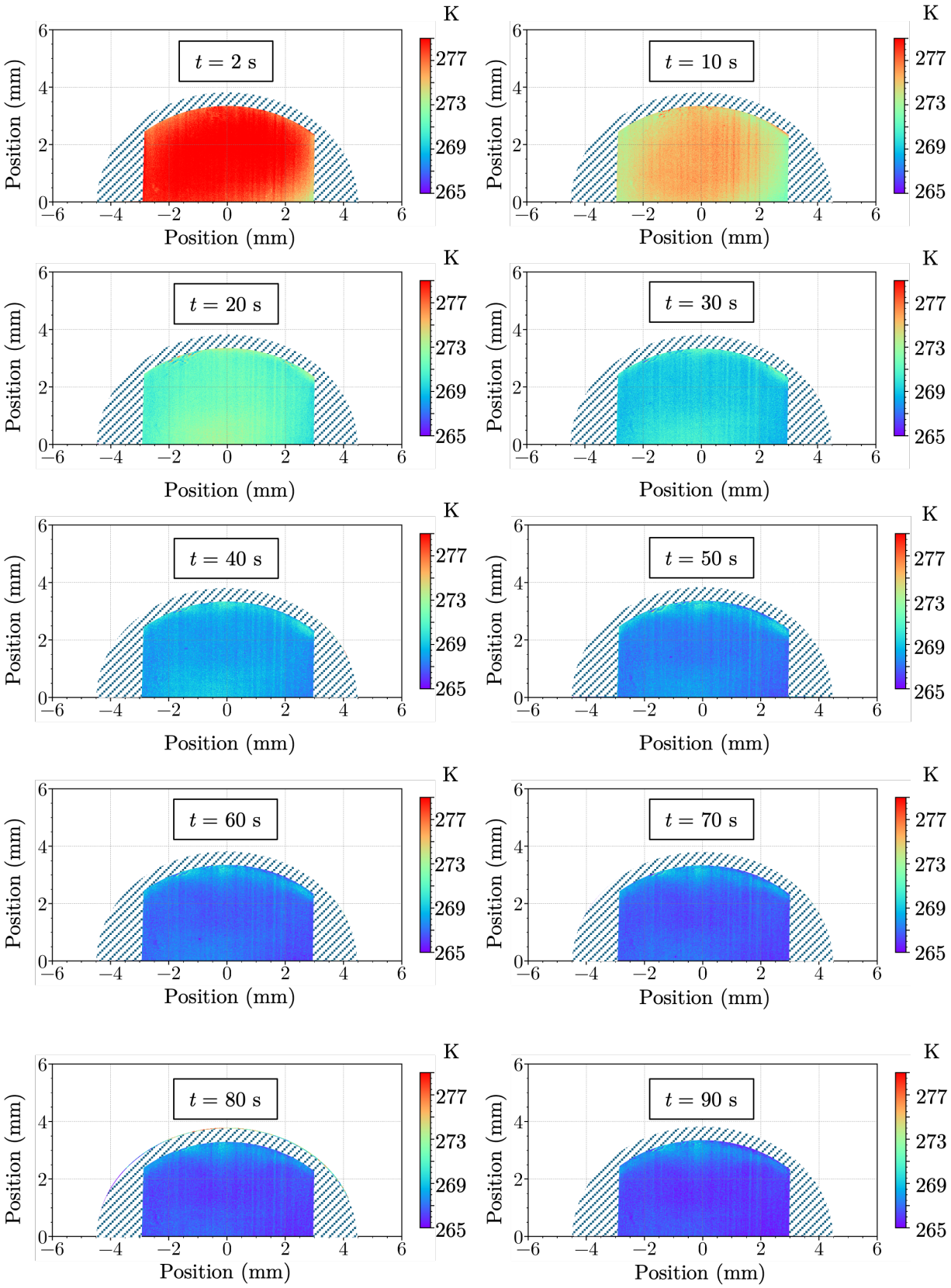


Figure 6.3: Instantaneous temperature fields from two-colour PLIF of a water drop with a volume of 0.25 ml in the absence of hydrate formation at a bulk cyclopentane temperature of 266 K. The colour bar denotes temperature.

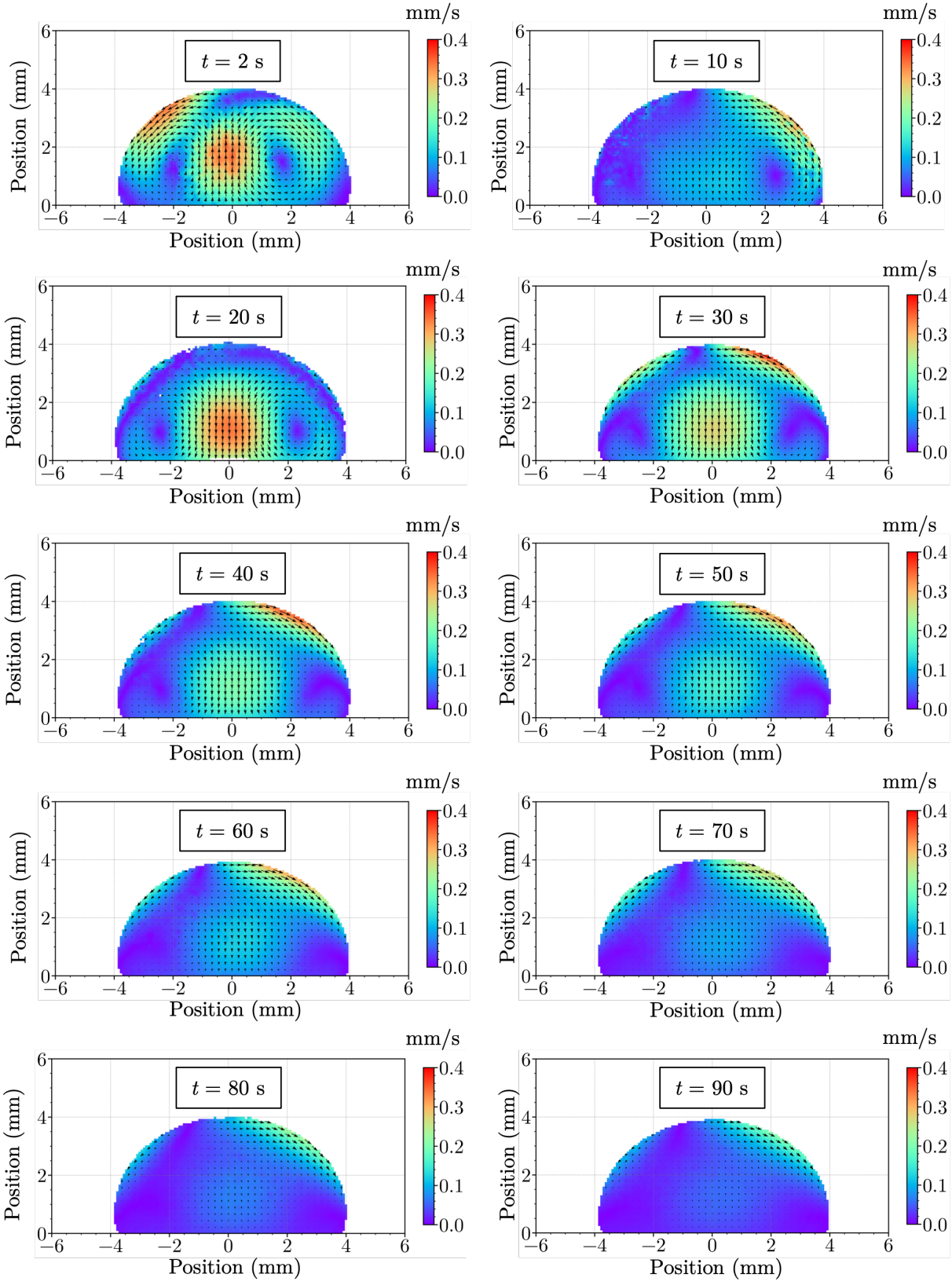


Figure 6.4: Instantaneous velocity fields from PIV of the internal flow in a water drop with a volume of 0.25 ml in the absence of hydrate formation at a temperature of 266 K. The colour bar denotes the flow speed.

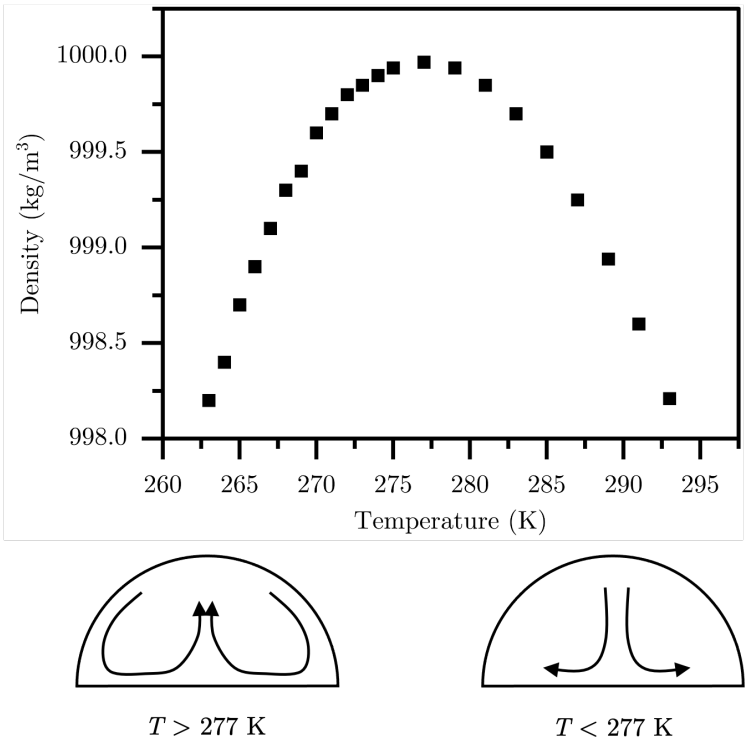


Figure 6.5: Density of water as a function of temperature [31, 32]. Direction of internal flow when water at room temperature is deposited in cold liquid cyclopentane.

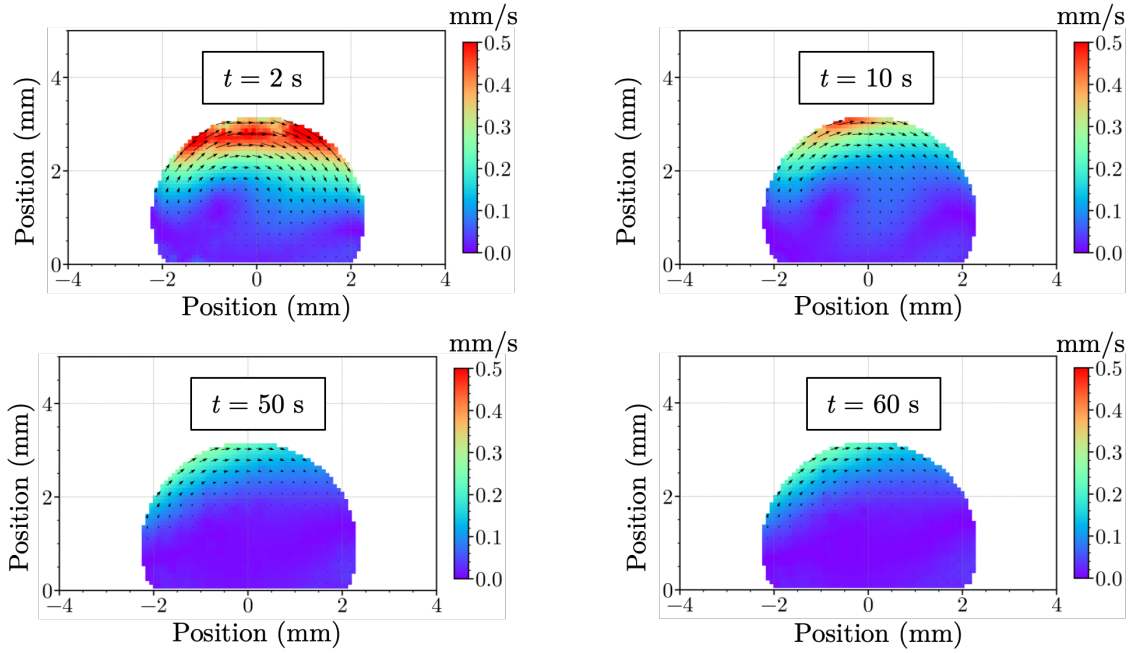


Figure 6.6: Instantaneous velocity fields from PIV of the internal flow in a water drop with a volume of 0.05 ml in the absence of hydrate formation at a temperature of 266 K. The colour bar denotes the flow speed.

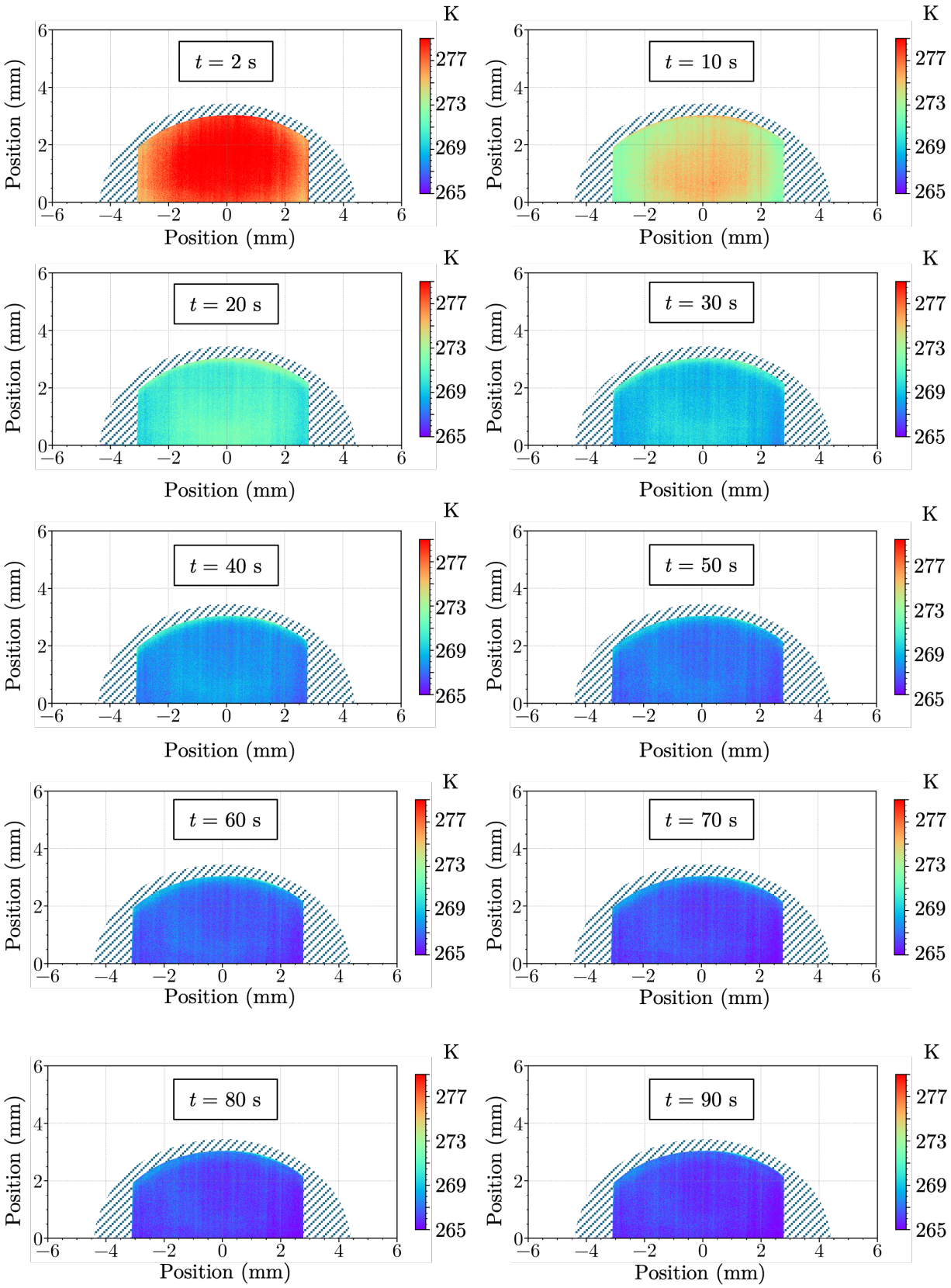


Figure 6.7: Instantaneous temperature fields from two-colour PLIF of a water drop with a volume of 0.25 ml in the presence of hydrate formation at a bulk cyclopentane temperature of 266 K. The colour bar denotes temperature.

6.2 Velocity measurements

The results obtained through the PIV measurements are presented, primarily focusing on the magnitude of velocity. First, the external and internal flows of the drop are assessed to compare the fluid motion in the two phases. The internal flow in the drop that is only subjected to cooling (in the absence of hydrate formation) is then presented by examining the effect of temperature on the internal flow. Finally, the temporal evolution of velocity is scrutinised, drawing comparisons between hydrate and non-hydrate cases.

6.2.1 External and internal flows

The magnitude of the velocities in the surrounding liquid cyclopentane (external) and the water drop (internal) are compared by taking a vertical profile along the centreline of the drop. Figure 6.8 shows an example of the averaged velocity magnitude profiles for a water drop with a volume of 0.25 ml (in the absence of hydrate formation) at a bulk cyclopentane temperature of 273 K. Two plots are presented, at $t = 2$ s and $t = 90$ s. The initial time is taken as 2 seconds to ensure that the internal flow is not influenced by the instabilities caused by drop injection into the liquid cyclopentane while the final time is taken as 90 seconds, corresponding to the thermal relaxation time, as discussed in Section 6.1. As seen in Figure 6.8, the speed of the flow in liquid cyclopentane is at a maximum, two orders of magnitude larger than the flow in the drop. In the event that hydrate is formed at the drop interface, the disturbance to the flow, either through the release of heat or through the presence of a rigid film would be more noticeable in the water drop as the surrounding environment is more dominated by convection whereas the flow in the drop is more confined. After 90 seconds, the external flow reduced significantly but is not entirely diminished. This is possibly because cooling for the hydrate cell is provided only on the side walls. Additionally, there is a small opening on the top cover for ease of access for drop injection. These two factors may have caused the natural convection in the hydrate cell. At 90 seconds, a small internal flow is also observed to be present near the drop interface due to shearing by the external flow.

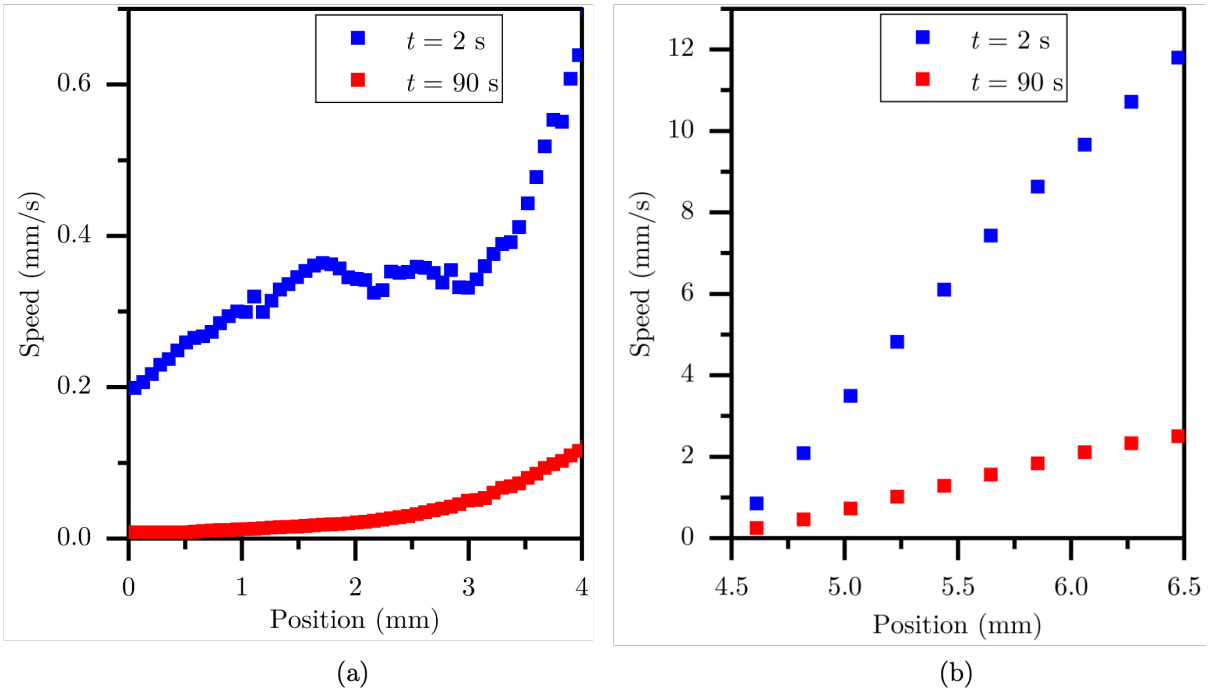


Figure 6.8: Vertical magnitude profiles along the centreline of the drop. (a) Internal flow (b) External flow.

6.2.2 Varying bulk liquid cyclopentane temperature

Figure 6.9 shows an example of the time snapshots of average horizontal flow speed profiles that passes through the two counteracting vortices (Figure 6.10 (a)) in the water drop (in the absence of hydrate formation) at varying liquid cyclopentane temperature (T = 273, 270 and 266 K). At T = 273 K, the internal flow appears to reduce over time, which is expected as the temperature in the drop equilibrates with the temperature of the surrounding liquid cyclopentane. The flow reversal as observed in the velocity vectors in Figure 6.4 is manifested by the reduction in speed at t = 10 s, followed by an increase in speed at t = 20 s for T = 266 K and at t = 30 s for T = 270 K. The effect in the change in flow direction is more prominent as the bulk cyclopentane temperature decreases due to the larger difference in water density between the edges and the core. This is also exhibited by the time moment at which the flow reversal occurs, whereby it happens earlier with cooler liquid cyclopentane temperature.

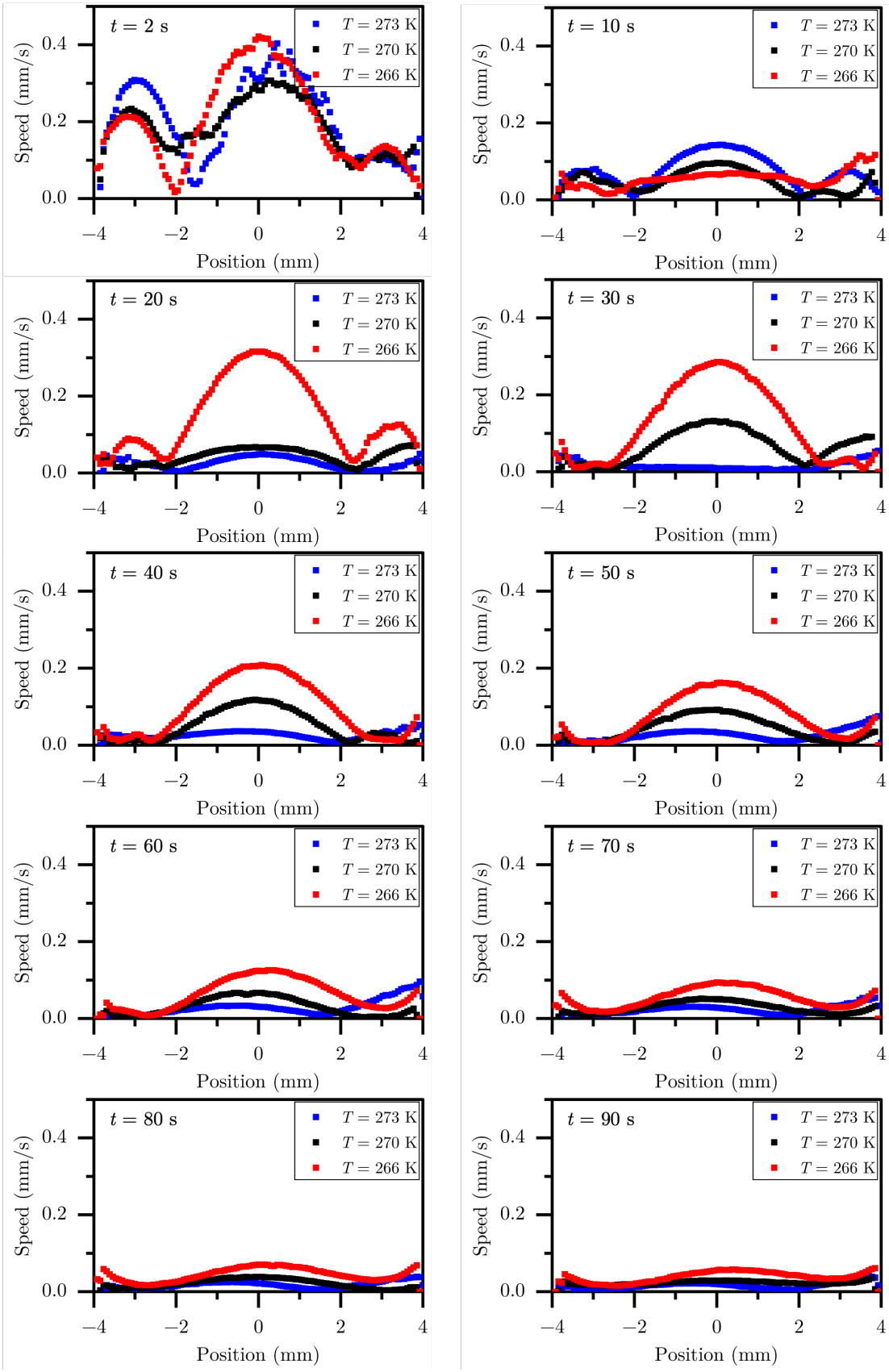
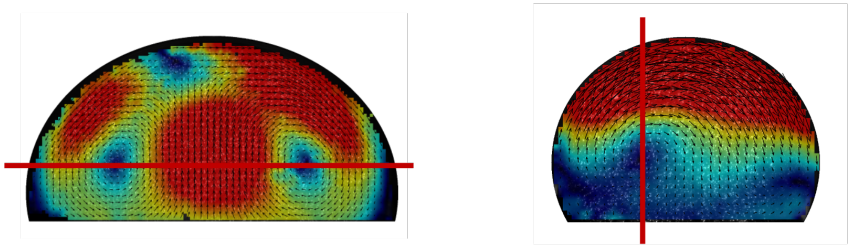


Figure 6.9: Time evolution of horizontal velocity magnitude profiles crossing the vortices inside the water drop (0.25 ml) in the absence of hydrate formation at varying liquid cyclopentane temperature.



(a) (b)

Figure 6.10: Geometry of flow speed profiles passing through the vortex/vortices (a) horizontal (b) vertical.

6.2.3 Velocity comparison between hydrate and non-hydrate cases

Similarly, the influence of hydrate formation on the internal flow is investigated by taking the horizontal profile of average flow speeds passing through the two counteracting vortices in the water drop. Figure 6.11 shows the evolution of the horizontal profiles for a 0.25 ml water drop in bulk liquid cyclopentane temperature of 270 K. The internal flows in both the hydrate and non-hydrate cases show similar characteristics, as previously described in Section 6.1. As the water drop cools, flow reversal as evident by the decrease in velocity magnitude at $t = 10$ s followed by an increase at $t = 30$ s. When the internal flow dies down with time, there is a slight difference in the internal flow between the hydrate and non-hydrate cases particularly at the periphery of the drop. However, as evident in the inlay at $t = 90$ s, the difference between the two cases is greater than the uncertainty of the PIV measurement that has a maximum uncertainty of ± 0.01 mm/s. When the drop is placed in liquid cyclopentane at a temperature of 266 K as shown in Figure 6.12 (also shown in the inlay at $t = 90$ s), the difference between the hydrate and non-hydrate cases is even more prominent. In this case, the deviation between the horizontal velocity magnitude profiles also appear earlier at $t = 80$ s.

For the case of the smaller water drop with a volume of 0.05 ml, taking a horizontal profile across the vortex is challenging due to low velocity at the bottom half of the drop as apparent in

the velocity fields shown in Figure 6.6. Hence, vertical velocity magnitude profiles (Figure 6.10 (b)) are used to compare the two different cases as shown in Figures 6.13 and 6.14 for water drops deposited in liquid cyclopentane at temperatures of 270 and 266 K, respectively. The average vertical velocity magnitude profiles begin to deviate at $t = 30$ s for 270 K and it occurs earlier at $t = 20$ s for 266 K. In this case, it also observed that difference between the profiles for hydrate and non-hydrate cases is more noticeable as the temperature in the liquid cyclopentane reduces, as shown in the inlays in Figures 6.13 and 6.14 at $t = 30$ s. As hydrate forms at the interface, the hydrate film forms a solid barrier between water and the surrounding liquid cyclopentane. Thus, the presence the hydrate film isolates the internal flow from the influence of the external flow in the surrounding phase. Moreover, when the temperature of the liquid cyclopentane reduces, water is subjected to a higher degree of subcooling which translates to a higher hydrate growth rate. Hence, the deviation between the velocity magnitude profiles for hydrate and non-hydrate cases appear earlier as liquid cyclopentane temperature reduces. No such difference is observed when liquid cyclopentane temperature is at 273 K for 0.05 and 0.25 ml water drops and at all temperatures for water drop at a volume of 0.7 ml.

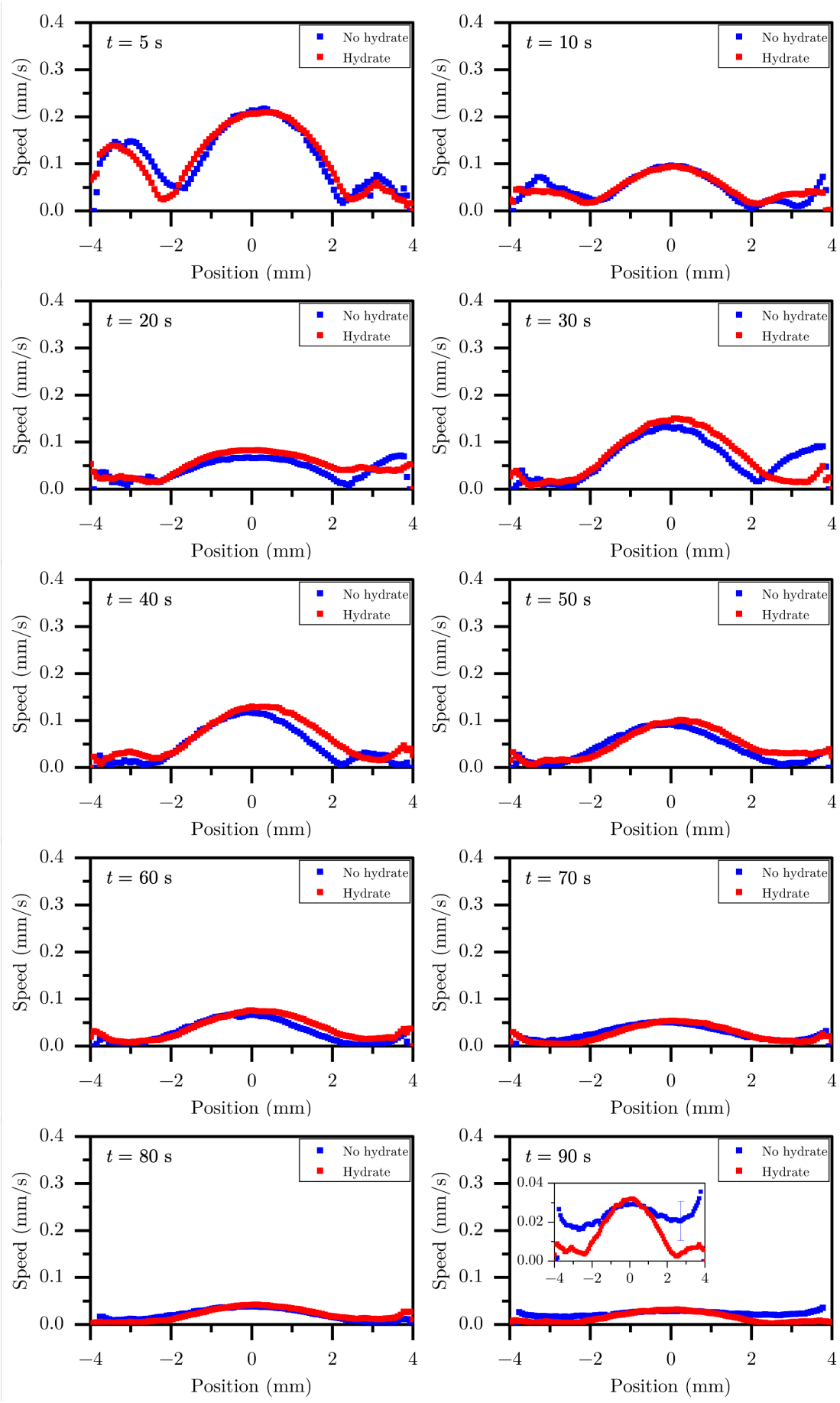


Figure 6.11: Time evolution of horizontal velocity magnitude profiles crossing the vortices inside the water drop (0.25 ml) for hydrate and non-hydrate cases at a liquid cyclopentane temperature of 270 K.

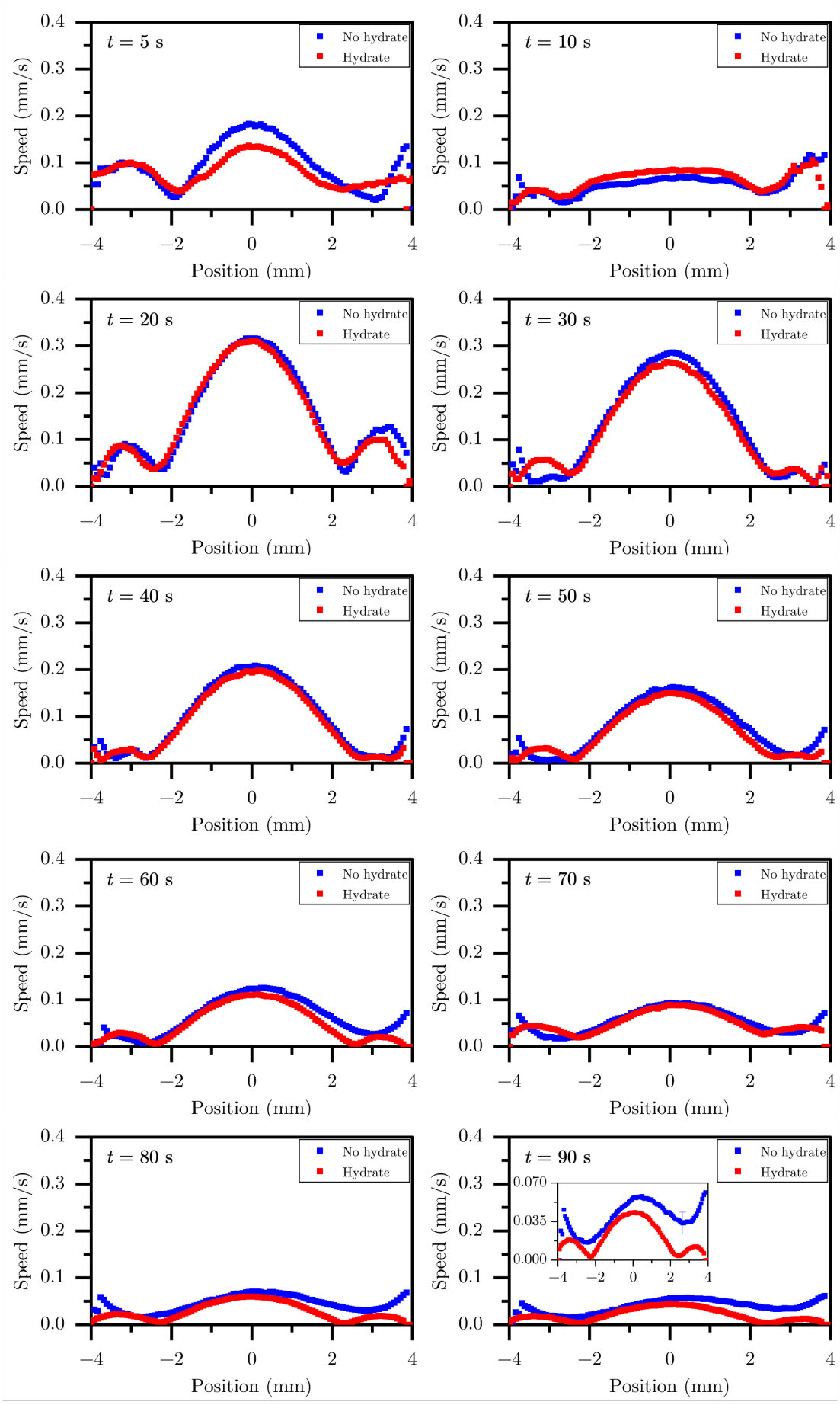


Figure 6.12: Time evolution of horizontal velocity magnitude profiles crossing the vortices inside the water drop (0.25 ml) for hydrate and non-hydrate cases at a liquid cyclopentane temperature of 266 K.

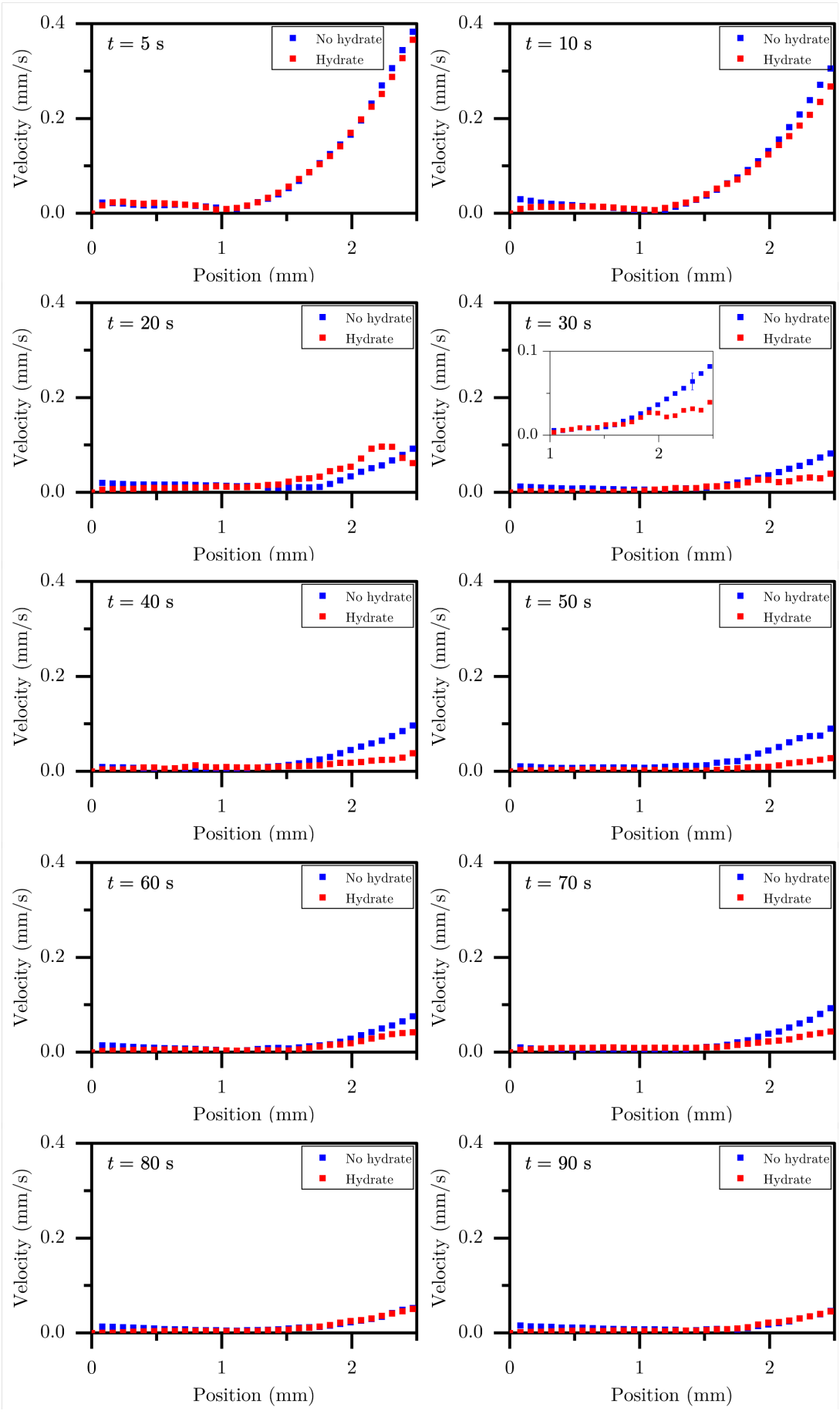


Figure 6.13: Time evolution of vertical velocity magnitude profiles crossing the vortex inside the water drop (0.05 ml) for hydrate and non-hydrate cases at a liquid cyclopentane temperature of 270 K.

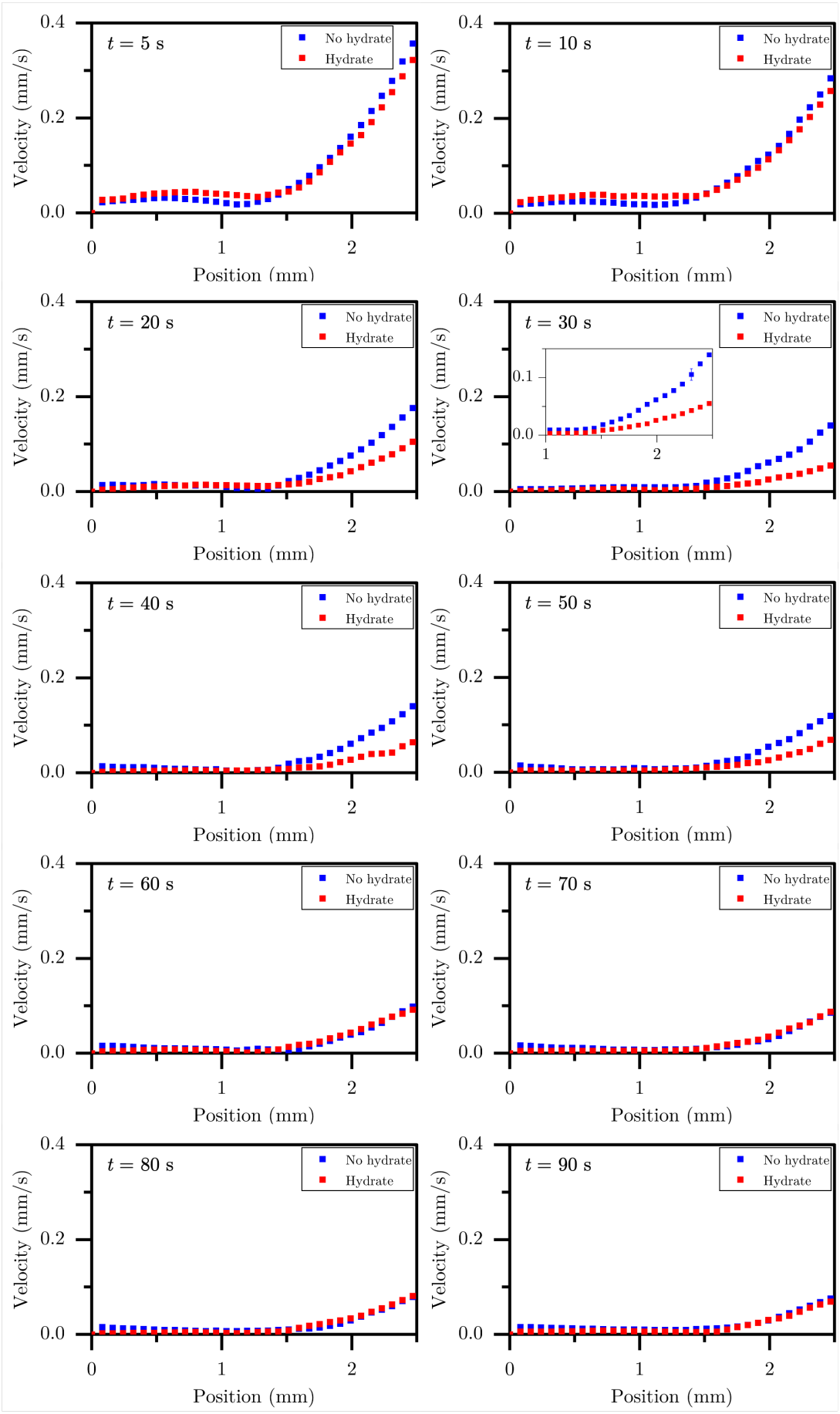


Figure 6.14: Time evolution of vertical velocity magnitude profiles crossing the vortex inside the water drop (0.05 ml) for hydrate and non-hydrate cases at a liquid cyclopentane temperature of 266 K.

6.3 Temperature measurements

The results obtained from both one-colour and two-colour PLIF measurements are presented in this section. First, validation of the PLIF measurements are shown, discussing limitations of the current measurement techniques. Then temperatures close to the drop interface are analysed to draw comparison between the hydrate and non-hydrate cases.

6.3.1 Validation of PLIF measurements

Identifying the location of the hydrate front is challenging because of the effects of convection. In addition, hydrates grow as spherulites at high degree of subcooling. In spherulitic growth, hydrates form as free-floating crystals that move along the drop interface, as discussed in Chapter 4. Since there is a confluence of flow from all sides of the drop towards the apex, any significant release of heat from the formation of hydrate anywhere on the interface will be apparent by an increase in temperature at the drop apex. As such, the temperature near the drop interface is quantitatively analysed by taking spatial average of temperature over an area at the drop apex.

As discussed in Section 3.7.2, there is a loss of data near the interface inside the water drop due to the curvature of the drop and the thickness of the laser sheet that limit the temperature information to a certain distance from the drop interface. Figure 6.15 shows an example image obtained from two-colour PLIF showing a region close to the drop interface where there is a dark band, in which temperature information could not be extracted. The example image also shows two red bands on the side of the drop which is caused by O-rings on glass substrate and therefore casted shadows as the drop is illuminated by laser from the bottom. These regions are excluded from the temperature analysis. The position where the temperature measurement obtained from PLIF thermometry gives a realistic value is first determined by validating the values with measurements from a thermocouple placed inside the drop from one side of the O-ring. After 240 seconds from when water drop was introduced into the cold liquid cyclopentane, the temperature inside the water drop is expected to stabilise. The validation was performed by

comparing the thermocouple measurement with the temperature measurements obtained from PLIF at 240 seconds, at a range of distance normal to the drop interface (from 0 to 1 mm).

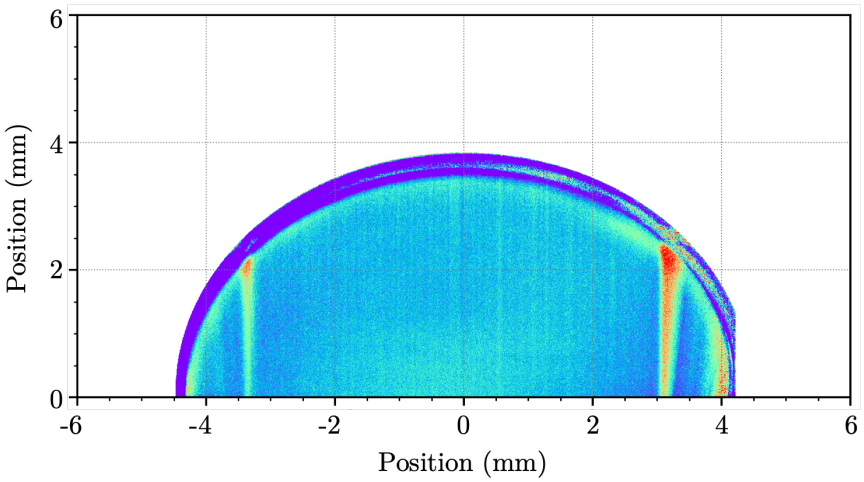


Figure 6.15: Example of two-colour PLIF image showing regions close to the drop interface where there is a loss of data as indicated by the dark band.

Figure 6.16 shows the temperature of a water drop in liquid cyclopentane at a bulk temperature of 273 K. As seen in Figure 6.16, the PLIF measurements between 0 to 0.3 mm significantly deviate from the thermocouple measurement and agree well only after a distance of 0.3 mm from the drop interface. The measurement from PLIF thermometry was also tested by comparing its variation with time against the thermocouple measurement. Figure 6.17 shows that the PLIF measurement at a distance of 1 mm from the interface and the thermocouple measurements agree reasonably well with each other. Since there are no other heat source for the water drop (assuming the hydrate cell is well insulated and heat gain from the environment is negligible), any temperature rise in the water drop at all three bulk temperatures in the hydrate experiments can only be attributed to the heat released during the exothermic hydrate formation process.

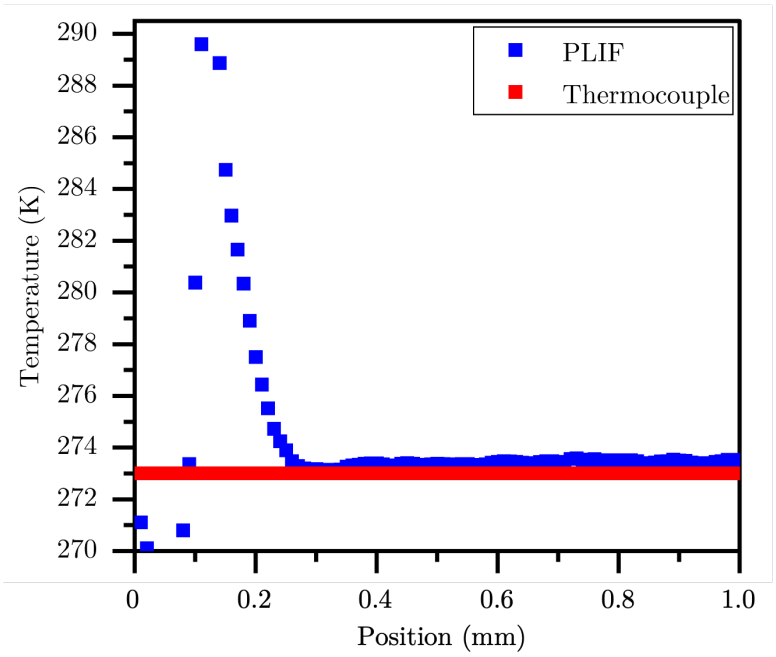


Figure 6.16: Temperature measurements obtained from PLIF thermometry at varying distance normal to the drop interface compared to thermocouple measurement after 240 seconds from the introduction of the water drop into liquid cyclopentane at 273.15 K in the absence of hydrate formation. The thermocouple measurement is shown in the figure only as a reference line and does not indicate temperature measurements at different points.

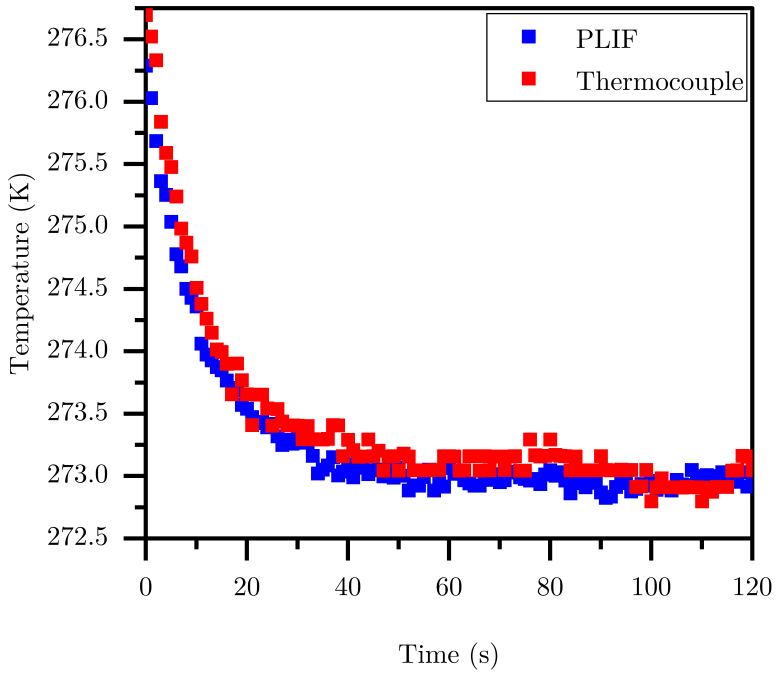


Figure 6.17: Comparisons between the variations of temperature measurements obtained from PLIF thermometry at 1 mm from the drop interface with the thermocouple measurements.

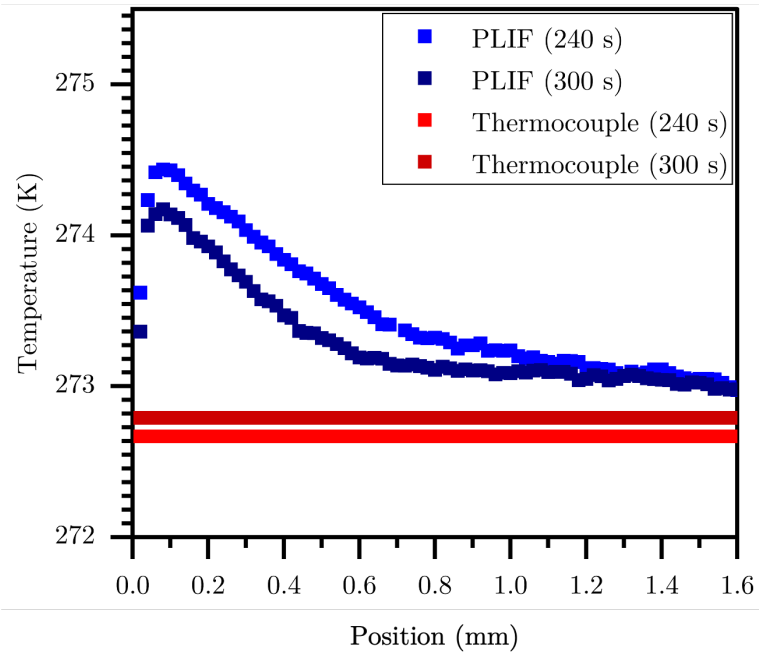


Figure 6.18: Temperature measurements obtained from one-colour PLIF thermometry at varying distance normal to the interface compared to the thermocouple readings at 240 and 300 seconds after the introduction of water drop in cold liquid cyclopentane.

The same validation procedure was performed for the PLIF measurements in cyclopentane. Figure 6.18 shows the variations of temperature obtained from one-colour PLIF in liquid cyclopentane at a range of distance normal to the the drop interface. Since the thermocouple in liquid cyclopentane was located on the top left hand corner of the region of interest (ROI) as shown in Figure 6.19, the PLIF measurements were evaluated as an average over an area between the angle of 42 to 52° at varying distance normal to the interface. It should be noted that the thermocouple was placed outside of the region of interest and slightly off from the laser optical path to avoid laser reflection. Placing the thermocouple within the optical path of the laser may introduce error into the measurement. Similar to the approach taken for the validation of PLIF measurements in the water drop, the temperature in cyclopentane after 240 seconds from the introduction of a water drop is expected to have stabilised. Moreover, no hydrate induction was performed and therefore the water was only subjected to a cool down process. However, the PLIF measurements give unexpectedly higher reading compared to the thermocouple measurement, particularly as it gets closer to the drop interface. The evaluation

of PLIF measurements at 300 seconds also show a similar pattern and appear to stabilise after a distance of 1 mm from the drop interface, with a deviation of approximately 0.3 K from the thermocouple reading, which is an acceptable difference given the uncertainties and distance of the area at which the temperature is evaluated from the thermocouple.

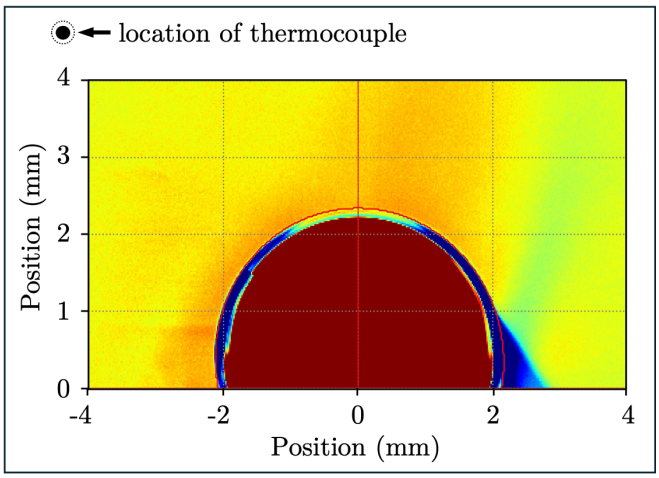


Figure 6.19: Example of one-colour PLIF image of nile red in cyclopentane at $t = 300$ s at a bulk cyclopentane temperature of 273 K in the absence of hydrate formation.

Figure 6.19 shows an example image obtained from one-colour PLIF in cyclopentane at $t = 300$ s when temperature in the hydrate cell is expected to be stable. It appears that there is a region close to the interface with higher intensity, which after image processing, translates to higher temperature. However, it is not plausible for a 0.05 ml water drop at room temperature to have caused approximately 1.4 K difference even after 300 seconds of being introduced into cyclopentane. It should be noted that the cyclopentane having a volume of 120 ml is continuously cooled to maintain a constant temperature. There are several reasons that could have contributed to a higher intensity near the drop interface. As the laser sheet strikes the water drop from above, a fraction of the light is reflected. A slight difference between the refractive indices of water and liquid cyclopentane ($n_\mathrm{t} = 1.33$ and $n_\mathrm{i} = 1.40$, respectively) results in a reflectance, R of 0.00066, assuming normal incidence (Equation 6.2).

$$R = \frac{n_i - n_t}{n_i + n_t} \tag{6.2}$$

Changes in light propagation, as a result of reflection, contributes to an increase in the image count captured by the camera and is not representative of the actual temperature. While the difference in refractive index allows the water drop to be visible in liquid cyclopentane and therefore aids in the visualisation of hydrate formation on the drop interface using direct imaging technique, it is disadvantageous for one-colour PLIF measurement. A limitation in the one-colour PLIF technique is that it cannot correct for light reflection. On the other hand, the two-colour PLIF technique is able to minimise the effect of reflection by taking the ratio of intensities between two fluorescent dyes and therefore would have been a better technique for temperature measurement in liquid cyclopentane. However, the scarcity of temperature-sensitive fluorescent dye that can dissolve in cyclopentane on top of the strict criteria for dye-mixture selections for two-colour PLIF makes the technique even more challenging to achieve for hydrate application.

It is also possible that there are other sources of heating that may have resulted in the regions close to the drop interface to appear hotter. Firstly, heat could potentially be gained from the small stream of dry air that is directed to the acrylic cover that encased the hydrate cell. This was done to avoid condensation that would block the optical path to the camera. Secondly, the pedestal, substrate and O-ring on which the sessile water drop is resting on could experience heating by the laser illumination especially during long experimental run. The temperature inside the water drop (Figure 6.17) measured using a thermocouple, however, showed no significant increase in temperature. Moreover, the thermocouple and two-colour PLIF measurement taken inside the water drop agree reasonably well. Therefore, heating by any of the mentioned sources is unlikely. Nevertheless, precaution is still taken by setting the frequency of image recording to 2 Hz specifically to minimise the heating effect while at the same time providing sufficient temporal resolution. Despite the limitation in the current one-colour PLIF technique in cyclopentane, it should be highlighted that at a distance away from the drop interface, the measurement technique gives comparable reading to the thermocouple measurement, as shown in Figure 6.20.

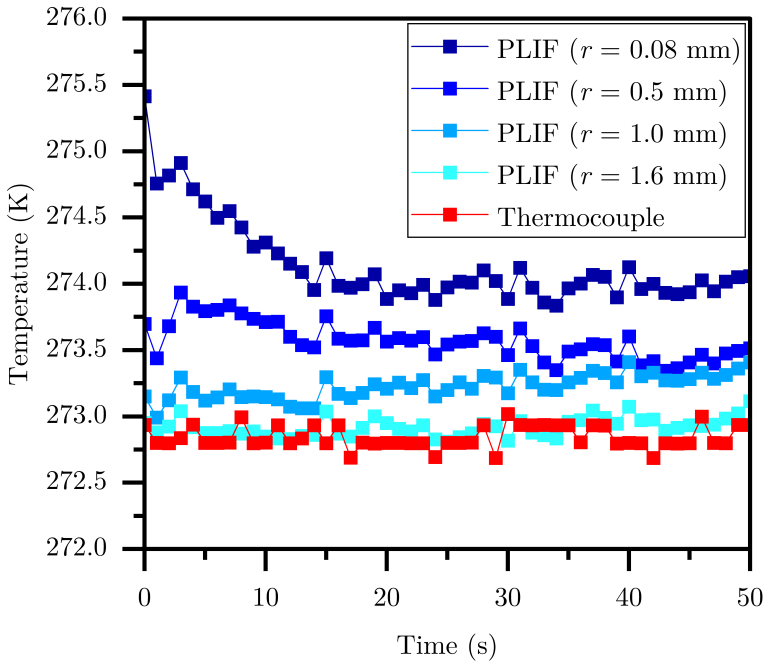


Figure 6.20: Comparisons between the variations of temperature measurement obtained from one-colour PLIF thermometry at various distance normal to the interface.

6.3.2 Temperature comparison between hydrate and non-hydrate cases

The influence of hydrate formation on temperature close to the drop interface is investigated by evaluating the spatially averaged temperature of an area (100 μm x 100 μm) with a distance of 0.5 mm from the drop interface both inside and outside of the water drop (Figure 6.21). When hydrate forms at the drop interface, temperature close to the drop interface is expected to rise as the heat of hydrate formation is released. Since the water drop undergoes two competing processes (cooling down and hydrate formation), the influence of hydrate formation is analysed by comparing its temperature profiles with the temperature profile of a drop that does not undergo hydrate formation.

Figure 6.22 shows comparisons between the temperature evolution of water drops at a volume of 0.25 ml, both in absence and presence of hydrate formation at three different liquid cyclopentane temperatures. While there is no observable difference between the temporal temperature profiles of hydrate and non-hydrate cases at liquid cyclopentane temperature of 273 and 270 K, there is an increase in temperature for the hydrate case at a temperature of 266 K with a maximum difference of 2.2 K at t = 23 s, which is greater than the estimated uncertainty of

two-colour PLIF measurement of ±1 K. When the volume of the water drop is decreased to 0.05 ml, it is observed that the temperature curves in the presence of hydrate deviate from the temperature curve in the absence of hydrate at liquid cyclopentane temperatures of 270 and 266 K. The maximum temperature difference at liquid cyclopentane temperature of 266 K is 3.3 K, occurring at $t = 11$ s. In both water drop sizes, the differences between the hydrate and non-hydrate cases are more prominent at a temperature of 266 K. Since the growth rate of hydrate increases with decreasing liquid cyclopentane temperature i.e., increasing degree of subcooling, more heat of hydrate formation is released, which contributes to the observable difference in temperature between the two cases. A larger surface to volume ratio for the 0.05 ml water drop compared to the 0.25 ml drop allows the hydrate case to be better distinguished from the hydrate case in the smaller drop.

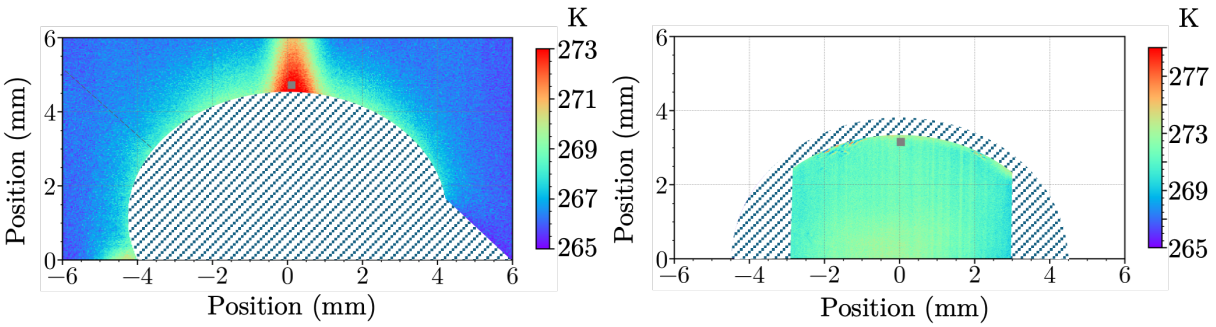
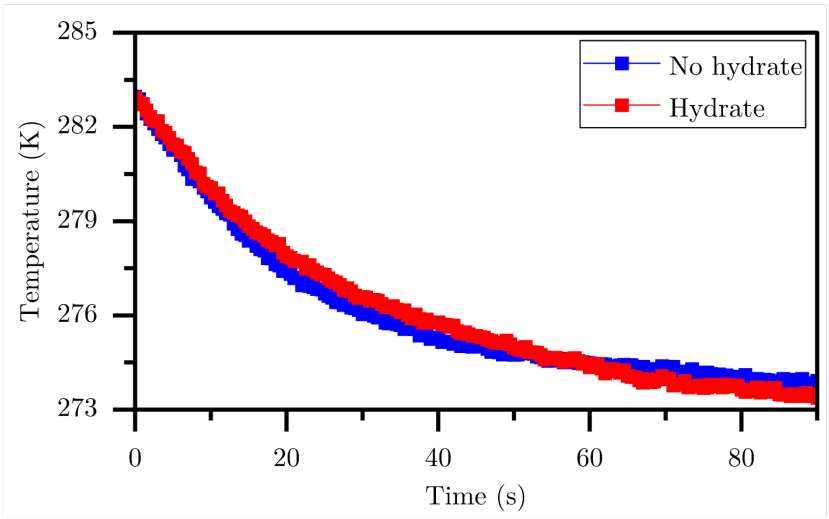
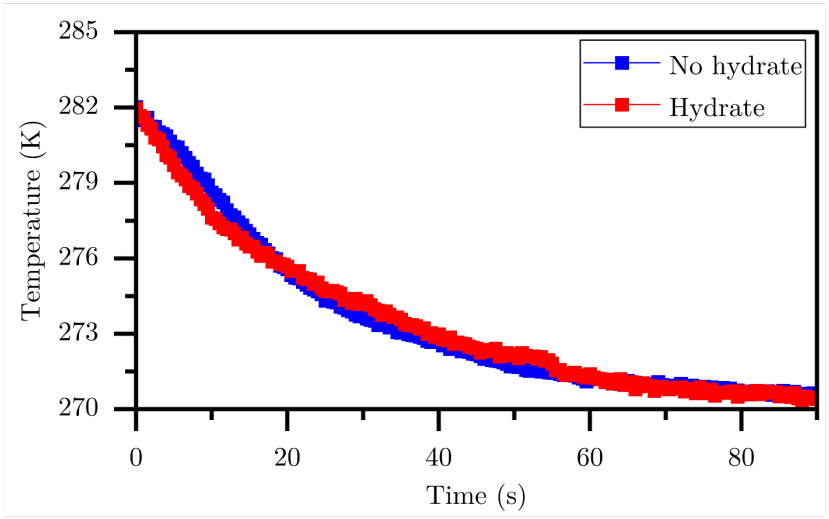


Figure 6.21: Locations of the temperature evaluation near the drop interface are indicated by the grey squares in the images.

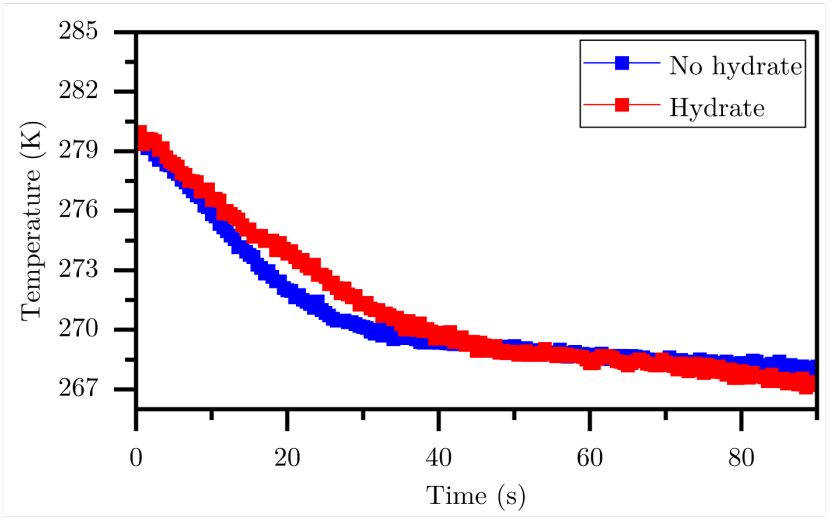
For the sake of rigor, the results from one-colour PLIF temperature measurement in cyclopentane evaluated as spatial average in an area (100 μm x 100 μm) at the drop apex are shown in Figures 6.24 and 6.25 for water drops with volumes of 0.25 and 0.05 ml, respectively. There is no observable difference between the hydrate and non-hydrate experiments likely due to errors in the measurement technique, as discussed earlier, that dwarfs any influence brought about by the formation of hydrate. Moreover, as discussed earlier in Section 6.2.1, the external flow is dominated by convection and therefore masked the influence of hydrate formation.



(a)

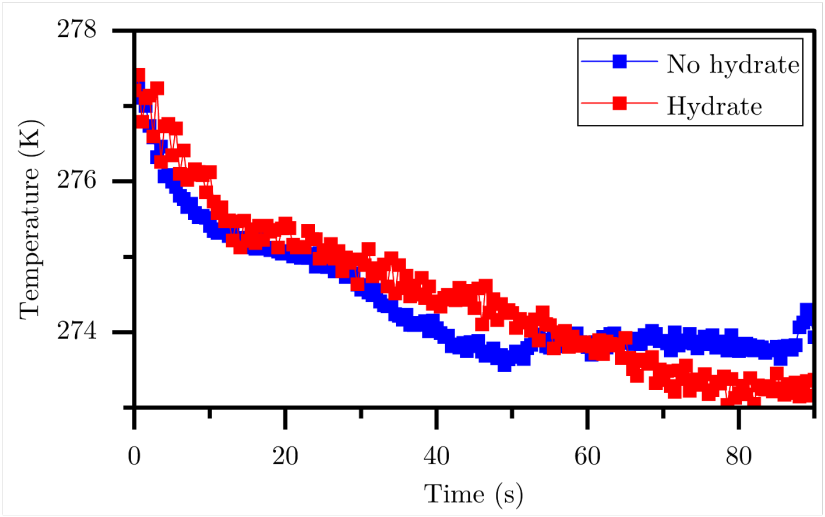


(b)

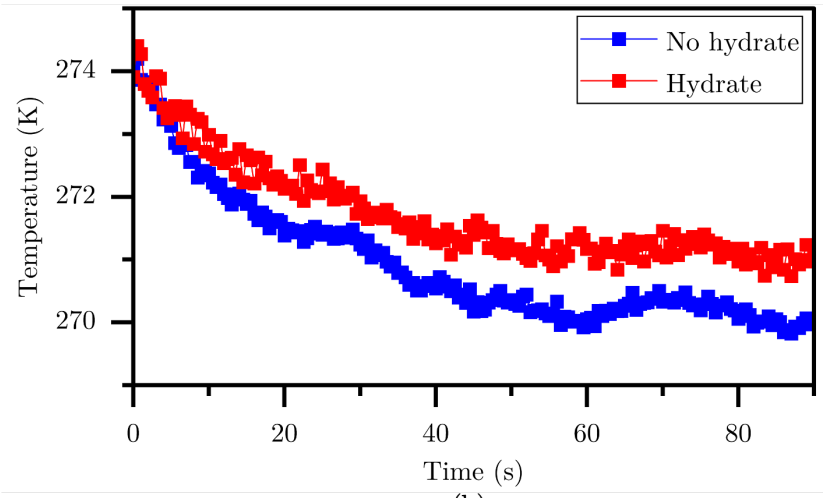


(c)

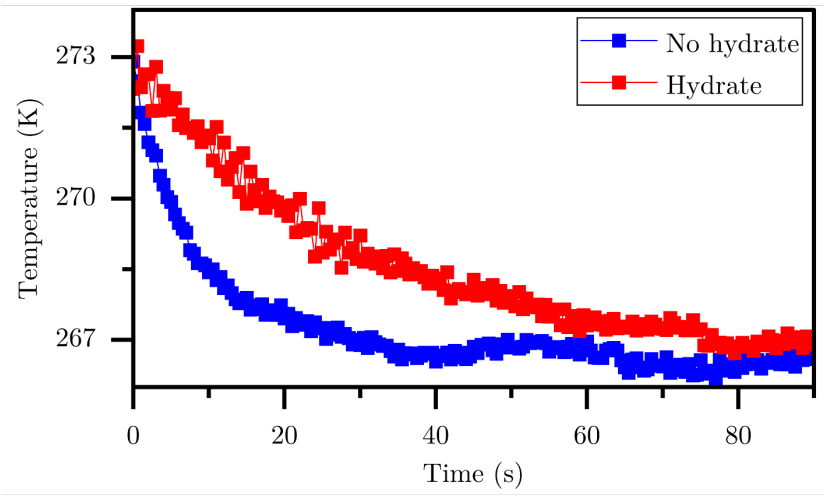
Figure 6.22: Evolution of temperature in water obtained using two-colour PLIF at varying liquid cyclopentane temperature: (a) 273 K, (b) 270 K and (c) 266 K, for a water drop with a volume of 0.25 ml.



(a)

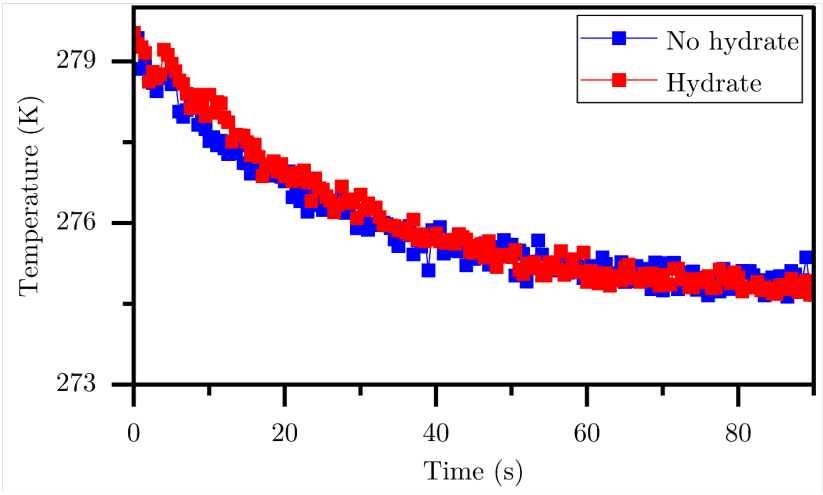


(b)

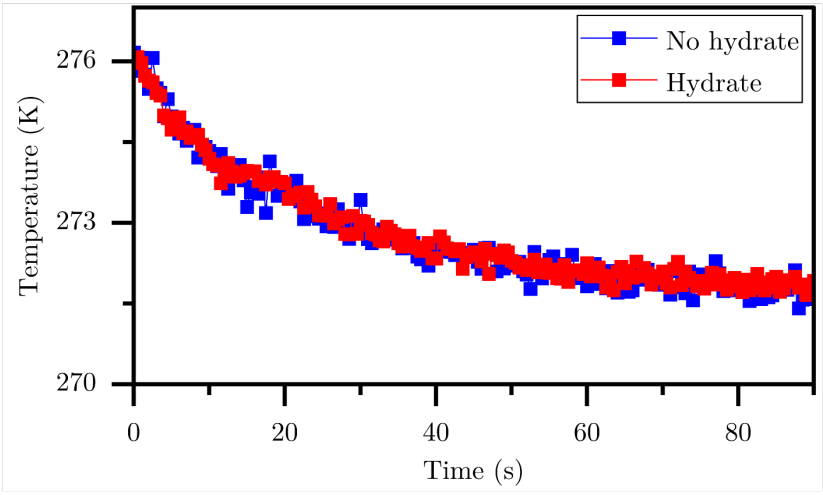


(c)

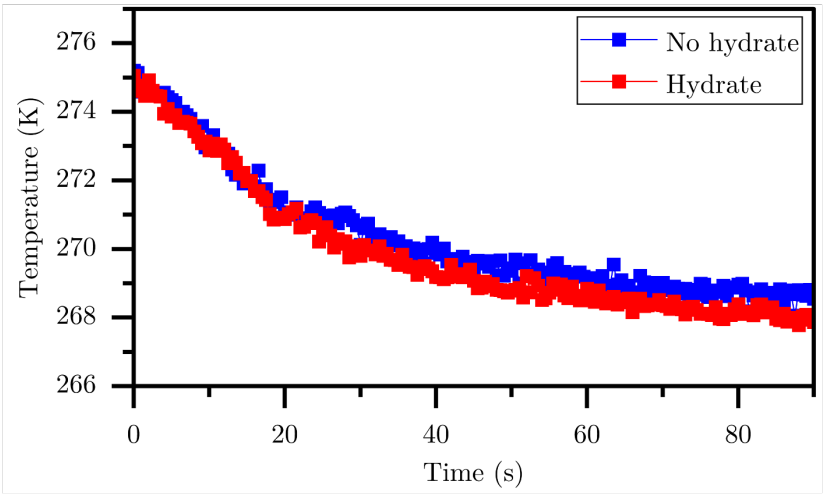
Figure 6.23: Evolution of temperature in water obtained using two-colour PLIF at varying liquid cyclopentane temperature: (a) 273 K, (b) 270 K and (c) 266 K, for a water drop with a volume of 0.05 ml.



(a)

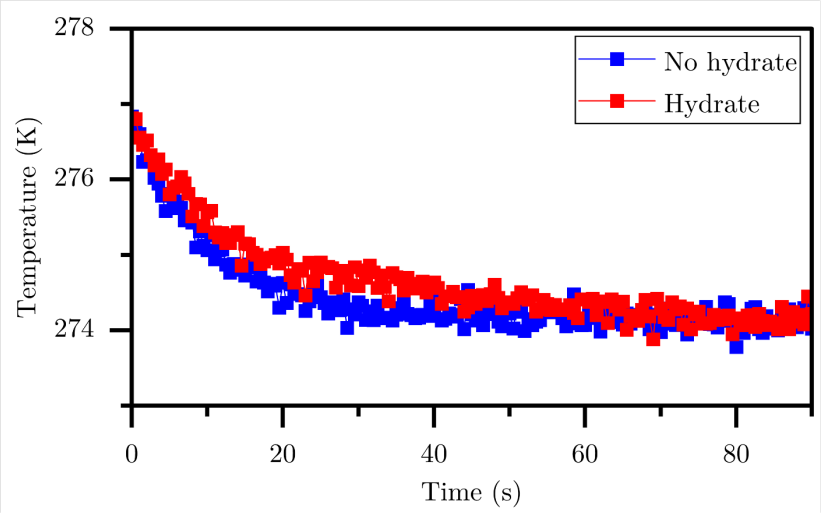


(b)

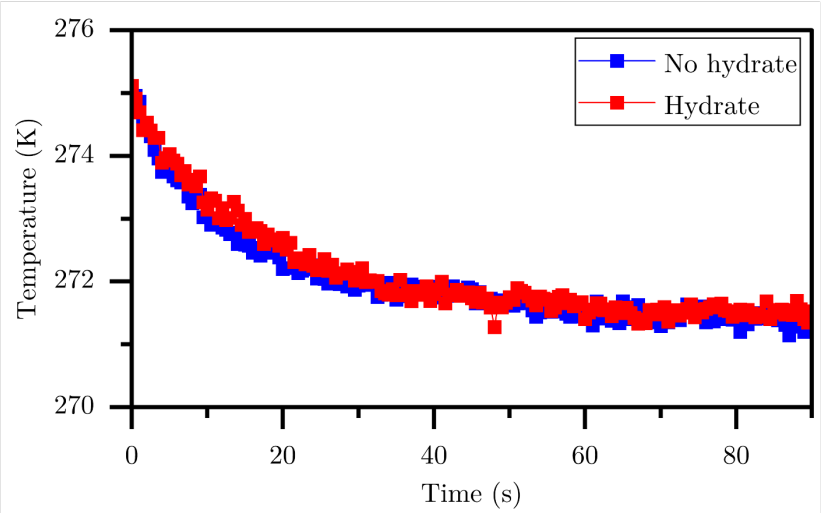


(c)

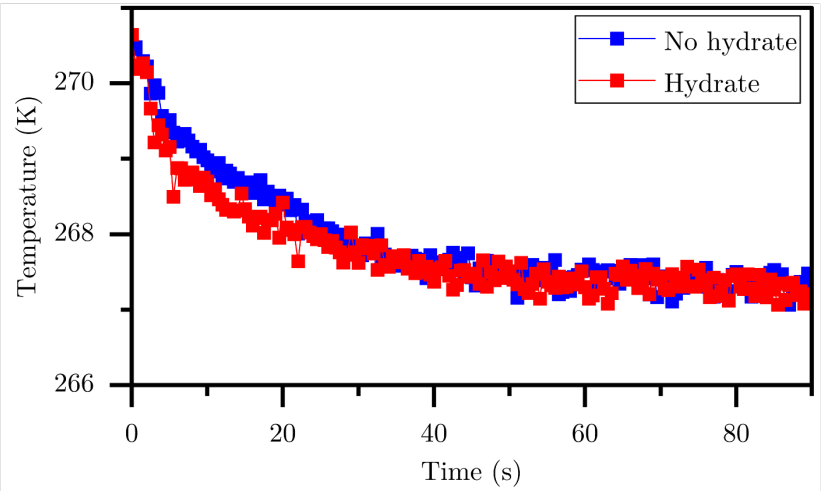
Figure 6.24: Evolution of temperature in cyclopentane obtained using one-colour PLIF at varying liquid cyclopentane temperature: (a) 273 K, (b) 270 K and (c) 266 K, for a water drop with a volume of 0.25 ml.



(a)



(b)



(c)

Figure 6.25: Evolution of temperature in cyclopentane obtained using one-colour PLIF at varying liquid cyclopentane temperature: (a) 273 K, (b) 270 K and (c) 266 K, for a water drop with a volume of 0.05 ml.

6.4 Summary

The influence of hydrate formation on temperature and flow in a water drop and the surrounding liquid cyclopentane were studied using three different techniques, i.e., one-colour PLIF thermometry, two-colour PLIF thermometry and PIV. Each of the technique were performed independently. Since the water drop was introduced into the cold liquid cyclopentane at room temperature to further accelerate hydrate induction (in addition to employing the memory effect of water), the water drop was subjected to two competing processes, i.e., cooling down by the surrounding liquid and the release of heat of hydrate formation. Therefore, the influence of hydrate formation was investigated by performing two separate cases in the absence and presence of hydrate formation. In the absence of hydrate formation, the memory effect of water was not utilised to delay hydrate formation and thus the drop only experienced cooling during the experimental window.

Temperature fields obtained using one-colour and two-colour PLIF thermometry provided visualisation of hot zones in cyclopentane and water, while the velocity fields obtained from PIV further confirmed the buoyancy effect in both phases that resulted in natural convection. The experiments were conducted at three different drop sizes with volumes of 0.05, 0.25 and 0.7 ml. While the flow behaviour in cyclopentane is observed to be the same for all drop sizes, the internal flow in the drop showed differing patterns. In a 0.05 ml drop, water flowed in a circular motion with one single vortex at the centre. When the drop volume was increased to 0.25 and 0.7 ml, the internal flow featured two counteracting vortices. The difference between the flow characteristics is due to the differing shapes of the drops, where the smaller drop is more spherical in shape and therefore is more constrained. In the larger drops, flow reversal was observed as it underwent cooling below 277 K. This can be attributed to the special property of water that has a maximum density at 277 K.

Temperature fields obtained in the presence of hydrate formation further confirmed that recalescence often times observed in drop freezing throughout the entire drop volume was not detected when hydrate was formed. This also confirmed that the hydrate experiments were not contaminated by ice even when water was supercooled. A temperature rise during hydrate formation, relative

to the non-hydrate case, was instead detected locally near the interface inside the drop. The difference in temperature between the hydrate non-hydrate cases is more prominent with decreasing liquid cyclopentane temperature due to higher hydrate growth at lower temperature. The difference in temperature between the two cases suggest that significant amount of heat from hydrate formation is released, which may affect the mechanism of hydrate growth. Further studies, which is out of the scope of the present work, shall look into how heat transfer influences hydrate growth. The influence of hydrate formation on temperature is also greater with decreasing drop size due to higher surface area to volume ratio. No observable difference in velocity was detected in the external flow as convection was more dominant, being almost two orders of magnitude greater than the internal flow. Limitation in the one-colour PLIF measurement was identified with reflection at the drop interface as the source of error.

Chapter 7

Conclusions and future outlooks

The work presented in this thesis has examined the phenomenon of hydrate formation on a liquid-liquid interface. It reveals the complex interaction of hydrodynamic and heat transfer phenomena during the crystalisation of hydrate. The literature review has highlighted the gaps in this area of research, its importance for the industry and the impact of this work in hopes that it will contribute to further understanding of the complex phenomenon. This chapter gives an overview of the main findings of the experimental work, that employed direct visualisation and advanced optical methods, specifically planar laser-induced fluorescene (PLIF) thermometry and particle image velocimetry (PIV), which have been applied for the first time in the literature for the study of hydrate. Recommendations for future work are also included.

7.1 Conclusions

In this study, the use of cyclopentane as an analogue for natural gas in the study of hydrate was explored. One of its primary advantages as a hydrate former is its ability to form hydrate at ambient pressure. This reduces the risk of operating flammable compounds at high pressure, which thus makes experiments safer. Due to similarities between freezing and hydrate formation, a study was performed to characterise the two phenomena both qualitatively using visualisation and quantitatively using thermocouple for temperature measurements to rule out ice contamination

at temperatures below the freezing point of water. Such characterisation opens opportunities for new experimental work to perform hydrate studies involving cyclopentane at a larger range of subcooling temperature. One of the interesting findings found from such exploration in the present work is the morphological variations observed in cyclopentane hydrate at ΔT greater than 7 K having dendritic and spherulitic moprhologies other than polygonal crystals observed at ΔT less than 7 K, which has not been previously reported in the literature. This also showed similarities between cyclopentane and natural gas hydrates, despite their differences in hydrate molecular structure, which proves the usability of cyclopentane as laboratory substitute of natural gas compounds.

A hydrate induction procedure was developed to reduce the experimental duration to within an acceptable time limit for a laboratory environment and to minimise the stochasticity of hydrate nucleation thus ensuring good experimental repeatability. Hydrate induction was achieved through memory effect of water from thawed ice. However, not the entire volume of thawed ice was used as template for hydrate formation to account for the requirement for uniform concentration of additives for PLIF and PIV measurements which required the thawed ice to be removed and replaced by freshly deposited drops. Moreover, deposition of new drops into the hydrate cell create a disturbance in the system which also aided hydrate nucleation. The protocol differs from other works that utilise ice and hydrate seeds as such techniques promotes freezing especially when temperature is below the freezing point of water. However, the current induction protocol prevents the phenomenon of hydrate formation from being studied in isolation as it would also involve convection.

Visualisation experiments also allowed the lateral growth rates of cyclopentane hydrate to be measured and compared with other works with differing experimental configurations, which highlights how experimental arrangements can influence the behaviour of hydrate growth. Several predictive models were compared to the lateral growth rates. Peng et al.'s [29] and modified Liu et al.'s [30] models showed good agreement with the experimental results. However, fitted parameters in these models limit their applicability to the investigated geometry and condition.

PLIF thermometry was employed to obtain whole-field temperature measurements in cyclopentane and water, whilst PIV was used to investigate the velocity fields in both liquid-liquid phases. Since PLIF has not been applied with cyclopentane as a solvent, and the temperature range of interest between 266 to 273 K has not been widely covered in the literature, the application of the technique for the study of hydrate formation began with a proper selection of temperature sensitive dyes. A number of options were explored (e.g., self-fluorescence of cyclopentane and dissolving commonly available hydrophilic dyes in universal solvent), which were unsuccessful due to certain limitations. In the end, commercially available fluorescent nile red was selected as the fluorophore in cyclopentane. Nile red was experimentally characterised to reveal its optical properties such as the absorption and emission spectra, temperature and concentration dependence and linearity of its fluorescence intensity with varying temperature and concentration to determine the optimum dye concentration and evaluate its temperature sensitivity. Spectral analysis of nile red in cyclopentane also revealed that it is not a suitable dye for two-colour/one-dye PLIF thermometry for wavelengths in the range of 540 nm to 700 nm at an excitation of 532 nm. However, there is potential for its application in two-colour/two-dye PLIF thermometry, which has yet to be explored. The detailed spectral analysis of fluorescent dyes used in this work represents an important contribution to the literature and can provide options for other works involving PLIF thermometry not only in its application in hydrate studies (using other types of hydrate formers) but also extends its application in other relevant areas because of its wide range of applicability.

Experimental results obtained from PLIF thermometry and PIV revealed that there are observable differences in temperature and velocity between hydrate and non-hydrate cases. The influence of hydrate formation was found to be more pronounced in the water drop as compared to the surrounding liquid cyclopentane. Fluid flow by natural convection in the surrounding liquid cyclopentane phase was found to be two orders of magnitude larger compared to the internal flow in the drop which suggest that the surrounding phase is dominated by convection. Flow visualisation performed inside the water drop also showed the influence of drop shape and size on the flow pattern and indicated that there is flow reversal due to changes in the density of water as it gets supercooled. This could potentially affect the mechanism of heat removal

from the hydrate front and subsequently affect the growth rate. The temperature profiles in the drop make evident that the influence of hydrate formation is more pronounced at lower liquid cyclopentane temperature and smaller drop size. This improves our understanding on the growth of hydrate film at the interface and therefore helps in having a better interpretation of the phenomenon for future modeling works. An experimental database has been compiled for temperature and velocity measurements at temperatures in the range of 266 to 273 K, which would be useful for additional studies and modeling work.

This study introduced several novel elements. Firstly, morphological transitions in cyclopentane hydrate was identified. Specifically, dendritic and spherulitic structures were observed at subcooling temperatures greater than 7 K. This was made possible by conducting hydrate experiments at temperatures below the freezing point of water with proper characterisation of freezing and hydrate formation to confirm that there was no ice interference in the hydrate experiments. Secondly, advanced optical techniques were developed for hydrate application that provided first detailed spatio-temporal thermal-flow characterisaation of cyclopentane hydrate using PLIF and PIV. The measurements offer new insights into how hydrate formation influences temperature and flow and can be used as reference for future works involving other types of hydrate former.

7.2 Recommendations for future work

The results from this work has identified a number of challenges in the application of experimental techniques to hydrate formation, which requires further studies and development that would not only be limited to the study of hydrates but also to a wide range of other applications of these optical diagnostic tools. The learning outcome from this work also provides a basis for future work. Recommendations for further research are outlined in this section.

- There is significant potential for the development of PLIF thermometry for hydrate studies. Firstly, expanding the options of suitable fluorescent dye in organic liquid would allow temperature measurements to be carried out using two-colour PLIF technique that

will not only reduce error caused by laser pulse-to-pulse fluctuation but also minimise the effect of reflection on the interface and thus providing a more accurate and realistic temperature measurements at regions close to the interface.

- To address the loss of useful data at areas near the drop interface, the experiments can be performed using a thinner laser sheet which would reduce the area of the dark band at the interface and allows temperature information closer to the drop interface to be extracted. This can be achieved by adding a cylindrical lens or changing the focal length of the cylindrical lenses on the laser beam.

- Evaluation of temperature and velocity measurements were only performed at a location near the drop apex, which is believed to be the point where the influence of hydrate is most felt based on the flow patterns and temperature fields obtained. Analysis at different points along the interface would provide a comprehensive picture of the influence of hydrate on temperature and velocity at different locations near the interface.

- In the current work, direct visualisation, PLIF thermometry and PIV were conducted in separate experiments. Interactions between different processes based on the measured parameters at this point can only be inferred. Simultaneous measurements would provide a detailed understanding of the interactions between hydrodynamics and heat transfer processes during hydrate formation. However, this effort requires careful planning as it will add on to the complexity of the experiment, not just on the optical arrangements but also on the interactions between the fluorescent dye and tracer particles. Moreover, adding more additives into the fluid may have an influence on hydrate formation and therefore should also be taken into consideration.

- It would also be of interest to extend the application of PLIF to other types of hydrate formers, where the hydrate growth rate is significantly higher and thus the influence of hydrate formation would be more prominent. This would also add dimensions to the experimental database and give further insights to the similarities and differences between different hydrate formers with the aim of providing a global overview of the characteristics of hydrate which will aid in future development of predictive models.

- There is possibility that current hydrate induction protocol causes streaks to appear on PLIF images potentially due to the presence of microdroplets on the substrate, which are remnants from thawed iced used for hydrate induction. Future work can explore other types of hydrate induction that not only removes the streak but is also able to minimise experimental duration and at the same time does not promote freezing. Alternatively, the experiments can be performed using a different type of hydrate former for which high degree of subcooling can be achieved at temperatures above the freezing point of water. In such a case, hydrate induction can be achieved through the use of ice and hydrate seeds.

- Adding more data points to visualisation experiments, particularly at a lower subcooling temperature would be useful to investigate the relation between hydrate growth rate and subcooling temperature to confirm the transition between the different types of crystal growth mode based on its morphology.

- Performing measurements of instantaneous hydrate growth rate would be useful to capture the dynamics of hydrate growth. In combination with instantaneous PLIF and PIV measurements, which has been successfully applied in the present work, it can be used to study the influence of heat transfer on the growth rate.

Bibliography

[1] E Dendy Sloan Jr. Fundamental principles and applications of natural gas hydrates. *Nature*, 426(6964):353–359, 2003.

[2] Craig J Taylor, Kelly T Miller, Carolyn A Koh, and E Dendy Sloan Jr. Macroscopic investigation of hydrate film growth at the hydrocarbon/water interface. *Chemical Engineering Science*, 62(23):6524–6533, 2007.

[3] Ryo Ohmura, Wataru Shimada, Tsutomu Uchida, Yasuhiko H Mori, Satoshi Takeya, Jiro Nagao, Hideki Minagawa, Takao Ebinuma, and Hideo Narita. Clathrate hydrate crystal growth in liquid water saturated with a hydrate-forming substance: variations in crystal morphology. *Philosophical Magazine*, 84(1):1–16, 2004.

[4] Shun Oya, Muhammad Aifaa, and Ryo Ohmura. Formation, growth and sintering of co2 hydrate crystals in liquid water with continuous co2 supply: Implication for subsurface co2 sequestration. *International Journal of Greenhouse Gas Control*, 63:386–391, 2017.

[5] Bahman Tohidi, Ross Anderson, M Ben Clennell, Rod W Burgass, and Ali B Biderkab. Visual observation of gas-hydrate formation and dissociation in synthetic porous media by means of glass micromodels. *Geology*, 29(9):867–870, 2001.

[6] Tsutomu Uchida, Takao Ebinuma, Jun'ichi Kawabata, and Hideo Narita. Microscopic observations of formation processes of clathrate-hydrate films at an interface between water and carbon dioxide. *Journal of crystal growth*, 204(3):348–356, 1999.

[7] Ryo Ohmura, Sadatoshi Matsuda, Tsutomu Uchida, Takao Ebinuma, and Hideo Narita.

Clathrate hydrate crystal growth in liquid water saturated with a guest substance: observations in a methane+ water system. *Crystal growth & design*, 5(3):953–957, 2005.

[8] Xin Jiang, Baojiang Sun, Zhiyuan Wang, Wantian Zhou, Jiakai Ji, and Litao Chen. Methane hydrate crystal growth on shell substrate. *Chinese Journal of Chemical Engineering*, 43:50–61, 2022.

[9] Ryo Tanaka, Riki Sakemoto, and Ryo Ohmura. Crystal growth of clathrate hydrates formed at the interface of liquid water and gaseous methane, ethane, or propane: variations in crystal morphology. *Crystal Growth and Design*, 9(5):2529–2536, 2009.

[10] Eugene A Smelik and HE King. Crystal-growth studies of natural gas clathrate hydrates using a pressurized optical cell. *American Mineralogist*, 82(1-2):88–98, 1997.

[11] Hiroki Ueno, Hotaka Akiba, Satoru Akatsu, and Ryo Ohmura. Crystal growth of clathrate hydrates formed with methane+ carbon dioxide mixed gas at the gas/liquid interface and in liquid water. *New Journal of Chemistry*, 39(11):8254–8262, 2015.

[12] Ju Dong Lee, Myungho Song, Robin Susilo, and Peter Englezos. Dynamics of methane-propane clathrate hydrate crystal growth from liquid water with or without the presence of n-heptane. *Crystal growth & design*, 6(6):1428–1439, 2006.

[13] So Young Lee, Hyoung Chan Kim, and Ju Dong Lee. Morphology study of methane–propane clathrate hydrates on the bubble surface in the presence of sds or pvcap. *Journal of crystal growth*, 402:249–259, 2014.

[14] Riku Matsuura, Shunsuke Horii, Saman Alavi, and Ryo Ohmura. Diversity in crystal growth dynamics and crystal morphology of structure-h hydrate. *Crystal Growth & Design*, 19(11):6398–6404, 2019.

[15] Prasad U Karanjkar, Jae W Lee, and Jeffrey F Morris. Surfactant effects on hydrate crystallization at the water–oil interface: hollow-conical crystals. *Crystal growth & design*, 12(8):3817–3824, 2012.

[16] Makoto Mitarai, Masatoshi Kishimoto, Donguk Suh, and Ryo Ohmura. Surfactant effects on the crystal growth of clathrate hydrate at the interface of water and hydrophobic-guest liquid. *Crystal Growth & Design*, 15(2):812–821, 2015.

[17] Masatoshi Kishimoto, Satoshi Iijima, and Ryo Ohmura. Crystal growth of clathrate hydrate at the interface between seawater and hydrophobic-guest liquid: effect of elevated salt concentration. *Industrial & engineering chemistry research*, 51(14):5224–5229, 2012.

[18] Riki Sakemoto, Hiroki Sakamoto, Kuniaki Shiraiwa, Ryo Ohmura, and Tsutomu Uchida. Clathrate hydrate crystal growth at the seawater/hydrophobic- guest- liquid interface. *Crystal growth & design*, 10(3):1296–1300, 2010.

[19] Minjun Cha, Seungjun Baek, Jeffrey Morris, and Jae W Lee. Hydrophobic particle effects on hydrate crystal growth at the water–oil interface. *Chemistry–An Asian Journal*, 9(1): 261–267, 2014.

[20] Yu-An Lim, Ponnivalavan Babu, Rajnish Kumar, and Praveen Linga. Morphology of carbon dioxide–hydrogen–cyclopentane hydrates with or without sodium dodecyl sulfate. *Crystal Growth & Design*, 13(5):2047–2059, 2013.

[21] Hideo Watanabe and Hideyuki Kato. Thermal conductivity and thermal diffusivity of twenty-nine liquids: Alkenes, cyclic (alkanes, alkenes, alkadienes, aromatics), and deuterated hydrocarbons. *Journal of Chemical & Engineering Data*, 49(4):809–825, 2004.

[22] Gwyn Ardeshir Mali, Antonin Chapoy, and Bahman Tohidi. Investigation into the effect of subcooling on the kinetics of hydrate formation. *The Journal of Chemical Thermodynamics*, 117:91–96, 2018.

[23] Shanrong Wang, Mingjun Yang, Weiguo Liu, Jiafei Zhao, and Yongchen Song. Investigation on the induction time of methane hydrate formation in porous media under quiescent conditions. *Journal of Petroleum Science and Engineering*, 145:565–572, 2016.

[24] Weiguo Liu, Shanrong Wang, Mingjun Yang, Yongchen Song, Shenglong Wang, and Jiafei Zhao. Investigation of the induction time for thf hydrate formation in porous media. *Journal of natural gas science and engineering*, 24:357–364, 2015.

[25] William Chaze, Ophélie Caballina, Guillaume Castanet, and Fabrice Lemoine. The saturation of the fluorescence and its consequences for laser-induced fluorescence thermometry in liquid flows. *Experiments in Fluids*, 57:1–18, 2016.

[26] Sang-Ok Lee and Kenneth DM Harris. Controlling the crystal morphology of one-dimensional tunnel structures: induced crystallization of alkane/urea inclusion compounds as hexagonal flat plates. *Chemical physics letters*, 307(5-6):327–332, 1999.

[27] David Julian McClements. Crystals and crystallization in oil-in-water emulsions: Implications for emulsion-based delivery systems. *Advances in colloid and interface science*, 174:1–30, 2012.

[28] Yasuhiko H Mori. Estimating the thickness of hydrate films from their lateral growth rates: application of a simplified heat transfer model. *Journal of crystal growth*, 223(1-2): 206–212, 2001.

[29] BZ Peng, A Dandekar, CY Sun, H Luo, QL Ma, WX Pang, and GJ Chen. Hydrate film growth on the surface of a gas bubble suspended in water. *The Journal of Physical Chemistry B*, 111(43):12485–12493, 2007.

[30] Zheng Liu, Hao Li, Litao Chen, and Baojiang Sun. A new model of and insight into hydrate film lateral growth along the gas–liquid interface considering natural convection heat transfer. *Energy & Fuels*, 32(2):2053–2063, 2018.

[31] DE Hare and CM Sorensen. The density of supercooled water. ii. bulk samples cooled to the homogeneous nucleation limit. *The Journal of chemical physics*, 87(8):4840–4845, 1987.

[32] Peter Linstrom and William Mallard. The nist chemistry webbook: A chemical data resource on the internet. (46), 2001-09-01 2001.

[33] AKM Jamaluddin, N Kalogerakis, and PR Bishnoi. Hydrate plugging problems in undersea natural gas pipelines under shutdown conditions. *Journal of Petroleum Science and engineering*, 5(4):323–335, 1991.

[34] Christina Tzotzi, Thomas Parenteau, M Gainville, A Sinquin, C Cassar, D Turner, D Greaves, R Bass, MK Decrin, D Larrey, et al. Hydrate plug management full scale test: Hydrate plug dissociation in an electrically heated pipe in pipe. In *8th International Conference on Gas Hydrates ICGH8-2014*, 2014.

[35] Cornelius B Bavoh, Omar Nashed, Amirun Nissa Rehman, Nurul Akmal Aqidah Binti Othaman, Bhajan Lal, and Khalik M Sabil. Ionic liquids as gas hydrate thermodynamic inhibitors. *Industrial & Engineering Chemistry Research*, 60(44):15835–15873, 2021.

[36] David Parks and Robert Amin. Novel subsea gas dehydration process, the process plant and dehydration performance. *Journal of Petroleum Science and Engineering*, 81:94–99, 2012.

[37] Lichao Cai. *Desalination via formation of binary clathrate hydrates*. PhD thesis, Princeton University, 2016.

[38] Tianbiao He, Sajitha K Nair, Ponnivalavan Babu, Praveen Linga, and Iftekhar A Karimi. A novel conceptual design of hydrate based desalination (hydesal) process by utilizing lng cold energy. *Applied energy*, 222:13–24, 2018.

[39] Qiang Zhang, Junjie Zheng, Baoyong Zhang, and Praveen Linga. Coal mine gas separation of methane via clathrate hydrate process aided by tetrahydrofuran and amino acids. *Applied Energy*, 287:116576, 2021.

[40] Gyeol Ko, Joonseop Lee, and Yongwon Seo. Separation efficiency and equilibrium recovery ratio of sf6 in hydrate-based greenhouse gas separation. *Chemical Engineering Journal*, 405:126956, 2021.

[41] Yohan Lee, Dongyoung Lee, Jong-Won Lee, and Yongwon Seo. Enclathration of co2 as a co-guest of structure h hydrates and its implications for co2 capture and sequestration. *Applied energy*, 163:51–59, 2016.

[42] Ponnivalavan Babu, Rajnish Kumar, and Praveen Linga. Pre-combustion capture of carbon dioxide in a fixed bed reactor using the clathrate hydrate process. *Energy*, 50: 364–373, 2013.

[43] Laurence Fournaison, Anthony Delahaye, Imen Chatti, and Jean-Pierre Petitet. Co2 hydrates in refrigeration processes. *Industrial & engineering chemistry research*, 43(20): 6521–6526, 2004.

[44] Tomohiro Ogawa, Tomonari Ito, Kenji Watanabe, Ken-ichi Tahara, Ryuzo Hiraoka, Jun-ichi Ochiai, Ryo Ohmura, and Yasuhiko H Mori. Development of a novel hydrate-based refrigeration system: A preliminary overview. *Applied thermal engineering*, 26(17-18):2157–2167, 2006.

[45] Vladimir R Belosludov, Oleg S Subbotin, Dmitrii S Krupskii, Rodion V Belosludov, Yoshiyuki Kawazoe, and Jun-ichi Kudoh. Physical and chemical properties of gas hydrates: Theoretical aspects of energy storage application. *Materials transactions*, 48 (4):704–710, 2007.

[46] Hari Prakash Veluswamy, Alison Jia Hui Wong, Ponnivalavan Babu, Rajnish Kumar, Santi Kulprathipanja, Pramoch Rangsunvigit, and Praveen Linga. Rapid methane hydrate formation to develop a cost effective large scale energy storage system. *Chemical Engineering Journal*, 290:161–173, 2016.

[47] Mehdi Stiti, Alexandre Labergue, Fabrice Lemoine, Sebastien Leclerc, and Didier Stemmelen. Temperature measurement and state determination of supercooled droplets using laser-induced fluorescence. *Experiments in Fluids*, 60:1–13, 2019.

[48] Sukanta Mondal, Gourhari Jana, Hemant K Srivastava, Garikapati N Sastry, and Pratim Kumar Chattaraj. Structure and stability of the sh binary hydrate cavity and host-guest versus guest-guest interactions therein: A dft approach. *Journal of Computational Chemistry*, 44(15):1446–1453, 2023.

[49] Hideki Tanaka. Stability and dynamics of ice and clathrate hydrate. In *Theoretical and computational chemistry*, pages 533–578. Elsevier, 1999.

[50] E Dendy Sloan Jr and Carolyn A Koh. *Clathrate hydrates of natural gases*. CRC press, 2007.

[51] Ju Dong Lee, Robin Susilo, and Peter Englezos. Methane–ethane and methane–propane hydrate formation and decomposition on water droplets. *Chemical Engineering Science*, 60(15):4203–4212, 2005.

[52] Richard Becker and Werner Döring. Kinetische behandlung der keimbildung in übersättigten dämpfen. *Annalen der physik*, 416(8):719–752, 1935.

[53] Amadeu K Sum, Carolyn A Koh, and E Dendy Sloan. Clathrate hydrates: from laboratory science to engineering practice. *Industrial & Engineering Chemistry Research*, 48(16):7457–7465, 2009.

[54] Muhammad Aifaa, Takehide Kodama, and Ryo Ohmura. Crystal growth of clathrate hydrate in a flowing liquid water system with methane gas. *Crystal Growth & Design*, 15 (2):559–563, 2015.

[55] Camilo Martinez, Juan F Sandoval, Nathalia Ortiz, Sebastian Ovalle, and Juan G Beltran. Mechanisms, growth rates, and morphologies of gas hydrates of carbon dioxide, methane, and their mixtures. *Methane*, 1(01), 2021.

[56] Akihisa Hirata and Yasuhiko H Mori. How liquids wet clathrate hydrates: some macroscopic observations. *Chemical engineering science*, 53(14):2641–2643, 1998.

[57] Jorge Peixinho, Valentin Ageorges, and Benoit Duchemin. Growth of clathrate hydrates from water drops in cyclopentane. *Energy & Fuels*, 32(3):2693–2698, 2017.

[58] Sanbao Dong, Chenwei Liu, Weiwei Han, Mingzhong Li, Jie Zhang, and Gang Chen. The effect of the hydrate antiagglomerant on hydrate crystallization at the oil–water interface. *ACS omega*, 5(7):3315–3321, 2020.

[59] Abdelhafid Touil, Daniel Broseta, Nelly Hobeika, and Ross Brown. Roles of wettability and supercooling in the spreading of cyclopentane hydrate over a substrate. *Langmuir*, 33(41):10965–10977, 2017.

[60] Qiang Sun, Mei Du, Xingxun Li, Xuqiang Guo, and Lanying Yang. Morphology

investigation on cyclopentane hydrate formation/dissociation in a sub-millimeter-sized capillary. *Crystals*, 9(6):307, 2019.

[61] I Sunagawa. Crystals: Growth, morphology and perfection cambridge univ, 2005.

[62] William W Mullins and Robert F Sekerka. Morphological stability of a particle growing by diffusion or heat flow. *Journal of applied physics*, 34(2):323–329, 1963.

[63] Sheng-Li Li, Chang-Yu Sun, Bei Liu, Zhi-Yun Li, Guang-Jin Chen, and Amadeu K Sum. New observations and insights into the morphology and growth kinetics of hydrate films. *Scientific reports*, 4(1):4129, 2014.

[64] Toshiyuki Nakamura, Takashi Makino, Takeshi Sugahara, and Kazunari Ohgaki. Stability boundaries of gas hydrates helped by methane—structure-h hydrates of methylcyclohexane and cis-1, 2-dimethylcyclohexane. *Chemical engineering science*, 58 (2):269–273, 2003.

[65] Akihiro Hachikubo, Atsushi Miyamoto, Kinji Hyakutake, K Abe, and H Shoji. Phase equilibrium studies on gas hydrates formed from various guest molecules and powder ice. In *Fourth International Conference on Gas Hydrates, Japan*, volume 1, pages 357–360, 2002.

[66] Erik M Freer, M Sami Selim, and E Dendy Sloan Jr. Methane hydrate film growth kinetics. *Fluid Phase Equilibria*, 185(1-2):65–75, 2001.

[67] Chang-Yu Sun, Guang-Jin Chen, and Lan-Ying Yang. Interfacial tension of methane+ water with surfactant near the hydrate formation conditions. *Journal of Chemical & Engineering Data*, 49(4):1023–1025, 2004.

[68] Misato Kitamura and Yasuhiko H Mori. Clathrate-hydrate film growth along water/methane phase boundaries—an observational study. *Crystal Research and Technology*, 48(8):511–519, 2013.

[69] Henry Delroisse, Jean-Philippe Torré, and Christophe Dicharry. Effect of a hydrophilic

cationic surfactant on cyclopentane hydrate crystal growth at the water/cyclopentane interface. *Crystal Growth & Design*, 17(10):5098–5107, 2017.

[70] R Larsen, A Lund, V Andersson, and KW Hjarbo. Conversion of water to hydrate particles. In *SPE Annual Technical Conference and Exhibition?*, pages SPE–71550. SPE, 2001.

[71] Erika P Brown and Carolyn A Koh. Micromechanical measurements of the effect of surfactants on cyclopentane hydrate shell properties. *Physical Chemistry Chemical Physics*, 18(1):594–600, 2016.

[72] Laura E. Dieker, Craig J. Taylor, Carolyn A. Koh, and E. Dendy Sloan. Micromechanical adhesion force measurements between cyclopentane hydrate particles, Jul 2008. URL `https://open.library.ubc.ca/cIRcle/collections/59278/items/1.0040979`.

[73] Markus Schremb and Cameron Tropea. Solidification of supercooled water in the vicinity of a solid wall. *Physical review E*, 94(5):052804, 2016.

[74] Faryar Tavakoli, Stephen H Davis, and H Pirouz Kavehpour. Freezing of supercooled water drops on cold solid substrates: initiation and mechanism. *Journal of Coatings Technology and Research*, 12:869–875, 2015.

[75] Jason P Hindmarsh, Alexander B Russell, and Xiao D Chen. Experimental and numerical analysis of the temperature transition of a suspended freezing water droplet. *International Journal of Heat and Mass Transfer*, 46(7):1199–1213, 2003.

[76] Juan G Beltrán and Phillip Servio. Morphological investigations of methane- hydrate films formed on a glass surface. *Crystal growth & design*, 10(10):4339–4347, 2010.

[77] Tsutomu Uchida, Ikuko Y Ikeda, Satoshi Takeya, Takao Ebinuma, Jiro Nagao, and Hideo Narita. Co2 hydrate film formation at the boundary between co2 and water: effects of temperature, pressure and additives on the formation rate. *Journal of crystal growth*, 237:383–387, 2002.

[78] Chang-Yu Sun, Guang-Jin Chen, Chang-Feng Ma, Qiang Huang, Hu Luo, and Qing-Ping Li. The growth kinetics of hydrate film on the surface of gas bubble suspended in water or aqueous surfactant solution. *Journal of Crystal Growth*, 306(2):491–499, 2007.

[79] Hannah M Stoner, Anh Phan, Alberto Striolo, and Carolyn A Koh. Water wettability coupled with film growth on realistic cyclopentane hydrate surfaces. *Langmuir*, 37(42): 12447–12456, 2021.

[80] Shane A Morrissy, Angus J McKenzie, Brendan F Graham, Michael L Johns, Eric F May, and Zachary M Aman. Reduction of clathrate hydrate film growth rate by naturally occurring surface active components. *Energy & Fuels*, 31(6):5798–5805, 2017.

[81] Maria Lourdes Martinez de Baños, Odile Carrier, Patrick Bouriat, and Daniel Broseta. Droplet-based millifluidics as a new tool to investigate hydrate crystallization: Insights into the memory effect. *Chemical Engineering Science*, 123:564–572, 2015.

[82] Kazuki Imasato, Hiroki Tokutomi, and Ryo Ohmura. Crystal growth behavior of methane hydrate in the presence of liquid hydrocarbon. *Crystal Growth & Design*, 15(1):428–433, 2015.

[83] Armin Kalita, Maximillian Mrozek-McCourt, Thomas F Kaldawi, Philip R Willmott, N Duane Loh, Sebastian Marte, Raymond G Sierra, Hartawan Laksmono, Jason E Koglin, Matt J Hayes, et al. Microstructure and crystal order during freezing of supercooled water drops. *Nature*, 620(7974):557–561, 2023.

[84] BJ Murray, SL Broadley, TW Wilson, SJ Bull, RH Wills, HK Christenson, and EJ Murray. Kinetics of the homogeneous freezing of water. *Physical Chemistry Chemical Physics*, 12(35):10380–10387, 2010.

[85] Edwin Roedder. Metastable superheated ice in liquid-water inclusions under high negative pressure. *Science*, 155(3768):1413–1417, 1967.

[86] JW Mullin. *Crystallization*, volume 124. Butterworth-Heinemann, 2001.

[87] V Natarajan, PR Bishnoi, and N Kalogerakis. Induction phenomena in gas hydrate nucleation. *Chemical Engineering Science*, 49(13):2075–2087, 1994.

[88] Lars Jensen, Kaj Thomsen, and Nicolas von Solms. Propane hydrate nucleation: Experimental investigation and correlation. *Chemical Engineering Science*, 63(12): 3069–3080, 2008.

[89] Yu Zhong and RE Rogers. Surfactant effects on gas hydrate formation. *Chemical engineering science*, 55(19):4175–4187, 2000.

[90] Dimo Kashchiev and Abbas Firoozabadi. Induction time in crystallization of gas hydrates. *Journal of crystal growth*, 250(3-4):499–515, 2003.

[91] Anthony Vysniauskas and PR Bishnoi. A kinetic study of methane hydrate formation. *Chemical Engineering Science*, 38(7):1061–1072, 1983.

[92] Son Ho-Van, Baptiste Bouillot, Daniel Garcia, Jérome Douzet, Ana Cameirao, Saheb Maghsoodloo-Babakhani, and Jean-Michel Herri. Crystallization mechanisms and rates of cyclopentane hydrates formation in brine. *Chemical engineering & technology*, 42(7): 1481–1491, 2019.

[93] Genti Zylyftari, Amit Ahuja, and Jeffrey F Morris. Nucleation of cyclopentane hydrate by ice studied by morphology and rheology. *Chemical Engineering Science*, 116:497–507, 2014.

[94] Wenxin Niu and Guobao Xu. Crystallographic control of noble metal nanocrystals. *Nano Today*, 6(3):265–285, 2011.

[95] Laureano Ortellado and Leopoldo R Gómez. Phase field modeling of dendritic growth on spherical surfaces. *Frontiers in Materials*, 7:163, 2020.

[96] James S Langer. Instabilities and pattern formation in crystal growth. *Reviews of modern physics*, 52(1):1, 1980.

[97] R Hilpert. Heat transfer from cylinders. *Forsch. Geb. Ingenieurwes*, 4(5):215, 1933.

[98] Shuichiro Hirai, Yutaka Tabe, Satoshi Kamijo, and Ken OKAZAKI. Lateral growth rates of co 2 clathrate-hydrate film. *Thermal Science and Engineering*, 8(5):1–6, 2000.

[99] Ryo Ohmura, Shigetoyo Kashiwazaki, and Yasuhiko H Mori. Measurements of clathrate-hydrate film thickness using laser interferometry. *Journal of crystal growth*, 218(2-4):372–380, 2000.

[100] Margaret Fishenden and OA Saunders. *An introduction to heat transfer*. The Clarendon Press, 1950.

[101] Witold M Lewandowski, Ewa Radziemska, Maciej Buzuk, and Henryk Bieszk. Free convection heat transfer and fluid flow above horizontal rectangular plates. *Applied energy*, 66(2):177–197, 2000.

[102] DA Saville and Stuart Winston Churchill. Laminar free convection in boundary layers near horizontal cylinders and vertical axisymmetric bodies. *Journal of Fluid Mechanics*, 29(2):391–399, 1967.

[103] S Co R Dennis, JD Hudson, and N Smith. Steady laminar forced convection from a circular cylinder at low reynolds numbers. *The Physics of Fluids*, 11(5):933–940, 1968.

[104] Takaaki Mochizuki and Yasuhiko H Mori. Clathrate-hydrate film growth along water/hydrate-former phase boundaries—numerical heat-transfer study. *Journal of crystal growth*, 290(2):642–652, 2006.

[105] Ryo Ohmura, Mikio Ogawa, Kenji Yasuoka, and Yasuhiko H Mori. Statistical study of clathrate-hydrate nucleation in a water/hydrochlorofluorocarbon system: Search for the nature of the "memory effect". *The Journal of Physical Chemistry B*, 107(22):5289–5293, 2003.

[106] CJ Brown and X Ni. Evaluation of rate of cyclopentane hydrate formation in an oscillatory baffled column using laser induced fluorescence and energy balance. *Chemical Engineering Journal*, 157(1):131–139, 2010.

[107] Shuichiro Hirai, Yutaka Tabe, Kunihiro Kuwano, Kuniyasu Ogawa, and KEN Okazaki. Mri measurement of hydrate growth and an application to advanced co2 sequestration technology. *Annals of the New York Academy of Sciences*, 912(1):246–253, 2000.

[108] Shuichiro Hirai, Ken Okazaki, Norio Araki, Koji Yoshimoto, Hiroshi Ito, and Kunio Hijikata. Experiments for dynamic behavior of carbon dioxide in deep sea. *Energy conversion and management*, 36(6-9):471–474, 1995.

[109] Yuichiro Sabase and Kazushige Nagashima. Growth mode transition of tetrahydrofuran clathrate hydrates in the guest/host concentration boundary layer. *The Journal of Physical Chemistry B*, 113(46):15304–15311, 2009.

[110] Roman Volkov and Pavel Strizhak. Temperature recording of the ice–water system using planar laser induced fluorescence. *Experimental Thermal and Fluid Science*, 131:110532, 2022.

[111] Jun Sakakibara, Koichi Hishida, and Masanobu Maeda. Measurements of thermally stratified pipe flow using image-processing techniques. *Experiments in Fluids*, 16:82–96, 1993.

[112] Tsuyoshi Nakajima, Motoyasu Utsunomiya, and Yuji Ikeda. Simultaneous measurement of velocity and temperature of water using ldv and fluorescence technique. In *Applications of Laser Techniques to Fluid Mechanics: 5th International Symposium Lisbon, Portugal, 9-12 July, 1990*, pages 34–53. Springer, 1991.

[113] Jeffrey A Sutton, Brian T Fisher, and James W Fleming. A laser-induced fluorescence measurement for aqueous fluid flows with improved temperature sensitivity. *Experiments in Fluids*, 45(5):869–881, 2008.

[114] M Wolff, A Delconte, F Schmidt, P Gucher, and F Lemoine. High-pressure diesel spray temperature measurements using two-colour laser-induced fluorescence. *Measurement Science and Technology*, 18(3):697, 2007.

[115] Pierre Doublet, Christine Lempereur, Mikael Orain, Virginel Bodoc, and Pierre Gajan.

Saturated laser-induced fluorescence in liquid kerosene seeded with a dye: influence of temperature and excitation intensity. *Applied Physics B*, 125:1–8, 2019.

[116] Matthias Koegl, Moritz Delwig, and Lars Zigan. Characterization of fluorescence tracers for thermometry and film thickness measurements in liquid coolants relevant for thermal management of electric and electronic components. *Sensors*, 22(22):8892, 2022.

[117] MCJ Coolen, RN Kieft, CCM Rindt, and AA Van Steenhoven. Application of 2-d lif temperature measurements in water using a nd: Yag laser. *Experiments in Fluids*, 27: 420–426, 1999.

[118] V Voulgaropoulos, GM Aguiar, OK Matar, M Bucci, and CN Markides. Temperature and velocity field measurements of pool boiling using two-colour laser-induced fluorescence, infrared thermometry and particle image velocimetry. In *10th international conference on multiphase flow*, pages 1–9, 2019.

[119] HJ Kim, KD Kihm, and JS Allen. Examination of ratiometric laser induced fluorescence thermometry for microscale spatial measurement resolution. *International Journal of Heat and Mass Transfer*, 46(21):3967–3974, 2003.

[120] K Hishida and J Sakakibara. Combined planar laser-induced fluorescence–particle image velocimetry technique for velocity and temperature fields. *Experiments in Fluids*, 29 (Suppl 1):S129–S140, 2000.

[121] Guilin Liu and Haiying Lu. Laser-induced fluorescence of rhodamine b in ethylene glycol solution. *Procedia Engineering*, 102:95–105, 2015.

[122] Henrik Rochlitz and Peter Scholz. Application of laser-induced fluorescence technique in a duct flow with one heated wall. *Experiments in Fluids*, 59(3):54, 2018.

[123] Matthias Bruchhausen, Fabrice Guillard, and Fabrice Lemoine. Instantaneous measurement of two-dimensional temperature distributions by means of two-color planar laser induced fluorescence (plif). *Experiments in fluids*, 38(1):123–131, 2005.

[124] J Coppeta and C Rogers. Dual emission laser induced fluorescence for direct planar scalar behavior measurements. *Experiments in Fluids*, 25(1):1–15, 1998.

[125] DA Walker. A fluorescence technique for measurement of concentration in mixing liquids. *Journal of Physics E: Scientific Instruments*, 20(2):217, 1987.

[126] P Lavieille, F Lemoine, G Lavergne, and M Lebouché. Evaporating and combusting droplet temperature measurements using two-color laser-induced fluorescence. *Experiments in fluids*, 31(1):45–55, 2001.

[127] P Lavieille, A Delconte, D Blondel, M Lebouché, and F Lemoine. Non-intrusive temperature measurements using three-color laser-induced fluorescence. *Experiments in fluids*, 36(5):706–716, 2004.

[128] Jun Sakakibara and Ronald J Adrian. Whole field measurement of temperature in water using two-color laser induced fluorescence. *Experiments in Fluids*, 26(1-2):7–15, 1999.

[129] M Behshad Shafii, Chee L Lum, and Manoochehr M Koochesfahani. In situ lif temperature measurements in aqueous ammonium chloride solution during uni-directional solidification. *Experiments in fluids*, 48:651–662, 2010.

[130] Gustavo M Aguiar, Victor Voulgaropoulos, Omar K Matar, Christos N Markides, and Matteo Bucci. Experimental investigation of bubble nucleation, growth and departure using synchronized ir thermometry, two-color lif and piv. In *18th International Topical Meeting on Nuclear Reactor Thermal Hydraulics (NURETH-18)*, 2019.

[131] Sichao Tan, Carlos E Estrada-Perez, Elvis E Dominguez-Ontiveros, and Yassin A Hassan. Experimental study of temperature sensitive dyes for planar laser induced fluorescence thermometer. In *International Conference on Nuclear Engineering*, volume 49323, pages 343–347, 2010.

[132] Linn Karlsson, Anna-Lena Ljung, and Staffan T. Lundström. Comparing internal flow in freezing and evaporating water droplets using piv. *Water*, 12(5):1489, 2020.

[133] Erik Fagerström and Anna-Lena Ljung. Internal flow in freezing and non-freezing water droplets at freezing temperatures. *International Journal of Heat and Mass Transfer*, 234: 126100, 2024.

[134] Victor Voulgaropoulos, Mohammadreza Kadivar, Mohammad Ardekani Moghimi, Mohamed Maher, Hameed Alawadi, Omar K Matar, and Christos N Markides. A combined experimental and computational study of phase-change dynamics and flow inside a sessile water droplet freezing due to interfacial heat transfer. *International Journal of Heat and Mass Transfer*, 180:121803, 2021.

[135] Masahiro Nakajima, Ryo Ohmura, and Yasuhiko H Mori. Clathrate hydrate formation from cyclopentane-in-water emulsions. *Industrial & Engineering Chemistry Research*, 47 (22):8933–8939, 2008.

[136] Zachary M Aman. *Interfacial phenomena of cyclopentane hydrate*. Colorado School of Mines, 2012.

[137] Harshad Pathak, Alexander Späh, Kyung Hwan Kim, Ifigeneia Tsironi, Daniel Mariedahl, Maria Blanco, Simo Huotari, Veijo Honkimäki, and Anders Nilsson. Intermediate range o–o correlations in supercooled water down to 235 k. *The Journal of Chemical Physics*, 150(22), 2019.

[138] CA Angell, J Shuppert, and JC Tucker. Anomalous properties of supercooled water. heat capacity, expansivity, and proton magnetic resonance chemical shift from 0 to-38%. *The Journal of Physical Chemistry*, 77(26):3092–3099, 1973.

[139] D Niedermeier, RA Shaw, S Hartmann, H Wex, T Clauss, J Voigtländer, and F Stratmann. Heterogeneous ice nucleation: exploring the transition from stochastic to singular freezing behavior. *Atmospheric Chemistry and Physics*, 11(16):8767–8775, 2011.

[140] Reuben Wu, Karen A Kozielski, Patrick G Hartley, Eric F May, John Boxall, and Nobuo Maeda. Probability distributions of gas hydrate formation. *AIChE Journal*, 59(7): 2640–2646, 2013.

[141] SJ Ahmadpanah, M Manteghian, and H Ganji. Effect of cyclopentane and sodium chloride on the formation kinetics of natural gas hydrate in different operating conditions. *Journal of Natural Gas Science and Engineering*, 99:104417, 2022.

[142] Meng-yang Li, Ming Gao, Qi-rong Zuo, Yu-gang Zhao, and Li-xin Zhang. Experimental and theoretical investigation on hydrate nucleation in tbab droplets. *Fuel*, 308:121994, 2022.

[143] Nobuyuki Otsu. A threshold selection method from gray-level histograms. *IEEE transactions on systems, man, and cybernetics*, 9(1):62–66, 1979.

[144] RE Herold and JB Ghandhi. Data normalization schemes for assessing mixture stratification from plif data. *SAE International Journal of Fuels and Lubricants*, 1(1): 559–569, 2009.

[145] Luis A Torres, Brian A Fleck, David J Wilson, and David S Nobes. Calibration of a planar laser induced fluorescence technique for use in large scale water facilities. *Measurement*, 46(8):2597–2607, 2013.

[146] AJ Ferrier, DR Funk, and PJW Roberts. Application of optical techniques to the study of plumes in stratified fluids. *Dynamics of Atmospheres and Oceans*, 20(1-2):155–183, 1993.

[147] Cameron Tropea, Alexander L Yarin, John F Foss, et al. *Springer handbook of experimental fluid mechanics*, volume 1. Springer, 2007.

[148] Harold Arthur Palmer. *Characterization of hydrocarbon-type hydrates*. The University of Oklahoma, 1997.

[149] TP Adamova, A Yu Manakov, and AS Stoporev. Laboratory reactor for visual examination of formation/decomposition of gas hydrates in water-oil systems. *Russian Journal of Applied Chemistry*, 92:607–613, 2019.

[150] Daniel Rosenfeld and William L Woodley. Deep convective clouds with sustained supercooled liquid water down to-37.5 c. *Nature*, 405(6785):440–442, 2000.

[151] Hans R Pruppacher. A new look at homogeneous ice nucleation in supercooled water drops. *Journal of the atmospheric sciences*, 52(11):1924–1933, 1995.

[152] BJ Murray, D O'sullivan, JD Atkinson, and ME Webb. Ice nucleation by particles immersed in supercooled cloud droplets. *Chemical Society Reviews*, 41(19):6519–6554, 2012.

[153] C Hoose and O Möhler. Heterogeneous ice nucleation on atmospheric aerosols: a review of results from laboratory experiments. *Atmospheric Chemistry and Physics*, 12(20): 9817–9854, 2012.

[154] Claudia Marcolli. Ice nucleation triggered by negative pressure. *Scientific reports*, 7(1): 16634, 2017.

[155] Elise Rosky, Will Cantrell, Tianshu Li, and Raymond A Shaw. Homogeneous ice nucleation rate at negative pressures: The role of the density anomaly. *Chemical Physics Letters*, 789:139289, 2022.

[156] Susmita Dash, Jolet de Ruiter, and Kripa K Varanasi. Photothermal trap utilizing solar illumination for ice mitigation. *Science advances*, 4(8):eaat0127, 2018.

[157] Alvaro G Marin, Oscar R Enriquez, Philippe Brunet, Pierre Colinet, and Jacco H Snoeijer. Universality of tip singularity formation in freezing water drops. *Physical review letters*, 113(5):054301, 2014.

[158] Jacco H Snoeijer and Philippe Brunet. Pointy ice-drops: How water freezes into a singular shape. *American Journal of Physics*, 80(9):764–771, 2012.

[159] Md Farhad Ismail and Prashant R Waghmare. Universality in freezing of an asymmetric drop. *Applied Physics Letters*, 109(23), 2016.

[160] Xuan Zhang, Xin Liu, Jingchun Min, and Xiaomin Wu. Shape variation and unique tip formation of a sessile water droplet during freezing. *Applied thermal engineering*, 147: 927–934, 2019.

[161] Stefan Jung, Manish K Tiwari, N Vuong Doan, and Dimos Poulikakos. Mechanism of supercooled droplet freezing on surfaces. *Nature communications*, 3(1):615, 2012.

[162] François Feuillebois, A Lasek, P Creismeas, F Pigeonneau, and A Szaniawski. Freezing of a subcooled liquid droplet. *Journal of colloid and interface science*, 169(1):90–102, 1995.

[163] Victor F Petrenko and Robert W Whitworth. *Physics of ice*. OUP Oxford, 1999.

[164] Aris Ikiades, Glen Howard, David J Armstrong, Mary Konstantaki, and Sam Crossley. Measurement of optical diffusion properties of ice for direct detection ice accretion sensors. *Sensors and Actuators A: physical*, 140(1):24–31, 2007.

[165] Christophe Dicharry, H Delroisse, J-P Torré, and G Barreto. Using microscopic observations of cyclopentane hydrate crystal morphology and growth patterns to estimate the antiagglomeration capacity of surfactants. *Energy & Fuels*, 34(5):5176–5187, 2019.

[166] Chenru Zhou, Chenwei Liu, Mingzhong Li, Zhen Liu, and Zhiyuan Wang. Investigation of the morphology of secondary nucleation of hydrate from a water droplet in liquid cyclopentane. *Energy & Fuels*, 38(3):1766–1780, 2024.

[167] Dongsheng Bai, Guangjin Chen, Xianren Zhang, Amadeu K Sum, and Wenchuan Wang. How properties of solid surfaces modulate the nucleation of gas hydrate. *Scientific reports*, 5(1):12747, 2015.

[168] Yuanfei Bi, Boxiao Cao, and Tianshu Li. Enhanced heterogeneous ice nucleation by special surface geometry. *Nature communications*, 8(1):15372, 2017.

[169] Baban Nagare, Claudia Marcolli, André Welti, Olaf Stetzer, and Ulrike Lohmann. Comparing contact and immersion freezing from continuous flow diffusion chambers. *Atmospheric Chemistry and Physics*, 16(14):8899–8914, 2016.

[170] Jun Chen, Guang-Jin Chen, Qing Yuan, Bin Deng, Li-Ming Tao, Chuan-Hua Li, Sheng-Xiong Xiao, Jian-Hong Jiang, Xu Li, and Jia-Yuan Li. Insights into induction time and agglomeration of methane hydrate formation in diesel oil dominated dispersed systems. *Energy*, 170:604–610, 2019.

[171] Meku Maruyama and Ryo Ohmura. Equilibrium properties and crystal growth of d2o+ cyclopentane hydrate for sustainable tritium separation. *The Canadian Journal of Chemical Engineering*, 101(2):718–725, 2023.

[172] María Lourdes Martínez de Baños, Nelly Hobeika, Patrick Bouriat, Daniel Broseta, Eduardo Enciso, Franck Clement, and Ross Brown. How do gas hydrates spread on a substrate? *Crystal Growth & Design*, 16(8):4360–4373, 2016.

[173] Prasad U Karanjkar, Jae W Lee, and Jeffrey F Morris. Calorimetric investigation of cyclopentane hydrate formation in an emulsion. *Chemical engineering science*, 68(1): 481–491, 2012.

[174] Takaaki Mochizuki and Yasuhiko H Mori. Simultaneous mass and heat transfer to/from the edge of a clathrate-hydrate film causing its growth along a water/guest-fluid phase boundary. *Chemical Engineering Science*, 171:61–75, 2017.

[175] K Boode and P Walstra. Partial coalescence in oil-in-water emulsions 1. nature of the aggregation. *Colloids and Surfaces A: Physicochemical and Engineering Aspects*, 81: 121–137, 1993.

[176] Roja Ergun, Richard W Hartel, and Patrick T Spicer. Kinetic effects on interfacial partitioning of fat crystals. *Food Structure*, 5:1–9, 2015.

[177] Phillip Servio and Peter Englezos. Morphology of methane and carbon dioxide hydrates formed from water droplets. *AIChE journal*, 49(1):269–276, 2003.

[178] W.K. Burton, N. Cabrera, and F.C. Frank. The growth of crystals and the equilibrium structure of their surfaces. *Philosophical Transactions of the Royal Society of London. Series A, Mathematical and Physical Sciences*, 243(866):299–358, 1951.

[179] Pablo Cubillas and Michael W Anderson. Synthesis mechanism: crystal growth and nucleation. *Zeolites and catalysis: synthesis, reactions and applications*, pages 1–55, 2010.

[180] László Gránásy, Tamás Pusztai, György Tegze, James A Warren, and Jack F Douglas. Growth and form of spherulites. *Physical Review E*, 72(1):011605, 2005.

[181] Christo N Nanev. Polyhedral instability—skeletal and dendritic growth. *Progress in crystal growth and characterization of materials*, 35(1):1–26, 1997.

[182] ME Glicksman and AO Lupulescu. Dendritic crystal growth in pure materials. *Journal of crystal growth*, 264(4):541–549, 2004.

[183] E Dendy Sloan. Gas hydrates: review of physical/chemical properties. *Energy & fuels*, 12(2):191–196, 1998.

[184] John W Biddle, Vincent Holten, Jan V Sengers, and Mikhail A Anisimov. Thermal conductivity of supercooled water. *Physical Review E—Statistical, Nonlinear, and Soft Matter Physics*, 87(4):042302, 2013.

[185] Bruno J Zwolinski and Lawrence D Eicher. High-precision viscosity of supercooled water and analysis of the extended range temperature coefficient. *The Journal of Physical Chemistry*, 75(13):2016–2024, 1971.

[186] Kenneth R Harris, Paula J Newitt, and Lawrence A Woolf. Temperature and density dependence of the viscosity of cyclopentane. *Journal of Chemical & Engineering Data*, 49(1):138–142, 2004.

[187] Andrea Taschin, Paolo Bartolini, Roberto Eramo, and Renato Torre. Supercooled water relaxation dynamics probed with heterodyne transient grating experiments. *Physical Review E—Statistical, Nonlinear, and Soft Matter Physics*, 74(3):031502, 2006.

[188] C.-M. Vassiliou, M. J. Assael, M. L. Huber, and R. A. Perkins. Reference correlations of the thermal conductivity of cyclopentane, iso-pentane, and n-pentane. *Journal of Physical and Chemical Reference Data*, 44(3):033102, 08 2015.

[189] Donald G Archer and Richard W Carter. Thermodynamic properties of the nacl+ h2o system. 4. heat capacities of h2o and nacl (aq) in cold-stable and supercooled states. *The Journal of Physical Chemistry B*, 104(35):8563–8584, 2000.

[190] GJ Szasz, JA Morrison, EL Pace, and JG Aston. Thermal properties of cyclopentane and

its use as a standard substance in low temperature thermal measurements. *The Journal of Chemical Physics*, 15(8):562–564, 1947.

[191] Vincent Holten, CE Bertrand, MA Anisimov, and JV Sengers. Thermodynamics of supercooled water. *The Journal of chemical physics*, 136(9), 2012.

[192] National Institute of Standards and Technology. Security requirements for cryptographic modules. Technical Report Federal Information Processing Standards Publications (FIPS PUBS) 140-2, Change Notice 2 December 03, 2002, U.S. Department of Commerce, Washington, D.C., 2001.

[193] Sheng-Li Li, Chang-Yu Sun, Bei Liu, Xiu-Jun Feng, Feng-Guang Li, Li-Tao Chen, and Guang-Jin Chen. Initial thickness measurements and insights into crystal growth of methane hydrate film. *AIChE Journal*, 59(6):2145–2154, 2013.

[194] RC Birkebak and A Abdulkadir. Heat transfer by natural convection from the lower side of finite horizontal, heated surface. In *Proceedings of Fourth Int. Heat Transfer Conference, Heat Transfer*, pages 1–10, 1970.

[195] Shefaza Esmail and Juan G Beltran. Methane hydrate propagation on surfaces of varying wettability. *Journal of Natural Gas Science and Engineering*, 35:1535–1543, 2016.

[196] V Voulgaropoulos, GM Aguiar, CN Markides, and M Bucci. Simultaneous laser-induced fluorescence, particle image velocimetry and infrared thermography for the investigation of the flow and heat transfer characteristics of nucleating vapour bubbles. *International Journal of Heat and Mass Transfer*, 187:122525, 2022.

[197] Joseph R Lakowicz and Ignacy Gryczynski. Fluorescence intensity decays of cyclohexane and methylcyclohexane with two-photon excitation from a high repetition rate frequency-doubled dye laser. *Biospectroscopy*, 1(1):3–8, 1995.

[198] Fumio Hirayama, William Rothman, and Sanford Lipsky. Fluorescence of saturated hydrocarbons. ii. the effect of alkyl substituents. *Chemical Physics Letters*, 5(5):296–298, 1970.

[199] Phillip Greenspan and Stanley D Fowler. Spectrofluorometric studies of the lipid probe, nile red. *Journal of lipid research*, 26(7):781–789, 1985.

[200] Ashim Kumar Dutta, Kenji Kamada, and Koji Ohta. Spectroscopic studies of nile red in organic solvents and polymers. *Journal of photochemistry and photobiology A: Chemistry*, 93(1):57–64, 1996.

[201] Matthias Koegl, Mohammad Pahlevani, and Lars Zigan. A novel approach for measurement of composition and temperature of n-decane/butanol blends using two-color laser-induced fluorescence of nile red. *Sensors*, 20(19):5721, 2020.

[202] Carlos E Estrada-Pérez, Yassin A Hassan, and Sichao Tan. Experimental characterization of temperature sensitive dyes for laser induced fluorescence thermometry. *Review of Scientific Instruments*, 82(7), 2011.

[203] MJ Hwang, DA Wright, A Kapur, and GD Holder. An experimental study of crystallization and crystal growth of methane hydrates from melting ice. *Journal of inclusion phenomena and molecular recognition in chemistry*, 8:103–116, 1990.

[204] Yingming Xie, Kaihua Guo, Deqing Liang, Shuanshi Fan, Jianming Gu, and Jinggui Chen. Gas hydrate fast nucleation from melting ice and quiescent growth along vertical heat transfer tube. *Science in China Series B: Chemistry*, 48:75–82, 2005.

[205] ED Sloan Jr and F Fleyfel. A molecular mechanism for gas hydrate nucleation from ice. *AIChE Journal*, 37(9):1281–1292, 1991.

[206] Sheng Dai, Joo Yong Lee, and J Carlos Santamarina. Hydrate nucleation in quiescent and dynamic conditions. *Fluid Phase Equilibria*, 378:107–112, 2014.

[207] RS Volkov and PA Strizhak. Using planar laser induced fluorescence to determine temperature fields of drops, films, and aerosols. *Measurement*, 153:107439, 2020.

Appendix A

Fluorescence spectra of cyclopentane

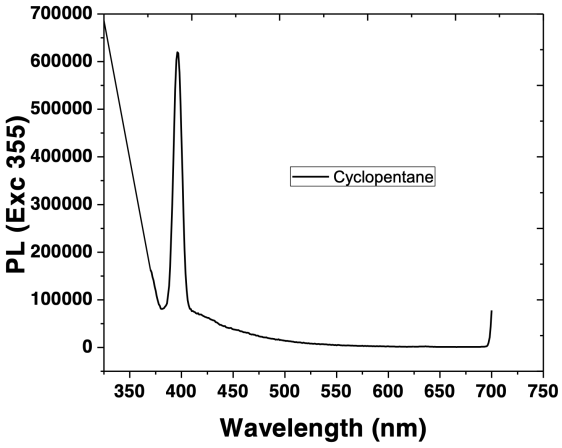


Figure A.1: Fluorescence spectra of cyclopentane at an excitation wavelength of 355 nm. The peak is artifact from the instrument.

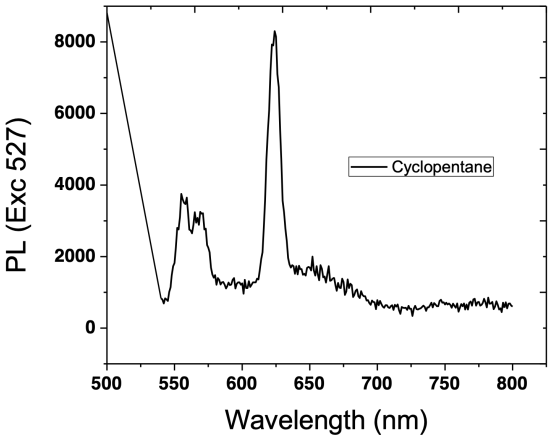


Figure A.2: Fluorescence spectra of cyclopentane at an excitation wavelength of 527 nm. The peak is artifact from the instrument.

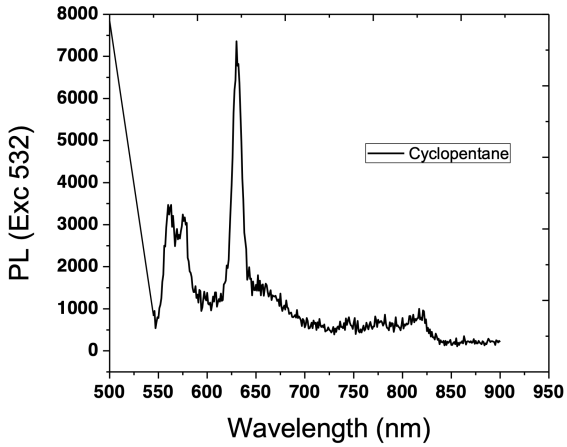


Figure A.3: Fluorescence spectra of cyclopentane at an excitation wavelength of 532 nm. The peak is artifact from the instrument.